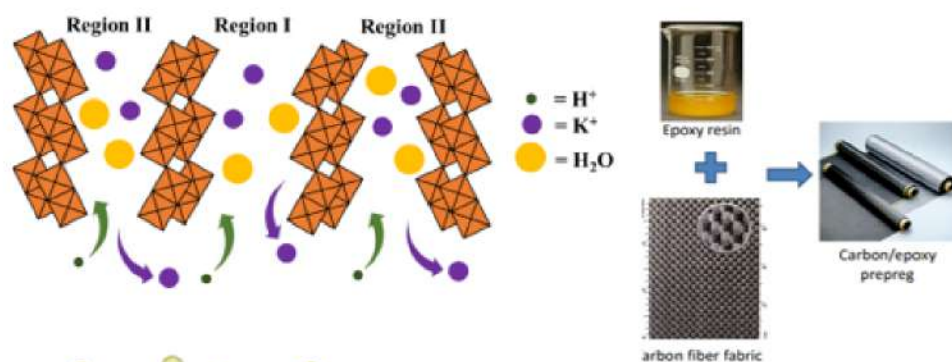
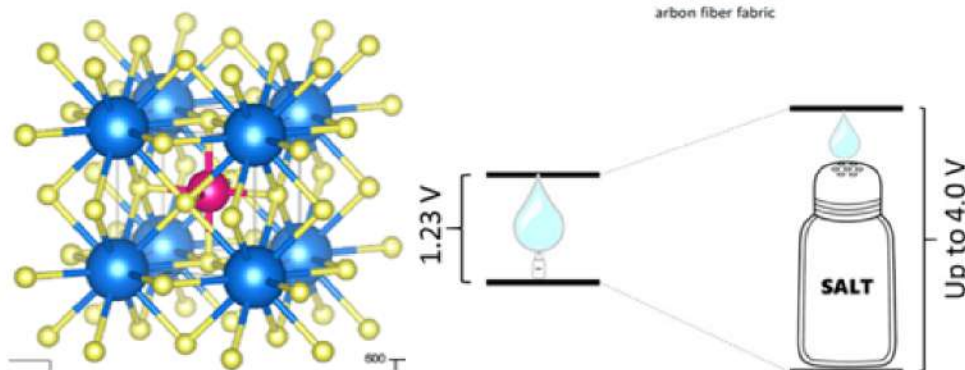


Eclética Química Journal

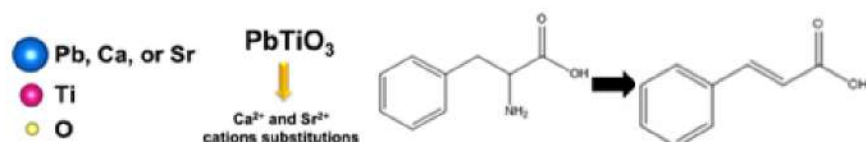
Volume 47 • special issue 2 • year 2022



Supercapacitors
Low-cost water-in-salt electrolytes for electrochemical energy storage applications: a short review



Thermal analysis
K₄Nb₆O₁₇ layered hexaniobate: revisiting the proton-exchanged reaction



Somatic embryos

Biosynthesis of tetrahydrobenzofuran neolignans in somatic embryos of *Ocotea catharinensis*

Thermal stability

Phenylalanine ammonia lyase: new insights from Piperaceae species

Cure kinetic

Studies of curing cycle of carbon fiber/epoxy resins (8552® and M21®) prepreps based on thermal and rheological analyses

Molecular docking

Analysis of the Pb_{0.30}Ca_xSr_yTiO₃ ternary system: The effect of Ca²⁺ and Sr²⁺ cations on the electrical properties of PbTiO₃



UNIVERSIDADE ESTADUAL PAULISTA

Reitor

Pasqual Barretti

Vice-Reitora

Maysa Furlan

Pró-Reitora de Graduação

Celia Maria Giacheti

Pró-Reitora de Pós-Graduação

Maria Valnice Boldrin

Pró-Reitor de Pesquisa

Edson Cocchieri Botelho

Pró-Reitor de Extensão Universitária e Cultura

Raul Borges Guimarães

Pró-Reitor de Planejamento Estratégico e Gestão

Estevão Tomomitsu Kimpara



INSTITUTO DE QUÍMICA

Diretor

Sidney José Lima Ribeiro

Vice-Diretora

Denise Bevilaqua

Editorial Team

Editor-in-Chief

Prof. Assis Vicente Benedetti, São Paulo State University, Institute of Chemistry, Araraquara, Brazil

Editors

Prof. Antonio Eduardo Mauro, São Paulo State University, Institute of Chemistry, Araraquara, Brazil

Prof. Horacio Heinzen, University of the Republic, Faculty of Chemistry, Montevideo, Uruguay

Prof. Marcos Carlos de Mattos, Federal University of Ceará, Center of Sciences, Fortaleza, Brazil

Prof. Maria Célia Bertolini, São Paulo State University, Institute of Chemistry, Araraquara, Brazil

Prof. Patrícia Hatsue Suegama, Federal University of Grande Dourados, Faculty of Exact and Technological Sciences, Dourados, Brazil

Prof. Paulo Clairmont Feitosa Lima Gomes, São Paulo State University, Institute of Chemistry, Araraquara, Brazil

Editorial Board

Prof. Bayardo Baptista Torres, University of São Paulo, Institute of Chemistry, São Paulo, Brazil

Prof. Enric Brillas, University of Barcelona, Faculty of Chemistry, Barcelona, Spain

Prof. Francisco de Assis Leone, University of São Paulo, Faculty of Philosophy, Sciences and Literature, Ribeirão Preto, Brazil

Prof. Ivano Gerardt Rolf Gutz, University of São Paulo, Institute of Chemistry, São Paulo, Brazil

Prof. Jairton Dupont, Federal University of Rio Grande do Sul, Institute of Chemistry, Porto Alegre, Brazil

Prof. José Antônio Maia Rodrigues, University of Porto, Faculty of Sciences, Porto, Portugal

Prof. Lauro Kubota, University of Campinas, Institute of Chemistry, São Paulo, Brazil

Prof. Massuo Jorge Kato, University of São Paulo, Institute of Chemistry, São Paulo, Brazil

Prof. Roberto Santana da Silva, University of São Paulo, Faculty of Pharmaceutical Sciences, Ribeirão Preto, Brazil

Prof. Verónica Cortés de Zea Bermudez, University of Trás-os-Montes and Alto Douro, School of Life and Environmental Sciences, Vila Real, Portugal

EDITORIAL PRODUCTION

Ctrl K Produção Editorial – Araraquara, Brazil

digite@ctrlk.com.br

Editorial**Waldemar Saffioti, The Centennial Birth of a Distinguished Professor (1922-2022)**

April 16th, 1999 marks the day the eminent chemistry professor Waldemar Saffioti passed away in Araraquara at age 77. Among Saffioti's numerous life accomplishments, there are three, in particular, that summarize his visionary and entrepreneurial spirit. Firstly, he gave birth to the first Chemistry Course in Sao Paulo's countryside, located in Araraquara city, which became the embryo of the current Araraquara Chemistry Institute – UNESP (IQAr). Secondly, in 1976, Saffioti started the Eclética Química Journal still published nowadays by the IQAr, which has adopted the peer review system since its origin. Lastly, the renowned professor wrote some of the chemistry books that helped set the standard for chemistry education and were widely adopted for a long time throughout Brazil.

Born on January 2nd, 1922, in Bragança Paulista (SP), Saffioti became Bachelor in Chemistry from the University of São Paulo (USP), in 1942. As a chemist, he worked at R.F. Matarazzo and F. Endoquímica S.A. industries for 6 months and as a technical assistant at the Rubber Laboratory of the Instituto Agrônômico do Norte (Ministry of Agriculture) in Belém (PA), Brazil, in association with North American scientists from April 1944 – December 1945.

From January 1946 to October 1948, Saffioti performed his doctoral degree at USP supervised by Prof. Heinrich Reimboldt. On November 13th, 1948, he presented his thesis "On sulfoxide and sulenoxide addition compounds with Aryl-Carbinol". During the same period, he taught chemistry at Colégio Estadual de Mogi das Cruzes (a high school from 7/1946 to 3/1949). From April 1949 to April 1956, he taught Chemistry and Physics at the Public Force Officers' Course in Sao Paulo State. In 1950, he was appointed effective Chemistry Teacher at Instituto de Educação Caetano de Campos (a high school in SP). On this occasion, Saffioti built a reputation in chemistry education when, in collaboration with Prof. Geraldo Camargo de Carvalho, he wrote a collection of three books to suit the three years of Chemistry High School education. Shortly after being released, Saffioti and Camargo's Chemistry Collection became a bestseller in Brazil being extensively adopted for nearly 20 years.

Saffioti became a Bachelor in Physics, in 1955, with a particular interest in Nuclear Energy. From April to July 1956, he worked as an Associate Researcher at Rio de Janeiro's Radiochemistry Laboratory of the Brazilian Center for Physical Research. In August 1956, he received a scholarship from the National Research Council (CNPq) to sponsor his training in Nuclear Energy at Pennsylvania State University and at Argonne National Laboratory. Between July 1957 and May 1958, he helped install the nuclear reactor from the Atomic Energy Institute of SP. In 1958, he was appointed Assistant Professor at the Department of Mineralogy and Petrography (USP), taught Physics and Chemistry of Minerals, and gave several lectures for research centers and universities in the fields of chemistry, nuclear energy, reactors, minerals, and Brazilian rubber. Those experiences led him to write a book on Principles of Nuclear Energy, edited four times between 1978-1982.

In 1962, Saffioti was already residing in Araraquara and dedicating great energy to overcoming the challenges involved in the foundation of the first Chemistry Course in SP's countryside. Such challenges involved the construction and installation of laboratories, finding qualified technical-administrative staff, financing and purchasing specialized equipment and chemicals, elaborating the course's curriculum, installing a fully equipped library, and subscribing to scientific journals. In addition to that, due to the lack of qualified professors in the region, Saffioti taught most of the classes until the newly formed chemistry course started to bear fruits. During start-up period, he was also elected several times Head of the Chemistry Department at the current Faculdade de Filosofia, Ciências e Letras de Araraquara (FFCLA).

In 1967, Saffioti presented his Lecturer Thesis entitled "On Some Asymmetric Intermolecular Complexes Created by Protonic Bonding" dealing mostly with hydrogen bonding. He supervised 61 Scientific Initiation projects and six PhDs, besides carrying out more than 100 scientific research. In 1968, he published a schoolbook on Chemistry Principles edited by Companhia Editora Nacional. In 1970, he did an internship at the CNRS Physical

Chemistry Laboratory in Vitry-Thiais, France, studying hydrogen-bonded binary complexes involving triphenylcarbinol and diphenylsulfoxide, diphenylselenoxide and triphenylarsinoxide using Raman and Infrared spectroscopies. Saffioti retired from academic life, in 1978, but remained politically active and was elected Director of the Unesp Chemistry Institute (IQAr) for the period from November 1984 to November 1988. He also became involved in local and national politics.

Saffioti's life accomplishments and utmost dedication to the student body were registered in significant tributes. When the Department of Chemistry (FFCLA) was transformed into the Araraquara's Chemistry Institute (1977), the IQAr's student association was permanently baptized as "DAWS" (Academic Directory Waldemar Saffioti), and the Regional Araraquara/São Carlos/Ribeirão Preto of the Brazilian Chemical Society bears the name "Regional Interior Paulista Waldemar Saffioti".

Contributions to this issue

A recent mini-review summarizes the latest developments on water-in-salt electrolytes produced with low-cost salts and with perspectives on their application in electrochemical energy storage. They represent an emerging field in batteries and supercapacitors that may overcome the safety concerns about the potential flammability of typical organic electrolytes. Following is described the layered hexaniobate of $K_4Nb_6O_{17}$ composition and its derivatives comprise nanostructured materials with suitable properties for application in catalysis, electrochemistry, and energy. This work focuses on the proton exchange efficiency of the $K_4Nb_6O_{17}$ and the phase resulting from the exchange of K^+ by H^+ ion. Another article describes the use of somatic embryos of *Ocotea catharinensis* as a model to investigate the biosynthetic pathway of tetrahydrobenzofuran neolignan formation utilizing feeding ^{13}C -labelled precursors. It was shown that using the protein fraction from the embryogenic cultures, the substrate coniferyl acetate was converted into isoeugenol, a putative precursor of neolignan formation. Afterward, the phenylpropanoids involved in the lignification process and the formation of numerous secondary compounds in plants with a variety of biological activities are described. The enzyme phenylalanine ammonia-lyase extracted from *Piper* and *Peperomia* species mediates the key entry point to the general phenylpropanoid pathway. In *Peperomia* species, the phenylpropanoid biosynthetic pathway seems to produce mainly tetrahydrofuran lignans of biological interest. In the sequence, the characterization of prepreg produced with two different commercial epoxy resins is described and the prepreg is used to investigate and optimize the curing cycle of structural components used in the aerospace industry. Completes this issue the research about the synthesis of powder and thin films of $Pb_{0.30}Ca_{0.10}Sr_{0.60}TiO_3$ and $Pb_{0.30}Ca_{0.60}Sr_{0.10}TiO_3$ ternary systems by the polymeric precursor method and the deposition of thin films on the Si/SiO₂/Ti/Pt substrate. The effects of Sr^{2+} and Ca^{2+} substitutions on the electrical and structural properties of the BaTiO₃ were theoretical and experimentally investigated.

This author would like to express his gratitude to Professor Antonio Carlos Massabni and Professor Cristo Bladimiro Melios, authors of the first IN MEMORIAN¹ article for the collaboration in writing and revising this Editorial.

Assis Vicente Benedetti

Editor-in-Chief

Eclet. Quim. J.

¹ The Eclética Química Journal thanks Química Nova for the permission of using the article "IN MEMORIAN", *Quim. Nova.* **1999**, 22 (4), 630-631, by A. C. Massabni, C. B. Melios and D. W. Franco.

Citation databases: Eclética Quim. J. is indexed



*Click on the images to follow the links.

EBSCO has no link available. The address is for subscribers only.

INSTRUCTIONS FOR AUTHORS

BEFORE YOU SUBMIT

1. Check **Eclét. Quim. J.'s focus and scope**

Eclética Química Journal is a peer-reviewed quarterly publication of the Institute of Chemistry of São Paulo State University (UNESP). It publishes original researches as articles, reviews and short reviews in **all areas of Chemistry**.

2. Types of papers

- a. Original articles
- b. Reviews
- c. Short reviews
- d. Communications
- e. Technical notes
- f. Articles in education in chemistry and chemistry-related areas

Manuscripts submitted for publication as full articles and communications must contain original and unpublished results and should not have been submitted elsewhere either partially or whole.

a. Original articles

The manuscript must be organized in sections as follows:

1. Introduction
 2. Experimental
 3. Results and Discussion
 4. Conclusions
- References

Sections titles must be written in bold and sequentially numbered; only the first letter should be in uppercase letter. Subsections, numbered as exemplified, should be written in normal and italic letters; only the first letter should be in uppercase letter.

Example:

1. Introduction

1.1 History

2. Experimental

2.1 Surface characterization

2.1.1 Morphological analysis

b. Reviews

Review articles should be original and present state-of-the-art overviews in a coherent and concise form covering the

most relevant aspects of the topic that is being revised and indicate the likely future directions of the field. Therefore, before beginning the preparation of a Review manuscript, send a letter (one page maximum) to the Editor with the subject of interest and the main topics that would be covered in the Review manuscript. The Editor will communicate his decision in two weeks. Receiving this type of manuscript does not imply acceptance to be published in **Eclét. Quím. J.** It will be peer-reviewed.

c. Short reviews

Short reviews should present an overview of the state-of-the-art in a specific topic within the scope of the Journal and limited to 5,000 words. Consider a table or image as corresponding to 100 words. Before beginning the preparation of a Short Review manuscript, send a letter (one page maximum) to the Editor with the subject of interest and the main topics that would be covered in the Short Review manuscript.

d. Communications

Communications should cover relevant scientific results and are limited to 1,500 words or three pages of the Journal, not including the title, authors' names, figures, tables and references. However, Communications suggesting fragmentation of complete contributions are strongly discouraged by Editors.

e. Technical notes

Descriptions of methods, techniques, equipment or accessories developed in the authors' laboratory, as long as they present chemical content of interest. They should follow the usual form of presentation, according to the peculiarities of each work. They should have a maximum of 25 pages, including figures, tables, diagrams, etc.

f. Articles in education in chemistry and chemistry-correlated areas

Research manuscript related to undergraduate teaching in Chemistry and innovative experiences in undergraduate and graduate education. They should have a maximum of 25 pages, including figures, tables, diagrams, and other elements.

3. Special issues

Special issues with complete articles dedicated to Symposia and Congresses and to special themes or in honor of scientists with relevant contributions in Chemistry and correlate areas can be published by **Eclét. Quím. J.** under the condition that a previous agreement with Editors is established. All the guides of the journal must be followed by the authors.

4. Approval

Ensure all authors have seen and approved the final version of the article prior to submission. All authors must also approve the journal you are submitting to.

ETHICAL GUIDELINES

Before starting the submission process, please be sure that **all ethical aspects mentioned below were followed.** Violation of these ethical aspects may preclude authors from submitting or publishing articles in **Eclét. Quím. J.**

a. Coauthorship: The corresponding author is responsible for listing as coauthors only researchers who have really taken part in the work, for informing them about the entire manuscript content and for obtaining their permission to submit and publish it.

b. Nonauthors: Explicit permission of a nonauthor who has collaborated with personal communication or discussion to the manuscript being submitted to **Eclet. Quím. J.** must be obtained before being cited.

c. Unbiased research: Authors are responsible for carefully searching for all the scientific work relevant to their reasoning irrespective of whether they agree or not with the presented information.

d. Citation: Authors are responsible for correctly citing and crediting all data taken from other sources. This requirement is not necessary only when the information is a result of the research presented in the manuscript being submitted to **Eclet. Chem. J.**

e. Direct quotations: The word-for-word reproduction of data or sentences as long as placed between quotation marks and correctly cited is not considered ethical deviation when indispensable for the discussion of a specific set of data or a hypothesis.

f. Do not cite: Master's Degree dissertations and PhD theses are not accepted; instead, you must cite the publications resulted from them.

g. Plagiarism: Plagiarism, self-plagiarism, and the suggestion of novelty when the material was already published are unaccepted by **Eclet. Quím. J.** Before reviewing a manuscript, the **Turnitin antiplagiarism software** will be used to detect any ethical deviation.

h. Simultaneous submissions of the same manuscript to more than one journal is considered an ethical deviation and is conflicted to the declaration has been done below by the authors.

i. Studies with humans or other animals: Before submitting manuscripts involving human beings, materials from human or animals, the authors need to confirm that the procedures established, respectively, by the institutional committee on human experimentation and Helsinki's declaration, and the recommendations of the animal care institutional committee were followed. Editors may request complementary information on ethical aspects.

COPYRIGHT NOTICE

The corresponding author transfers the copyright of the submitted manuscript and all its versions to **Eclet. Quím. J.**, after having the consent of all authors, which ceases if the manuscript is rejected or withdrawn during the review process.

When a published manuscript in **Eclet. Quím. J.** is also published in other Journal, it will be immediately withdrawn from **Eclet. Quím. J.** and the authors informed of the Editor decision.

Self-archive to institutional, thematic repositories or personal webpage is permitted just after publication. The articles published by **Eclet. Quím. J.** are licensed under the **Creative Commons Attribution 4.0 International License**.

PUBLICATION CHARGES

Eclética Química Journal is supported by the Institute of Chemistry/UNESP and publication is free of charge for authors.

MANUSCRIPT PREPARATION

COVER LETTER

We provide a template to help you prepare your cover letter. To download it, click [here](#).

The cover letter **MUST** include:

1. Identification of authors

- a. The authors' full names (they must be written in full and complete, separated by comma)

João M. José	Incorrect
J. M. José	Incorrect
João Maria José	Correct!

- b. E-mail addresses and affiliations (**neither more nor less than two instances**) of all authors;
- c. ORCID ID links;
- d. A plus sign (+) indicating the corresponding author.

Example:

Author Full Name¹⁺, Author Full Name²

1. University, Faculty or Institute, City, Country.
2. Company, Division or Sector or Laboratory, City, Country.

+ Author 1: address@mail.com, ORCID: <https://orcid.org/xxxx-xxxx-xxxx-xxxx>

Author 2: address@mail.com, ORCID: <https://orcid.org/xxxx-xxxx-xxxx-xxxx>

2. Authors' contribution

We request authors to include author contributions according to CRediT taxonomy standardized contribution descriptions. **CRediT (Contributor Roles Taxonomy)** is a high-level taxonomy, including 14 roles, that can be used to represent the roles typically played by contributors to scientific scholarly output. The roles describe each contributor's specific contribution to the scholarly output.

- a. Please, visit this link (<https://casrai.org/credit/>) to find out which role(s) the authors fit into;
- b. **Do not modify the role names; do not write "all authors" in any role. Do not combine two or more roles in one line.**
- c. If there are any roles that no author has engaged in (such as funding in papers that were not funded), write "Not applicable" in front of the name of the role;
- d. Write the authors' names according to the **American Chemistry Society (ACS) citation style**.

Example:

Conceptualization: Foster, J. C.; O'Reilly, R. K.

Data curation: Varlas, S.; Couturaud, B.; Coe, J.; O'Reilly, R. K.

Formal Analysis: Foster, J. C.; Varlas, S.

Funding acquisition: Not applicable.

Investigation: Foster, J. C.; O'Reilly, R. K.

Methodology: Coe, J.; O'Reilly, R. K.

Project administration: O'Reilly, R. K.

Resources: Coe, J.

Software: Not applicable.

Supervision: O'Reilly, R. K.

Validation: Varlas, S.; Couturaud, B.

Visualization: Foster, J. C.

Writing – original draft: Foster, J. C.; Varlas, S.; Couturaud, B.; Coe, J.; O'Reilly, R. K.

Writing – review & editing: Foster, J. C.; Varlas, S.; Couturaud, B.; Coe, J.; O'Reilly, R. K.

4. Indication of reviewers

We kindly ask the authors to suggest **five** suitable reviewers, providing full name, affiliation, and email.

5. Other information

- a. The authors must write one paragraph remarking the novelty and relevance of the work;
- b. The corresponding author must declare, on behalf of the other authors, that the manuscript being submitted is original and its content has not been published previously and is not under consideration for publication elsewhere;
- c. The authors must inform if there is any conflict of interest.

6. Acknowledgements and funding

Acknowledgements and funding information will be requested after the article is accepted for publication.

7. Data availability statement

A data availability statement informs the reader where the data associated with your published work is available, and under what conditions they can be accessed. Therefore, authors must inform if:

Data will be available upon request;

All dataset were generated or analyzed in the current study; or

Data sharing is not applicable.

MANUSCRIPT

We provide a template to help you prepare your manuscript. To download it, click [here](#).

1. General rules

Only manuscripts written in English will be accepted. British or American usage is acceptable, but they should not be mixed. Non-native English speakers are encouraged to have their manuscripts professionally revised before submission.

Manuscripts must be sent in editable files as *.doc, *.docx or *.odt. The text must be typed using font style Times New Roman and size 12. Space between lines should be 1.5 mm and paper size A4, top and bottom margins 2.5 cm, left and right margins 2.0 cm.

All contributions must include an **abstract** (170 words maximum), **three to five keywords** and a **graphical abstract** (8 cm wide × 8 cm high).

Supplementary information: all type of articles accepts supplementary information (SI) that aims at complementing the main text with material that, for any reason, cannot be included in the article.

TITLE

The title should be concise, explanatory and represent the content of the work. The title must have only the first letter of the sentence in uppercase. The following are not allowed: acronyms, abbreviations, geographical location of the research, en or em dashes (which must be replaced by a colon). Titles do not have full point.

ABSTRACT

Abstract is the summary of the article. The abstract must be written as a running text not as structured topics, but its content should present background, objectives, methods, results, and conclusion. It cannot contain citations. The text should be written in a single paragraph with a **maximum of 170 words**.

KEYWORDS

Keywords are intended to make it easier for readers to find the content of your text. As fundamental tools for database indexing, they act as a gateway to the text. The correct selection of keywords significantly increases the chances that a document will be found by researchers on the topic, and consequently helps to promote the visibility of an article within a myriad of publications.

FIGURES, TABLES AND EQUATIONS

Figures, tables and equations must be written with initial capital letter followed by their respective number and period, in bold, without adding zero “**Table 1**”, preceding an explanatory title. Tables, Figures and Equations should appear after the first citation and should be numbered according to the ascending order of appearance in the text (1, 2, 3...).

Figures, tables, schemes and photographs already published by the same or different authors in other publications may be reproduced in manuscripts of **Eclet. Quim. J.** only with permission from the editor house that holds the copyright.

Nomenclature, abbreviations, and symbols should follow IUPAC recommendations.

DATA AVAILABILITY STATEMENT

The data availability statement informs the reader where the data associated with your work is available, and under what conditions they can be accessed. They also include links (where applicable) to the data set.

- The data are available in a data repository (cite repository and the DOI of the deposited data);
- The data will be available upon request;
- All data sets were generated or analyzed in the current study;
- Data sharing is not applicable (in cases where no data sets have been generated or analyzed during the current study, it should be declared).

GRAPHICAL ABSTRACT

The graphical abstract must summarize the manuscript in an interesting way to catch the attention of the readers. As already stated, it must be designed with 8 cm wide × 8 cm high, and a 900-dpi resolution is mandatory for this journal. It must be submitted as *.jpg, *.jpeg, *.tif or *.ppt files as supplementary file.

We provide a template to help you prepare your GA. To download it, click [here](#).

SUPPLEMENTARY INFORMATION

When appropriate, important data to complement and a better comprehension of the article can be submitted as Supplementary File, which will be published online and will be made available as links in the original article. This might include additional figures, tables, text, equations, videos or other materials that are necessary to fully document the research contained in the paper or to facilitate the readers' ability to understand the work.

Supplementary material should be presented in appropriate .docx file for text, tables, figures and graphics. All supplementary figures, tables and videos should be referred in the manuscript body as "Table S1, S2...", "Fig. S1, S2..." and "Video S1, S2 ...".

At the end of the main text the authors must inform: This article has supplementary information.

Supplementary information will be located following the article with a different DOI number from that of the article, but easily related to it.

CITATION STYLE GUIDE

From 2021 on, the **Eclat. Quim. J.** will follow the **ACS citation style**.

Indication of the sources is made by authorship and date. So, the reference list is organized alphabetically by author.

Each citation consists of two parts: the in-text citation, which provides brief identifying information within the text, and the reference list, a list of sources that provides full bibliographic information.

We encourage the citation of primary research over review articles, where appropriate, in order to give credit to those who first reported a finding. Find out more about our commitments to the principles of **San Francisco Declaration on Research Assessment (DORA)**.

What information you must cite?

- a. Exact wording taken from any source, including freely available websites;
- b. Paraphrases of passages;
- c. Summaries of another person's work;
- d. Indebtedness to another person for an idea;
- e. Use of another researchers' work;
- f. Use of your own previous work.

You do not need to cite **common knowledge**.

Example:

Water is a tasteless and odorless liquid at room temperature (common knowledge, no citation needed)

In-text citations

You can choose to cite your references within or at the end of the phrase, as showed below.

Within the cited information:

One author: Finnegan states that the primary structure of this enzyme has also been determined (2004).

Two authors: Finnegan and Roman state that the structure of this enzyme has also been determined (2004).

Three or more authors: Finnegan *et al.* state that the structure of this enzyme has also been determined (2004).

At the end of the cited information:

One author: The primary structure of this enzyme has also been determined (Finnegan, 2004).

Two authors: The primary structure of this enzyme has also been determined (Finnegan and Roman, 2004).

Three or more authors: The primary structure of this enzyme has also been determined (Finnegan *et al.*, 2004).

If you need to cite more than one reference in the same brackets, separate them with semicolon and write them in alphabetic order:

The primary structure of this enzyme was determined (Abel *et al.*, 2011; Borges, 2004; Castro *et al.*, 2021).

Bibliographic references

Article from scientific journals

Foster, J. C.; Varlas, S.; Couturaud, B.; Coe, J.; O'Reilly, R. K. Getting into Shape: Reflections on a New Generation of Cylindrical Nanostructures' Self-Assembly Using Polymer Building Block. *J. Am. Chem. Soc.* **2019**, *141* (7), 2742–2753. <https://doi/10.1021/jacs.8b08648>

Book

Hammond, C. *The Basics of Crystallography and Diffraction*, 4th ed.; International Union of Crystallography Texts on Crystallography, Vol. 21; Oxford University Press, 2015.

Book chapter

Hammond, C. Crystal Symmetry. In *The Basics of Crystallography and Diffraction*, 4th ed.; International Union of Crystallography Texts on Crystallography, Vol. 21; Oxford University Press, 2015; pp 99–134.

Book with editors

Mom the Chemistry Professor: Personal Accounts and Advice from Chemistry Professors Who Are Mothers, 2nd ed.; Woznack, K., Charlebois, A., Cole, R. S., Marzabadi, C. H., Webster, G., Eds.; Springer, 2018.

Website

ACS Publications Home Page. <https://pubs.acs.org/> (accessed 2019-02-21).

Document from a website

American Chemical Society, Committee on Chemical Safety, Task Force for Safety Education Guidelines. *Guidelines for Chemical Laboratory Safety in Academic Institutions*. American Chemical Society, 2016. <https://www.acs.org/content/dam/acsorg/about/governance/committees/chemicalsafety/publications/acs-safety-guidelines-academic.pdf> (accessed 2019-02-21).

Conference proceedings

Nilsson, A.; Petersson, F.; Persson, H. W.; Jönsson, H. Manipulation of Suspended Particles in a Laminar Flow. In *Micro Total Analysis Systems 2002, Proceedings of the μ TAS 2002 Symposium*, Nara, Japan, November 3–7, 2002; The Netherlands, 2002; pp 751–753. https://doi.org/10.1007/978-94-010-0504-3_50

Governmental and legislation information

Department of Commerce, United States Patent and Trademark Office. Section 706.02 Rejection of Prior Art [R-

07.2015]. *Manual of Patent Examining Procedure (MPEP)*, 9th ed., rev. 08.2017, last revised January 2018. <https://www.uspto.gov/web/offices/pac/mpep/s706.html#d0e58220> (accessed 2019-03-20).

Patent

Lois-Caballe, C.; Baltimore, D.; Qin, X.-F. Method for Expression of Small RNA Molecules within a Cell. US 7 732 193 B2, 2010.

Streaming data

American Chemical Society. Game of Thrones Science: Sword Making and Valyrian Steel. *Reactions*. YouTube, April 15, 2015. <https://www.youtube.com/watch?v=cHRcGoje4j4> (accessed 2019-02-28).

For more information, you can access the [ACS Style Quick Guide](#) and the [Williams College LibGuides](#).

SUBMITTING YOUR MANUSCRIPT

The corresponding author should submit the manuscript online by clicking [here](#). If you are a user, register by clicking [here](#).

At the **User home** page, click in **New submission**.

In Step 1, select a section for your manuscript, verify one more time if you followed all these rules in **Submission checklist**, add Comments for the Editor if you want to, and click Save and continue.

In Step 2, you will **upload your manuscript**. Remember it will pass through a double-blind review process. So, do not provide any information on the authorship.

In Step 3, enter **submission's metadata**: authors' full names, valid e-mail addresses and ORCID ID links (with "http" not "https"). Add title, abstract, contributors and supporting agencies, and the list of references.

In Step 4, upload the **cover letter**, the **graphical abstract** and other **supplementary material** you want to include in your manuscript.

In Step 5, you will be able to check all submitted documents in the **File summary**. If you are certain that you have followed all the rules until here, click in **Finish submission**.

REVIEW PROCESS

The time elapsed between the submission and the first response of the reviewers is around three months. The average time elapsed between submission and publication is around seven months.

Resubmission (manuscripts "rejected in the present form" or subjected to "revision") must contain a letter with the responses to the comments/criticism and suggestions of reviewers/editors should accompany the revised manuscript. All modifications made to the original manuscript must be highlighted.

If you want to check our Editorial process, click [here](#).

EDITOR'S REQUIREMENTS

Authors who have a manuscript accepted in **Eclet. Quim. J.** may be invited to act as reviewers.

Only the authors are responsible for the correctness of all information, data and content of the manuscript submitted to **Eclet. Quim. J.** Thus, the Editors and the Editorial Board cannot accept responsibility for the correctness of the material published in **Eclet. Quim. J.**

Proofs

After accepting the manuscript, **Eclet. Quim. J.** technical assistants will contact you regarding your manuscript page proofs to correct printing errors only, i.e., other corrections or content improvement are not permitted. The proofs shall be returned in three working days (72 h) via email.

Appeal

Authors may only appeal once about the decision regarding a manuscript. To appeal against the Editorial decision on your manuscript, the corresponding author can send a rebuttal letter to the editor, including a detailed response to any comments made by the reviewers/editor. The editor will consider the rebuttal letter, and if deemed appropriate, the manuscript will be sent to a new reviewer. The Editor decision is final.

Contact

If you have any question, please contact our team:

Prof. Assis Vicente Benedetti
Editor-in-Chief
ecletica.iq@unesp.br

Letícia Amanda Miguel and Jéssica Odoni
Technical support
ecletica@ctrlk.com.br

SUMMARY

EDITORIAL BOARD	3
EDITORIAL.....	4
DATABASE.....	6
INSTRUCTIONS FOR AUTHORS	7

SHORT REVIEW

Low-cost water-in-salt electrolytes for electrochemical energy storage applications: a short review	18
<i>Alan Massayuki Perdizio Sakita, Rodrigo Della Noce</i>	

ORIGINAL ARTICLES

$K_4Nb_6O_{17}$ layered hexaniobate: revisiting the proton-exchanged reaction.....	30
<i>Mariana Pires Figueiredo, Vera Regina Leopoldo Constantino</i>	
Biosynthesis of tetrahydrobenzofuran neolignans in somatic embryos of <i>Ocotea catharinensis</i>	37
<i>Érica Luiz dos Santos, Eny Iochevet Segal Floh, Massuo Jorge Kato</i>	
Phenylalanine ammonia lyase: new insights from Piperaceae species	67
<i>Andreia de Araújo Morandim-Giannetti, Lidiane Gaspareto Felipe, Vânia Aparecida de Freitas Formenton Macedo dos Santos, Massuo Jorge Kato, Maysa Furlan</i>	
Studies of curing cycle of carbon fiber/epoxy resins (8552 [®] and M21 [®]) prepregs based on thermal and rheological analyses	83
<i>Sheila Marques Silva, Carolina Paiva Nascimento Silva, Thiago de Carvalho Silva, Mirabel Cerqueira Rezende, Edson Cocchieri Botelho, Michelle Leali Costa</i>	
Analysis of the $Pb_{0.30}Ca_xSr_yTiO_3$ ternary system: The effect of Ca^{2+} and Sr^{2+} cations on the electrical properties of $PbTiO_3$	100
<i>Amanda Fernandes Gouveia, Lara Kelly Ribeiro, Marcelo Assis, Elson Longo, Juan Andrés, Fenelon Martinho Lima Pontes</i>	

Low-cost water-in-salt electrolytes for electrochemical energy storage applications: a short review

Alan Massayuki Perdizio Sakita¹⁺, Rodrigo Della Noce²

1. University of São Paulo, São Carlos Institute of Chemistry, São Carlos, Brazil.
2. Federal University of Pará, Institute of Exact and Natural Sciences, Belém, Brazil.

+Corresponding author: Alan Massayuki Perdizio Sakita, **Phone:** +551633738042, **Email address:** ampsakita@gmail.com

ARTICLE INFO

Article history:

Received: May 11, 2021

Accepted: August 28, 2021

Updated: July, 28, 2022

Published: August 17, 2022

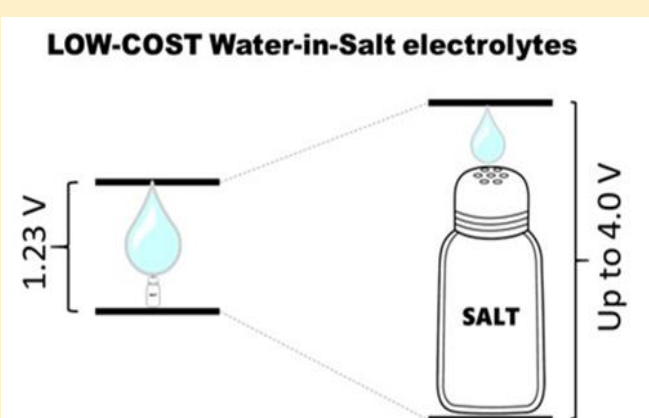
Keywords

1. water-in-salt electrolytes
2. batteries
3. supercapacitors
4. electrochemical energy storage

Section Editor: Assis Vicente Benedetti

ABSTRACT: The utilization of aqueous electrolytes is an emerging field in batteries and supercapacitors to overcome the safety concerns about the flammability of the typical organic electrolytes employed in these devices. Yet, aqueous diluted electrolytes limit the electrochemical stability window (ESW) restricting the device cell voltage. Surprisingly, the use of water-in-salt electrolytes (WISEs) has demonstrated the capability of suppressing the free water content of solution leading to an ESW expansion. On the other hand, since the first report of WISEs, most of these electrolytes have employed expensive salts for their preparation, hindering the replacement of the current electrolytes, utilized in energy storage devices,

by WISEs. On the other hand, in recent years, the employment of low-cost salts for WISEs has been investigated as a strategy to circumvent these economic issues revealing to be feasible for widening the cell voltage. Herein, we summarize the recent progress and developments of WISEs produced with low-cost salts providing the challenges and perspectives toward their application in electrochemical energy storage.



CONTENTS

1. Introduction
2. Brief fundamental aspects
3. Water in single salt electrolyte (WISSE)
4. Water in bi-salt (WIBSE)
5. Redox-active WISEs
6. Is the performance of WISE employed in EES devices competitive?
7. Perspectives

- Authors' contribution**
Data availability statement
Funding
Acknowledgments
References



1. Introduction

Since the pioneering work of [Suo *et al.* \(2015\)](#), water-in-salt electrolytes (WISEs) have attracted much attention in the field of electrochemical energy storage (EES) by allowing the use of aqueous electrolytes in Li-ion batteries (LIBs). However, [Smith and Dunn \(2015\)](#) highlighted the cost of the salt used by Suo's group to prepare their WISEs, suggesting the investigation of less expensive salts to produce such electrolytes. The insights of this work were readily accepted by the scientific community that started to explore different strategies to overcome this cost issue. WISEs are simply formed by dissolving a large amount of salts, in general, more than 5 molal (mol kg^{-1}) into water ([Gambou-Bosca and Bélanger, 2016](#); [Suo *et al.*, 2015](#)). At these high salt concentrations, the activity of water is suppressed, and the electrochemical stability window (ESW) can be broadened up to 4.0 V, exceeding by far the thermodynamic limit of water decomposition of 1.23 V. This enhancement in ESW leads to EES devices, such as batteries and supercapacitors, with wider cell voltage, an important parameter to improve their energy density. Although the improvements in ESW by using WISEs in comparison with typical diluted solutions, the main advantage of these solvents is their non-flammable nature, which makes them promising to replace the current organic electrolyte used in Li-ion batteries and supercapacitors. Yet, to promote the large-scale application of WISEs their costs need to be competitive enough to allow their applications mentioned above. In the early developments, WISEs were mainly composed of lithium salts with fluorinated organic anions, such as lithium bis(trifluoromethylsulfonyl)imide (LiTFSI) ([Gambou-Bosca and Bélanger, 2016](#); [Suo *et al.*, 2015](#); [C. Yang *et al.*, 2017](#)). The scarce content of lithium in Earth's crust and the technical issues in preparing such anions (TFSI) make this salt costly compared with the traditional organic electrolytes. In a brief search for analytical grade components of both electrolytes, 10 g of LiTFSI has an average price about 90 USD, while 100 mL of 1.0 mol L^{-1} LiPF_6 in propylene costs approximately 150 USD. Nevertheless, this amount of 10 g of LiTFSI only allows preparing a few milliliters of WISE. Therefore, the development of cost-effective WISEs has been a constant challenge for many scientists around the world to extend the utilization of these promising electrolytes. In this review, we discuss and explore the recent efforts on the development of low-cost WISEs for energy storage purposes and enumerate opportune strategies to circumvent their status. Specifically, the fundamental aspects of WISEs are

discussed in terms of their preparation and characteristics. The concepts of water-in-single-salt-electrolyte (WISSE) and water in bi-salt electrolyte (WIBSE), as well as their state-of-the-art, are also provided. Additionally, the current trend in redox-active WISEs are reviewed. Regarding WISEs application, their utilization in EES devices is discussed besides some future directions and perspectives in order to boost their use in both academia and industry.

2. Brief fundamental aspects

The preparation of WISEs is simply done by two main components: water and salt. Yet, the salt must meet the high solubility requirement to be an eligible candidate for preparing this kind of electrolyte. Most of the highly soluble salts are composed of cations and anions with a large difference in their sizes. For instance, alkaline chlorides have the highest solubility for LiCl ($\sim 20 \text{ mol L}^{-1}$) which has a ratio cation/anion size of 0.53, while NaCl ($\sim 6 \text{ mol L}^{-1}$) and KCl ($\sim 4.4 \text{ mol L}^{-1}$) shown 0.69 and 0.91 of ratio, respectively. Additionally, RbCl and CsCl show higher solubility than that of KCl. Also, such a tendency is not observed for acetates that display the crescent solubility following the sequence $\text{KAc} > \text{NaAc} > \text{LiAc}$. Despite the solubility of several salts being easily found in Handbooks, the lattice and hydration energy play important roles in the future development of novel WISES since these energies are directly related to the salt solubility.

As expected, these salts need to dissociate in water forming ions that work as charge carriers in the electrolyte. Contrary to dilute solutions where those ions are surrounded by a high content of water molecules forming the solvation sheath, in WISEs the ions experience unusual ion solvation due to the low water content in the solution. [Figure 1a](#) shows a schematic of the microscopic structure of ions in dilute (salt-in-water) and high concentrated (water-in-salt) solution for LiTFSI salt ([Suo *et al.*, 2015](#)). It is seen that water molecules are arranged around the Li^+ in salt-in-water, while in WISE there is the formation of ions pair clusters solvated by a few water molecules. Due to the low water content in WISE, the free H_2O molecules are scarce in solution leading to a high stability potential window of the resulting electrolyte. Notwithstanding the suppression of the water-splitting reactions in WISE, the formation of the ion pair decreases the ionic conductivity of the electrolyte ([Chava *et al.*, 2020](#); [Lim *et al.*, 2018](#)), as shown in [Fig. 1b](#), which is a drawback to achieve high power density in energy storage devices.

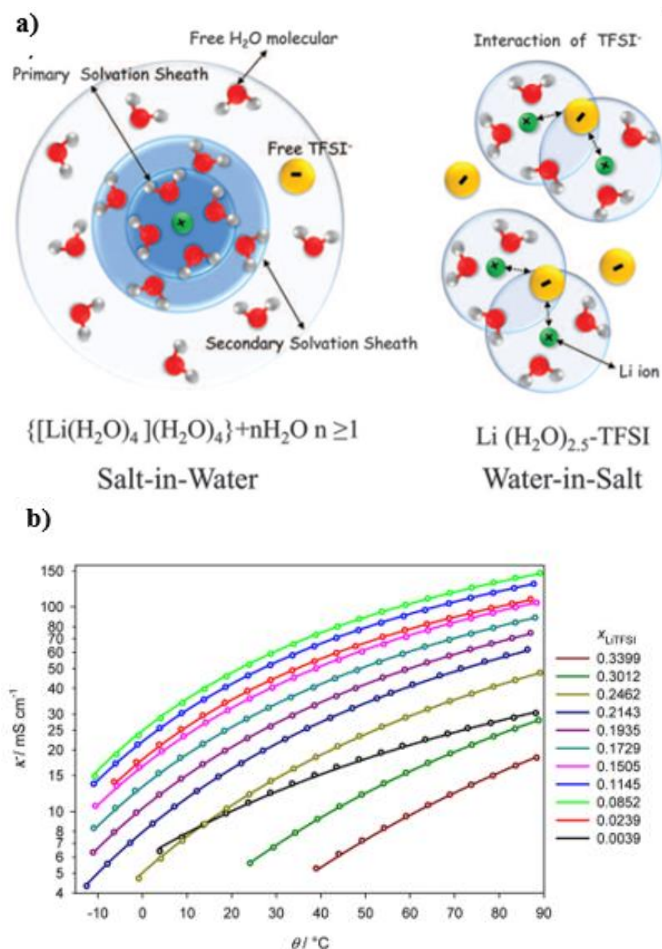


Figure 1. (a) Scheme of the Li⁺ first solvation sheath in salt-in-water and water-in-salt solutions (Suo *et al.*, 2015); (b) Ionic conductivity vs. Temperature for LiTFSI electrolytes in various mole fractions (Ding and Xu, 2018).

Source: from Suo *et al.* (2015) and Ding and Xu (2018) with permission from the American Association for the Advancement of Science and Journal of American Chemical Society, respectively.

3. Water in single salt electrolyte (WISSE)

When WISEs are prepared with only one salt dissolved in water, they have designated water-in-single-salt electrolyte (WISSE), which is the most common form observed in the current literature. WISSEs were the former concept of this class of electrolytes demonstrated by Suo *et al.* (2015), however, one year later a variant containing two salts, called water-in-bisalt electrolyte (WIBSE), was developed by the same authors (Suo *et al.*, 2016). In this section is explored the low-cost WISSEs (LC-WISSEs), displaying their drawbacks and advantages.

The same idea employed to LiTFSI was applied to different alkaline salts, e.g., acetates

(Chen *et al.*, 2020a; b; J. Han *et al.*, 2018; 2020a; b; Leonard *et al.*, 2018; Lukatskaya *et al.*, 2018; Stigliano *et al.*, 2021; Thareja and Kumar, 2021), formats (T. Liu *et al.*, 2019; S. Liu *et al.*, 2022), perchlorates (Bu *et al.*, 2019a; b; Dou *et al.*, 2019; Serva *et al.*, 2021; Thareja and Kumar, 2021; Y. Zhang *et al.*, 2022), and nitrates (Adil *et al.*, 2022; Chen *et al.*, 2021; Guo *et al.*, 2019; Thareja and Kumar, 2021), and most of them also allow the extension of the potential window, but with lower costs compared to those of Li-based salts. Even though Lithium salts are the most studied due to their current application in LIBs, only its chlorides and perchlorates can be used to prepare solutions with >8 mol kg⁻¹ concentrations. Yet, LiCl WISSEs have only a few studies for supercapacitor applications (Y. Zhu *et al.*, 2022). M. Lee *et al.* (2019) evaluated some typical Li and Na salts, such as sulfates, nitrates, and perchlorates for preparing WISSEs. Despite the high solubility of the nitrate, only the sodium perchlorate solutions, close to the saturation condition, displayed Raman band characteristics of water-in-salt behavior (Fig. 2a). Also, the authors performed linear sweep voltammetry in electrolytes with different contents of NaClO₄ to evaluate the ESW onto gold electrodes, showing that an increase of the concentration from 1 mol kg⁻¹ up to 17 mol kg⁻¹ of this salt permits to enlarge of the ESW in 1.0 V, reaching 2.7 V in supersaturated conditions. This value of ESW is consonant to that acquired by Bu *et al.* (2019a) which found 2.8 V (Fig. 2b) by using stainless steel electrodes in 17 mol kg⁻¹ NaClO₄ electrolyte. Yet, in these two studies, the Raman spectra of sodium perchlorate WISSE display a broader band at 3200-3500 cm⁻¹, instead of only a sharp peak (~3550 cm⁻¹) as observed for 21 mol kg⁻¹ LiTFSI electrolyte, which suggests the presence of free water molecules. Even if the molar ratio cation/water of LiTFSI and NaClO₄ WISSEs is similar, the presence of free water molecules in the latter is a drawback. For instance, LiTFSI WISEs were employed in LIBs with metallic lithium anode (C. Yang *et al.*, 2017) and demonstrated its low reactivity in this WISE. To the best of our knowledge, sodium perchlorate WISSEs have not been evaluated as its reactivity to alkali metals and previous reports describe the infeasibility of its direct use in conventional WISE (Im *et al.*, 2021). However, the NaClO₄ WISSE was applied to Na-ion batteries constructed with NaTi₂(PO₄)₃ anode and Na₄Fe₃(PO₄)₂(P₂O₇) cathode, displaying a 2 V cell voltage with long-term stability over 200 cycles (M. Lee *et al.*, 2019). This electrolyte was also applied to carbon-based symmetric supercapacitors (Bu *et al.*, 2019a) and exhibits a working potential window of 2.3 V for the assembled device with specific capacitance

(C_{sp}) ca. 30 F g^{-1} . Moreover, Ragone plot normalized by the electrolyte prices (Fig. 2c) reveals a better cost-benefit ratio for NaClO_4 than that of LiTFSI WISSE,

indicating that such perchlorate is a promising candidate for low-cost electrolytes.

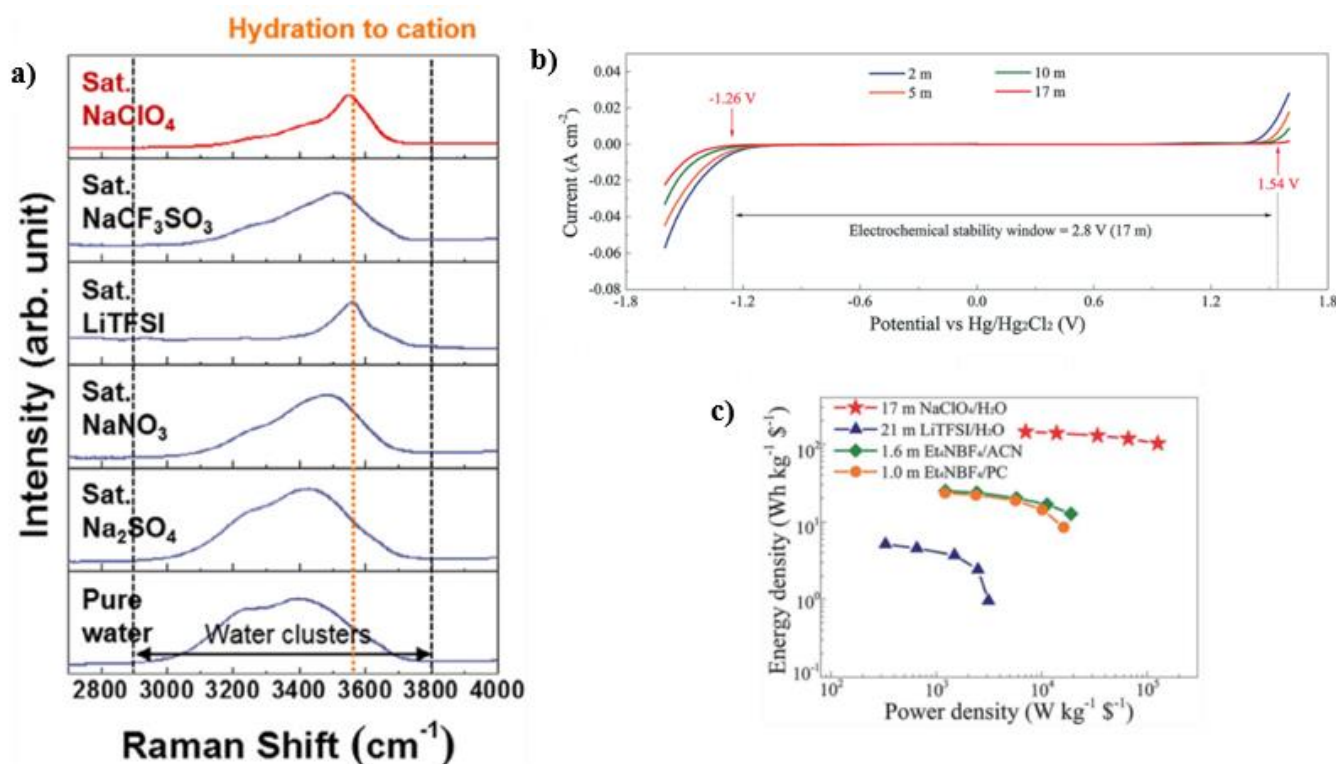


Figure 2. (a) Raman spectra of saturated solutions of Na_2SO_4 , NaNO_3 , LiTFSI , NaCF_3SO_3 and NaClO_4 in water (M. Lee *et al.*, 2019). (b) ESW of electrolytes containing different concentrations of NaClO_4 and (c) Ragone plot normalized by the electrolyte prices (Bu *et al.*, 2019a). The “m” inside the figures means mol kg^{-1} .”

Source: Reproduced from M. Lee *et al.* (2019) and Bu *et al.* (2019a) with permission from Elsevier and Royal Society of Chemistry, respectively.

Besides perchlorates, acetates and formates allow producing WISSEs with expressive molal concentrations, much higher than that of 21 mol kg^{-1} achieved with LiTFSI , what at first glance looks like a good option for water-in-salt electrolytes. However, only the potassium acetate and formate are soluble enough to reach the WISE condition, which restrains the application of these WISSEs, for example, in supercapacitors and K-ion batteries. Potassium acetate is allowed to produce 27 mol L^{-1} solutions at room temperature according to the solubility table provided in Handbooks, but concentrations up to 32 mol kg^{-1} is also reported in literature (J. Han *et al.*, 2018). The ESW of this electrolyte can achieve values around 3.2 V (Leonard *et al.*, 2018) and Raman spectrum reveals low-intensity bands between $3000\text{--}4000 \text{ cm}^{-1}$, indicating the suppressed water activity (J. Han *et al.*, 2018). Nevertheless, ^1H NMR and DSC of 27 mol kg^{-1} CH_3COOK (Thareja and Kumar, 2021) suggest that acetate anions are less effective H-bond breakers than

ClO_4^- , which readily affects the cell voltage. While perchlorate WISSEs allow cell voltages up to 2.7 V in symmetric supercapacitors constructed with N-rGO, acetate-based electrolytes show a depressed cell voltage of 2.0 V (Thareja and Kumar, 2021; Tian *et al.*, 2017) (Fig. 3a), almost equal to diluted electrolytes (Bu *et al.*, 2019a). Unfortunately, WISSEs with potassium formate have not been deeply investigated like acetate WISSEs, but in a single report, the authors claimed to reach 4.0 V of ESW (T. Liu *et al.*, 2019).

It is important to highlight that the anion nature has a strong influence on the cell voltage, which is totally related to how the water molecules are structured in solution. The recent work of Reber *et al.* (2021) described the influence of kosmotropic and chaotropic anions, reporting the unviability of using acetate WISSEs for high voltage applications owing to its kosmotropic characteristic (Fig. 3b). The kosmotropic effect of such anion leads to the water organization in huge clusters, which makes the electrolyte prone to

water splitting reactions. Despite the use of chaotropic anions is more suitable to reach high voltage devices, they need to act as a solid-electrolyte interphase (SEI) former to prevent the water-reduction process in metal-ion battery (An *et al.*, 2016). Yet even chaotropic salts that can form SEI may not be totally adequate to attain high voltages. Droguet *et al.* (2020) described that SEI

formation in LiTFSI WISSEs are not able to protect the electrode of the water reduction, which has several impacts on the capacity fading in LIBs. On the other hand, supercapacitors do not need the presence of this protective layer, making the development of WISSEs for this purpose more focused in strategies to enhance the cell voltage.

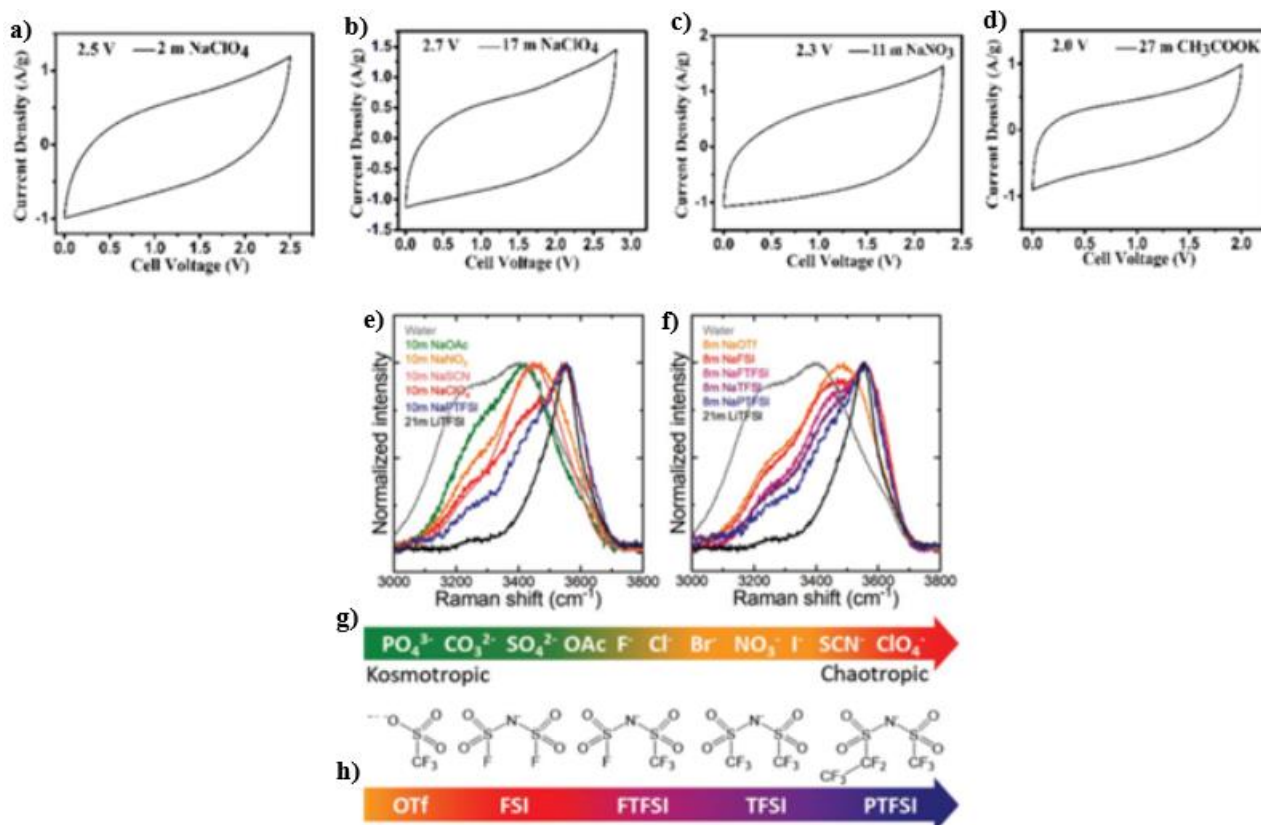


Figure 3. Cyclic voltammograms of symmetric supercapacitors constructed with N-rGO in (a) 2 mol kg⁻¹ NaClO₄; (b) 17 mol kg⁻¹ NaClO₄; (c) 11 mol kg⁻¹ NaNO₃; (d) 27 mol kg⁻¹ CH₃COOK (Thareja and Kumar, 2021); (e) and (f) Raman spectra of several WISSEs; (g) and (h) Kosmotropic and chaotropic series of anions in water (Reber *et al.*, 2021). The “m” inside the figures means mol kg⁻¹.”

Source: Reproduced from Thareja *et al.* (2021) and Reber *et al.* (2021) with permission from American Chemical Society and WILEY, respectively.

In terms of transition metal salts, only few WISSEs have been reported in literature being AlCl₃ (Pan *et al.*, 2019), Al(ClO₄)₃ (Zafar *et al.*, 2022a), ZnCl₂ (Sun *et al.*, 2022; B. Yang *et al.*, 2022), and Zn(ClO₄) (Zafar *et al.*, 2022b) the only traced out so far. Yet, AlCl₃ is not so soluble, and the evidence of low free water content is questionable (Pan *et al.*, 2019), as NaNO₃ WISSEs (Guo *et al.*, 2019). On the other hand, ZnCl₂ can be used to produce solutions up to 31 mol L⁻¹ which makes its WISSE interesting for Zinc batteries. L. Zhang *et al.* (2019) evaluated the effect of ZnCl₂ content in the electrolyte, claiming lower capacity fade when 30 mol kg⁻¹ is employed instead of 1 mol L⁻¹,

depicting capacity retention of 51.1% after 100 cycles at 50 mA g⁻¹. In other work, Wu *et al.* (2019) also employed ZnCl₂ WISSE in a dual-ion battery, where the high concentration of salt hinders the ferrocene anode dissolution and shifts the potential of the reactions, as expected by the Nernst equation. Therefore, ZnCl₂ WISSEs have a higher concern about increasing the activity of the Zn²⁺ ion in solution than achieving higher ESW. Evidently, the ESW is an important issue for Zn-ion batteries, since the zinc plating in diluted aqueous solution has the inevitable hydrogen evolution reaction (Ma *et al.*, 2020).

Additionally, the aforementioned works do not describe any evidence about the WISE behavior in their electrolytes, which are not so impressive for such applications but allows a better comprehension of water-in-salt electrolytes.

4. Water in bi-salt (WIBSE)

The use of mixed salts in WISE has been proved as a smart approach to overcome the preclusion of low-cost lithium salts that are not soluble enough to reach low water content in the electrolyte. In fact, the addition of lithium might appear only as a strategy to allow the use of low-cost WISE for LIBs, but its implications go further than expected. [Lukatskaya et al. \(2018\)](#) were the first researchers to produce, characterize and apply WISEs with two acetate salts. Although the idea of combining two high-soluble salts appeared earlier in the work of [Suo et al. \(2016\)](#), who employed mixed LiTFSI+LiOTf salts, the combination of acetates goes further allowing higher capacities for both electrodes. To reach a better composition of the acetates mixture the authors evaluated several ratios of KAc mixed with LiAc and found the formation of a eutectic-like mixture, where the water-to-cation ratio is smaller than that for pure KAc. Similarly, [Chen et al. \(2020a\)](#) evaluated several WISEs based on alkaline acetates, realizing that CsAc can reach higher ESW than that of KAc, due to the higher solubility of the former. Conversely to the upkeep of ESW observed by the [Lukatskaya et al. \(2018\)](#), the CsAc+LiAc electrolyte displayed a slight decrease, which is unreasonable because the higher content of salts should produce higher ESW. Lithium-free mixed WISEs were recently evaluated by [J. Han et al. \(2020b\)](#) that also employed acetate salts to prepare the electrolytes. The WIBSE prepared with 32 mol kg⁻¹ KAc + 8 mol kg⁻¹ NaAc, called 32K8N, attained an ESW of 2.4 V onto stainless steel, which is slightly lower than the one obtained by Lukatskaya and Chen groups. Apart from that, these authors employed Differential Electrochemical Mass Spectrometry (DEMS) to prove the stability of the produced WIBSE. According to their results, no O₂, H₂, and CO₂ evolutions were detected in the potential range of ESW that is an important observation as gas evolution is one of the processes involved in capacity fading. A recent work by [Turgeman et al. \(2022\)](#) also demonstrated the feasibility of using WIBSE for Li-ion batteries. The authors developed an electrolyte by mixing LiCl and CsCl salts under high concentrations, which can work stably in a TiO₂/LMO Li-ion battery for up to 1500 cycles.

The water-in-bisalts using low-cost salts are still a new field to be explored and lack of works in literature.

To the best of our knowledge, only these three quoted works have been studied the mixed acetates WISE. Interestingly, the concept introduced by [Reber et al. \(2021\)](#) of kosmotropism and chaotropism of the ions has a direct relationship on the WIBSE and may be applied for developing new mixed electrolytes. [Jenkins and Marcus \(1995\)](#) described that the nature of the ions can make the solution more viscous or more fluid in comparison with the pure water and designated such behavior as kosmotropic and chaotropic, respectively. For instance, LiAc is well reported as a chaotropic agent used for biological purposes and its behavior in the mixed WISEs can be interpreted as follows. Although the acetate anion displays a moderate kosmotropic effect, Li⁺ is a bit more chaotropic than K⁺ ([Salis and Ninham, 2014](#)), which can increase the solubility of the species as observed in eutectic phase systems. Similarly, the production of LiClO₄+NaClO₄ may be interesting to improve the solubility of both species, since the Li⁺ displays a higher chaotropic effect compared with that of Na⁺ ([Rossetto et al., 2008](#)).

Despite the high cost of LiTFSI, the recent work of [Xu et al. \(2022\)](#) described the development of a ternary WISE containing LiTFSI-KOH-CO(NH₂)₂-H₂O, with lower content of the Li salt (4.5 mol kg⁻¹), which was successfully employed in Li-ion battery. Although the use of eutectic mixtures is not so recent ([Lukatskaya et al., 2018](#)), these authors added a non-electrolytic salt to produce its electrolyte that allowed expanding the ESW up to 3.3 V.

5. Redox-active WISEs

Recently, the employment of redox-active species on WISEs has demonstrated a suitable strategy to enhance the energy density of hybrid supercapacitors. [J. Park et al. \(2022\)](#) developed a NaClO₄ WISE containing bromine and cobaltocene species as positive and negative redox shuttling, respectively. The authors found high power and energy densities for a supercapacitor constructed with single-walled carbon nanotube (SWNT) electrodes and the dual-redox active species. Although the advantage in enhancing the energy storage parameters, the cross-diffusion of the redox species is the main drawback that can lead to a fast self-discharge of the device as proved by the authors. In such case, the use of ion-exchange membranes is suitable to prevent cross-diffusion, but its employment is quite difficult considering the current shape of commercial cells. The use of bromine and iodine salts as redox-active species were also evaluated for micro-supercapacitors ([Meng et al., 2022](#); [Wang et al., 2022](#)) and displayed an expressive

enhancement of the electrode capacity due to the redox reactions.

6. Is the performance of WISE employed in EES devices competitive?

The current scientific scenario of energy storage devices is a competition for finding the best process or materials that often only care about the final performance. Although the recent developments of low-cost WISEs, much effort is still needed to understand these electrolytes. In terms of WISEs utilization in supercapacitors, which is a simple device, the main advantage is related to widening the cell voltage that allows for achieving high energy densities. In the work of [Bu et al. \(2019a\)](#) the sodium perchlorate WISSE allows the carbon-based device to work in a cell voltage of 2.3 V and a specific capacitance about 30 F g^{-1} . [Pang et al. \(2020\)](#) subjected a symmetric cell containing NaClO_4 WISSE to 2.4 V cell voltage, but the non-triangular shape of the galvanostatic charge-discharge curves suggests a low energy efficiency for their devices. They obtained a specific capacitance of 59 F g^{-1} for such a device, slightly higher than Bu's device, which can be attributed to the Faradaic process evidently present in that work. Comparisons between the obtained specific capacitances with WISSEs are difficult to be done since most of the works employ different electrode materials for constructing their devices. For instance, devices with YP-50F electrodes with sodium perchlorate WISSEs reveal higher specific capacitances than those using LiTFSI ([Bu et al., 2019a](#)). [Tian et al. \(2017\)](#) attained 69 F g^{-1} for a symmetric device with activated carbon (AC) electrodes and potassium acetate WISE. However, these authors prepared the electrolyte with 75 wt. % of KAc, which is related to a 7.64 mol kg^{-1} concentration and might have a high content of free water. A comparative study of different WISEs reveals ([Guo et al., 2019](#)) that capacitance increases in the order $12 \text{ mol kg}^{-1} \text{ NaNO}_3 > 17 \text{ mol kg}^{-1} \text{ NaClO}_4 > 21 \text{ mol kg}^{-1} \text{ LiTFSI} > 27 \text{ mol kg}^{-1} \text{ KAc}$. Even if the $12 \text{ mol kg}^{-1} \text{ NaNO}_3$ does not display the Raman band characteristic of WISEs, this expressive concentration was able to extend the cell voltage to 2 V. Since the ions in WISEs have a bit different ionic size than that in dilute solutions, it is expected in the future the evaluation of carbon materials with distinct pore size distributions to improve the compatibility among the device components.

Until now, the WIBSEs have not been evaluated for supercapacitor devices, but the difference in the ionic size of the components should be interesting to improve the specific capacitance. Furthermore, much of the

commercial devices operate with at least 2.7 V ([Yassine and Fabris, 2017](#)), which is slightly higher than the cell voltage commonly utilized for supercapacitors with LC-WISSEs. Also, none of the LiTFSI WISSEs can reach such voltage. Another important issue that is questionable even in most lab-scale devices is the lifespan that commercial supercapacitors have strong retention after more than 500,000 cycles. The work of Bu's group evaluated the constructed supercapacitor at 1 A g^{-1} , and the capacitance loses 20% of its initial value after 10,000 cycles. This retention value is much lower than the required for commercial supercapacitors and none of the works investigated the reason that leads to this fading process. Additionally, the charge storage efficiency is another confusing parameter in supercapacitors that might be carefully evaluated for WISE. The coulombic efficiency is also an important parameter, but to assign it as the energy efficiency the galvanostatic charge-discharge curves need to be a straight line, otherwise, it can overestimate both efficiency and cell voltage. Commercial supercapacitors have high energy efficiencies ([Eftekhari, 2017](#)) reaching values close to 100%, but most of the lab-scale devices are far from this value ([Laheäär et al., 2015](#)). Although some works display the near triangular shape of galvanostatic charge/discharge (GCD) curves, most of them show deviations from the linear behavior close to the limit of the cell voltage.

For metal-ion batteries, the use of LC-WISE often involves cathodes and anodes that have been previously evaluated in diluted electrolytes, but under this condition exhibit low cyclability. $\text{LiMn}_2\text{O}_4/\text{TiO}_2$ electrodes are known to display battery behavior in LiSO_4 electrolytes ([S. Liu et al., 2011](#)), but their capacity retention is poor due to water splitting process. Yet, the use of WIBSE of LiAc+KAc allowed the device to operate with a higher cell voltage, however, the cycling tests were performed up to 100 times for the cathode which does not permit ensure the lifetime expansion. In terms of specific capacity, both electrodes of the device depicted similar values to those obtained in an organic electrolyte containing LiPF₆, reaching specific capacities around 90 and 120 mAh g^{-1} at 0.1 A g^{-1} for anode and cathode, respectively. Similarly, [M. Lee et al. \(2019\)](#) studied the application of NaClO_4 WISSE for Na-ion batteries constructed with $\text{Na}_4\text{Fe}_3(\text{PO}_4)_2(\text{P}_2\text{O}_7)$ cathode and $\text{NaTi}_2(\text{PO}_4)_3$ anode, which was also evaluated in diluted aqueous electrolytes ([Fernández-Ropero et al., 2018](#); [S. Park et al., 2011](#)). The authors displayed a notable cycle stability for the device when WISSE was employed, improving the capacity retention and coulombic efficiency to 75% and 99%, respectively. [Leonard et al. \(2018\)](#) performed a comparative study of potassium

acetate WISSE and KPF_6 in an organic electrolyte to evaluate $\text{KTi}_2(\text{PO}_4)$ anodes, finding better kinetics for the WISSE than that in non-aqueous electrolyte. They also described the formation of SEI consisting of a carbon layer upon the anode material, which may come from the acetate reduction, nevertheless, further studies are still needed to improve the discussion of SEI growth in such electrolytes. Moreover, the electrode was cycled 11k times and displayed 69% capacity retention, a value that is expressive for battery materials. Although LC-WISEs applied to batteries seem to be a good strategy to overcome economical and safety concerns, the energy density and self-discharge for these electrolytes are far from the metal-ion batteries using aprotic solvents (Droguet *et al.*, 2020). Thus, extensive investigations dedicated to comparing electrode materials in typical non-aqueous electrolytes and WISEs are valuable for ensuring the viability of replacing the currently employed electrolytes.

Besides comparing the energy and power densities of devices constructed with WISEs, the self-discharge must be evaluated even more when working with redox-active WISEs that often display cross-over diffusion of active species. In terms of WISSEs for supercapacitors, only few works employing low-cost salts have investigated the self-discharge of such devices and most of them have studied quasi-solid-state electrolytes that exhibits tortuous path for electrical charges diffusion (Deng *et al.*, 2021; Fan *et al.*, 2020; Shi *et al.*, 2022). For conventional liquid electrolytes, Zheng *et al.* (2022) displayed those high concentrated electrolytes based on LiCl and LiBr (14 mol L^{-1}) show suppressed self-discharge when compared with their diluted solutions (1 M) for MXene-based electrodes. Also, when working with metal ion batteries the self-discharge study can clarify the solid electrolyte interface dissolution (Droguet *et al.*, 2020).

7. Perspectives

The use of LC-WISEs is very recent and has a limited number of salts that fits the requirements for preparing them. However, this research field still has a variety of opportunities that can be used to improve the current state-of-art of such electrolytes. Here, we highlight some promising approaches in developing WISEs, exploring from the basics to their final application in energy storage devices.

Initially, the structure of WISEs should be deeply investigated and the boundary conditions to achieve such kind of electrolyte needs to be well defined. Suo *et al.* (2015) described WISEs as a solution where the number of water molecules capable to solvate the ions is far below the solvation number of conventional diluted

electrolytes. They described concentrations $>5 \text{ mol kg}^{-1}$ behaving like a WISE, which is expected for each LiTFSI that exhibits 11 molecules of water. While Li^+ first solvation shell can accommodate 4 water molecules the TFSI- supports an average of 6 molecules at 5 mol kg^{-1} (S. Han, 2018), which is in agreement with WISE definition. Other alkali cations, e.g., Na^+ and K^+ are allowed to support 5-6 water molecules (Luo *et al.*, 2015), a bit more than for Li^+ , suggesting that lower salt concentrations can be used to produce WISEs in this case. Nevertheless, anion hydration and the formation of ion pairs should be also considered, but the last may have more importance in concentrated solutions. For instance, NaClO_4 diluted solutions may have 6 and 4 (Bergstroem *et al.*, 1991) water in the first hydration sheath of cation and anion, respectively. On average, by considering no ion pair formation the WISE behavior of NaClO_4 solutions should be reached in similar concentrations of LiTFSI , around 5 mol kg^{-1} . Yet, Raman spectra of LC-WISE even display a weak response assigned to water clustering that suggests the presence of small content of free water in the solution. Therefore, elucidating the microscopic structure of the WISE solution is needed to improve the comprehension of these electrolytes. Although the algebraic estimate leads to assert about the formation of WISE, even low contents of free water can reflect in high molar concentration of H_2O , which limits the ESW.

Chaotropic salts reveal to be more interesting than kosmotropic ones for WISEs preparations, but the latter has lower costs than the former. The combination of these two kinds of salts should be valuable to reach a better cost/benefit WISE. Differently from the mixture of acetates previously described, the utilization of salts with different anions should be interesting, as demonstrated for W. Lee *et al.* (2018), Sennu *et al.* (2020), Suo *et al.* (2016) and J. Zhu *et al.* (2020). The balance between highly soluble chaotropic and kosmotropic salts should be a strategy to suppress the free water content. Sennu *et al.* (2020) studied mixtures of $\text{NaTFSI} + \text{NaAc}$ as an approach that allows the extension of the ESW. They claimed that the addition of NaAc to form a WIBSE can neutralize the acidic environment of the NaTFSI WISSE, leading to an electrolyte with improved stability.

Moreover, the investigation of cosolvents acting as additives in WISEs are interesting and has been proved to be effective for enhancing the electrolyte properties. For example, Dou *et al.* (2018) prepared acetonitrile/water-in-salt electrolyte (AWISE) which allowed to achieve the same cell voltage of WISE, but using only 5 mol kg^{-1} LiTFSI . In fact, there are no reports describing the chaotropic effect of acetonitrile in water, but the use of cosolvents also decreases the content of

water that is useful because this approach should allow decreasing the amount of salt employed in preparing WISEE. Furthermore, the viscosity and conductivity of AWISE are more adequate for energy storage purposes than in WISE. A similar behavior was observed when with AWISE prepared with NaClO₄ (Dou *et al.*, 2019), where the Raman spectra suggest lower free water content compared with this perchlorate WISSE (Bu *et al.*, 2019a). Certainly, the use of acetonitrile displays implications about flammability concerns, but the authors describe that this AWISE is non-flammable under the proposed experimental conditions.

Therefore, there are many promising opportunities unexplored yet that can permit the utilization of these green, low-cost and safe WISEs. Although the great importance in highlighting the performance and improving cell voltage of devices constructed with WISEs, the electrolyte needs to be well studied to allow further rational developments. Viscosity and conductivity measurements of the electrolytes at different concentrations should be conducted since they are important to evaluate the formation of the ion pair. The characterization of the electrolyte by Raman spectroscopy and NMR is needed to understand the chemical environment of the water molecules and also permits comprehending the ionic association. Despite the rapid progress in the field, the necessity of performing such measurements is vital for the development and utilization of new WISEs.

Authors' contribution

Conceptualization: Sakita, A. M. P.; Della Noce, R.

Data curation: Sakita, A. M. P.

Formal Analysis: Not applicable

Funding acquisition: Not applicable

Investigation: Not applicable

Methodology: Not applicable

Project administration: Not applicable

Resources: Not applicable

Software: Not applicable

Supervision: Not applicable

Validation: Not applicable

Visualization: Not applicable

Writing – original draft: Sakita, A. M. P.; Della Noce, R.

Writing – review & editing: Sakita, A. M. P.; Della Noce, R.

Data availability statement

Data sharing is not applicable

Funding

Fundação de Amparo à Pesquisa do Estado de São Paulo (FAPESP). Grant No: 21/14163-5.

Acknowledgments

The authors would like to thank Instituto de Química - UNESP for all the contributions to their academic careers. In addition, we would like to express our gratitude to the editor Prof. Assis Benedetti for the invitation to participate in this special issue.

References

- Adil, M.; Ghosh, A.; Mitra, S. Water-in-Salt Electrolyte-Based Extended Voltage Range, Safe, and Long-Cycle-Life Aqueous Calcium-Ion Cells. *ACS Appl. Mater. Interfaces*. **2022**, *14* (22), 25501–25515. <https://doi.org/10.1021/acsami.2c04742>
- An, S. J.; Li, J.; Daniel, C.; Mohanty, D.; Nagpure, S.; Wood, D. L. The state of understanding of the lithium-ion-battery graphite solid electrolyte interphase (SEI) and its relationship to formation cycling. *Carbon N Y* **2016**, *105*, 52–76. <https://doi.org/10.1016/j.carbon.2016.04.008>
- Bergstroem, P. A.; Lindgren, J.; Kristiansson, O. An IR study of the hydration of ClO₄⁻, NO₃⁻, I⁻, Br⁻, Cl⁻, and SO₄²⁻ anions in aqueous solution. *J. Phys. Chem.* **1991**, *95* (22), 8575–8580. <https://doi.org/10.1021/j100175a031>
- Bu, X.; Su, L.; Dou, Q.; Lei, S.; Yan, X. A Low-Cost “Water-in-Salt” Electrolyte for a 2.3 V High-Rate Carbon-Based Supercapacitor. *J. Mat. Chem. A* **2019a**, *7* (13), 7541–7547. <https://doi.org/10.1039/C9TA00154A>
- Bu, X.; Zhang, Y.; Su, L.; Dou, Q.; Xue, Y.; Lu, X. A 2.4-V Asymmetric Supercapacitor Based on Cation-Intercalated Manganese Oxide Nanosheets in a Low-Cost “Water-in-Salt” Electrolyte. *Ionics*. **2019b**, *25* (12), 6007–6015. <https://doi.org/10.1007/s11581-019-03141-y>
- Chava, B. S.; Wang, Y.; Sivasankar, V. S.; Das, S. Water-Free Localization of Anion at Anode for Small-Concentration Water-in-Salt Electrolytes Confined in Boron-Nitride Nanotube. *Cell Rep. Physical Science*. **2020**, *1* (11), 100246. <https://doi.org/10.1016/j.xcrp.2020.100246>
- Chen, S.; Lan, R.; Humphreys, J.; Tao, S. Effect of cation size on alkali acetate-based ‘water-in-bisalt’ electrolyte and its application in aqueous rechargeable lithium battery. *Applied Materials Today* **2020a**, *20*, 100728. <https://doi.org/10.1016/j.apmt.2020.100728>

- Chen, S.; Lan, R.; Humphreys, J.; Tao, S. Salt-Concentrated Acetate Electrolytes for a High Voltage Aqueous Zn/MnO₂ Battery. *Energy Storage Mater.* **2020b**, *28*, 205–215. <https://doi.org/10.1016/j.ensm.2020.03.011>
- Chen, S.; Sun, P.; Sun, B.; Humphreys, J.; Zou, P.; Xie, K.; Tao, S. Nitrate-based ‘oversaturated gel electrolyte’ for high-voltage and high-stability aqueous lithium batteries. *Energy Storage Mater.* **2021**, *37*, 598–608. <https://doi.org/10.1016/j.ensm.2021.02.038>
- Deng, Y.; Wang, H.; Zhang, K.; Shao, J.; Qiu, J.; Wu, J.; Wu, Y.; Yan, L. A High-voltage quasi-solid-state flexible supercapacitor with a wide operational temperature range based on a low-cost “water-in-salt” hydrogel electrolyte. *Nanoscale.* **2021**, *13* (5), 3010–3018. <https://doi.org/10.1039/D0NR08437A>
- Ding, M. S.; Xu, K. Phase Diagram, Conductivity, and Glass Transition of LiTFSI-H₂O Binary Electrolytes. *J. Phys. Chem. C.* **2018**, *122* (29), 16624–16629. <https://doi.org/10.1021/acs.jpcc.8b05193>
- Dou, Q.; Lei, S.; Wang, D.-W.; Zhang, Q.; Xiao, D.; Guo, H.; Wang, A.; Yang, H.; Li, Y.; Shi, S.; Yan, X. Safe and high-rate supercapacitors based on an “acetonitrile/water in salt” hybrid electrolyte. *Energy Environ. Sci.* **2018**, *11* (11), 3212–3219. <https://doi.org/10.1039/C8EE01040D>
- Dou, Q.; Lu, Y.; Su, L.; Zhang, X.; Lei, S.; Bu, X.; Liu, L.; Xiao, D.; Chen, J.; Shi, S.; Yan, X. A Sodium Perchlorate-Based Hybrid Electrolyte with High Salt-to-Water Molar Ratio for Safe 2.5 V Carbon-Based Supercapacitor. *Energy Storage Mater.* **2019**. <https://doi.org/10.1016/j.ensm.2019.03.016>
- Droguet, L.; Grimaud, A.; Fontaine, O.; Tarascon, J.-M. Water-in-Salt Electrolyte (WiSE) for Aqueous Batteries: A Long Way to Practicality. *Adv. Energy Mater.* **2020**, *10* (43), 2002440. <https://doi.org/10.1002/aenm.202002440>
- Eftekhari, A. Energy Efficiency: A Critically Important but Neglected Factor in Battery Research. *Sustainable Energy Fuels.* **2017**, *1* (10), 2053–2060. <https://doi.org/10.1039/C7SE00350A>
- Fan, L.-Q.; Geng, C.-L.; Wang, Y.-L.; Sun, S.-J.; Huang, Y.-F.; Wu, J.-H. Design of a redox-active “water-in-salt” hydrogel polymer electrolyte for superior-performance quasi-solid-state supercapacitors. *New J. Chem.* **2020**, *44* (39), 17070–17078. <https://doi.org/10.1039/D0NJ04102E>
- Fernández-Ropero, A. J.; Zarrabeitia, M.; Reynaud, M.; Rojo, T.; Casas-Cabanas, M. Toward Safe and Sustainable Batteries: Na₄Fe₃(PO₄)₂P₂O₇ as a Low-Cost Cathode for Rechargeable Aqueous Na-Ion Batteries. *J. Phys. Chem. C.* **2018**, *122* (1), 133–142. <https://doi.org/10.1021/acs.jpcc.7b09803>
- Gambou-Bosca, A.; Bélanger, D. Electrochemical characterization of MnO₂-based composite in the presence of salt-in-water and water-in-salt electrolytes as electrode for electrochemical capacitors. *J. Power Sources.* **2016**, *326*, 595–603. <https://doi.org/10.1016/j.jpowsour.2016.04.088>
- Guo, J.; Ma, Y.; Zhao, K.; Wang, Y.; Yang, B.; Cui, J.; Yan, X. High-Performance and Ultra-Stable Aqueous Supercapacitors Based on a Green and Low-Cost Water-In-Salt Electrolyte. *ChemElectroChem.* **2019**, *6* (21), 5433–5438. <https://doi.org/10.1002/celec.201901591>
- Han, J.; Zhang, H.; Varzi, A.; Passerini, S. Fluorine-Free Water-in-Salt Electrolyte for Green and Low-Cost Aqueous Sodium-Ion Batteries. *ChemSusChem.* **2018**, *11* (21), 3704–3707. <https://doi.org/10.1002/cssc.201801930>
- Han, S. Dynamic features of water molecules in superconcentrated aqueous electrolytes. *Scic. Rep.* **2018**, *8* (1), 9347. <https://doi.org/10.1038/s41598-018-27706-5>
- Han, J.; Mariani, A.; Zhang, H.; Zarrabeitia, M.; Gao, X.; Carvalho, D. V.; Varzi, A.; Passerini, S. Gelified Acetate-Based Water-in-Salt Electrolyte Stabilizing Hexacyanoferrate Cathode for Aqueous Potassium-Ion Batteries. *Energy Storage Mater.* **2020a**, *30*, 196–205. <https://doi.org/10.1016/j.ensm.2020.04.028>
- Han, J.; Zarrabeitia, M.; Mariani, A.; Jusys, Z.; Hekmatfar, M.; Zhang, H.; Geiger, D.; Kaiser, U.; Behm, R. J.; Varzi, A.; Passerini, S. Halide-free water-in-salt electrolytes for stable aqueous sodium-ion batteries. *Nano Energy.* **2020b**, *77*, 105176. <https://doi.org/10.1016/j.nanoen.2020.105176>
- Im, E.; Ryu, J. H.; Baek, K.; Moon, G. D.; Kang, S. J. “Water-in-Salt” and NASICON Electrolyte-Based Na–CO₂ Battery. *Energy Storage Mater.* **2021**, *37*, 424–432. <https://doi.org/10.1016/j.ensm.2021.02.031>
- Jenkins, H. D. B.; Marcus, Y. Viscosity B-Coefficients of Ions in Solution. *Chem. Rev.* **1995**, *95* (8), 2695–2724. <https://doi.org/10.1021/cr00040a004>
- Laheäär, A.; Przygocki, P.; Abbas, Q.; Béguin, F. Appropriate Methods for Evaluating the Efficiency and Capacitive Behavior of Different Types of Supercapacitors. *Electrochem. Commun.* **2015**, *60*, 21–25. <https://doi.org/10.1016/j.elecom.2015.07.022>
- Lee, W. S. V.; Xiong, T.; Loh, G. C.; Tan, T. L.; Xue, J. Optimizing Electrolyte Physicochemical Properties toward 2.8 V Aqueous Supercapacitor. *ACS Appl. Energy Mater.* **2018**, *1* (7), 3070–3076. <https://doi.org/10.1021/acsaem.8b00751>
- Lee, M. H.; Kim, S. J.; Chang, D.; Kim, J.; Moon, S.; Oh, K.; Park, K. Y.; Seong, W. M.; Park, H.; Kwon, G.; Lee, B.; Kang, K. Toward a low-cost high-voltage sodium aqueous rechargeable battery. *Mater. Today.* **2019**, *29*, 26–36. <https://doi.org/10.1016/j.mattod.2019.02.004>
- Leonard, D. P.; Wei, Z.; Chen, G.; Du, F.; Ji, X. Water-in-Salt Electrolyte for Potassium-Ion Batteries. *ACS Energy Lett.* **2018**, *3* (2), 373–374. <https://doi.org/10.1021/acsenrgylett.8b00009>
- Lim, J.; Park, K.; Lee, H.; Kim, J.; Kwak, K.; Cho, M. Nanometric Water Channels in Water-in-Salt Lithium Ion

- Battery Electrolyte. *J. Am. Chem. Soc.* **2018**, *140* (46), 15661–15667. <https://doi.org/10.1021/jacs.8b07696>
- Liu, S.; Ye, S. H.; Li, C. Z.; Pan, G. L.; Gao, X. P. Rechargeable Aqueous Lithium-Ion Battery of $\text{TiO}_2/\text{LiMn}_2\text{O}_4$ with a High Voltage. *J. Electrochem. Soc.* **2011**, *158* (12), A1490. <https://doi.org/10.1149/2.094112jes>
- Liu, T.; Tang, L.; Luo, H.; Cheng, S.; Liu, M. A Promising water-in-salt electrolyte for aqueous based electrochemical energy storage cells with a wide potential window: highly concentrated HCOOK. *Chem. Commun.* **2019**, *55* (85), 12817–12820. <https://doi.org/10.1039/C9CC05927J>
- Liu, S.; Klukas, R.; Porada, T.; Furda, K.; Fernández, A. M.; Balducci, A. Potassium formate-based electrolytes for high performance aqueous electrochemical capacitors. *J. Power Sources.* **2022**, *541*, 231657. <https://doi.org/10.1016/j.jpowsour.2022.231657>
- Lukatskaya, M. R.; Feldblyum, J. I.; Mackanic, D. G.; Lissel, F.; Michels, D. L.; Cui, Y.; Bao, Z. Concentrated mixed cation acetate “water-in-salt” solutions as green and low-cost high voltage electrolytes for aqueous batteries. *Energy Environ. Sci.* **2018**, *11* (10), 2876–2883. <https://doi.org/10.1039/C8EE00833G>
- Luo, Z.-X.; Xing, Y.-Z.; Ling, Y.-C.; Kleinhammes, A.; Wu, Y. Electroneutrality Breakdown and Specific Ion Effects in Nanoconfined Aqueous Electrolytes Observed by NMR. *Nat. Commun.* **2015**, *6*, 6358. <https://doi.org/10.1038/ncomms7358>
- Ma, L.; Chen, S.; Li, N.; Liu, Z.; Tang, Z.; Zapien, J. A.; Chen, S.; Fan, J.; Zhi, C. Hydrogen-Free and Dendrite-Free All-Solid-State Zn-Ion Batteries. *Adv. Mat.* **2020**, *32* (14), 1908121. <https://doi.org/10.1002/adma.201908121>
- Meng, C.; Zhou, F.; Liu, H.; Zhu, Y.; Fu, Q.; Wu, Z.-S. Water-in-Salt Ambipolar Redox Electrolyte Extraordinarily Boosting High Pseudocapacitive Performance of Micro-Supercapacitors. *ACS Energy Lett.* **2022**, *7* (5), 1706–1711. <https://doi.org/10.1021/acscenergylett.2c00329>
- Pan, W.; Wang, Y.; Zhang, Y.; Kwok, H. Y. H.; Wu, M.; Zhao, X.; Leung, D. Y. C. A low-cost and dendrite-free rechargeable aluminium-ion battery with superior performance. *J. Mater. Chem. A.* **2019**, *7* (29), 17420–17425. <https://doi.org/10.1039/C9TA05207K>
- Pang, M.; Jiang, S.; Zhao, J.; Zhang, S.; Wang, R.; Li, N.; Liu, R.; Pan, Q.; Qu, W.; Xing, B. “Water-in-salt” electrolyte enhanced high voltage aqueous supercapacitor with carbon electrodes derived from biomass waste-ground grain hulls. *RSC Adv.* **2020**, *10* (58), 35545–35556. <https://doi.org/10.1039/D0RA07448A>
- Park, S. I.; Gocheva, I.; Okada, S.; Yamaki, J. Electrochemical Properties of $\text{NaTi}_2(\text{PO}_4)_3$ Anode for Rechargeable Aqueous Sodium-Ion Batteries. *J. Electrochem. Soc.* **2011**, *158* (10), A1067. <https://doi.org/10.1149/1.3611434>
- Park, J.; Lee, J.; Kim, W. Redox-Active Water-in-Salt Electrolyte for High-Energy-Density Supercapacitors. *ACS Energy Lett.* **2022**, *7* (4), 1266–1273. <https://doi.org/10.1021/acscenergylett.2c00015>
- Reber, D.; Grissa, R.; Becker, M.; Kühnel, R. S.; Battaglia, C. Anion Selection Criteria for Water-in-Salt Electrolytes. *Adv. Energy. Mater.* **2021**, *11* (5), 2002913. <https://doi.org/10.1002/aenm.202002913>
- Rossetto, H. L.; Souza, M. F.; Pandolfelli, V. C. Chaotropic substances and their effects on the mechanical strength of Portland cement-based materials. *Mat. Res.* **2008**, *11* (2), 183–185. <https://doi.org/10.1590/S1516-14392008000200012>
- Salis, A.; Ninham, B. W. Models and mechanisms of Hofmeister effects in electrolyte solutions, and colloid and protein systems revisited. *Chem. Soc. Rev.* **2014**, *43* (21), 7358–7377. <https://doi.org/10.1039/C4CS00144C>
- Sennu, P.; Chua, R.; Dintakurti, S. S. H.; Hanna, J. V.; Ramabhadran, R. O.; Aravindan, V.; Madhavi, S. Supersaturated “water-in-salt” hybrid electrolyte towards building high voltage Na-ion capacitors with wide temperatures operation. *J. Power Sources.* **2020**, *472*, 228558. <https://doi.org/10.1016/j.jpowsour.2020.228558>
- Serva, A.; Dubouis, N.; Grimaud, A.; Salanne, M. Confining Water in Ionic and Organic Solvents to Tune Its Adsorption and Reactivity at Electrified Interfaces. *Acc. Chem. Res.* **2021**, *54* (4), 1034–1042. <https://doi.org/10.1021/acs.accounts.0c00795>
- Shi, M.; Yang, W.; Zhang, Z.; Zhao, M.; Wang, Z. L.; Lu, X. Hydrogels with highly concentrated salt solution as electrolytes for solid-state supercapacitors with a suppressed self-discharge rate. *J. Mater. Chem. A.* **2022**, *10* (6), 2966–2972. <https://doi.org/10.1039/D1TA08709F>
- Smith, L.; Dunn, B. Opening the Window for aqueous electrolytes. *Science.* **2015**, *350* (6263), 918–918. <https://doi.org/10.1126/science.aad5575>
- Stigliano, P. L.; Pianta, N.; Bonizzoni, S.; Mauri, M.; Simonutti, R.; Lorenzi, R.; Vigani, B.; Berbenni, V.; Rossi, S.; Mustarelli, P.; Ruffo, R. A physico-chemical investigation of highly concentrated potassium acetate solutions towards applications in electrochemistry. *Phys. Chem. Chem. Phys.* **2021**, *23* (2), 1139–1145. <https://doi.org/10.1039/D0CP04151C>
- Sun, L.; Yao, Y.; Dai, L.; Jiao, M.; Ding, B.; Yu, Q.; Tang, J.; Liu, B. Sustainable and high-performance Zn dual-ion batteries with a hydrogel-based water-in-salt electrolyte. *Energy Storage Mater.* **2022**, *47*, 187–194. <https://doi.org/10.1016/j.ensm.2022.02.012>
- Suo, L.; Borodin, O.; Gao, T.; Olguin, M.; Ho, J.; Fan, X.; Luo, C.; Wang, C.; Xu, K. “Water-in-salt” electrolyte enables high-voltage aqueous lithium-ion chemistries. *Science.* **2015**, *350* (6263), 938–943. <https://doi.org/10.1126/science.aab1595>

- Suo, L.; Borodin, O.; Sun, W.; Fan, X.; Yang, C.; Wang, F.; Gao, T.; Ma, Z.; Schroeder, M.; von Cresce, A.; Russell, S. M.; Armand, M.; Angell, A.; Xu, K.; Wang, C. Advanced High-Voltage Aqueous Lithium-Ion Battery Enabled by “Water-in-Bisalt” Electrolyte. *Angew. Chem.* **2016**, *128* (25), 7252–7257. <https://doi.org/10.1002/ange.201602397>
- Thareja, S.; Kumar, A. “water-In-Salt” Electrolyte-Based High-Voltage (2.7 V) Sustainable Symmetric Supercapacitor with Superb Electrochemical Performance - An Analysis of the Role of Electrolytic Ions in Extending the Cell Voltage. *ACS Sustainable Chem. Eng.* **2021**, *9* (5), 2338–2347. <https://doi.org/10.1021/acssuschemeng.0c08604>
- Tian, Z.; Deng, W.; Wang, X.; Liu, C.; Li, C.; Chen, J.; Xue, M.; Li, R.; Pan, F. Superconcentrated aqueous electrolyte to enhance energy density for advanced supercapacitors. *Funct. Mater. Lett.* **2017**, *10* (6), 1750081. <https://doi.org/10.1142/S1793604717500813>
- Turgeman, M.; Wineman-Fisher, V.; Malchik, F.; Saha, A.; Bergman, G.; Gavriel, B.; Penki, T. R.; Nimkar, A.; Baranaukaite, V.; Aviv, H.; Levi, M. D.; Noked, M.; Major, D. T.; Shpigel, N.; Aurbach, D. A cost-effective water-in-salt electrolyte enables highly stable operation of a 2.15-V aqueous lithium-ion battery. *Cell Rep. Physical Science.* **2022**, *3* (1), 100688. <https://doi.org/10.1016/j.xcrp.2021.100688>
- Wang, X.; Bak, S. M.; Han, M.; Shuck, C. E.; McHugh, C.; Li, K.; Li, J.; Tang, J.; Gogotsi, Y. Surface Redox Pseudocapacitance of Partially Oxidized Titanium Carbide MXene in Water-in-Salt Electrolyte. *ACS Energy Lett.* **2022**, *7* (1), 30–35. <https://doi.org/10.1021/acsenerylett.1c02262>
- Wu, X.; Xu, Y.; Zhang, C.; Leonard, D. P.; Markir, A.; Lu, J.; Ji, X. Reverse Dual-Ion Battery via a ZnCl₂ Water-in-Salt Electrolyte. *J. Am. Chem. Soc.* **2019**, *141* (15), 6338–6344. <https://doi.org/10.1021/jacs.9b00617>
- Xu, J.; Ji, X.; Zhang, J.; Yang, C.; Wang, P.; Liu, S.; Ludwig, K.; Chen, F.; Kofinas, P.; Wang, C. Aqueous electrolyte design for super-stable 2.5 V LiMn₂O₄ || Li₄Ti₅O₁₂ pouch cells. *Nat. Energy.* **2022**, *7* (2), 186–193. <https://doi.org/10.1038/s41560-021-00977-5>
- Yang, C.; Chen, J.; Qing, T.; Fan, X.; Sun, W.; von Cresce, A.; Ding, M. S.; Borodin, O.; Vatamanu, J.; Schroeder, M. A.; Eidson, N.; Wang, C.; Xu, K. 4.0 V Aqueous Li-Ion batteries. *Joule.* **2017**, *1* (1), 122–132. <https://doi.org/10.1016/j.joule.2017.08.009>
- Yang, B.; Qin, T.; Du, Y.; Zhang, Y.; Wang, J.; Chen, T.; Ge, M.; Bin, D.; Ge, C.; Lu, H. Rocking-chair proton battery based on a low-cost “water in salt” electrolyte. *Chem. Commun.* **2022**, *58* (10), 1550–1553. <https://doi.org/10.1039/D1CC06325A>
- Yassine, M.; Fabris, D. Performance of commercially available supercapacitors. *Energies.* **2017**, *10* (9), 1340. <https://doi.org/10.3390/en10091340>
- Zafar, Z. A.; Abbas, G.; Silhavi, M.; Knizek, K.; Kaman, O.; Sonia, F. J.; Kumar, P.; Jiricek, P.; Houdková, J.; Frank, O.; Cervenka, J. Reversible anion intercalation into graphite from aluminum perchlorate “water-in-salt” electrolyte. *Electrochim. Acta.* **2022a**, *404*, 139754. <https://doi.org/10.1016/j.electacta.2021.139754>
- Zafar, Z. A.; Abbas, G.; Knizek, K.; Silhavi, M.; Kumar, P.; Jiricek, P.; Houdková, J.; Frank, O.; Cervenka, J. Chaotropic anion based “water-in-salt” electrolyte realizes a high voltage zn-graphite dual-ion battery. *J. Mater. Chem. A.* **2022b**, *10* (4), 2064–2074. <https://doi.org/10.1039/D1TA10122F>
- Zhang, L.; Rodríguez-Pérez, I. A.; Jiang, H.; Zhang, C.; Leonard, D. P.; Guo, Q.; Wang, W.; Han, S.; Wang, L.; Ji, X. ZnCl₂ “Water-in-Salt” electrolyte transforms the performance of vanadium oxide as a zn battery cathode. *Adv. Funct. Mater.* **2019**, *29* (30), 1902653. <https://doi.org/10.1002/adfm.201902653>
- Zhang, Y.; Xu, J.; Li, Z.; Wang, Y.; Wang, S.; Dong, X.; Wang, Y. All-climate aqueous Na-Ion batteries using “water-in-salt” electrolyte. *Sci. Bull.* **2022**, *67* (2), 161–170. <https://doi.org/10.1016/j.scib.2021.08.010>
- Zheng, W.; Halim, J.; Rosen, J.; Barsoum, M. W. Aqueous electrolytes, MXene-Based supercapacitors and their self-discharge. *Adv. Sustain. Syst.* **2022**, *3* (2), 2100147. <https://doi.org/10.1002/aesr.202100147>
- Zhu, J.; Xu, Y.; Fu, Y.; Xiao, D.; Li, Y.; Liu, L.; Wang, Y.; Zhang, Q.; Li, J.; Yan, X. Hybrid aqueous/nonaqueous water-in-bisalt electrolyte enables safe dual ion batteries. *Small.* **2020**, *16* (17), 1905838. <https://doi.org/10.1002/smll.201905838>
- Zhu, Y.; Zheng, S.; Lu, P.; Ma, J.; Das, P.; Su, F.; Cheng, H.-M.; Wu, Z.-S. Kinetic regulation of mxene with water-in-licl electrolyte for high-voltage micro-supercapacitors. *Natl. Sci. Ver.* **2022**, nwac024. <https://doi.org/10.1093/nsr/nwac024>

$K_4Nb_6O_{17}$ layered hexaniobate: revisiting the proton-exchanged reaction

Mariana Pires Figueiredo¹, Vera Regina Leopoldo Constantino¹⁺

1. University of São Paulo, Institute of Chemistry, São Paulo, Brazil.

+Corresponding author: Vera Regina Leopoldo Constantino, **Phone:** +551130919152, **Email address:** vrlconst@iq.usp.br

ARTICLE INFO

Article history:

Received: August 30, 2021

Accepted: November 10, 2021

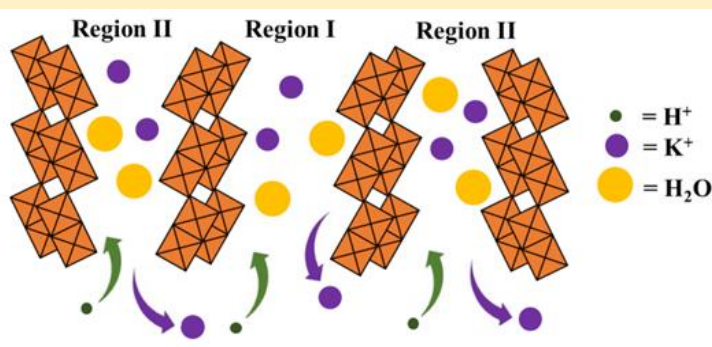
Published: August 17, 2022

Keywords

1. intercalation compounds
2. acidic niobate
3. ion-exchange reaction
4. thermal analysis

Section Editor: Assis Vicente Benedetti

ABSTRACT: The layered hexaniobate of $K_4Nb_6O_{17}$ composition and its derivatives comprise nanostructured materials that exhibit suitable properties for application in catalysis, electrochemistry, and energy, for instance. The exchange of K^+ cations to obtain the acidic or protonic niobate form is the main route to originate appropriate precursors to promote the hexaniobate exfoliation, yielding a dispersion of thin layers (2D particles) that can be scrolled under exclusive conditions. Hexaniobate presents two regions (I and II), being the former considered more accessible than region II. In this work, the proton exchange efficiency of the $K_4Nb_6O_{17}$ was investigated by thermogravimetric analysis coupled to mass spectrometry (TGA-MS) and metal analysis by inductively coupled plasma spectroscopy (ICP). The products of thermal decomposition profile of the $H_xK_{(4-x)}Nb_6O_{17}$ phase were isolated at defined temperature values and characterized by X-ray diffractometry and Raman spectroscopy. The cation exchange percentages obtained by TGA-MS (68.0%) and by quantification of deintercalated K^+ by ICP (64.0%) are similar and endorse that region II can also be modified and, consequently, contribute to the exfoliation process.



1. Introduction

The interest in layered hexaniobates is motivated by their physicochemical properties and the possibility of application as precursors for the development of nanostructured materials to attend catalysis (Wei and Nakato, 2009), electrochemistry (Elumalai *et al.*, 2021), and energy (Maeda *et al.*, 2009) fields, for instance. Such materials present general formula $A_4Nb_6O_{17} \cdot nH_2O$ (with $A = K^+, Rb^+, \text{ or } Cs^+$) and orthorhombic unit cell: $a = 7.83 \text{ \AA}$, $b = 32.21 \text{ \AA}$, and $c = 6.46 \text{ \AA}$ (Gasperin and Le Bihan, 1980; 1982). The distorted octahedrons $[NbO_6]$ units are bounded by the edges and the vertices, generating layers with structure called ReO_3 -type deficient double strand (Bizeto *et al.*, 2006; Rao and Raveau, 1998), as shown in Fig. 1. The three-dimensional structure is formed by the layers stacking in a face-to-face arrangement. Due to the high amount of oxygen atoms coordinated to niobium atoms, hexaniobate presents high layer charge density, which can make the intercalation process by ion exchange reaction (a topotactic reaction) a challenging process. The electroneutrality of the negatively charged layers is maintained by alkali metal cations present in the interlayer region.

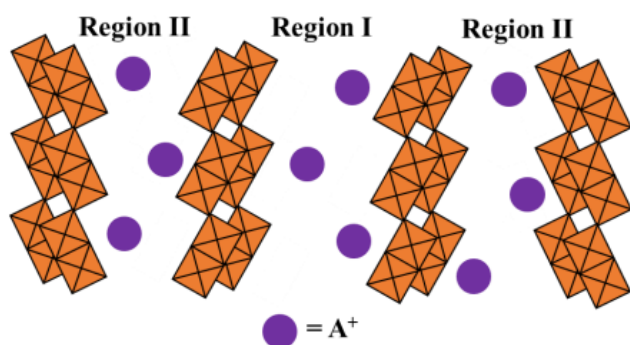


Figure 1. Schematic representation of the layered hexaniobate structure.

One of the most prominent characteristics of $A_4Nb_6O_{17} \cdot nH_2O$ material is the interlayer differentiation, which can be explored to tune its chemical and physical properties. Reported for the first time by Gasperin and Le Bihan (1980), the so-called interlayer I and II regions of the hexaniobate matrix (Fig. 1) present different cations array and behaviors in relation to the hydration process. Ions in the interlayer I can be hydrated, which can make it more accessible than interlayer II.

Consequently, it is supposed that region II is not involved in ion exchange reactions (Kimura *et al.*, 2014; Shiguihara *et al.*, 2010). However, for the $K_4Nb_6O_{17}$ hexaniobate, it is reported that K^+ can be exchanged by multivalent cations in region I but cations exchange in

region II is limited to monovalent cations (Müller-Warmuth and Schöllhorn, 1994).

The exchange of cations to obtain the acidic or protonic niobate form aims to produce precursors able to encapsulate bulky species, such as tetrabutylammonium ion, and support the osmotic swelling facilitating the exfoliation process (Shiguihara *et al.*, 2007). Dispersed exfoliated nanosheets can curl themselves resulting in nanoscrolls with variable diameters, formed according to adjusted experimental conditions. Hence, the reactivity of hexaniobate regarding the layer's separation is affected by the protonation level. Exfoliated nanosheets are investigated for the preparation of thin films targeting coatings or hybrid self-assembled multifunctional systems with a great interest for sensors, among several other applications (Bizeto *et al.*, 2009).

Considering the most studied hexaniobate composition, $K_4Nb_6O_{17}$, the phase resulting from the exchange of K^+ ion by H^+ (or hydronium ion, H_3O^+) is frequently represented by the $H_2K_2Nb_6O_{17}$ formula (Liu *et al.*, 2017; Shiguihara *et al.*, 2010; Silva *et al.*, 2018). However, other works (Guo *et al.*, 2020; Li *et al.*, 2016) have considered proton-exchange values greater than 50%, although chemical elemental quantifications are not provided. In another case, the isolated acid phase was generically expressed as $H_xK_{(4-x)}Nb_6O_{17}$ (Hu *et al.*, 2014). There is no agreement regarding the extension of H^+ intercalation and the quantification of the exchange extension is rarely reported. Thus, the investigation concerning the proton exchange reaction involving the $K_4Nb_6O_{17}$ phase is of interest and required to tune hexaniobate properties.

In this work, the $K_4Nb_6O_{17}$ proton exchange reaction is revisited. Thermogravimetric analysis coupled to mass spectrometry (TGA-MS) was used to assess the proton exchange efficiency of $K_4Nb_6O_{17}$, and the result was compared to the deintercalated amount of K^+ obtained by Inductively Coupled Plasma Optical Emission Spectroscopy (ICP-AES). Additionally, X-ray diffraction (XRD) and Raman spectroscopy were employed to characterize the acidic hexaniobate treated at defined temperature values to better assign the thermal events and, consequently, the extension of the proton exchange.

2. Experimental

2.1 Reagents

Niobium(V) oxide (CBMM – 99,98%, optic degree), potassium carbonate (Merck – p.a.), and nitric acid (Synth – P.A.) were used as received.

2.2 Synthesis of $K_4Nb_6O_{17}$ phase

The potassium layered hexaniobate was synthesized by the ceramic method. Nb_2O_5 and K_2CO_3 solids (with K_2CO_3 in 10 mol% excess related to stoichiometric proportions) were manually ground together, added to a platinum crucible, and heated at 1000 °C in two steps of 5 h. The rate of heating was maintained in 15 °C min⁻¹. The solid was washed with deionized water by centrifugation cycles for the removal of residual K_2O and then dried at 80 °C for 24 h.

2.3 Preparation of $H_xK_{(4-x)}Nb_6O_{17}$ phase by ion exchange reaction

The $H_xK_{(4-x)}Nb_6O_{17}$ phase was obtained under mild conditions suspending 1 g of $K_4Nb_6O_{17} \cdot nH_2O$ in 40 mL of 6 mol L⁻¹ HNO_3 solution under stirring at 60 °C. After 24 h, the supernatant and the deionized water portions used to wash the solid were transferred to a filter from Millipore Express[®] plus with 0.22 µm pore diameter. All liquid collected as a filtrate was added to a 250 mL flask and the volume was completed with deionized water; later, the amount of K^+ cation was quantified by chemical analysis.

2.4 Thermal treatment of $H_xK_{(4-x)}Nb_6O_{17}$ sample

Four portions of the $H_xK_{(4-x)}Nb_6O_{17}$ sample were separately added to crucibles and thermal treated at 250, 300, 350, or 400 °C for 30 min.

2.5 Instruments

XRD patterns of $K_4Nb_6O_{17}$ and $H_xK_{(1-x)}Nb_6O_{17}$ powdered samples were recorded in a Rigaku MiniFlex equipment, using Cu anode (1.518 Å), scan range 1.5–70°(2θ), and scan step of 0.015° (2θ)/2s.

Thermogravimetric analysis coupled to mass spectrometry (TGA-MS) was performed in a Netzsch thermal analyzer model TGA/DSC 490 PC Luxx coupled to an Aëolos 403 C mass spectrometer, using platinum crucible, from room temperature to 600 °C, and heating rate of 10 °C min⁻¹ under synthetic air flow of 50 mL min⁻¹.

Raman spectra were recorded in a Bruker FT-Raman (laser wavelength = 1064 nm), at 50 mW and 512 scans, resolution of 4 cm⁻¹, and gain of 32.

ICP-AES analysis of potassium element from the supernatant of the ion exchange reaction was performed in an Spectro Analytical Instruments equipment at the Central Analítica of Instituto de Química (Universidade de São Paulo – USP).

The synthesis of the $K_2Nb_6O_{17}$ phase and the thermal treatment of $H_xK_{(4-x)}Nb_6O_{17}$ sample were proceeded in a Carbolite RHF 1500 furnace.

3. Results and discussion

Figures 2a and 2b show the XRD patterns of $K_4Nb_6O_{17}$ and $H_xK_{(4-x)}Nb_6O_{17}$ samples, respectively, displaying narrow and intense peaks related to the basal spacing, which profiles agree with the literature (Bizeto and Constantino, 2004; Madaro *et al.*, 2011; Nassau *et al.*, 1969). For the $K_4Nb_6O_{17}$ precursor, no reflections concerning the Nb_2O_5 nor K_2O reagents were identified. The positions of the (02n0) peaks are in agreement with the tri-hydrated potassium layered hexaniobate. (Bizeto and Constantino, 2004; Nassau *et al.*, 1969; Shiguihara *et al.*, 2007). Basal spacing ($d(040)$) is equal to 9.36 Å. After the exchange of K^+ ions by H^+ cations, the (040) peak is displaced towards higher angles region in agreement with the intercalation of hydrated H^+/H_3O^+ cations, conducting to the decrease in the basal spacing to 7.97 Å, as shown in Fig. 2b.

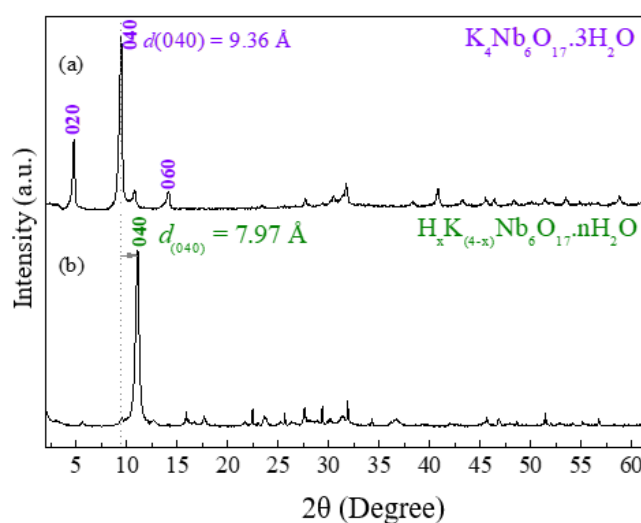


Figure 2. XRD patterns of hydrated (a) $K_4Nb_6O_{17}$ and (b) $H_xK_{(4-x)}Nb_6O_{17}$ samples.

The dehydroxylation process of the $H_xK_{(4-x)}Nb_6O_{17}$ phase was investigated by heating the sample at different temperature values. Figure 3 shows the XRD patterns of the $H_xK_{(4-x)}Nb_6O_{17}$ sample and the thermal treated material at 250, 300, 350, and 400 °C. The increase in the temperature promotes a progressive reduction in the intensity of the (040) peak, already evident for the sample heated at 250 °C, as well as the decrease in the $d(040)$ basal spacing, indicating the partial collapse of the layered structure because de dehydroxylation process.

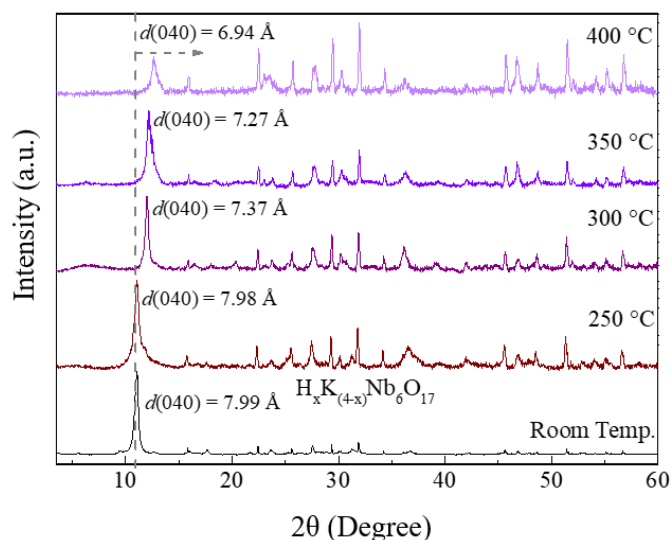


Figure 3. XRD patterns of $H_xK_{(4-x)}Nb_6O_{17}$ sample and the products isolated after the thermal treatment at 250, 300, 350, and 400 °C.

Figure 4 shows the Raman spectra of $H_xK_{(4-x)}Nb_6O_{17}$ and the thermal treated samples. For the nonthermal treated sample, the bands in the 200 – 300 cm^{-1} region are attributed to the bending of the Nb–O–Nb bond. Slightly-distorted octahedra originate the bands in the 500 – 700 cm^{-1} range, while the bands between 850 and 1000 cm^{-1} are assigned to highly-distorted $[NbO_6]$ units, in which the terminal Nb–O groups present double bond character (Bizeto *et al.*, 2010). Increasing the temperature value, the band around 940 cm^{-1} progressively decreases in intensity because of the condensation of the terminal Nb–O groups. Bands at around 545 and 666 cm^{-1} are shift towards lower energy region with heat intensification, what can be related to difications in the $[NbO_6]$ octahedra and with the formation of new Nb–O–Nb bonds. Shifts observed for the sample treated at 250 °C in comparison to the original material indicate that dehydroxylation already started at about this temperature value, in agreement with XRD results.

Figure 5 presents TGA-DTG (A) and DSC-MS (B) curves of the $H_xK_{(4-x)}Nb_6O_{17}$ sample in which four main mass loss events are observed (Fig. 5a). The first and second endothermic events occurring from room temperature up to 130 °C and in the 130 – 230 °C range are related to the release of superficially adsorbed and intercalated water molecules (Fig. 5b, MS curve of the fragment $m/z = 18$). The third (at about 230 – 310 °C) and fourth (in 310 – 600 °C range) mass loss events can be related to the dehydroxylation of the dehydrated matrix by the condensation of -OH terminal groups originated from the bond established between the

interlayer H^+ and the niobyl (Nb=O) group, promoting the formation of new chemical bonds.

The thermal decomposition of the $H_xK_{(4-x)}Nb_6O_{17}$ material can be expressed by Eq. 1 (Bizeto and Constantino, 2004).

Table 1 presents the detailed mass loss percentages from TGA results (Fig. 5) related to the $H_xK_{(4-x)}Nb_6O_{17}$ sample, as well as the number of mols of released water molecules in the four mass loss events. For all samples, the third mass loss event is the less pronounced and initiates at around 230 °C.

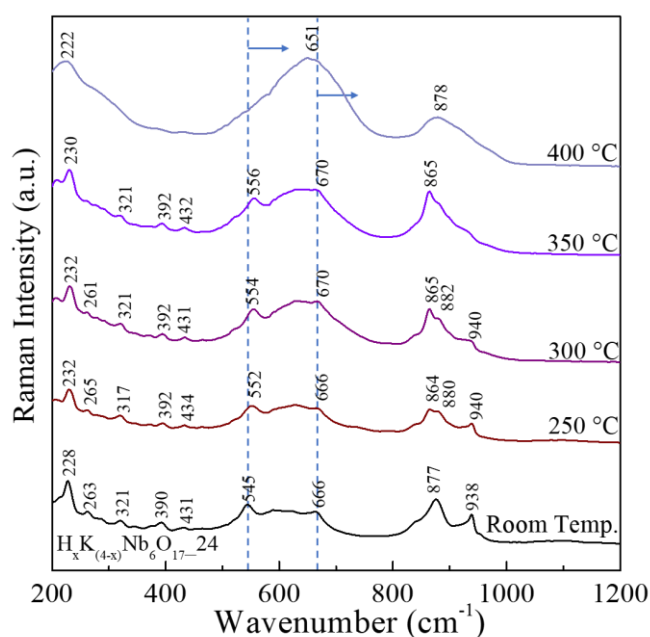
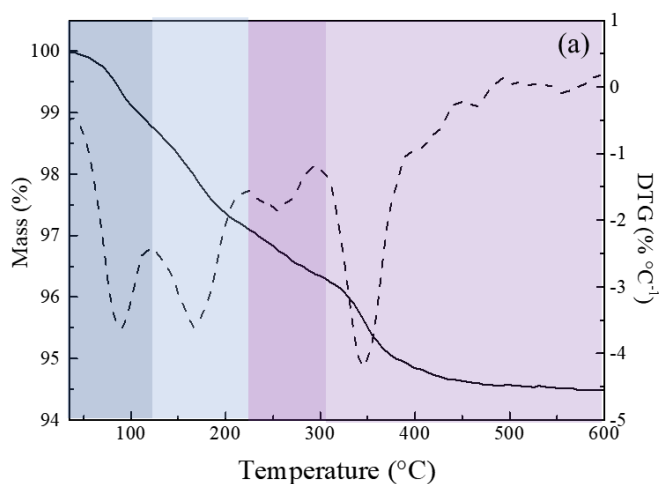


Figure 4. Raman spectra of $H_xK_{(4-x)}Nb_6O_{17}$ sample and the products isolated after the thermal treatment at 250, 300, 350, and 400 °C.



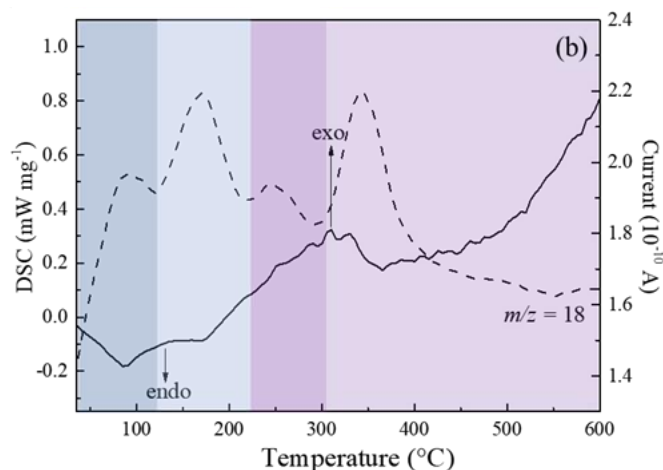


Figure 5. TGA (solid line) and DTG (dashed line) (a) and DSC (solid line) and MS (dashed line) (b) curves of $H_xK_{(4-x)}Nb_6O_{17}$ sample.

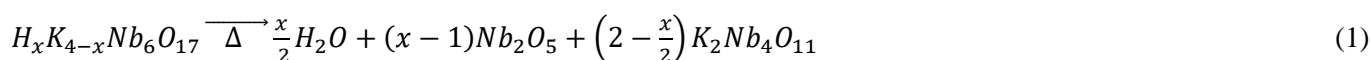


Table 2. Proton exchange percentages calculated from TGA and ICP-AES data

4° TGA mass loss event (%)	3° and 4° TGA mass loss event (%)	ICP – AES (%)
45.8	68.0	64.0

From results displayed in Tab. 2, considering only the fourth mass loss event for the calculation of the proton exchange percentage, the value is close to 50% (45.8%). Bizeto and Constantino (2004) calculated the exchange percentage for the $H_xK_{(4-x)}Nb_6O_{17}$ sample prepared by suspending the $K_4Nb_6O_{17}$ phase in 6 mol L^{-1} HNO_3 solution at 60 °C for three days. In that work, it was considered that the dehydroxylation occurs from 315 °C. Thus, the last TGA mass loss event was considered for the calculation of ion exchange percentage, resulting in about 50%. However, when considered here both the third and the fourth events corresponding to the dehydroxylation, proton exchange percentage was much higher (68.0%) and closer to that one observed from ICP-AES quantification (64.0%). Thus, regions I and II were hydrated and could undergo the exchange of K^+ by H^+ ion.

In this work, the hexaniobate dehydroxylation process was studied for a more precise determination of its starting temperature, shown to be below 300 °C. Accordingly, the quantification of K^+ cations by ICP-AES endorsed the necessity to consider both third and fourth mass loss events for the determination of the extension of the proton exchange reaction from TGA analysis. Moreover, results presented here indicate that region II can also be hydrated in a meaningful amount

Table 1. DTG peaks, mass loss percentages for the respective temperature ranges of TGA mass loss events for the $H_xK_{(4-x)}Nb_6O_{17}$ material and the amount of released water molecules.

Temperature range (°C)	DTG peak (°C)	Δ% mass	Amount of released water (mol)
25-130	88	1.37	0.71
130-230	166	1.52	0.78
230-310	256	0.84	0.44
310-600	347	1.80	0.92

Table 2 shows the proton exchange percentages calculated from TGA (Tab. 1), considering only the fourth or both third and fourth mass loss events, and the exchange percentages obtained from ICP-AES analyses of potassium, considering the Eq. 1.

and experience the intercalation of H^+ cations. Acid phase obtained under mild experimental conditions reported in this study can be expressed as $H_{2.7}K_{1.3}Nb_6O_{17}$ or $H_{2.6}K_{1.3}Nb_6O_{17}$, calculated from TGA and ICP-AES, respectively.

4. Conclusions

The XRD patterns confirmed the formation of the $K_4Nb_6O_{17} \cdot 3H_2O$ and $H_xK_{(4-x)}Nb_6O_{17}$ phases. From ICP-AES results, proton exchange was equal to 64.0%. Comparatively, results from TGA indicated 45.8% and 68.0% of proton exchange when considered hydroxylation event above 230 or 310 °C, respectively. These analytical data, combined to the XRD and Raman spectroscopic analyses of the acid hexaniobate heated from 250 to 400 °C, indicate that dehydroxylation process starts around 230 °C. Region II can also be hydrated and have K^+ cations exchanged by H^+ . TGA-MS is a suitable tool to determine the level of protonation of hexaniobate, assisting the investigation of experimental approaches to improve the niobate exfoliation, such as ultrasonication, because exfoliation depends on the reactivity of the acidic intermediate phase.

Authors' contribution

Conceptualization: Constantino, V. R. L.

Data curation: Figueiredo, M. P.; Constantino, V. R. L.

Formal Analysis: Figueiredo, M. P.

Funding acquisition: Constantino, V. R. L.

Investigation: Figueiredo, M. P.
Methodology: Figueiredo, M. P.; Constantino, V. R. L.
Project administration: Constantino, V. R. L.
Resources: Constantino, V. R. L.
Software: Not applicable.
Supervision: Constantino, V. R. L.
Validation: Figueiredo, M. P.
Visualization: Figueiredo, M. P.
Writing – original draft: Figueiredo, M. P.
Writing – review & editing: Figueiredo, M. P.; Constantino, V. R. L.

Data availability statement

All data sets were generated or analyzed in the current study.

Funding

Conselho Nacional de Desenvolvimento Científico e Tecnológico (CNPq). Grant No: 305446/2017-7.

Acknowledgments

The authors are grateful to the Laboratório de Espectroscopia Molecular Hans Stammreich (Institute of Chemistry – USP) for the Raman spectra recording.

References

- Bizeto, M. A.; Constantino, V. R. L.; Structural Aspects and Thermal Behavior of the Proton Exchanged Layered Niobate $K_4Nb_6O_{17}$. *Mater. Res. Bull.* **2004**, *39* (11), 1729–1736. <https://doi.org/10.1016/j.materresbull.2004.05.001>
- Bizeto, M. A.; Christino, F. P.; Tavares, M. F. M.; Constantino, V. R. L. Aspectos estruturais relacionados ao processo de troca iônica no niobato lamelar $K_4Nb_6O_{17}$. *Quim. Nova.* **2006**, *29* (6), 1215–1220. <https://doi.org/10.1590/S0100-40422006000600013>
- Bizeto, M. A.; Shiguihara, A. L.; Constantino, V. R. L. Layered niobate nanosheets: building blocks for advanced materials assembly. *J. Mater. Chem.* **2009**, *19* (17), 2512–2525. <https://doi.org/10.1039/b821435b>
- Bizeto, M. A.; Leroux, F.; Shiguihara, A. L.; Temperini, M. L. A.; Sala, O.; Constantino, V. R. L. Intralamellar structural modifications related to the proton exchanging in $K_4Nb_6O_{17}$ layered phase. *J. Phys. Chem. Solids.* **2010**, *71* (4), 560–564. <https://doi.org/10.1016/j.jpcs.2009.12.036>
- Elumalai, S.; Vadivel, S.; Yoshimura, M. Interlayer-modified two-dimensional layered hexaniobate $K_4Nb_6O_{17}$ as an anode

material for lithium-ion batteries. *Mater. Adv.* **2021**, *2* (6), 1957–1961. <https://doi.org/10.1039/D1MA00055A>

Gasperin, M.; Le Bihan, M.-T. Un niobate de rubidium d'un type structural nouveau: $Rb_4Nb_6O_{17} \cdot 3H_2O$. *J. Solid State Chem.* **1980**, *33* (1), 83–89. [https://doi.org/10.1016/0022-4596\(80\)90550-2](https://doi.org/10.1016/0022-4596(80)90550-2)

Gasperin, M.; Le Bihan, M.T. Mecanisme d'hydratation des niobates alcalins lamellaires de formule $A_4Nb_6O_{17}$ (A = K, Rb, Cs). *J. Solid State Chem.* **1982**, *43* (3), 346–353. [https://doi.org/10.1016/0022-4596\(82\)90251-1](https://doi.org/10.1016/0022-4596(82)90251-1)

Guo, C.; Zhu, J.; He, J.; Hu, L.; Zhang, P.; Li, D. Catalytic oxidation/photocatalytic degradation of ethyl mercaptan on α - $MnO_2@H_4Nb_6O_{17}$ -NS nanocomposite. *Vacuum.* **2020**, *182*, 109718. <https://doi.org/10.1016/j.vacuum.2020.109718>

Hu, C.; Zhang, L.; Cheng, L.; Chen, J.; Hou, W.; Ding, W. A comparison of H^+ -restacked nanosheets and nanoscrolls derived from $K_4Nb_6O_{17}$ for visible-light degradation of dyes. *J. Energy Chem.* **2014**, *23* (2), 136–144. [https://doi.org/10.1016/S2095-4956\(14\)60128-5](https://doi.org/10.1016/S2095-4956(14)60128-5)

Kimura, N.; Kato, Y.; Suzuki, R.; Shimada, A.; Tahara, S.; Nakato, T.; Matsukawa, K.; Mutin, P.H.; Sugahara, Y. Single- and Double-Layered Organically Modified Nanosheets by Selective Interlayer Grafting and Exfoliation of Layered Potassium Hexaniobate. *Langmuir.* **2014**, *30* (4), 1169–1175. <https://doi.org/10.1021/la404223x>

Li, D.; Li, Q.; He, J.; Hu, L.; Hu, J. Niobate nanoscroll composite with Fe_2O_3 particles under moderate conditions: assembly and application research. *New J. Chem.* **2016**, *40* (1), 136–143. <https://doi.org/10.1039/C5NJ02120K>

Liu, X.; Que, W.; Chen, P.; Tian, Y.; Liu, J.; He, Z.; Zhou, H.; Kong, L. B. Facile preparation of protonated hexaniobate nanosheets and its enhanced photocatalytic activity. *Nanotechnology.* **2017**, *28* (23), 235702. <https://doi.org/10.1088/1361-6528/aa6b4f>

Madaro, F.; Sæterli, R.; Tolchard, J.; Einarsrud, M.-A.; Holmestad, R.; Grande, T. Molten salt synthesis of $K_4Nb_6O_{17}$, $K_2Nb_4O_{11}$ and KNb_3O_8 crystals with needle- or plate-like morphology. *CrystEngComm.* **2011**, *13* (5), 1304–1313. <https://doi.org/10.1039/C0CE00413H>

Maeda, K.; Eguchi, M.; Lee, S.-H. A.; Youngblood, W. J.; Hata, H.; Mallouk, T. E. Photocatalytic Hydrogen Evolution from Hexaniobate Nanoscrolls and Calcium Niobate Nanosheets Sensitized by Ruthenium(II) Bipyridyl Complexes. *J. Phys. Chem. C.* **2009**, *113* (18), 7962–7969. <https://doi.org/10.1021/jp900842e>

Müller-Warmuth, W.; Schöllhorn, R. Progress in Intercalation Research. In *Physics and Chemistry of Materials with Low-Dimensional Structures*; Springer, 1994.

Nassau, K.; Shiever, J. W.; Bernstein, J. L. Crystal Growth and Properties of Mica-Like Potassium Niobates. *J. Electrochem. Soc.* **1969**, *116* (3), 348–353.

Rao, C. N. R.; Raveau, B. *Transition Metal Oxides: Structure, Properties, and Synthesis of Ceramic Oxides*. Wiley, 1998.

Shiguihara, A. L.; Bizeto, M. A.; Constantino, V. R. L. Exfoliation of layered hexaniobate in tetra(n-butyl)ammonium hydroxide aqueous solution. *Colloids Surf. A: Physicochem. Eng. Asp.* **2007**, *295* (1–3), 123–129. <https://doi.org/10.1016/j.colsurfa.2006.08.040>

Shiguihara, A.; Bizeto, M. A.; Constantino, V. R. L. Chemical modification of niobium layered oxide by tetraalkylammonium intercalation. *J. Braz. Chem. Soc.* **2010**, *21* (7), 1366–1376. <https://doi.org/10.1590/S0103-50532010000700024>

Silva, C. H. B.; Iliut, M.; Muryn, C.; Berger, C.; Coldrick, Z.; Constantino, V. R. L., Temperini, M. L. A., Vijayaraghavan, A. Ternary nanocomposites of reduced graphene oxide, polyaniline and hexaniobate: Hierarchical architecture and high polaron formation. *Beilstein J. Nanotechnol.* **2018**, *9*, 2936–2946. <https://doi.org/10.3762/bjnano.9.272>

Wei, Q.; Nakato, T. Preparation of a layered hexaniobate–titania nanocomposite and its photocatalytic activity on removal of phenol in water. *J. Porous. Mater.* **2009**, *16* (2), 151–156. <https://doi.org/10.1007/s10934-007-9179-2>

Biosynthesis of tetrahydrobenzofuran neolignans in somatic embryos of *Ocotea catharinensis*

Érica Luiz dos Santos¹, Eny Iochevet Segal Floh², Massuo Jorge Kato¹⁺

1. University of São Paulo, Institute of Chemistry, São Paulo, Brazil.
2. University of São Paulo, Institute of Biosciences, São Paulo, Brazil.

+Corresponding author: Massuo Jorge Kato, **Phone:** +55 11 30911886, **Email address:** massuojorge@gmail.com

ARTICLE INFO

Article history:

Received: September 20, 2021

Accepted: February 11, 2022

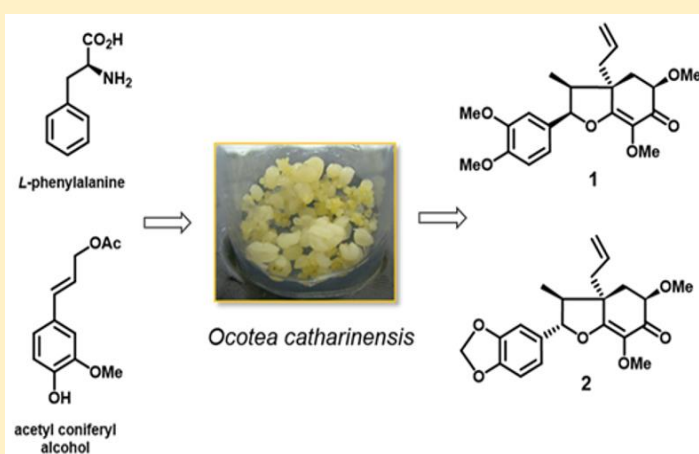
Published: August 17, 2022

Section Editor: Assis Vicente Benedetti

Keywords

1. Lauraceae
2. *Ocotea catharinensis*
3. somatic embryos
4. ¹³C labelling
5. phenylpropanoids

ABSTRACT: Somatic embryos of *Ocotea catharinensis* were used as a model to investigate the biosynthetic pathway of tetrahydrobenzofuran neolignan formation by means of feeding ¹³C-labelled precursors followed by analysis using MS and ¹³C NMR. Isotopomers of *L*-[¹³C]-phenylalanine administered to embryos were incorporated into tetrahydrobenzofuran neolignans and the analysis of ¹³C NMR clearly revealed the enriched position of precursors. While feeding a series of putative intermediate including [8-¹³C]-ferulic acid, [8-¹³C]-glycoferulic acid, and [8-¹³C]-coniferyl alcohol were not successful in incorporation to the neolignans, the [8-¹³C]-coniferyl acetate was detected as an intermediate in the biosynthesis of the neolignan 5'-methoxy-porosin. In the bioconversion assay using the protein fraction from the embryogenic cultures, only the substrate coniferyl acetate was converted into isoeugenol, which together with eugenol, is one of the putative precursors of neolignan formation. These findings support that the tetrahydrobenzofuran neolignans are derived from the oxidative coupling between units of *E*- isoeugenol and 5'-methoxy-eugenol leading to a regio- and stereospecific products.



1. Introduction

Lauraceae is a large family of higher plants, comprising about 50 genera with approximately 3000 species. Fossil records show that the first Lauraceae species appeared during the middle of the Cretaceous period and for this reason this plant family is considered one of the most primitive families of Angiosperms belonging to the Magnoliidae clade (Doyle and Endress, 2000; Endress and Doyle, 2009). Some species of this family are widely commercialized and appreciated for their culinary uses, such as cinnamon (*Cinnamomum zeylanicum* and *C. cassia*) (Anand *et al.*, 2016) and avocado (*Persea americana*) (Cervantes-Paz and Yahia, 2021; Jimenez *et al.*, 2021). The genus *Ocotea*, one of the Brazilian genera with wide occurrence in the tropics, provide high quality wood with species like *Ocotea catharinensis* and *O. acutifolia* often been used in construction and carpentry (Montagna *et al.*, 2018). Furthermore, species from the Lauraceae family like *Cinnamomum camphora* in Asia, popularly known as camphor and *Aniba rosiodora*, source of rosewood in South America, are rich in essential oils and are used worldwide in perfumery (Amaral *et al.*, 2017; Amazonas *et al.*, 2020).

The secondary metabolites most frequently found in Lauraceae are phenylpropanoids and their dimeric compounds neolignans (Aiba *et al.*, 1975; 1977; Funasaki *et al.*, 2009; Rozo-Lugo *et al.*, 2018), in addition to flavonoids (David *et al.*, 1994; Rossi *et al.*, 1997), pyrones (Nehme *et al.*, 2008; Rossi *et al.*, 1997), and alkaloids (Gottlieb, 1972; Teles *et al.*, 2019). *Ocotea catharinensis* is a native species to the Atlantic Forest of Brazil, found in the states of Paraná, Santa Catarina, Rio Grande do Sul and São Paulo. Due to the high quality of its wood and difficulty in propagation, however, its natural population has decreased significantly, resulting in its inclusion in the list of endangered species (Montagna *et al.*, 2018). Therefore, a somatic embryogenesis system has been developed with the aim of increasing cultivation and propagation. Phytochemical studies of *O. catharinensis* somatic embryos, stems and leaves have shown that neolignans, especially those of a tetrahydrobenzofuranoid and bicyclooctanoid type, constitute the main secondary metabolites produced by this species (Funasaki *et al.*, 2009).

From a biosynthetic point of view, lignans, neolignans and related compounds are interconnected through the general phenylpropanoid pathway that has the amino acid *L*-phenylalanine as a primary precursor.

Then, by a series of enzymatic steps the formation of cinnamyl alcohols is achieved deriving propenylbenzenes and allylbenzenes, which are supposedly the direct precursors of neolignans in *Ocotea* and other plant species (Anterola and Lewis, 2002; Ferrer *et al.*, 2008; Sartorelli *et al.*, 2001; Suzuki and Umezawa, 2007).

The key step involved in the formation of neolignans is the oxidative coupling reaction in which the phenoxide radicals produced by an oxidase may undergo the dimerization reaction followed by further intramolecular polar or by pericyclic reactions determining the main neolignan sub-classes to be formed (Gottlieb, 1972). Examples of these neolignans are the tetrahydrobenzofuran and bicyclooctane [3.2.1] neolignans frequently found in Lauraceous species (Alvarenga *et al.*, 1977; Coy-Barrera *et al.*, 2009; Salleh and Ahmad, 2017). Specifically, tetrahydrobenzofuran-6(2*H*)- and dihydrobenzofuran-6(2*H*)-neolignans such as porosin (Aiba *et al.*, 1976), and mirandin (Aiba *et al.*, 1977) were characterized from Lauraceae species. Nevertheless, to date, the biosynthetic pathways leading to neolignan formation are restricted to the steps required for the formation of allyl and propenylphenols and only one case was addressed to investigate the neolignan formation in *Piper* species (Sartorelli *et al.*, 2001). Interestingly, the acetylation of *p*-coumaric alcohol to form an intermediate prone to be reduced by a reductase, suggest that the leaving group is required for the elimination of the alcohol. This step was demonstrated using enzymatic conversion from cell cultures of basil (*Ocimum basilicum*), for which the specific enzyme eugenol synthase (EGS) requires coniferyl acetate and NADPH to form eugenol (Vassão *et al.*, 2006). In the case of *Petunia* flower cultures, an enzyme homologous to that found in basil, isoeugenol synthase (IGS), also uses coniferyl acetate and NADPH as substrates to catalyse the formation of *E*-isoeugenol. Two mechanisms proposed for the elimination of the acetate group for the formation of allyl and propenylphenols involves a direct attack of the hydride from NADPH at the C-9 carbon of the side chain, leading to the formation of isoeugenol or the attack of the hydride to the C-7 carbon leading to the conjugated elimination of acetyl group giving rise to the eugenol (Koeduka *et al.*, 2006; Vassão *et al.*, 2006). For this reason, herein, we used the somatic embryos and a series of potential ¹³C-labeled substrates to investigate what the biosynthetic precursors and intermediates of tetrahydrobenzofuran neolignans are in *Ocotea catharinensis*.

2. Experimental

2.1 Reagents

Pyridine and piperidine were, respectively, distilled under reduced pressure in the presence of KOH (25 g L⁻¹) and, stored with a 4 Å molecular sieve, in a vacuum desiccator protected from light. Ethyl ether (Et₂O) and tetrahydrofuran (THF), separately, were dried using metallic sodium and distilled over benzofuran for synthetic preparations. The dichloromethane, spectroscopic degree, was left under anhydrous calcium chloride (CaCl₂) for 12 h after which it was filtered and distilled under reduced pressure in the presence of calcium hydride (CaH₂). It was stored on a 4 Å molecular sieve, protected from light in a dry N₂ (g) atmosphere. HPLC grade toluene was used without prior treatment. Chromatographic and spectroscopic analysis used analytical grade solvents (Merck[®], Tedia[®] and J.T. Baker[®]) and purified water in the Milli-Q system (Millipore[®]). The reagents were obtained commercially with a high degree of purity, were used without previous purification.

2.2 High Performance Liquid Chromatography (HPLC)

Chromatographic analyses were carried out using a Shimadzu chromatograph model SCL-10Avp, equipped with two analytical pumps model LC-10AD, connected to a diode array detector model SPD-M10Avp with an automatic injector model SIL-9A, controlled by a communication module SCL-10AVP. The samples were solubilized in MeOH: H₂O (8:1 v/v), filtered through a 0.45 µm Millex[®] membranes and injected on a Phenomenex[®] reverse phase C-18 column (Luna C-18 150 x 4.6 mm, 5 µm). The data was analysed using the program Class-VP version 6.10 program. The solvent system used in the HPLC analysis consisted of a mixture of CH₃CN:H₂O (2:3) for 18 min; CH₃CN:H₂O (4:1) for 2 min; CH₃CN:H₂O (2:3) for 6 min and the detector was set at λ 280 nm.

2.3 Analytical and preparative thin layer chromatography

TLC analyses were performed on Merck[®] plates, silica gel 60, with fluorescence indicator F254, with aluminum support thickness 0.2 mm. Prep-TLC purification were performed on 20 x 20 cm glass plates with 1.0 mm thick silica gel 60 from Merck[®] and fluorescence indicator F₂₅₄. The plates were developed

under UV 254 and 366 nm or after being sprayed with a solution of sulfuric vanillin, followed by heating. For preparative thin layer radial chromatography, round glass plates were used, covered with a 2.0 mm thick layer of Kieselgel 60 F₂₅₄ were used. The samples (about 100 mg) were solubilized in hexane:EtOAc (1:1) and recovered according to the UV visible bands.

2.4 Column chromatography

The purification of compounds using column chromatography was performed on glass chromatographic column, with length and diameter of the column determined according to the sample masses to be fractionated. Merck[®] 0.063 – 0.200 mm (70–230 mesh ASTM) silica gel 60 and C18 reverse phase silica were used as the stationary phases. The proportion of silica used for the column was approximately 20 times the mass of the sample to be purified.

2.5 High performance liquid chromatography coupled to the mass spectrometer (HPLC-ESI)

The extracts from the somatic embryos fed with precursors were analysed by high performance liquid chromatography coupled to a mass spectrometry detector (HPLC-ESIMS). Mass spectrometry analysis was performed on a Bruker, Esquire 2000 plus in a positive electrospray mode, capillary voltage 4.5 kV and skimmer 70 V.

2.6 Electronic Ionization Mass spectrometry

The mass spectra with electron impact ionization, were recorded on a Shimadzu mass spectrometer model GCMS-QP2010, equipped with a capillary column DB-5 (30 m x 0.25 mm, i.d. 0.25 µm).

2.7 Nuclear Magnetic Resonance

The nuclear magnetic resonance analyses were performed at the Analytical Center of the Institute of Chemistry of the University of São Paulo (IQ – USP). The spectra were recorded on Bruker AC200 (200 MHz), Varian Gemini 200 (200 MHz), Varian Inova 300 (300 MHz) and Bruker DRX 500 (500 MHz) spectrometers. The samples were solubilized in CDCl₃ (Isotec[®] Inc. and Aldrich[®]). The chemical shifts (δ) of the obtained spectra are described as ppm in relation to the TMS signal, used as an internal reference standard in all samples (0.05%).

2.8 Embryos of *Ocotea catharinensis*

Fruits of *Ocotea catharinensis* Mez. (Lauraceae) were collected in the Serra da Cantareira State Park of the Forest Institute of São Paulo, São Paulo–SP. To obtain the somatic embryos, the seeds were treated and inoculated according to the methodology described (Moura–Costa *et al.*, 1993). The embryos were kept in WPM culture medium (Wood Plant Medium) (Lloyd and McCown, 1980), supplemented with sucrose (20 g/L), sorbitol (22 g L⁻¹), glutamine (0.4 g L⁻¹) and phytigel (Phytigel, Sigma Co., USA) (2 g L⁻¹). The pH of the medium was adjusted to 5.8 with NaOH before adding the phytigel. Then, the media were distributed in test tubes (8 mL/tube), closed, and autoclaved at 120 °C for 15 min, at 1.1 kgf cm⁻². After 21 weeks of cultivation, the somatic embryos in the globular stage were inoculated in a new culture medium, for the maintenance of embryogenic cultures *in vitro*.

2.9 Extraction and purification of neolignans from somatic embryos of *Ocotea catharinensis*

The analysis of the content of embryos of *O. catharinensis* was investigated using fresh embryos (130 g) crushed in N₂ (l) and extracted with MeOH:H₂O (9:1) using an Ultraturrax apparatus (T25 basic, IKA Labortechnik®) at 11,000 rpm. The solution was extracted twice with chloroform solutions, which were combined and dried yielding 480 mg of a CDCl₃ fraction. The CHCl₃ fraction was then submitted to a chromatographic column, with flash silica, eluted with CH₂Cl₂:EtOAc (1:2), followed by CH₂Cl₂:Acetone (1:1) (Funasaki *et al.*, 2009). The fractions were pooled after TLC analysis and samples containing the major neolignans 5'-methoxyporosin and armenin B were subjected to further separation by prep-TLC. Standard neolignans were used as control samples to monitor the purification of ¹³C-labelled compounds after incorporations of substrates.

2.10 HPLC profile of somatic embryo extracts

The chromatographic profile of the extracts from the embryos was analyzed by HPLC using the standards compounds isolated from *O. catharinensis* embryos. The extracts were filtered through a 0.45 µm Millipore filter and a Sep-Pack C-18 filter eluted in MeOH: H₂O (9:1) to eliminate the lipophilic matrix. The chromatographic analysis was carried out as described (See item 2.2).

2.11 Feeding of L-[1-¹³C]-, L-[2-¹³C]- and L-[3-¹³C]-phenylalanine in embryos of *O. catharinensis*

In vitro culture of 21 days-old somatic embryos with were transferred to Petri dishes containing two sheets of filter paper. The embryos were left on the plates for 30 min, at room temperature, in a laminar flow hood in order to dehydrate. Solutions containing 0.5 and 1.0 mg of L-[1-¹³C]-phenylalanine in 100 µL of Milli-Q Water were administered to 1.0 g of embryos in Petri dishes. Solutions of each concentration were fed in triplicate for 12, 24, 48, 72 and 96 h, in a culture room, in the presence of incandescent light, at 25 °C, with replacement of the precursor solution when required. As a control, 1.0 g of embryos was used without the addition of the labeled precursor. After each incubation time, the samples were crushed in liquid nitrogen, extracted with MeOH:H₂O (9:1) and the solutions were partitioned with chloroform. The chloroform was evaporated under an N₂ stream, the fractions were resuspended in MeOH:H₂O (9:1), filtered through a 0.45 µm Millipore filter and analyzed using HPLC-ESI, in order to quantify the incorporation of the ¹³C-labelled precursor into the neolignans. Then, the optimum incubation time was defined as 72 h and a concentration of 1.0 mg/100 µL solutions of L-[2-¹³C]-phenylalanine and L-[3-¹³C]-phenylalanine were fed under the same condition, with the experiments being carried out in triplicate and analyzed by HPLC-ESI. In the case of the incubation of the embryos with the respective L-phenylalanine isotopomers, 8.0 g of embryos divided into Petri dishes with 4.0 g each were incubated and 800 µL of the solution (1 mg mL⁻¹) were administered to the embryos of each plate for 72 h, with replenishment of the solution (800 µL) every 24 h. The neolignans isolated were subjected to ¹H and ¹³C NMR analysis.

2.12 Administration of [8-¹³C]-ferulic acid

For the preparation of [8-¹³C]-ferulic acid and all ¹³C-labelled compounds, see [Supplementary Material](#). The incubation of somatic embryos with [8-¹³C]-ferulic acid was carried out under the same conditions as the L-phenylalanine isotopomers. In the first assay for the incorporation, [8-¹³C]-ferulic acid was solubilized in 0.5 µL of DMSO, 0.5 µL of 0.5% NaOH solution with the remaining volume filled with Milli-Q Water. Each of the concentrations, 0.25, 0.5 and 1.0 mg of the acid in 100 µL of the solution were tested for 12, 24, 48, 72 and 96 h. The quantification of the incorporation was determined by HPLC-ESI analysis. In the second assay, [8-¹³C]-ferulic acid was solubilized in H₂O:acetone

(4:1) and was tested under the same conditions as the first incubation with the experiments being carried out in triplicate. The embryos were incubated in larger quantities by solubilizing [8-¹³C]-ferulic acid in H₂O:acetone (4:1) at 0.5 mg in 100 μL, for 48 h, with replacement of the precursor solution every 24 h. The obtained extracts were subjected to purification and the neolignans were analyzed by ¹H and ¹³C NMR analysis.

2.13 Administration of [8-¹³C]-glycoferulic acid

Due to the low solubility of [8-¹³C]-ferulic acid in aqueous medium, the alternative approach was to prepare the [8-¹³C]-glycoferulic acid. The embryos were incubated under the same conditions as the previous precursors, with the tested concentrations being 0.25, 0.5 and 1.0 mg of [8-¹³C]-glycoferulic acid solubilized in 100 μL of Milli-Q water. Each concentration was tested for the same timeframe of 12–96 h. The experiments were carried out in triplicate. The crude extracts of the incubated embryos and the control samples were analyzed using CG-MS (EI) analysis.

2.14 Administration of [8-¹³C]-coniferyl alcohol

The [8-¹³C]-coniferyl alcohol was administered to embryos under the same conditions as [8-¹³C]-ferulic acid, with concentrations at 0.25, 0.5 and 1.0 mg in 100 μL of H₂O:acetone (4:1). Each solution at various concentrations was incubated with the embryos for the timeframe of 12–96 h. The obtained extracts were subjected to the HPLC-ESI analysis as described. Embryos were also incubated with [8-¹³C]-coniferyl alcohol at large scale, under the same conditions as [8-¹³C]-ferulic acid, to obtain the neolignans for NMR analysis.

2.15 Administration of [8-¹³C]-coniferyl acetate

The embryos were incubated with the respective test concentrations of 0.25; 0.5 and 1.0 mg in 100 μL of Milli-Q Water solution containing 0.5 μL of methanol. The solutions were tested separately for the timeframe of 12–96 h. The extracts were prepared as before, and the fractions were subjected to GC-MS analysis. An amount of approximately 4.0 g of embryos were incubated with 800 μL of the solution containing [8-¹³C]-coniferyl acetate solubilized in water (1 mg.100 μL⁻¹) for 72 h, with replacement of the precursor solution every 24 h. The neolignans were isolated and subjected to ¹H and ¹³C NMR analysis.

2.16 Preparation of extracts from embryos incubated with ¹³C-precursors

After optimization conditions for incorporation, larger quantities (8.0 g) of the embryos were incubated with ¹³C-precursors. The extracts incubated with the labelled precursors were prepared accordingly, and the chloroform fractions (100 mg) were subjected to prep-TLC fractionation using hexane:EtOAc (7:3), 3 elutions, yielding about 6.0 mg of the pure neolignans.

2.17 Extraction of soluble proteins from somatic embryos of *O. catharinensis*

Approximately 8.0 g of 21-day old embryos grown *in vitro* were ground in liquid nitrogen using a mortar and pestle with 100 mL of 0.1 g L⁻¹ sodium phosphate buffer, pH 7.0 and 10% (w/w) (800 mg) of PVPP. The extract was centrifuged for 30 min at 9,000 rpm (4 °C). The supernatant was filtered through a miracloth and the residue was stored at (4 °C) for later extraction of cell wall proteins. The obtained supernatant contains soluble proteins, which were precipitated by the addition of 80% (NH₄)₂SO₄ solution. The supernatant was discarded, and the residue was resuspended in 3.0 mL of phosphate buffer and stored at -80 °C for further assays.

2.18 Extraction of proteins contained in cellular microsomes

The residue obtained after the second centrifugation was resuspended in 10 mL of 0.1 mol L⁻¹ Tris-HCl buffer, pH 7.5 and homogenized with a mortar and pestle after which the solution was centrifuged for 90 min at 48,000 rpm (4 °C). The obtained supernatant was precipitated by the addition of 80% (NH₄)₂SO₄ solution and was then centrifuged for 90 min at 48,000 rpm (4 °C). The supernatant was discarded, and the residue was resuspended in 3.0 mL of 0.1 mol L⁻¹. Tris-HCl buffer, pH 7.5. The solution corresponds to the proteins contained in cellular microsomes and was stored at -80 °C, before use.

The amount of protein present in the enzymatic extract of the embryos was determined by classical method (Bradford, 1976). For each assay, a standard curve of bovine serum albumin (BSA) was determined, as BSA was used as the standard protein. The content of soluble proteins obtained in the enzymatic extract was 8.32 mg mL⁻¹ whereas for the fraction corresponding to the proteins contained in cellular microsomes it was 4.21 mg mL⁻¹.

2.19 Incubation assays of coniferyl acetate with enzyme extracts

The enzymatic conversion assays were developed according to published procedures (Lu *et al.*, 2004; Vassão *et al.*, 2006). The coniferyl acetate was tested with several enzymatic fractions, obtained from the somatic embryos of *O. catharinensis*. The solution for the enzymatic conversion had 100 μL of enzymatic extract, a solution of 20 μL of 25 mmol L^{-1} coniferyl acetate in methanol, 76 μL of 40 mmol L^{-1} MES buffer (pH 5.0) and 4 μL of 50 mmol L^{-1} NADPH yielding a final volume of 200 μL . After 30 min of incubation at 28 $^{\circ}\text{C}$, the reaction was terminated by extraction with EtOAc (2 x 500 μL). As a control, only the precursor and the enzymatic preparation were incubated in 40 mmol L^{-1} MES buffer (pH 5.0). In the enzymatic conversion assay, the standards were incubated under the same conditions as the reactions, without adding the enzymatic fractions. The enzymatic fractions, the precursor coniferyl acetate and the possible products of the reaction (eugenol and *E*-isoeugenol) were analyzed by HPLC in a Phenomenex[®] reverse phase C-18 column (Luna C-18 150 x 4.6 mm, 5 μm), with a flow of 1 mL min^{-1} , a detector at λ 280 nm and, using the eluent H₂O (A) and CH₃CN (B) as follow: initial time 0 min (A:B, 4:1), 27 min (A:B, 1:1), 28.5 min (A:B, 0:1), 31.5 min (A:B, 0:1), 33–55 min (A:B, 4:1).

2.20 Incubation assays of *E*-isoeugenol and 5'-methoxy-eugenol with enzymatic extracts

The unlabeled phenylpropanoids *E*-isoeugenol and 5'-methoxy-eugenol were incubated together with the enzymatic fractions from embryos under different conditions to determine optimal conversion to the corresponding neolignans 5'-methoxy-porosin and armenin B. The enzymatic conversion reaction was carried out with 100 μL of enzymatic extract, 10 μL of 25 mmol L^{-1} *E*-isoeugenol and 10 μL of 25 mmol L^{-1} 5'-methoxy-eugenol in methanol, 5 μL of 1 mg mL^{-1} of horseradish peroxidase, 5 μL of 10 mmol.L^{-1} H₂O₂, 5 μL of 50 mmol L^{-1} NADPH, 110 μL of 40 mmol L^{-1} MES buffer (pH 5.0) and 5 μL of 50 mmol L^{-1} NADPH, for a final volume of 250 μL . After 1.0 h of incubation at 28 $^{\circ}\text{C}$, the reaction was terminated by extraction with EtOAc (2x 500 μL). The precursors, the possible products of the reaction, the control and the enzymatic fractions were analyzed by HPLC as previously described.

3. Results and discussion

3.1 Analysis of somatic embryo extracts from *O. catharinensis*

The content of the embryos of *O. catharinensis* had been previously described to contain the neolignans 5'-methoxy-porosin (1) and armenin B (2) (Fig. 1) (Funasaki *et al.*, 2009). For this study, the HPLC analysis of the embryos and the identification of these neolignans was consistent with previous data allowing the incorporations of ¹³C-labeled precursors using EI-MS, ESI and ¹³C NMR analysis.

The neolignans 5'-methoxy-porosin (1) and armenin-B (2) (Fig. 1) were purified and used as chromatographic standards in the ¹³C-precursor incorporation experiments. These two neolignans were confirmed by analysis of ¹H NMR, ¹³C NMR and analysis of EI-MS data and matched with those described by Ishige *et al.* (1991).

The mass spectra obtained by EI-MS of the 5'-methoxy-porosin neolignan, showed peaks according to the fragmentation proposal described and comparison with the published data (Ishige *et al.*, 1991). Armenin B was identified by comparing the ¹H and ¹³C NMR data with the data described (Aiba *et al.*, 1978; Felicio *et al.*, 1986; Ishige *et al.*, 1991).

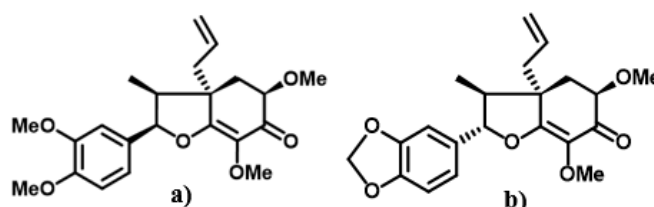


Figure 1. Chemical structures of neolignans 5'-methoxy-porosin (a) and armenin B (b) from somatic embryos of *Ocotea catharinensis*.

Source: Adapted from Funasaki *et al.* (2009).

3.2 Analysis of the incorporations of *L*-[1-¹³C]-, *L*-[2-¹³C]- and *L*-[3-¹³C]-phenylalanine

The experiments with ¹³C-isotopomers of *L*-phenylalanine were performed to determine the optimal incubation time to reach the maximum incorporation of ¹³C-precursors into the neolignans 5'-methoxy-porosin (MM= 388 Da) and armenin B (MM= 372 Da) (Fig. 2). The percentage of ¹³C incorporations in the neolignans was determined by means of HPLC-ESI analysis of the crude extracts from embryos fed with the substrates and compared with the isotopic contribution to M+1 and M+2 in natural abundance neolignans (Tab. 1).

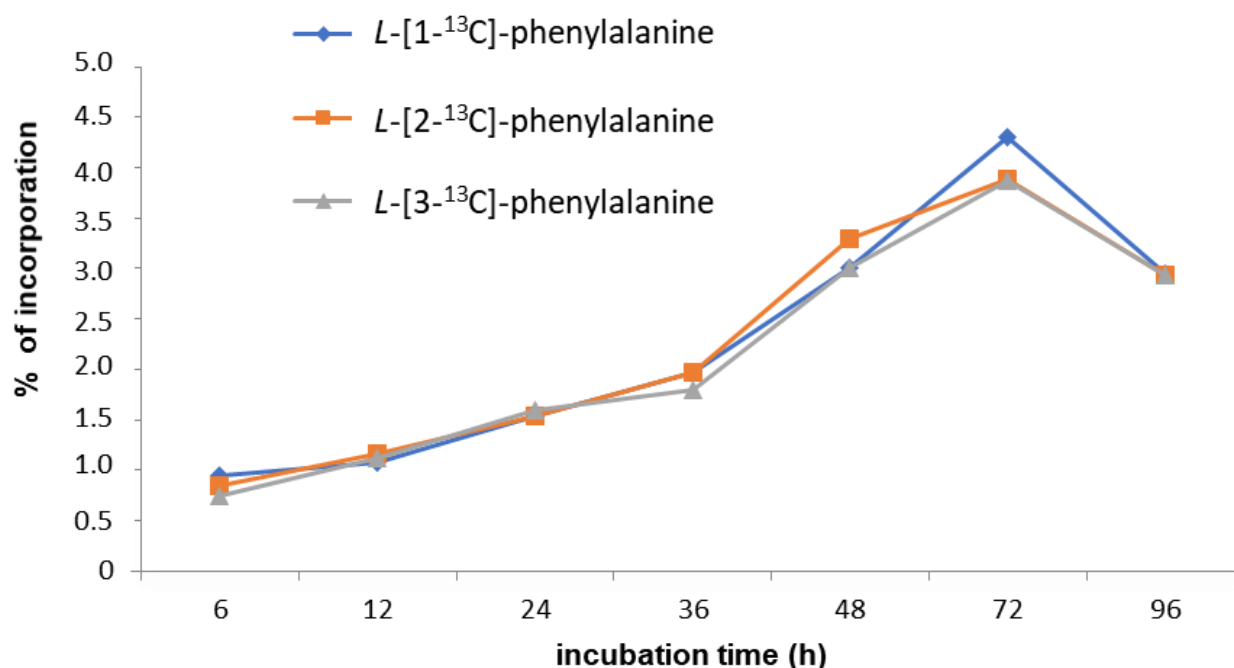


Figure 2. Time course of incorporation of isotopomers of *L*-phenylalanine into 5'-methoxy-porosin (**1**).

Table 1. ESI data showing incorporation of isotopomers of *L*-phenylalanine into 5'-methoxy-porosin (**1**) and armenin B (**2**) in embryos of *Ocotea catharinensis*.

<i>L</i> -[1- ¹³ C]-phenylalanine						
Ions	5'-methoxy-porosin (1)			armenin B (2)		
	[M+H] ⁺	[M+H+1] ⁺	[M+H+2] ⁺	[M+H] ⁺	[M+H+1] ⁺	[M+H+2] ⁺
	389	390	391	373	374	375
% of incorporation	100	9.0	2.2	100	7.2	1.2
<i>L</i> -[1- ¹³ C]-phenylalanine						
Ions	5'-methoxy-porosin (1)			armenin B (2)		
	[M+H] ⁺	[M+H+1] ⁺	[M+H+2] ⁺	[M+H] ⁺	[M+H+1] ⁺	[M+H+2] ⁺
	389	390	391	373	374	375
% of incorporation	100	8.6	1.98	100	6.6	1.1
<i>L</i> -[1- ¹³ C]-phenylalanine						
Ions	5'-methoxy-porosin (1)			armenin B (2)		
	[M+H] ⁺	[M+H+1] ⁺	[M+H+2] ⁺	[M+H] ⁺	[M+H+1] ⁺	[M+H+2] ⁺
	389	390	391	373	374	375
% of incorporation	100	8.8	2.0	100	6.8	1.4

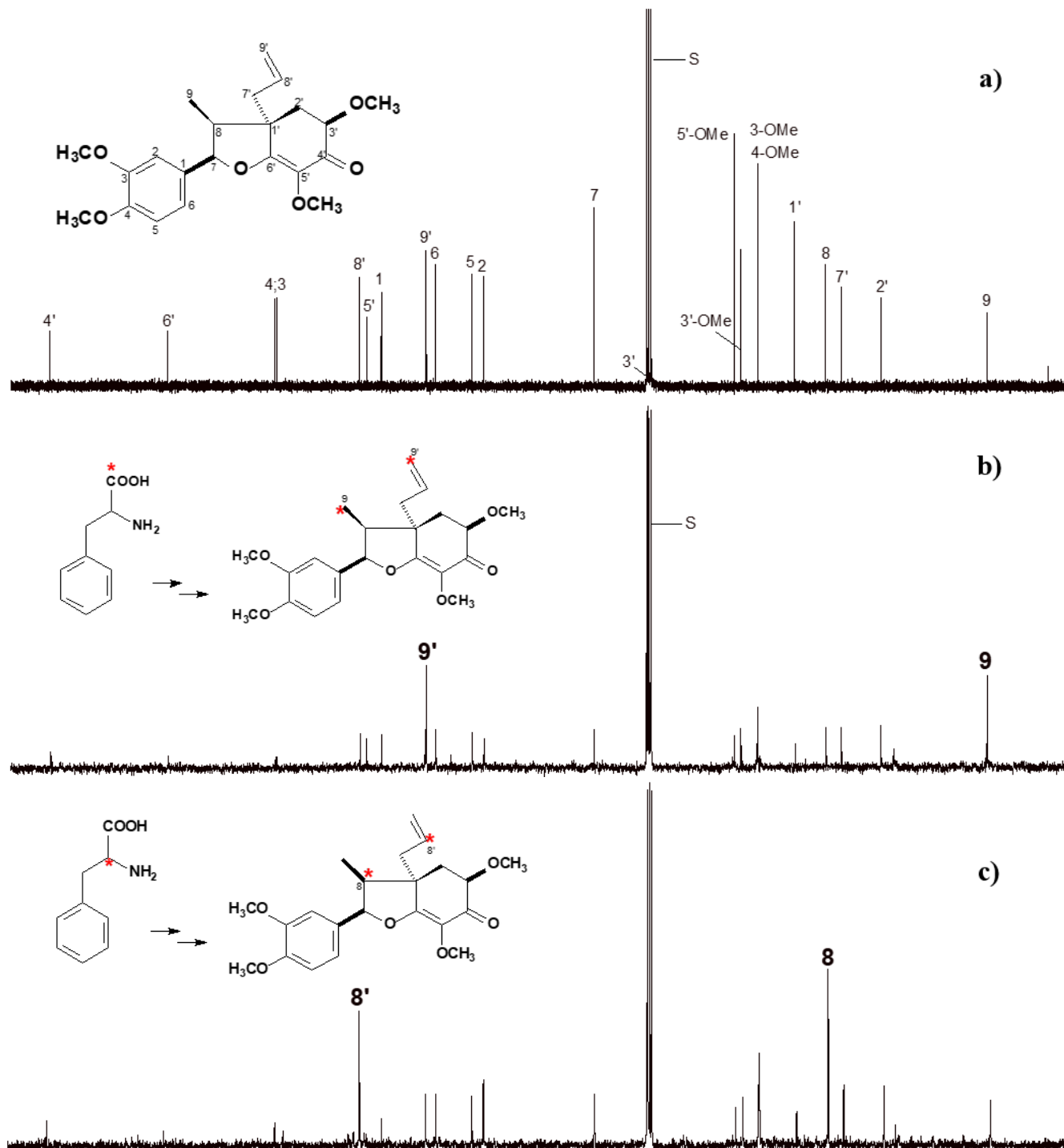
In the mass spectrum of unlabeled 5'-methoxy-porosin the peaks at m/z 389 [M+H]⁺, 390 [M+H+1]⁺ and 391 [M+H+2]⁺ indicated the expected molecular ions and the ions resulting from incorporation of one or two ¹³C atoms. In the case of unlabeled armenin B, the peaks of molecular ions were observed at m/z 373 [M+H]⁺, 374 [M+H+1]⁺ and 375 [M+H+2]⁺.

Considering the natural abundance of ¹³C in the neolignans, the calculations to obtain the percentage of ¹³C incorporated were performed by comparing the relative intensity of the molecular mass ([M+H]⁺), ([M+H+1]⁺), and ([M+H+2]⁺) of the unlabeled neolignans with that of the enriched neolignans. The

highest incorporation of *L*-phenylalanine isotopomers in both neolignans was observed at 72 h. The neolignans isolated from the extracts obtained after the incubation period of 72 h were subjected to ¹³C NMR analysis to characterize the enrichment position after incorporation of *L*-phenylalanine isotopomers into the structures of the 5'-methoxy-porosin (**1**) and armenin B (**2**). The comparison of the ¹³C NMR spectrum of the unlabeled 5'-methoxy-porosin (6.0 mg) (control), with the spectrum of the labelled (6.0 mg) with *L*-[1-¹³C]-phenylalanine, showed an increase in the intensity of the peaks corresponding to the C-9 (δ 11.7 ppm) and C-9'

(δ 119.9 ppm) carbons (Fig. 3). Likewise, administration of *L*-[2- ^{13}C]-phenylalanine resulted in a product with ^{13}C NMR signals enriched at positions C-8 (δ 42.7 ppm) and C-8' (δ 132.7 ppm). The spectrum of the neolignan

incubated with *L*-[3- ^{13}C]-phenylalanine had the positions C7 (δ 87.5 ppm) and C7' (δ 39.8 ppm) enriched (Fig. 3).



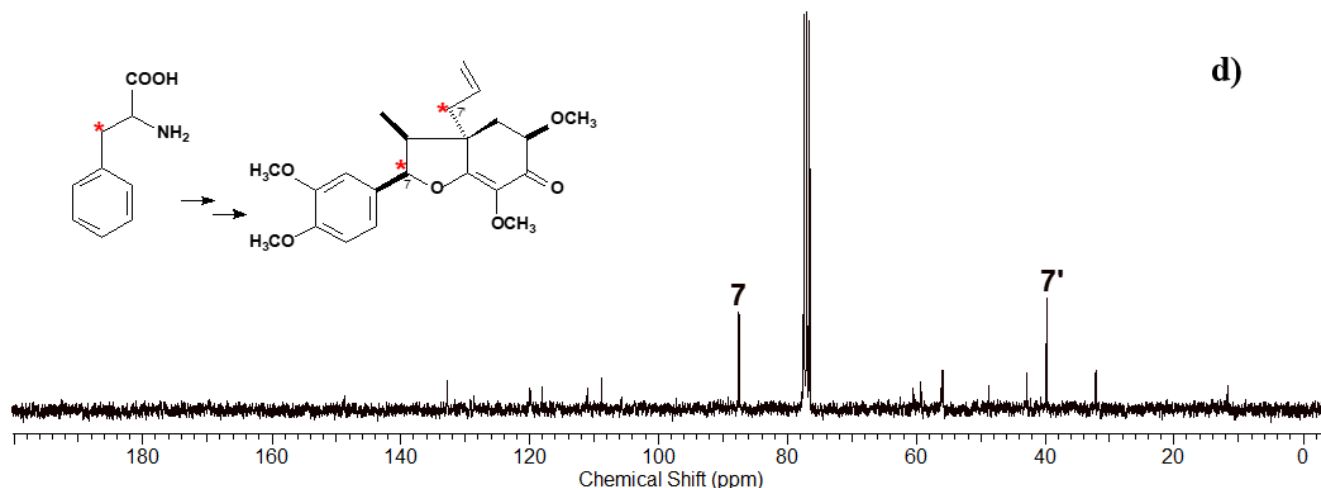
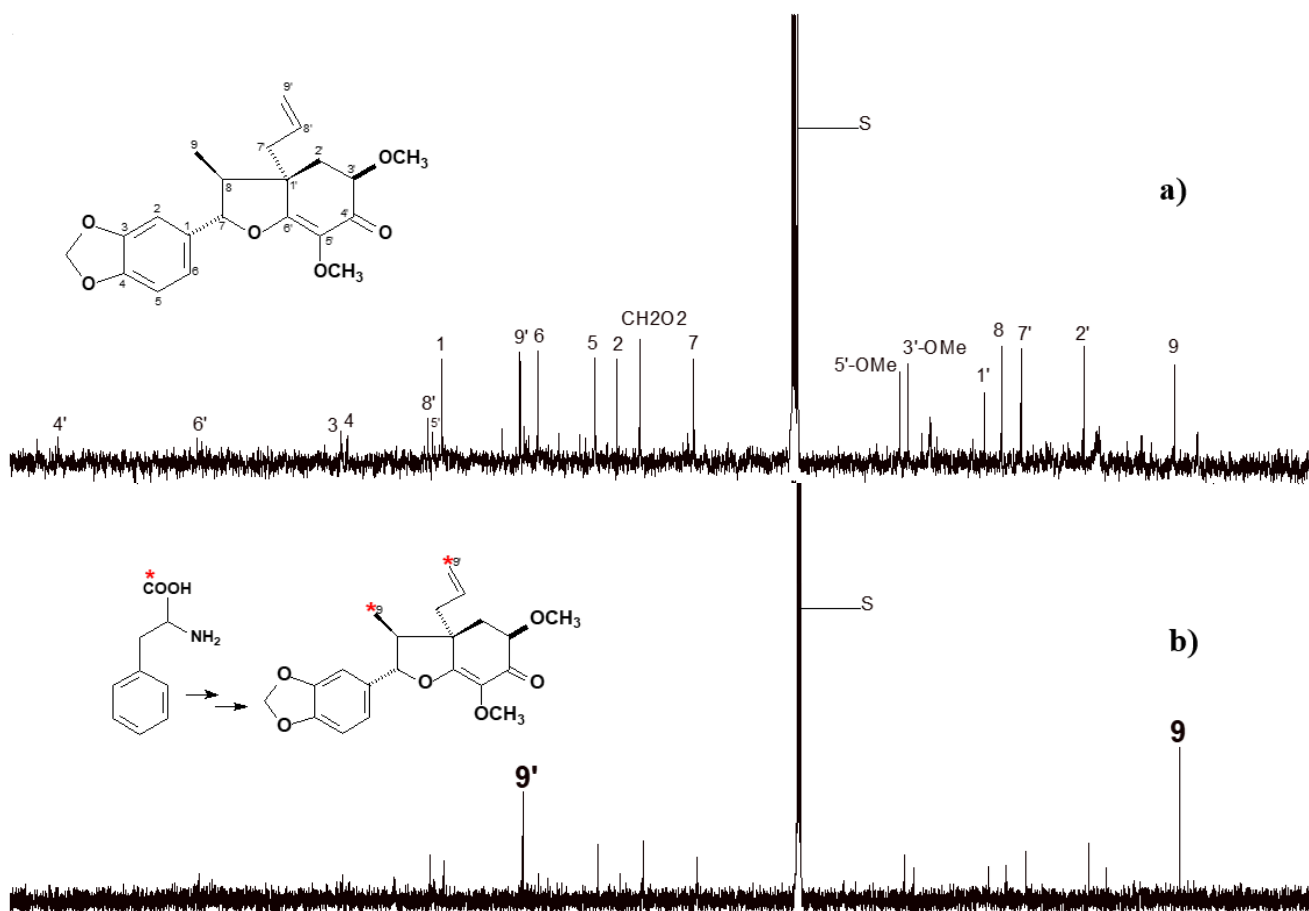


Figure 3. ^{13}C NMR spectra of: (a) natural abundance 5'-methoxy-porosin; (b) Incorporation with L -[1- ^{13}C]-phenylalanine; (c) Incorporation with L -[2- ^{13}C]-phenylalanine and (d) incorporation with L -[3- ^{13}C]-phenylalanine. S: CDCl_3 .

The ^{13}C NMR analysis for armenin B (5.0 mg) showed a similar profile of increased signals as that of 5'-methoxy-porosin. The incubation with L -[1- ^{13}C]-phenylalanine led to an increase in the intensity of the C9 (δ 17.5 ppm) and C9' (δ 120.0 ppm) carbons (Fig. 4). While the one enriched with L -[2- ^{13}C]-phenylalanine

showed an increase in signal intensity in C8 (δ 44.6 ppm) and C8' (δ 132.5 ppm) carbons. The administration of L -[3- ^{13}C]-phenylalanine, meanwhile, showed signals enriched at positions C-7 (δ 93.8 ppm) and C-7' (δ 40.8 ppm) (Fig. 4).



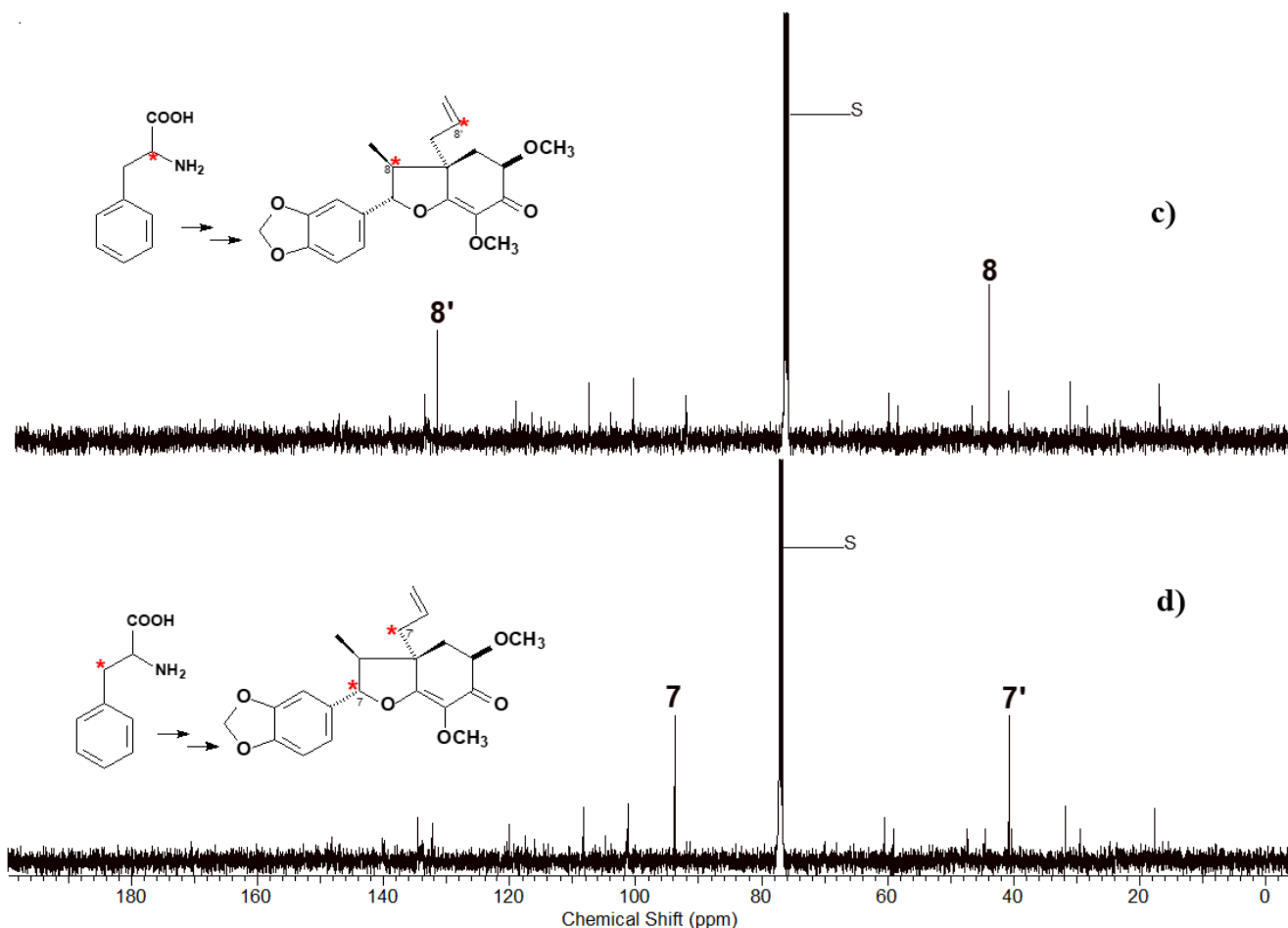


Figure 4. ^{13}C NMR of natural abundance armenin B (a); Incorporation with L -[1- ^{13}C]-phenylalanine (b); Incorporation with L -[2- ^{13}C]-phenylalanine (c) and incorporation with L -[3- ^{13}C]-phenylalanine (d). S: CDCl_3 .

The first isotopic labelling studies involving the biosynthetic study of the phenylpropanoid anethole using *Pimpinella anisum* with ^{14}C -labeled L -phenylalanine resulted in the incorporation of the intact side chain of the amino acid into anethole (Manitto *et al.*, 1974). While the HPLC-ESI analysis showed the incorporation of L -phenylalanine isotopomers in the structure of neolignans in *O. catharinensis*, the ^{13}C NMR spectra confirmed that the carbon incorporation pattern of ^{13}C with L -[1- ^{13}C], L -[2- ^{13}C]- and L -[3- ^{13}C]-phenylalanine. The data is consistent with the proposed formation of neolignans by the phenylpropanoid pathway, with the intact incorporation of the two L -phenylalanine molecules into the structure of neolignans, without rearrangement of the amino acid side chain. The first isotopic labelling studies involving the biosynthetic study of the phenylpropanoid anethole using *Pimpinella anisum* with ^{14}C -labeled L -phenylalanine resulted in the incorporation of the intact side chain of the amino acid into anethole (Manitto *et al.*, 1974). While the HPLC-ESI analysis showed the incorporation of L -phenylalanine isotopomers in the structure of neolignans

in *O. catharinensis*, the ^{13}C NMR spectra confirmed that the carbon incorporation pattern of ^{13}C with L -[1- ^{13}C], L -[2- ^{13}C]- and L -[3- ^{13}C]-phenylalanine. The data is consistent with the proposed formation of neolignans by the phenylpropanoid pathway, with the intact incorporation of the two L -phenylalanine molecules into the structure of neolignans, without rearrangement of the amino acid side chain.

3.3 Analysis of [8- ^{13}C]-ferulic acid incorporation

The HPLC-ESI analysis of the crude extracts of the somatic embryos of *O. catharinensis* incubated with [8- ^{13}C]-ferulic acid together with the control, did not show incorporation of the precursor to the neolignans. Extracts of the embryos were prepared after 12, 24, 48, 72 and 96 h of incubation. The embryos were incubated in large scale with [8- ^{13}C]-ferulic acid for 48 h, as during this time the embryos were less oxidized. The purified 5'-methoxy-porsin (5.0 mg) and armenin B (5.0 mg) neolignans were subjected to ^1H and ^{13}C NMR analysis. In the case of incorporation with [8- ^{13}C]-ferulic acid,

supposedly the enrichment with carbon thirteen would be in the positions of C8 and C8' of the corresponding neolignans. The ^{13}C NMR spectra of the control samples, 5'-methoxy-porosin and armenin B (Fig. 4) were compared with those resulting from the incubations and no detectable changes were observed in the peaks intensity corresponding to C8 and C8' of the neolignans (data not shown).

Previous biosynthetic studies have demonstrated the incorporation of 0.053% of $[8-^{14}\text{C}]$ -ferulic acid in the podophyllotoxin lignan, isolated from young plants of *Podophyllum hexandrum* (Jackson and Dewick, 1984). However, methylchavicol, isolated from *Ocimum basilicum* leaves after incubation with p - $[8-^{14}\text{C}]$ -coumaric acid, similarly to the incorporation of ferulic acid, did not show any incorporation in its structure (Vassão *et al.*, 2006). Supposedly, these results may be a consequence of the toxic nature of the precursor to the plant in this case, to the embryos of *O. catharinensis* because, after 48 h the embryos were completely oxidized. The low solubility of ferulic acid in aqueous solution may also have caused difficulties in transporting it to the biosynthesis site (Davin *et al.*, 2003; Vassão *et al.*, 2006).

3.4 Analysis of $[8-^{13}\text{C}]$ -glycoferulic acid incorporation

The biosynthetic studies looking at the origin of the lignans arctin and phillyrin lignans in *Forsythia* shoots were carried out using ferulic acid, coniferyl alcohol and glycosylated coniferaldehyde, labelled with ^3H and ^{14}C (Stöckigt and Klischies, 1977). Therefore, the glycosylation of the phenolic hydroxyl would contribute to minimize the oxidation of the acid, due to the higher solubility of the substrate in water and, consequently, improve its absorption in the plant. Based on this principle, $[8-^{13}\text{C}]$ -glycoferulic acid was administered to somatic embryos of *O. catharinensis*, at different time intervals and different concentrations to determine optimal conditions for its incorporation into the neolignans. Therefore, extracts with natural abundance and those incubated with $[8-^{13}\text{C}]$ -glycoferulic acid were analyzed by mass spectrometry (EI). From the proposed fragmentation of 5'-methoxy-porosin, it was observed that the peaks at m/z 178, 319 and 358 Da of the control sample, should show the peaks enriched with carbon thirteen at m/z in 179, 320 and 360 Da, respectively. The embryos showed better appearance and longer

incubation time at 72 h and, therefore, from these experiments, extracts were obtained and subjected to the separation of the neolignans by prep-TLC. According to the hypothesis suggested for the pathway of formation of neolignans (Fig. 5), there should be incorporation in the positions of C8 and C8', originating from $[8-^{13}\text{C}]$ -ferulic acid. However, the comparison of the relative intensities of ^{13}C NMR peaks of naturally abundant neolignans with those incubated with $[8-^{13}\text{C}]$ -glycoferulic acid did not show any increase in intensity at the C8 and C8' positions (data not shown).

3.5 Analysis of the incorporation of $[8-^{13}\text{C}]$ -coniferyl alcohol

In vitro administrations of $[8-^{13}\text{C}]$ -coniferyl alcohol in *O. catharinensis* embryos were performed at different concentrations, time intervals (12, 24, 48, 72 and 96 h) and, in the absence and presence of light, to identify optimal conditions for absorption and metabolism in neolignans **1** and **2**.

The comparison of the HPLC-ESI spectra of the crude extracts of the somatic embryos of *O. catharinensis* incubated with $[8-^{13}\text{C}]$ -coniferyl alcohol with the control samples, showed that this substrate was not incorporated into the 5'-methoxy-neolignans porosin and armenin B. According to the biosynthetic proposal for the formation of neolignans, we expected to observe the incorporation of one alcohol molecule at the position of C-8 and the other at C-8' in the structure of neolignans **1** and **2**. Nevertheless, similarly to the case of ferulic acid and its glycosylated version embryos incubated with $[8-^{13}\text{C}]$ -coniferyl alcohol for 48 h, time interval with embryos were not fully oxidized and submitted to ESI, EI or ^1H and ^{13}C NMR analysis did not show any increase in carbon intensity at positions C-8 and C-8' when compared to the control (data not shown). It is assumed that the rapid degradation of coniferyl alcohol prior to its entry into the biosynthetic path, coupled with its low solubility in an aqueous medium did not result in the enrichment with carbon thirteen of the corresponding neolignans **1** and **2**, as expected. In a contrasting experiment using enzymatic conversion, the biosynthesis of the lignan (-)-secoisolariciresinol was investigated in *Forsythia intermedia*. The precursor $[9-^2\text{H}_2]$ -coniferyl alcohol in that study served as a precursor to the coupling reactions in the presence of NADPH and H_2O_2 (Katayama *et al.*, 1992).

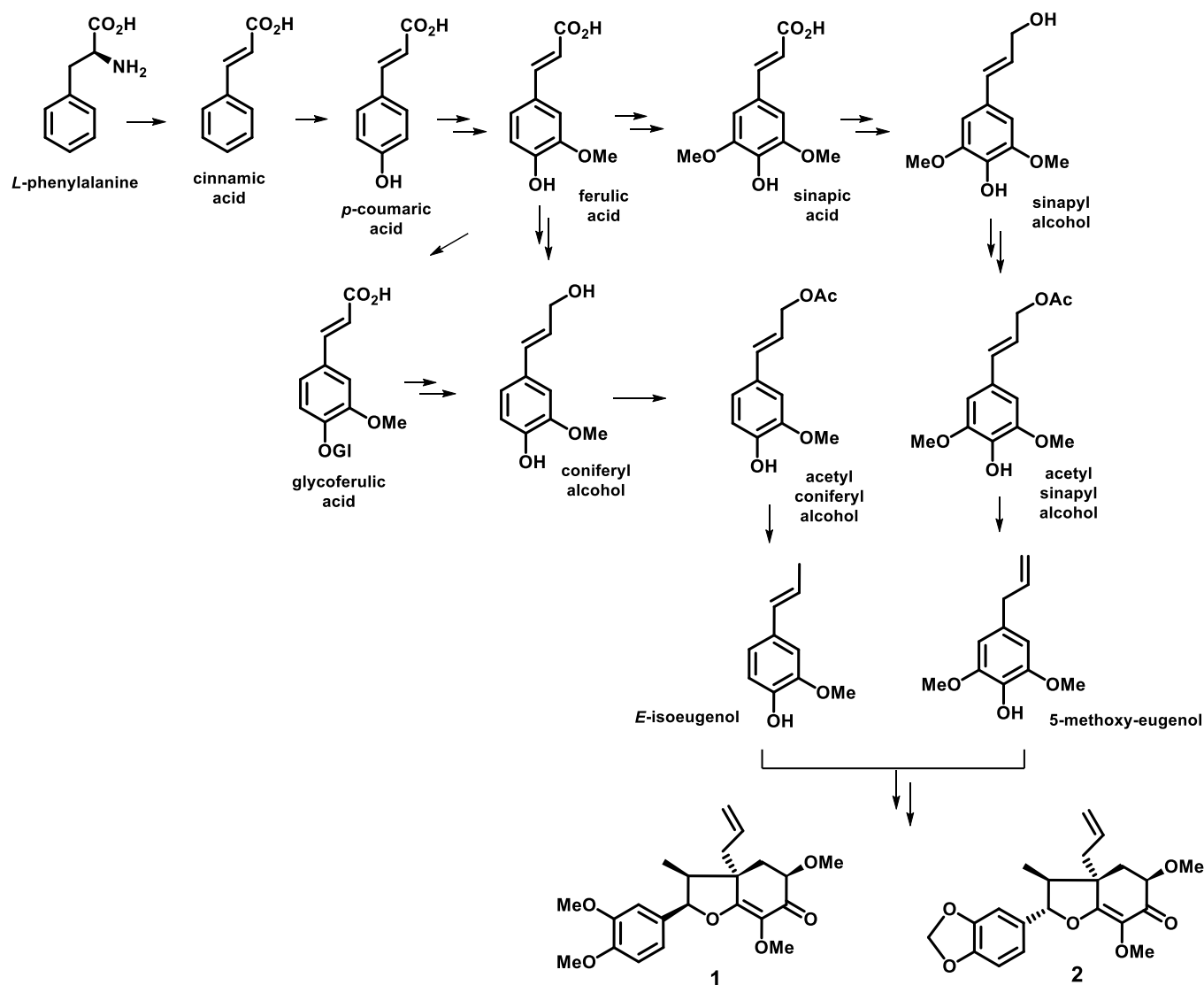


Figure 5. Biosynthetic pathway of tetrahydrobenzofuran neolignans in embryonic cultures of *O. catharinensis*.

3.6 Analysis of the incorporation of [8-¹³C]-coniferyl acetate

The [8-¹³C]-coniferyl acetate was next chosen because it presents a good leaving group, whose exit is carried out by reductive elimination. This phenylpropanoid precursor would have the additional stage of activation by acetylation and was recently described as an important biosynthetic intermediate for lignans (Ferrer *et al.*, 2008; Koeduka *et al.*, 2013; Vassão *et al.*, 2006). Therefore, similarly to the previous precursors, the incubation of [8-¹³C]-coniferyl acetate in embryos of *O. catharinensis* in the time frame of 12–96 h was tested. Mass spectrometry (EI) was used to analyze the crude extract of the fractions resulting from incorporation and control, to determine the percentage of

¹³C incorporation into the neolignans. The incorporation of the substrate occurred for 72 h of incubation.

The mass spectrum of 5'-methoxy-porsin revealed fragment ions in *m/z* 179 and *m/z* 320 Da with an increased intensity when compared with the spectra of the control samples. The level of incorporations were 5.48% and 5.77%, respectively, while in the fragment ion at *m/z* 358 Da, ¹³C incorporations of 3.20% were observed in the [M+1]⁺ 359 Da and of 2.12% in the [M+2]⁺ 360 Da (Figure S14). Therefore, incorporation of the two [8-¹³C]-coniferyl acetate molecules could be observed in 5'-methoxy-porsin. Curiously, similar incorporation to armenin B was not observed in the mass spectra of the enriched crude extract.

According to the biosynthetic proposal for the formation of neolignans, in the case of incorporation with [8-¹³C]-coniferyl acetate, supposedly enrichment

with carbon thirteen would also be in the positions of the C8 and C8' of the neolignans between the ^{13}C NMR spectra of the 5'-methoxy-porosin control sample as compared to the incubated one. The spectra showed an

increase in the intensity of C8' (δ 132.7 ppm) and in C8 (δ 42.8 ppm) (Fig. 6). Armenin B was obtained in a very small amounts and did not allow a good quality ^{13}C NMR spectrum.

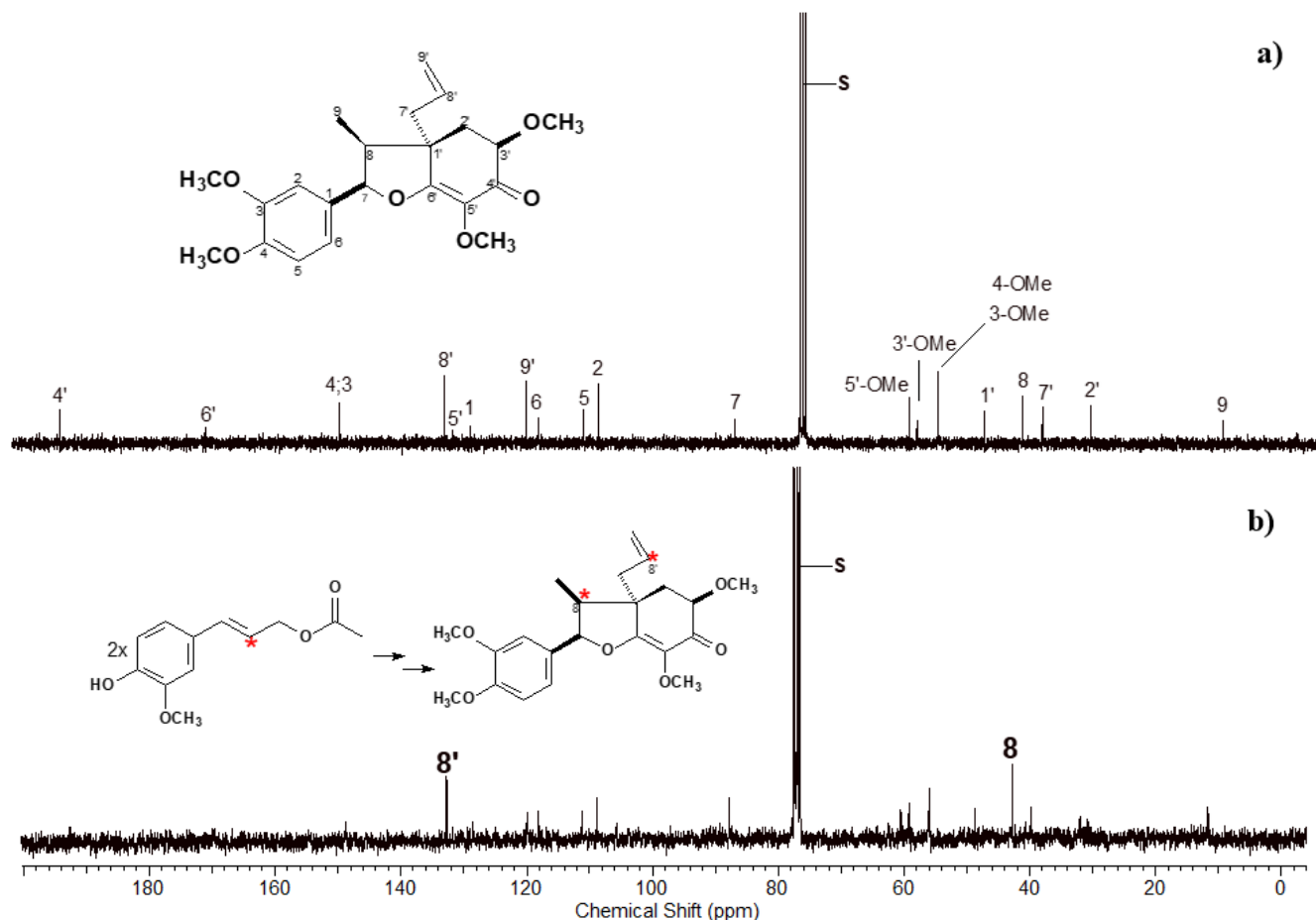


Figure 6. ^{13}C NMR of 5'-methoxy porosin at natural abundance (a) and of 5'-methoxy porosin after incubation with [8- ^{13}C]-coniferyl acetate (b).

The positions of the hydrogens directly linked to the ^{13}C -enriched carbon atom were confirmed through the HSQC spectrum, in which it was possible to observe the correlations of hydrogen at δ 2.56 (H-8), with δ 42.8 (C-8), as well as of hydrogens at δ 5.95 (H-8'), with δ 132.8 (C-8'). The HMBC contour map showed correlations of δ 2.56 (H-8) with δ 11.7 (C-9), δ 39.8 (C-7') and with δ 169.9 (C-6'). The hydrogens at δ 5.95 (H-8') directly linked to C-8' correlate with δ 39.8 (C-7') as well as with δ 48.8 (C1').

The results obtained from mass spectra (EI), ^{13}C NMR, HSQC and HMBC contour maps, confirmed that the entire 5'-methoxy-porosin skeleton was formed by the condensation of two molecules of [8- ^{13}C]-coniferyl acetate, which was transformed by a sequence of enzymatic steps.

3.7 Enzymatic conversion with intermediate phenylpropanoid substrates

The conversion of precursors using enzymatic fractions obtained from embryos of *O. catharinensis* were analyzed by HPLC. The crude extracts obtained from various incubation times allowed us to determine the ability to convert coniferyl acetate into eugenol or *E*-isoeugenol. The comparison of the analysis by HPLC of the control (enzymatic extract and MES buffer) (Fig. 7a), with the enzyme fractions and the respective standards, allowed us to identify the conversion of coniferyl acetate into *E*-isoeugenol as an enzyme conversion product (Fig. 7b).

For the elimination of the acetate group and the formation of *E*-isoeugenol it was demonstrated that if the nucleophilic attack of the hydride, originating from

NADPH, occurs at the C-9 carbon of the side chain of the coniferyl acetate, it would lead to the formation of propenylphenol. If the hydride attack occurs at C-8, it would lead to the formation of eugenol (Koeduka *et al.*, 2006; 2013; Vassão *et al.*, 2006).

These results, combined with the incorporation of two molecules of [8-¹³C]-coniferyl acetate to 5'-methoxy-porosin, corroborate the pathway in which *E*-isoeugenol is required for the formation of the 5'-neolignans methoxy-porosin and armenin B.

Similarly, the conversion of *E*-isoeugenol and 5-methoxy-eugenol in 5'-methoxy-porosin or in

armenin B was attempted. According to the proposed biosynthesis scheme, the substrate would undergo oxidative coupling by the action of enzymes (dirigent protein) leading to the production of tetrahydrobenzofuran neolignans. The analysis of the enzymatic conversion of the precursors *E*-isoeugenol and 5-methoxy-eugenol to neolignan 5'-methoxy-porosin was done by HPLC and no coupling reaction between of *E*-isoeugenol and 5-methoxy-eugenol in tetrahydrobenzofuran neolignans was observed. Only the signals referring to the compounds of the enzymatic fraction and the precursors were observed.

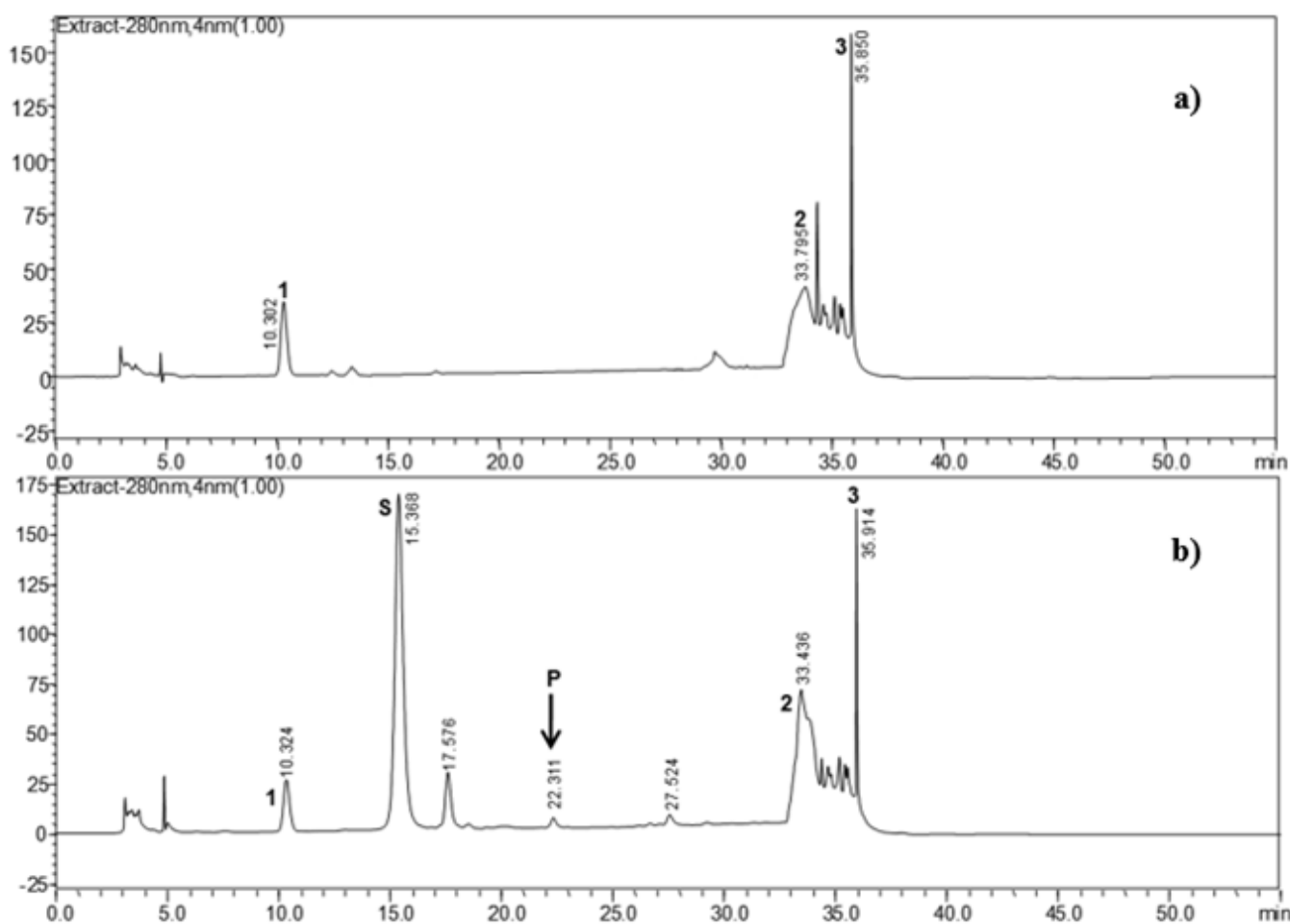


Figure 7. HPLC analysis of the conversion of substrates by enzymatic fraction of *O. catharinensis* embryos. (a) Control indicating the presence of endogenous compounds in the enzyme fraction; (b) Conversion of coniferyl acetate to *E*-isoeugenol. (P) *E*-isoeugenol formed by the reaction; (S): substrate coniferyl acetate.

4. Conclusions

The embryos of *O. catharinensis* was shown to contain revealed to be a unique source of tetrahydrobenzofuran neolignans as indicated by the HPLC-PDA analysis. Therefore, it was used as a model for the biosynthetic studies because of the easy protocol

to feed labelled precursors and chemical composition without many interferences. The analysis of enriched crude extracts using ¹³C *L*-phenylalanine isotopomers as substrates and mass spectrometric analysis of the products indicated ¹³C enrichment in the tetrahydrobenzofuran neolignans 5'-methoxy-porosin and armenin B. The ¹³C NMR analysis confirmed

unequivocally the labelling of the ^{13}C position in the structures of the neolignans. The use of various isotopomers of *L*-phenylalanine showed an intact incorporation of the side chain of two phenylalanine molecules in the respective neolignans without any rearrangement.

Biosynthetic investigation involving a more specific precursor in the pathway showed the incorporation of two molecules of [8- ^{13}C]-coniferyl acetate in 5'-methoxy-porosin. This conversion was confirmed using enzymatic conversion assays, with conversion of coniferyl acetate into *E*-isoeugenol which is considered an intermediate precursor for the formation of tetrahydrobenzofuran neolignans.

These results support the hypothesis that tetrahydrobenzofuran neolignans would result from the oxidative coupling between radical units produced from *E*-isoeugenol and 5-methoxy-eugenol. Since the neolignans are optically active, the key enzymatic dimerization reaction would be responsible for the regio- and stereospecificity of the coupling reaction.

Authors' contribution

Conceptualization: Kato, M. K.

Data curation: Santos, E. L.; Kato, M. K.; Floh, E. I. S.

Formal Analysis: Santos, E. L.; Kato, M. K.; Floh, E. I. S.

Funding acquisition: Kato, M. K.; Floh, E. I. S.

Investigation: Santos, E. L.

Methodology: Santos, E. L.

Project administration: Kato, M. K.; Floh, E. I. S.

Resources: Kato, M. K.; Floh, E. I. S.

Software: Not applicable.

Supervision: Kato, M. K.; Floh, E. I. S.

Validation: Kato, M. K.; Floh, E. I. S.

Visualization: Santos, E. L.

Writing – original draft: Santos, E. L.; Kato, M. K.; Floh, E. I. S.

Writing – review & editing: Santos, E. L.; Kato, M. K.; Floh, E. I. S.

Data availability statement

All data sets were generated or analyzed in the current study.

Funding

Fundação de Amparo à Pesquisa do Estado de São Paulo (FAPESP). Grant No: 2014-50316-7.

Conselho Nacional de Desenvolvimento Científico e Tecnológico (CNPq). Grant No: 304607/2019-3.

Coordenação de Aperfeiçoamento de Pessoal de Nível Superior (CAPES).

Acknowledgments

Not applicable.

References

Aiba, C. J.; Fernandes, J. B.; Gottlieb, O. R.; Maia, J. G. S. Neolignans from an *Aniba* species. *Phytochemistry*. **1975**, *14* (7), 1579–1604. [https://doi.org/10.1016/0031-9422\(75\)85358-1](https://doi.org/10.1016/0031-9422(75)85358-1)

Aiba, C. J.; Gottlieb, O. R.; Yoshida, M.; Mourão, J. C.; Gottlieb, H. E. Structure of porosin. *Phytochemistry* **1976**, *15* (6), 1031–1032. [https://doi.org/10.1016/S0031-9422\(00\)84397-6](https://doi.org/10.1016/S0031-9422(00)84397-6)

Aiba, C. J.; Gottlieb, O. R.; Pagliosa, F. M.; Yoshida, M.; Magalhães, M. T. Neolignans from *Nectandra miranda*. *Phytochemistry*. **1977**, *16* (6), 745–748. [https://doi.org/10.1016/S0031-9422\(00\)89245-8](https://doi.org/10.1016/S0031-9422(00)89245-8)

Aiba, C. J.; Gottlieb, O. R.; Maia, J. G. S.; Pagliosa, F. M.; Yoshida, M. Benzofuranoid neolignans from *Licaria armeniaca*. *Phytochemistry*. **1978**, *17* (11), 2038–2039. [https://doi.org/10.1016/S0031-9422\(00\)88765-8](https://doi.org/10.1016/S0031-9422(00)88765-8)

Alvarenga, M. A. D.; Castro, O. C.; Giesbrecht, A. M.; Gottlieb, O. R. Bicyclo[3.2.1]octanoid neolignans from *Aniba simulans*. *Phytochemistry*. **1977**, *16* (11), 1801–1804. [https://doi.org/10.1016/0031-9422\(71\)85093-8](https://doi.org/10.1016/0031-9422(71)85093-8)

Amaral, W.; Deschamps, C.; Bizzo, H. R.; Pinto, M. A. S.; Biasi, L. A.; Silva, L. E., Essential Oil Yield and Composition of Native Tree Species from Atlantic forest, South of Brazil. *J. Essent Oil-Bear. Plants*. **2017**, *20* (6), 1525–1535. <https://doi.org/10.1080/0972060X.2017.1346484>

Amazonas, D. R.; Oliveira, C.; Barata, L. E. S.; Tepe, E. J.; Kato, M. J.; Mourão, R. H. V.; Yamaguchi, L. F. Chemical and Genotypic Variations in *Aniba rosiodora* from the Brazilian Amazon Forest. *Molecules*. **2020**, *26* (1), 69. <https://doi.org/10.3390/molecules26010069>


Anand, V.; Varalakshmi, Prasana, Kumar, S., Pushpa, Hedina, A. *Cinnamomum zeylanicum* Linn. The spice with multi potential. *Sys. Rev. Pharm*. **2016**, *7* (1), 14–29. <https://doi.org/10.5530/srp.2016.7.3>

Anterola, A. M.; Lewis, N. G. Trends in lignin modification: A comprehensive analysis of the effects of genetic manipulations/mutations on lignification and vascular

- integrity. *Phytochemistry*. **2002**, *61* (3), 221–294. [https://doi.org/10.1016/S0031-9422\(02\)00211-X](https://doi.org/10.1016/S0031-9422(02)00211-X)
- Bradford, M. M. A rapid and sensitive method for the quantitation of microgram quantities of protein utilizing the principle of protein–dye binding. *Anal. Biochem.* **1976**, *72* (1–2), 248–254. [https://doi.org/10.1016/0003-2697\(76\)90527-3](https://doi.org/10.1016/0003-2697(76)90527-3)
- Cervantes–Paz, B.; Yahia, E. M. Avocado oil: Production and market demand, bioactive components, implications in health, and tendencies and potential uses. *Compr. Rev. Food Sci. Food Saf.* **2021**, *20* (4), 4120–4158. <https://doi.org/10.1111/1541-4337.12784>
- Coy–Barrera, E. D.; Cuca–Suarez, L. E.; Sefkow, M. PAF–antagonistic bicyclo[3.2.1]octanoid neolignans from leaves of *Ocotea macrophylla* Kunth. (Lauraceae). *Phytochemistry* **2009**, *70* (10), 1309–1314. <https://doi.org/10.1016/j.phytochem.2009.07.010>
- David, J. M.; Yoshida, M.; Gottlieb, O. R. Neolignans from bark and leaves of *Ocotea porosa*. *Phytochemistry*. **1994**, *36* (2), 491–499. [https://doi.org/10.1016/S0031-9422\(00\)97102-4](https://doi.org/10.1016/S0031-9422(00)97102-4)
- Davin, L. B.; Wang, C.–Z.; Helms, G. L.; Lewis, N. G. [¹³C]–Specific labeling of 8–2' linked (–)-*cis*-blechnic, (–)-*trans*-blechnic and (–)-brainic acids in the fern *Blechnum spicant*. *Phytochemistry*. **2003**, *62* (3), 501–511. [https://doi.org/10.1016/S0031-9422\(02\)00540-X](https://doi.org/10.1016/S0031-9422(02)00540-X)
- Doyle, J. A.; Endress, P. K. Morphological Phylogenetic Analysis of Basal Angiosperms: Comparison and Combination with Molecular Data. *Int. J. Plant Sci.* **2000**, *161* (S6), S121–S153. <https://doi.org/10.1086/317578>
- Endress, P. K.; Doyle, J. A. Reconstructing the ancestral angiosperm flower and its initial specialization. *Am. J. Bot.* **2009**, *96* (1), 22–66. <https://doi.org/10.3732/ajb.0800047>
- Felicio, J. D.; Motidome, M.; Yoshida, M.; Gottlieb, O. R. Further neolignans from *Ocotea–aciphylla*. *Phytochemistry*. **1986**, *25* (7), 1707–1710. [https://doi.org/10.1016/S0031-9422\(00\)81240-6](https://doi.org/10.1016/S0031-9422(00)81240-6)
- Ferrer, J.–L.; Austin, M. B.; Stewart Júnior, C.; Noe, J. P. Structure and function of enzymes involved in the biosynthesis of phenylpropanoids. *Plant Physiol. Biochem.* **2008**, *46* (3), 356–370. <https://doi.org/10.1016/j.plaphy.2007.12.009>
- Funasaki, M.; Lordello, A. L. L.; Viana, A. M.; Santa–Catarina, C.; Floh, E. I. S.; Yoshida, M.; Kato, M. J. Neolignans and Sesquiterpenes from Leaves and Embryogenic Cultures of *Ocotea catharinensis* (Lauraceae). *J. Braz. Chem. Soc.* **2009**, *20* (5), 853–859. <https://doi.org/10.1590/S0103-50532009000500008>
- Gottlieb, O. R. Chemosystematics of the lauraceae. *Phytochemistry*. *11* (5), 1537–1570. [https://doi.org/10.1016/0031-9422\(72\)85001-5](https://doi.org/10.1016/0031-9422(72)85001-5)
- Ishige, M.; Motidome, M.; Yoshida, M.; Gottlieb, O. R. Neolignans from *Ocotea catharinensis*. *Phytochemistry*. **1991**, *30* (12), 4121–4128. [https://doi.org/10.1016/0031-9422\(91\)83479-5](https://doi.org/10.1016/0031-9422(91)83479-5)
- Jackson, D. E.; Dewick, P. M. Biosynthesis of *podophyllum* lignans–i. cinnamic acid precursors of podophyllotoxin in *Podophyllum hexandrum*. *Phytochemistry*. **1984**, *23* (5), 1029–1035. [https://doi.org/10.1016/S0031-9422\(00\)82603-5](https://doi.org/10.1016/S0031-9422(00)82603-5)
- Jimenez, P.; Garcia, P.; Quitral, V.; Vasquez, K.; Parra–Ruiz, C.; Reyes–Farias, M.; Garcia–Diaz, D. F.; Robert, P.; Encina, C.; Soto–Covasich, J. Pulp, Leaf, Peel and Seed of Avocado Fruit: A Review of Bioactive Compounds and Healthy Benefits. *Food Rev. Int.* **2021**, *37* (6), 619–655. <https://doi.org/10.1080/87559129.2020.1717520>
- Katayama, T.; Davin, L. B.; Lewis, N. G. An extraordinary accumulation of (–)-pinoresinol in cell–free extracts of *Forsythia intermedia*: evidence for enantiospecific reduction of (+)-pinoresinol. *Phytochemistry*. **1992**, *31* (11), 3875–3881. [https://doi.org/10.1016/S0031-9422\(00\)97545-9](https://doi.org/10.1016/S0031-9422(00)97545-9)
- Koeduka, T.; Fridman, E.; Gang, D. R.; Vassao, D. G.; Jackson, B. L.; Kish, C. M.; Orlova, I.; Spassova, S. M.; Lewis, N. G.; Noel, J. P.; Baiga, T. J.; Dudareva, N.; Pichersky, E. Eugenol and isoeugenol, characteristic aromatic constituents of spices, are biosynthesized via reduction of a coniferyl alcohol ester. *Proc. Natl. Acad. Sci.* **2006**, *103* (26), 10128–10133. <https://doi.org/10.1073/pnas.0603732103>
- Koeduka, T.; Suzuki, S.; Iijima, Y.; Ohnishi, T.; Suzuki, H.; Watanabe, B.; Shibata, D.; Umezawa, T.; Pichersky, E.; Hiratake, J. Enhancement of production of eugenol and its glycosides in transgenic aspen plants via genetic engineering. *Biochem. Biophys. Res. Comm.* **2013**, *436* (1), 73–78. <https://doi.org/10.1016/j.bbrc.2013.05.060>
- Lloyd, G.; McCown, B. Commercially–feasible micropropagation of mountain laurel, *Kalmia latifolia*, by use of shoot–tip culture. *Comb. Proc. Int. Plant Prop. Soc.* **1980**, *30*, 421–427.
- Lu, F.; Ralph, J.; Morreel, K.; Messens, E.; Boerjan, W. Preparation and relevance of a cross–coupling product between sinapyl alcohol and sinapyl *p*–hydroxybenzoate. *Org. Biomol. Chem.* **2004**, *2* (20), 2888–2890. <https://doi.org/10.1039/b411428k>
- Manitto, P.; Monti, D.; Gramatica, P. Biosynthesis of anethole in *Pimpinella anisum* L. *Tetrahedron Lett.* **1974**, *15* (17), 1567–1568. [https://doi.org/10.1016/S0040-4039\(01\)82521-1](https://doi.org/10.1016/S0040-4039(01)82521-1)

- Montagna, T.; Silva, J. Z.; Pikart, T. G.; Reis, M. S. Reproductive ecology of *Ocotea catharinensis*, an endangered tree species. *Plant Biol.* **2018**, *20* (5), 926–935. <https://doi.org/10.1111/plb.12847>
- Moura–Costa, P. H.; Viana, A. M.; Mantell, S. H. *In vitro* plantlet regeneration of *Ocotea catharinensis*, an endangered Brazilian hardwood forest tree. *Plant Cell, Tissue and Organ Cult.* **1993**, *35* (3), 279–286. <https://doi.org/10.1007/BF00037282>
- Nehme, C. J.; Moraes, P. L. R.; Tininis, A. G.; Cavalheiro, A. J. Intraspecific variability of flavonoid glycosides and styrylpyrones from leaves of *Cryptocarya mandioccana* Meisner (Lauraceae). *Biochem. Syst. Ecol.* **2008**, *36* (8), 602–611. <https://doi.org/10.1016/j.bse.2008.05.001>
- Rossi, M. H.; Yoshida, M.; Maia, J. G. S. Neolignans, styrylpyrones and flavonoids from an *Aniba* species. *Phytochemistry*, **1997**, *45* (6), 1263–1269. [https://doi.org/10.1016/S0031-9422\(97\)00075-7](https://doi.org/10.1016/S0031-9422(97)00075-7)
- Rozo–Lugo, C.; Cuca–Suárez, L. E.; Schmidt, T. J.; Coy–Barrera, E. Tetrahydrobenzofuran–6(2H)–one Neolignans from *Ocotea heterochroma*: Their Platelet Activating Factor (PAF) Antagonistic Activity and in Silico Insights into the PAF Receptor Binding Mode. *J. Nat. Prod.* **2018**, *81* (9), 1968–1975. <https://doi.org/10.1021/acs.jnatprod.8b00189>
- Salleh, W. M. N. H. W.; Ahmad, F. Phytochemistry and biological activities of the genus *Ocotea* (Lauraceae): A review on recent research results (2000–2016). *J. Applied Pharm. Sci.* **2017**, *7* (5), 204–218. <https://doi.org/10.7324/JAPS.2017.70534>
- Sartorelli, P.; Benevides, P. J. C.; Ellensohn, R. M.; Rocha, M. V. A. F.; Moreno, P. R. H.; Kato, M. J. Enantioselective conversion of *p*–hydroxypropenylbenzene to (+)–conocarpan in *Piper regnellii*. *Plant Sci.* **2001**, *161* (6), 1083–1088. [https://doi.org/10.1016/S0168-9452\(01\)00512-X](https://doi.org/10.1016/S0168-9452(01)00512-X)
- Stöckigt, J.; Klischies, M. Biosynthesis of lignans: Part I. Biosynthesis of arctiin (3) and phillyrin (5). *Holzforschung* **1977**, *31* (2), 41–44. <https://doi.org/10.1515/hfsg.1977.31.2.41>
- Suzuki, S.; Umezawa, T. Biosynthesis of lignans and norlignans. *J. Wood Sci.* **2007**, *53* (4), 273–284. <https://doi.org/10.1007/s10086-007-0892-x>
- Teles, M. M. R. S.; Pinheiro, A. A. V.; Dias, C. S.; Tavares, J. F.; Barbosa Filho, J. M.; Cunha, E. V. L. Alkaloids of the Lauraceae. Alkaloids: *Chem. Biol.* **2019**, *82*, 147–304. <https://doi.org/10.1016/bs.alkal.2018.11.002>
- Vassão, D. G.; Gang, D. R.; Koeduka, T.; Jackson, B.; Pichersky, E.; Davin, L. B.; Lewis, N. G. Chavicol formation in sweet basil (*Ocimum basilicum*): cleavage of an esterified C9 hydroxyl group with NAD(P)H–dependent reduction. *Org. Biomol. Chem.* **2006**, *4* (14), 2733–2744. <https://doi.org/10.1039/B605407B>

Biosynthesis of tetrahydrobenzofuran neolignans in somatic embryos of *Ocotea catharinensis*

Érica Luiz dos Santos¹, Eny Iochevet Segal Floh², Massuo Jorge Kato¹⁺

1. University of São Paulo, Institute of Chemistry, São Paulo, Brazil.
2. University of São Paulo, Institute of Biosciences, São Paulo, Brazil.

+Corresponding author: Massuo Jorge Kato, **Phone:** +55 11 30911886, **Email address:** massuojorge@gmail.com

ARTICLE INFO

Article history:

Received: September 20, 2021

Accepted: February 11, 2022

Published: August 17, 2022

Section Editor: Assis Vicente Benedetti

Keywords

1. Lauraceae
2. *Ocotea catharinensis*
3. somatic embryos
4. ¹³C labelling
5. phenylpropanoids

Preparation of substrates used in incorporation reactions and enzymatic assays

Substrates were first synthesized with reagents not labeled with carbon thirteen and used in in vitro enzyme conversion assays, while those enriched with ¹³C were used in incorporation reactions in somatic embryos of *O. catharinensis*.

1. Synthesis of [8-¹³C]-ferulic acid

The [8-¹³C]-ferulic acid was prepared by Knoevenagel condensation between [2-¹³C]-malonic acid and vanillin catalyzed by aromatic amines (Katayama *et al.*, 1992). In a 125 mL flask equipped with magnetic stirring and reflux condenser, 642 mg (3.08 mmol) of [2-¹³C]-malonic acid, 878 mg (5.77 mmol) of vanillin dissolved in 3.5 mL of pyridine, one drop of piperidine and one drop of aniline previously distilled were added. The reaction mixture was refluxed in a silicone oil bath at 60 °C for 24 h, then for further 1 h at 100 °C and cooled to room temperature. This preparation was carried out twice. The suspension was solubilized in 15 mL of water at 80 °C, cooled to room temperature and acidified with HCl (pH 1-2). The resulting opaque solution was extracted with ethyl acetate (3 x 50 mL), the organic phases were combined and concentrated to ca. 25 mL volume and extracted with 5% NaHCO₃ solution (2 x 50 mL). The aqueous fractions were combined and

extracted with dichloromethane (4 x 20 mL) to remove unreacted vanillin, acidified with HCl (until pH 1-2) and extracted with ethyl acetate (3 x 50 mL). The ethyl acetate phases were extracted with saturated NaCl solution (80 mL), dried with anhydrous Na₂SO₄ and evaporated, yielding [8-¹³C]-ferulic acid crystals (973 mg, 81.0%) which was confirmed by ¹H and ¹³C NMR spectra. The final product, about 2.0 g, was used without purification.

2. Preparation of [8-¹³C]-coniferyl alcohol

In a round bottom flask containing porcelain beads, 1.5 g (7.72 mmol) of [8-¹³C]-ferulic acid, prepared previously as described in item 3.4.1, dissolved in 90 mL of methanol and 300 µL of concentrated sulfuric acid. The temperature was increased before reflux began, with the reflux solvent dried continuously via a Soxhlet extractor containing CaCl₂ and blue bulk silica gel. After 9 h of reaction, the mixture was cooled to room temperature, neutralized with 6.0 g of NaHCO₃, filtered and evaporated to dryness in a rotavaporator. The resulting residue was transferred to a 250 mL separatory funnel, solubilized in 70 mL dichloromethane and 50 mL distilled water. The aqueous phase was again extracted with dichloromethane (3 x 70 mL). The organic phases were combined, evaporated to 25 mL and extracted with 70 mL of saturated NaCl solution, dried over Na₂SO₄ and evaporated under reduced pressure. 1.48 g (92.5%) of the



product were obtained and identified by ^1H NMR and ^{13}C NMR spectra. The product was used without purification.

500 mg (12.54 mmol) of LiAlH_4 solubilized in 15 mL of dry ethyl ether were added to a 100 mL three-neck flask, equipped with magnetic stirring, addition funnel, septum and under nitrogen atmosphere, at $-25\text{ }^\circ\text{C}$. A solution of 479.26 mg (12.53 mmol) of [8- ^{13}C]-methyl ferulate diluted in 15 mL of dry ethyl ether was added dropwise to the solution under stirring for about 40 min. The mixture was stirred for 1 h at $-25\text{ }^\circ\text{C}$ and accompanied by TLC, hexane:ethyl acetate 7:3. After this period, the flask containing the reaction mixture was transferred to a 400 mL beaker containing crushed ice and 5 mL of ethyl acetate was slowly added to the flask to destroy excess LiAlH_4 . The resulting solution was transferred to a 125 mL separatory funnel, added 50 mL of ethyl acetate and distilled water which was added slowly to cause the formation of precipitated lithium salt. The solution was filtered, and the aqueous phase was washed with ethyl acetate (3 x 50 mL) to extract the lithium salt. The organic phases were combined, extracted with 50 mL of saturated NaCl solution, filtered over Na_2SO_4 , dried on a rotary evaporator, providing 398 mg (79.6%) of the crude product. Part of the [8- ^{13}C]-coniferyl alcohol was applied to a prep-TLC and eluted with CH_2Cl_2 :EtOH 97:3 twice. The fraction corresponding to [8- ^{13}C]-coniferyl alcohol was extracted from silica with acetone. The pure product was confirmed by ^1H NMR and ^{13}C NMR spectra.

The protocol was performed according to a procedure described (Mohri *et al.*, 2003). In a 100 mL round bottom flask, a solution containing 22 mL of chloroform, 2.0 g (13.11 mmol) of vanillin, 2.69 g (8.82 mmol) of acetobromoglucose was added and 2.14 g (6.53 mmol) of tetra n-butylammonium bromide (Bu_4NBr). Then, at room temperature, under stirring, 22 mL of NaOH (1.0 mol L^{-1}) were added. The resulting mixture was stirred vigorously for 1 h at room temperature and, accompanied by TLC, hexane:EtOAc (7:3), until the starting reagent was completely consumed. The resulting solution was extracted with ethyl acetate (2 x 30 mL) and the organic phases combined, washed with NaOH solution (1.0 mol L^{-1}), saturated NaCl solution, dried with anhydrous Na_2SO_4 and evaporated to dryness in rotary evaporator. The product obtained was recrystallized from ethanol providing 2.85 g (43.6%) and identified by ^1H NMR and ^{13}C NMR.

The methodology used in this reaction was developed according to a procedure described (Stöckigt and Klischies, 1977). The acetylated acid was prepared through the Knoevenagel condensation reaction. In a system set up according to item 3.4.1, 100 mg (0.961

mmol) of [2- ^{13}C]-malonic acid, 949.88 mg (1.05 mmol) of glycoacetyl vanillin were added to a 100 mL flask, 3.5 mL of pyridine, one drop of piperidine and one drop of aniline previously distilled. After the reaction time, the reaction mixture was diluted with 2.0 mL of Milli-Q water and 500 μL of acetic acid. The acetylated acid was recrystallized from 95% ethyl alcohol, yielding 904.32 mg (93.5%) of pure product. Tetra-O-acetyl- β -D-glycopyranosyl [8- ^{13}C]-ferulic acid was identified by ^1H NMR and ^{13}C NMR spectra.

The deacetylation of tetra-O-acetyl- β -D-glycopyranosyl [8- ^{13}C]-ferulic acid was performed according to a procedure described (Mohri *et al.*, 2003) with some modifications. In a 100 mL round bottom flask, a solution of tetra-O-acetyl- β -D-glycopyranosyl [8- ^{13}C]-ferulic acid (500 mg, 0.953 mmol) in 5% NH_3 -MeOH (50 mL) was added. The solution was stirred for 2 h at room temperature and followed by C18 silica TLC, MeOH:H $_2$ O (1:1), until the starting material was completely consumed. The reaction mixture was concentrated under reduced pressure in an exhaust hood and then extracted with water (20 mL) and ethyl acetate (20 mL) (in the aqueous phase it contains the glycosylated product and in the organic part of the product that did not glycosylate). The respective phases were concentrated in a rotaevaporator. The residue from the aqueous phase (280 mg) was solubilized in methanol, drops of Milli-Q water and then applied to a C18 silica chromatographic (CC) column, eluted with 1:1 MeOH:H $_2$ O. Fractions containing the product were combined and evaporated in vacuum, providing 213 mg (62.7%) of pure product. ^1H and ^{13}C NMR spectra confirmed the structure of [8- ^{13}C]-glycoferulic acid.

3. Preparation of [8- ^{13}C]-coniferyl acetate

The preparation of this precursor was developed in four steps according to a procedure described (Bastos *et al.*, 2005; Koeduka *et al.*, 2006). Methyl [8- ^{13}C]-ferulate (500 mg, 2.40 mmol), tert-butyldimethylsilane chloride (434.07 mg, 2.88 mmol, 1.2 eq) and imidazole (326 mg, 4.8 mmol, 2 eq.) were added into a 50 mL round bottom flask. The open balloon was placed inside a beaker, surrounded by vermiculite, and the set was placed inside a conventional microwave oven. The reaction mixture was heated for 2 min at a power of 90 W and after a cooling period (2-3 min), the reaction mixture was heated again at 180 W power. The reaction was followed by TLC, hexane:EtOAc (7:3), until the methyl [8- ^{13}C]-ferulate was fully consumed. The reaction was terminated by adding 15 mL of Milli-Q water, followed by extraction with ethyl ether. The organic phases were combined, dried over Na_2SO_4 , and evaporated under

reduced pressure. This methodology was carried out in two steps starting from 500 mg and 450 mg of methyl [8-¹³C]-ferulate. The crude product was purified by chromatotron, eluting with hexane:EtOAc (7:3) resulting in 1.21 mg (82.3%) of pure product which was identified by ¹H NMR and ¹³C NMR.

In a three-neck flask containing magnetic stirring, addition funnel, septum and under nitrogen atmosphere were added, at room temperature, 1.0 g (3.11 mmol) of the ester prepared in step 1 (item 3.4.4) and 30 mL of dry THF distilled under metallic sodium and benzophenone. The reaction mixture was cooled to 0 °C in an ice bath and stirred for 30 min. After this period, 30 mL of diisobutylaluminum hydride in THF (DIBAL-H, 10.0 eq.) was added dropwise through an addition funnel over a period of 1.0 h. The ice bath was removed, and the reaction mixture was kept at room temperature with stirring for about 2.0 h. The reaction was followed by TLC, hexane:EtOAc (7:3), until all the starting material was consumed. The reaction mixture was again cooled to 0 °C and terminated by the addition of 62 mL of 100 mM Rochele salt aqueous solution (potassium sodium tartrate). 50 mL of ethyl acetate were added to the reaction medium, and the residue of the aluminum salt was solubilized by adding about 10 mL of HCl (1.0 mol L⁻¹). The biphasic mixture was filtered through celite and 62 mL of saturated NaCl solution was added. The aqueous phase was again extracted with ethyl acetate (3 x 50 mL). The organic phases were combined, dried over Na₂SO₄, and concentrated on a rotary evaporator. The crude product obtained was purified by chromatotron, eluted with hexane:EtOAc (7:3). Fractions containing the alcohol were pooled, concentrated on a rotaevaporator under reduced pressure, providing 848 mg (92.7%) of pure product which was confirmed by ¹H and ¹³C NMR signals.

802 mg (2.52 mmol) of [8-¹³C]-coniferyl alcohol with the phenolic hydroxyl protected with TBS, 5.31 mL of toluene, 2.12 mL of pyridine, were added to the flask at room temperature, 500 μL of acetic anhydride (5.05 mmol) and 3.18 mg of 4-*N,N*-dimethylaminopyridine (DMAP, 0.027 mmol). The reaction mixture was followed by TLC (hexane:EtOAc, 7:3), which indicated when the starting material was completely consumed. The reaction was stirred for 1 h. The crude product from the reaction was concentrated under reduced pressure, with successive washings with toluene (20 mL) to eliminate excess anhydride and pyridine. The resulting oil was solubilized in 25 mL of ethyl acetate, extracted with 1.0 mol L⁻¹ HCl (3 x 25 mL) and saturated NaCl solution (2 x 25 mL). The aqueous phases were combined and re-extracted with ethyl acetate (3 x 25 mL). The organic phases were combined,

dried with anhydrous Na₂SO₄, filtered, and concentrated on a rotary evaporator. The crude product was purified by chromatotron, eluting with hexane:EtOAc (7:3), resulting in 704 mg (82.7%) of pure product which was identified by ¹H and ¹³C NMR.

500 mg (1.49 mmol) of [8-¹³C]-coniferyl acetate with the protected phenolic hydroxyl were added to a three-neck flask, equipped with magnetic stirring, addition funnel, septum, under nitrogen atmosphere and at room temperature. with TBS and 15 mL of dry THF. The solution was cooled to 0 °C in an ice bath, with stirring for 30 min. After this period, through an addition funnel, 3.0 mL of tetrabutylammonium fluoride at 1.2 mol L⁻¹ in THF was slowly added to the reaction medium kept at 0 °C. Then, the reaction was kept under stirring for another 30 min. 30 mL of cold ethyl acetate were added to the reaction mixture, followed by 30 mL of 1 mol L⁻¹ HCl solution and 30 mL of saturated NaCl solution. The phases were separated, and the aqueous phases were again extracted with EtOAc (2 x 30 mL). The organic phases were grouped, dried over Na₂SO₄, and concentrated in a rotaevaporator. The crude product (423.0 mg) was subjected to CC, eluted with CH₂Cl₂:MeOH (9:1), resulting in 212 mg (64.4%) of the pure product which was identified by ¹H spectra and ¹³C NMR.

4. Preparation of *E*-isoeugenol

Vanillin (500 mg, 3.28 mmol), tert-butyltrimethylsilane chloride (593.2 mg, 3.94 mmol, 1.2 eq.) and imidazole (446.46 mg, 6.56 mmol, 2.0 eq.) were added to a 50 mL round bottom flask. The system was kept open and submitted to a conventional microwave oven, followed by heating and the reaction was followed by TLC. This methodology was performed in three steps starting from 500 mg of vanillin. The crude product was purified by chromatotron, eluted with hexane:EtOAc (7:3) resulting in 2.28 g (87.02%) of pure product which was identified by ¹H NMR and ¹³C NMR.

In a 500 mL round bottom flask, 12 mL (150 mmol) of iodoethane and 39.40 g (150 mmol) of triphenylphosphine were dissolved in 100 mL of dry THF. The reaction was refluxed and stirred for about 96 h at 95 °C. At the end of this period, the formation of a white solid was observed which was washed with ice-cold hexane by filtration on a Buchner funnel. Then, the solid was dried in a desiccator under pressure for approximately 90 h. 58.26 g of crude product were obtained. Ethyltriphenylphosphonium iodide was confirmed by ¹H NMR and ¹³C NMR data.

4.1 Wittig Condensation Reaction

This protocol was developed with some modifications (Bastos *et al.*, 2005). To a system with a 125 mL three-neck flask, containing magnetic stirring, addition funnel, septum and under nitrogen atmosphere, 30 mL of dry THF was added. The solution was cooled to $-75\text{ }^{\circ}\text{C}$ and added dropwise, via syringe, 4.0 mL (8.57 mmol) of *n*-BuLi in hexane to 2.16 mol L^{-1} . The light-yellow colored solution was kept under stirring for 30 min at $0\text{ }^{\circ}\text{C}$. After this period, 3.76 g (8.98 mmol) of ethyltriphenylphosphonium iodide were added at $0\text{ }^{\circ}\text{C}$. Upon adding the salt, the solution changed color from pale yellow to wine red. The solution was kept under stirring for another 30 min. After this period, a solution of 2.28 g (8.57 mmol) of vanillin with the phenolic hydroxyl protected with TBS in 10 mL of dry THF was added dropwise over about 30 min. The final solution turned light yellow and was kept under stirring at room temperature for approximately 24 h. After this period, 50 mL of Milli-Q water was added to the reaction. The aqueous phase was extracted with hexane (5 x 50 mL) followed by extraction with EtOAc (2 x 50 mL). The organic phases were separately concentrated on a rotaevaporator. Then, the hexane phase was filtered through a CC of silica and washed with portions of 100% hexane, followed by hexane:EtOAc (9:1). The solvent was removed on a rotaevaporator resulting in 682 mg (28.6%) of a yellowish oil. The product was identified by ^1H NMR analysis which indicated the formation of a mixture of the *Z*- and *E*-isoeugenol isomers.

4.2 Photoisomerization reaction of *E*- and *Z*-isoeugenol

A photoisomerization reaction of the product obtained in step 3 was carried out to obtain an enantiomeric excess of the isomer *E*-isoeugenol.

In a glass ampoule containing a magnetic stirrer, 340 mg (1.28 mmol) of the hydroxyl-protected *E*- and *Z*-isoeugenol and 80 μL (0.384 mmol, 0.3 eq.) of diphenyl sulfide in 3.0 mL of dry hexane. Light (60 Watts) was applied directly to the closed system (at room temperature and kept under stirring in silicone oil) for 16 h. Then, the system was opened, and the solvent evaporated. The crude product (298 mg, 83% yield) was purified by CCDP eluted in hexane:EtOAc 100:1. The pure product was confirmed by ^1H NMR and ^{13}C NMR.

250 mg (0.898 mmol) of *E*-isoeugenol with the phenolic hydroxyl protected with TBS and 3.0 mL of dry THF. The solution was cooled to $0\text{ }^{\circ}\text{C}$ in an ice bath and kept under stirring for 30 min. After this period, through

an addition funnel, 312 μL of tetrabutylammonium fluoride at 1.2 mol L^{-1} in THF was slowly added to the reaction medium kept at $0\text{ }^{\circ}\text{C}$. The reaction was kept under stirring for 30 min, followed by TLC and eluted with hexane:EtOAc (7:3), followed by extraction with ethyl acetate. The crude product (200 mg) was purified by CC eluted with 4:1 hexane:ethyl acetate. 152 mg (61% yield) of pure product was obtained which was confirmed by ^1H NMR and ^{13}C NMR.

The protocol was developed according to a procedure described (Boschi *et al.*, 2006). The reaction was carried out in a 50 mL three-neck flask, under nitrogen atmosphere and addition funnel. A solution of 2.0 mL (10.3 mmol) of commercial 5-methoxy-eugenol in 20 mL of dichloromethane was prepared. To this solution were added 2.86 mL of triethylamine (20.5 mmol) and 0.04 g (0.29 mmol) of *N,N*-dimethylaminopyridine (DMAP). The mixture was cooled to $0\text{ }^{\circ}\text{C}$ and 1.93 mL (20.5 mmol) of acetic anhydride was added dropwise via an addition funnel. The reaction mixture was left under stirring at room temperature for 20 min. The final solution was diluted with 30 mL of dichloromethane, washed with saturated NaCl solution (2 x 30 mL), dried over Na_2SO_4 and concentrated on a rotaevaporator yielding 2.30 g (97%) which was used without purification. The formation of 4-allyl-2,6-dimethoxyphenyl acetate was confirmed by ^1H and ^{13}C NMR analysis.

Ozonolysis was performed as described, with some modifications (Schiaffo and Dussault, 2008). 4-Allyl-2,6-dimethoxyphenyl acetate, 500 mg (2.12 mmol) was placed in a round bottom flask and solubilized in 95:5 acetone: H_2O at a concentration of 0.15 mol L^{-1} . The solution was cooled to $0\text{ }^{\circ}\text{C}$ and a flow of O_3/O_2 was bubbled into the reaction mixture through a disposable pipette attached to an aquarium pump. The reaction was followed by TLC, hexane:ethyl acetate (7:3). After the starting material was completely consumed, the reaction mixture was diluted with 25 mL of water and extracted with dichloromethane (2 x 25 mL). The organic phases were combined and concentrated on a rotaevaporator. This reaction was repeated three more times, starting with 500 mg of the reagent. The crude product was purified by chromatotron and eluted with hexane:EtOAc (7:3). Fractions were followed by CCD. Fractions containing the product were pooled, concentrated on a rotaevaporator, providing 772 g, (38% yield) of pure product, which was identified by ^1H and ^{13}C NMR.

4.3 Wittig condensation reaction

To a 6.0 mL of dry THF, cooled to $-75\text{ }^{\circ}\text{C}$, 1.5 mL (3.24 mmol, 1 eq.) were added *n*-BuLi in hexane

(2.16 mol L⁻¹). The solution was kept under stirring for 30 min at 0 °C and then 1.57 g (3.88 mmol) of methyl-triphenylphosphonium iodide were added and the reaction was kept under stirring for another 30 min at 0 °C. Then, was added a solution containing 772 mg (3.24 mmol) of the acetylated aldehyde in 3.0 mL of dry THF. The system was left under stirring at room temperature for 24 h. The reaction was terminated by adding 5 mL of Milli-Q water, followed by extraction with hexane and ethyl acetate. The crude product was purified by CC, eluted with hexane:EtOAc (9:1) followed by 100% EtOAc. The pure 234 mg product (30.6%) was identified by ¹H and ¹³C NMR.

4.4 Deprotection reaction of the acetate group

The deacetylation of 5-methoxy-eugenol was carried out as follow. In a 50 mL round bottom flask, a solution of 5-methoxy-eugenol 234 mg (0.99 mmol) was added acetylated in 5% NH₃ -MeOH (23.4 mL). The solution was stirred for about 2 h at room temperature and followed by TLC, 9:1 hexane:EtOAc, until the starting material was completely consumed. The reaction mixture was concentrated under reduced pressure in an exhaust hood and then extracted with Milli-Q water, hexane, hexane:EtOAc (9:1) and 100% EtOAc. The pure 5-methoxy-eugenol product (128 mg, 66.6% yield) was confirmed by ¹H and ¹³C NMR data.

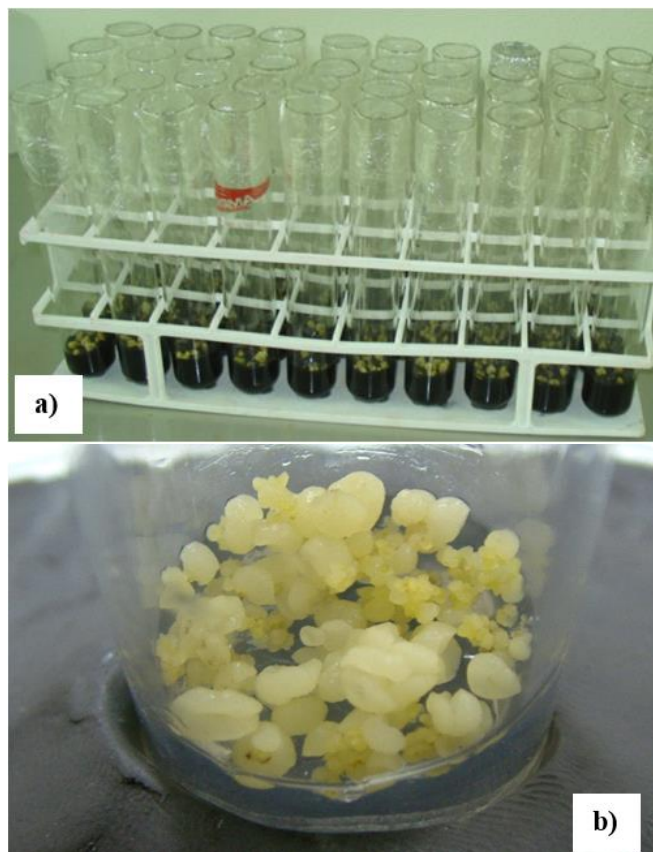


Figure S1. (a) *In vitro* culture of *O. catharinensis* embryos; (b) Somatic embryos in the globular stage.

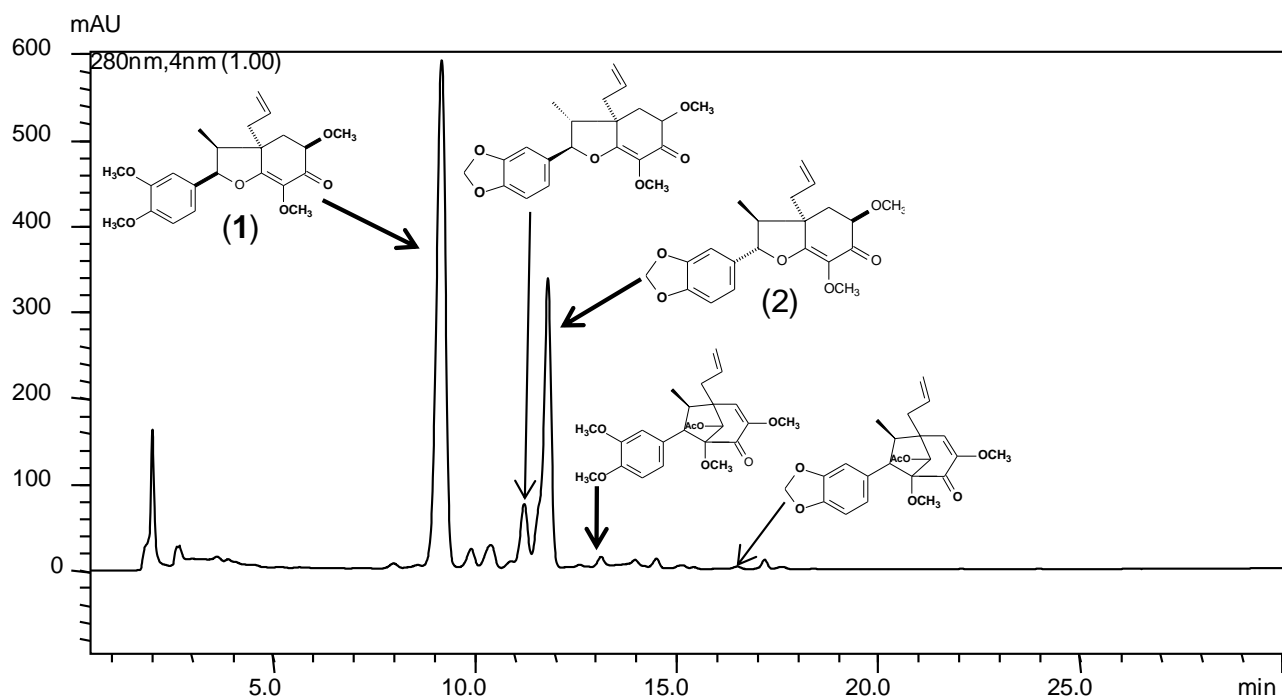


Figure S2. Chromatographic profile by HPLC (detection at 280 nm) of CHCl₃ extract from somatic embryos of *O. catharinensis*.

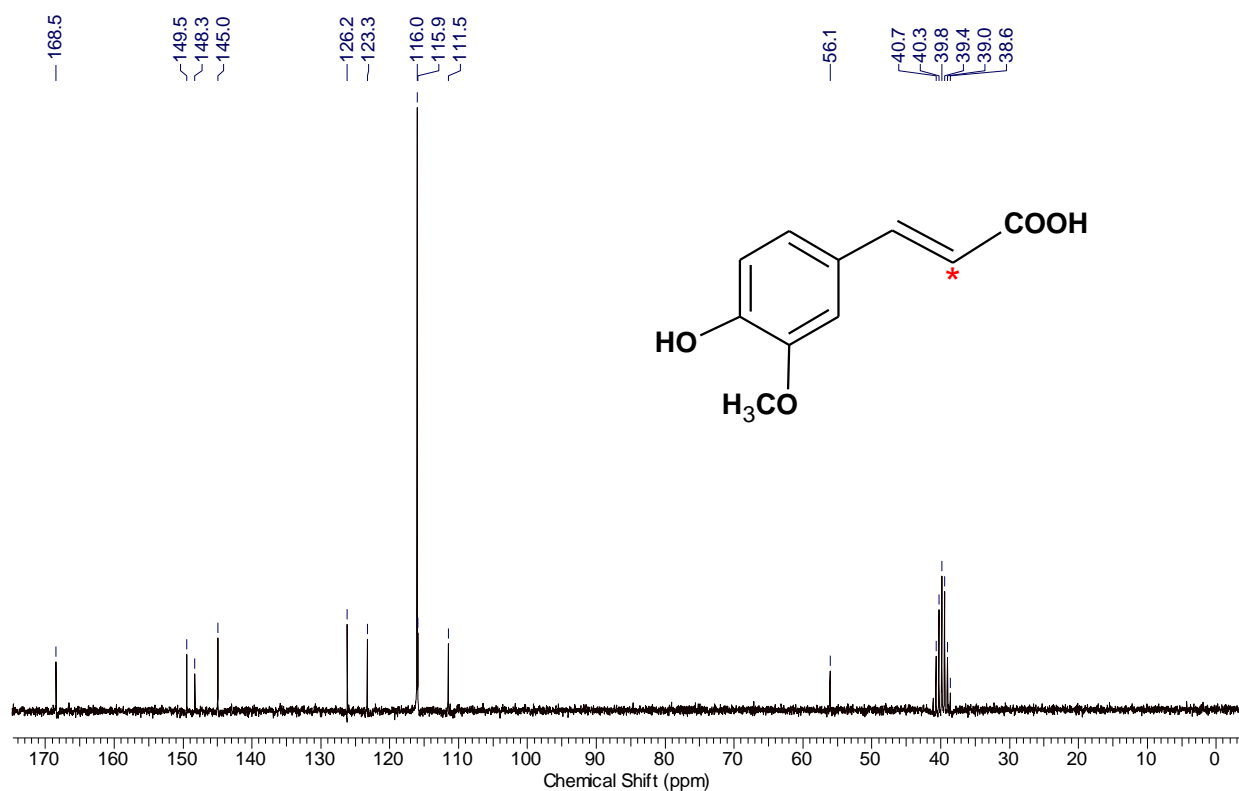


Figure S3. ^{13}C NMR spectrum (DMSO, 200 MHz) of [8- ^{13}C]-ferulic acid.

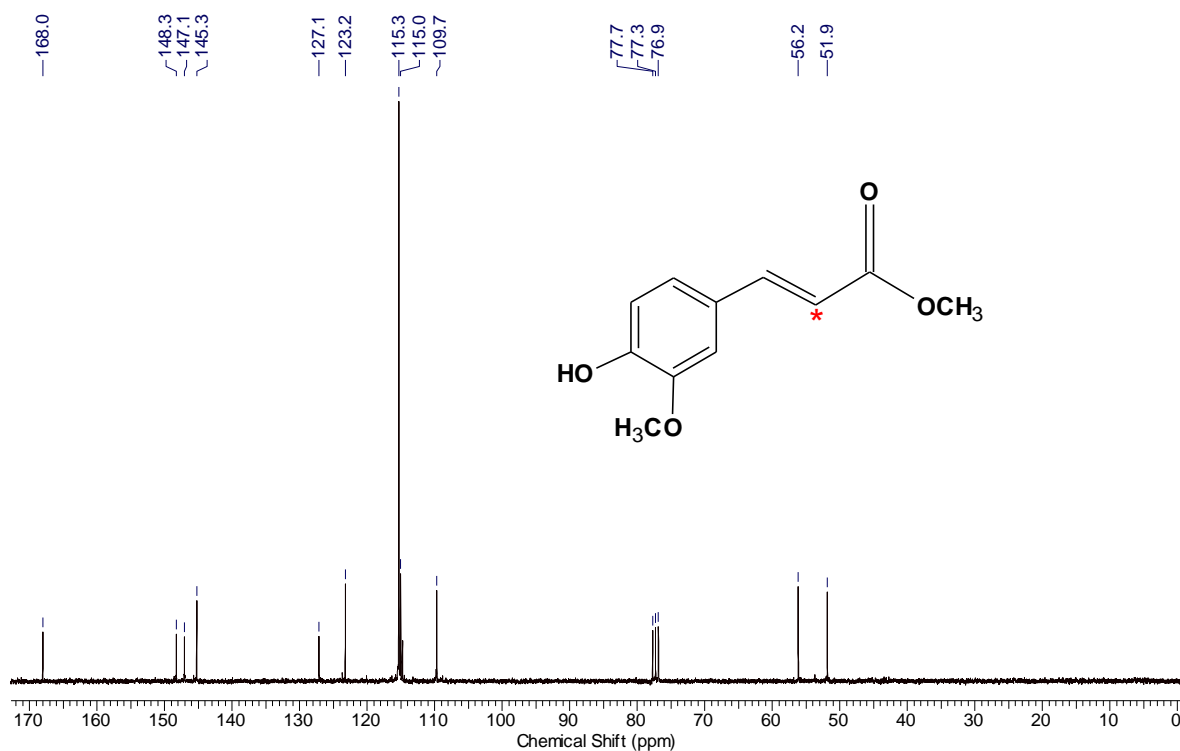


Figure S4. ^{13}C NMR spectrum (CDCl_3 , 200 MHz) of methyl [8- ^{13}C]-ferulate.

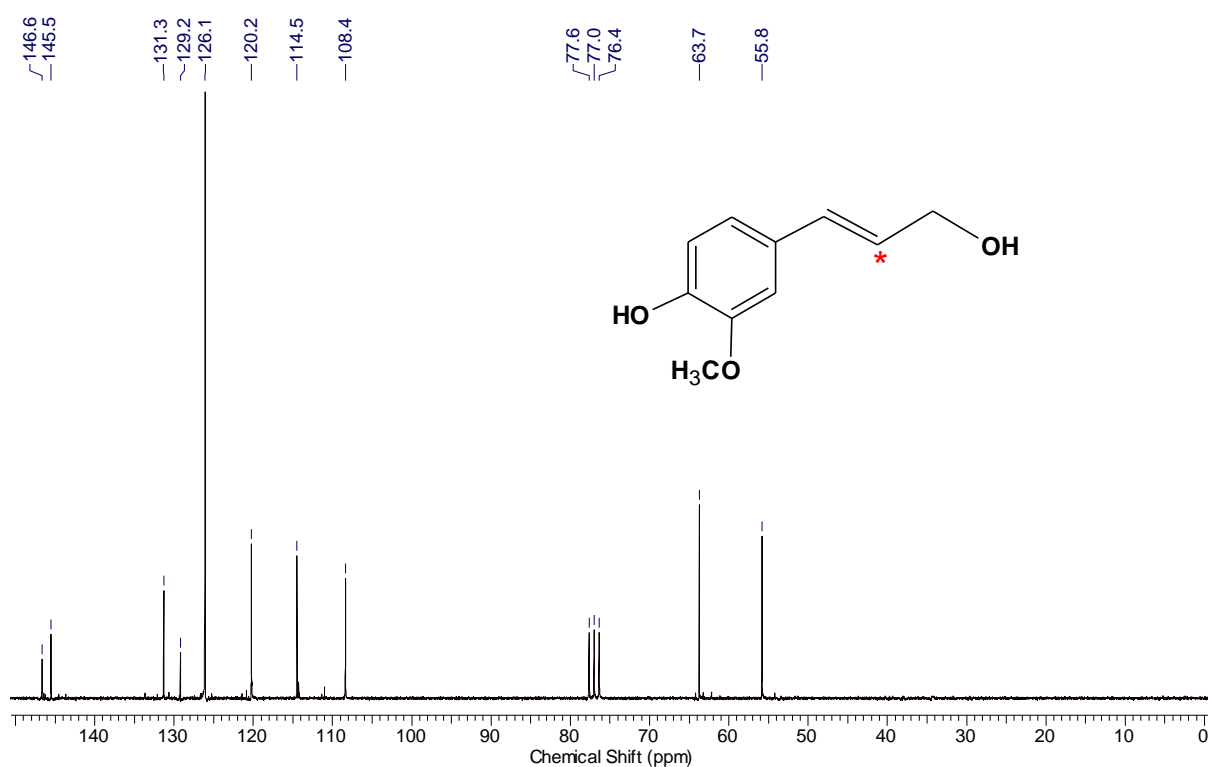


Figure S5. ^{13}C NMR (CDCl_3 , 200 MHz) spectrum of $[8-^{13}\text{C}]$ -coniferyl alcohol.

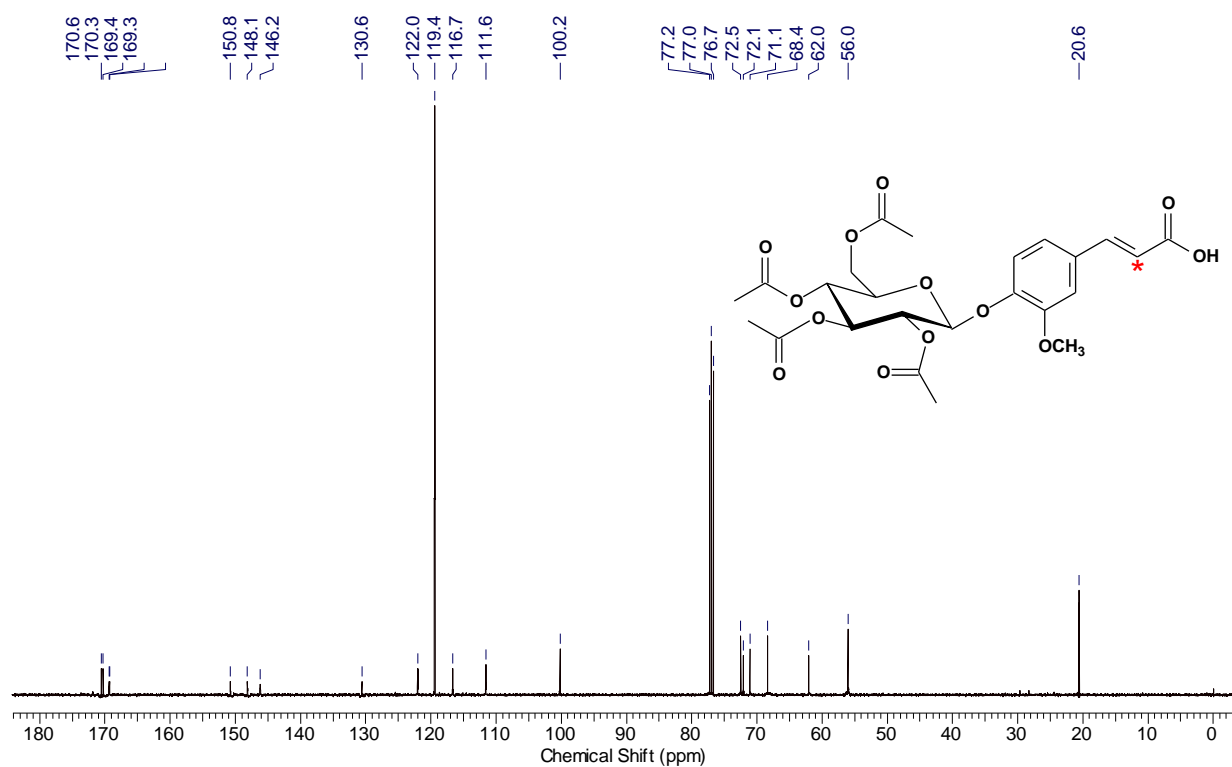


Figure S6. ^{13}C NMR (CDCl_3 , 50 MHz) spectrum of $[8-^{13}\text{C}]$ -glycoferulic acid.

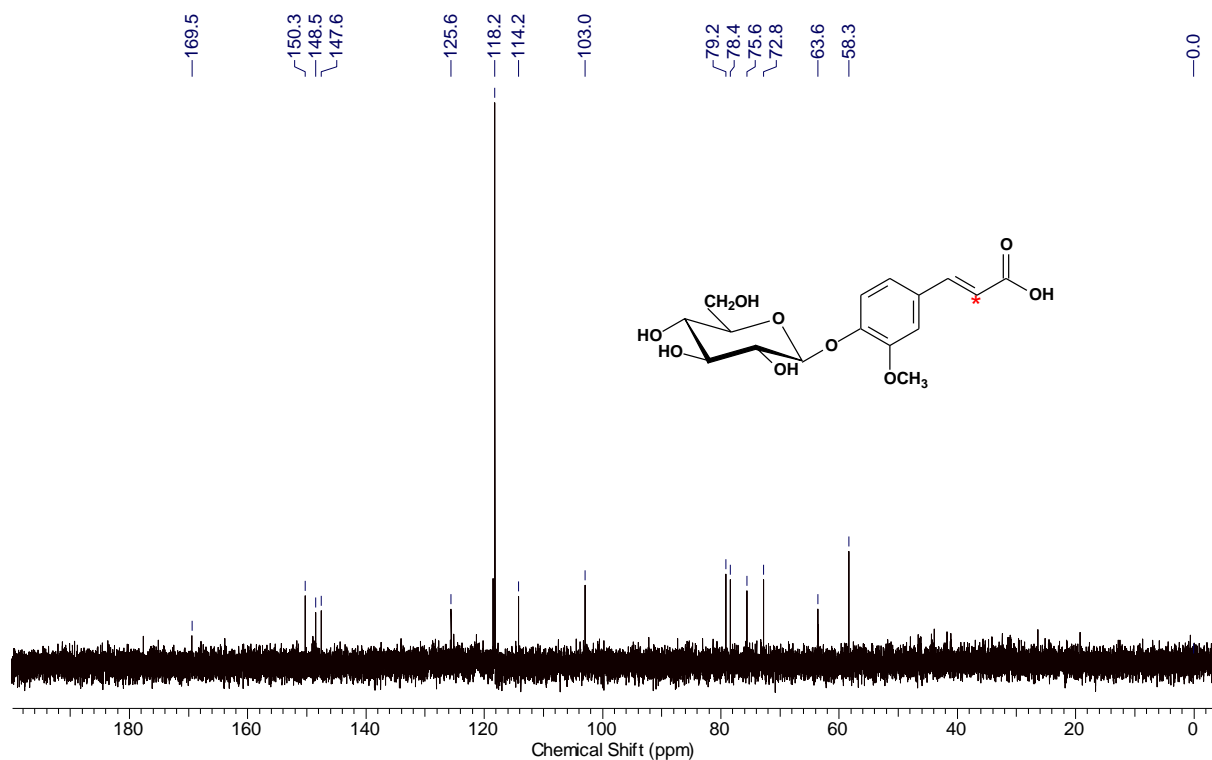


Figure S7. ^{13}C NMR spectrum (D_2O , 50 MHz) $[8\text{-}^{13}\text{C}]$ -glycoferulic acid.

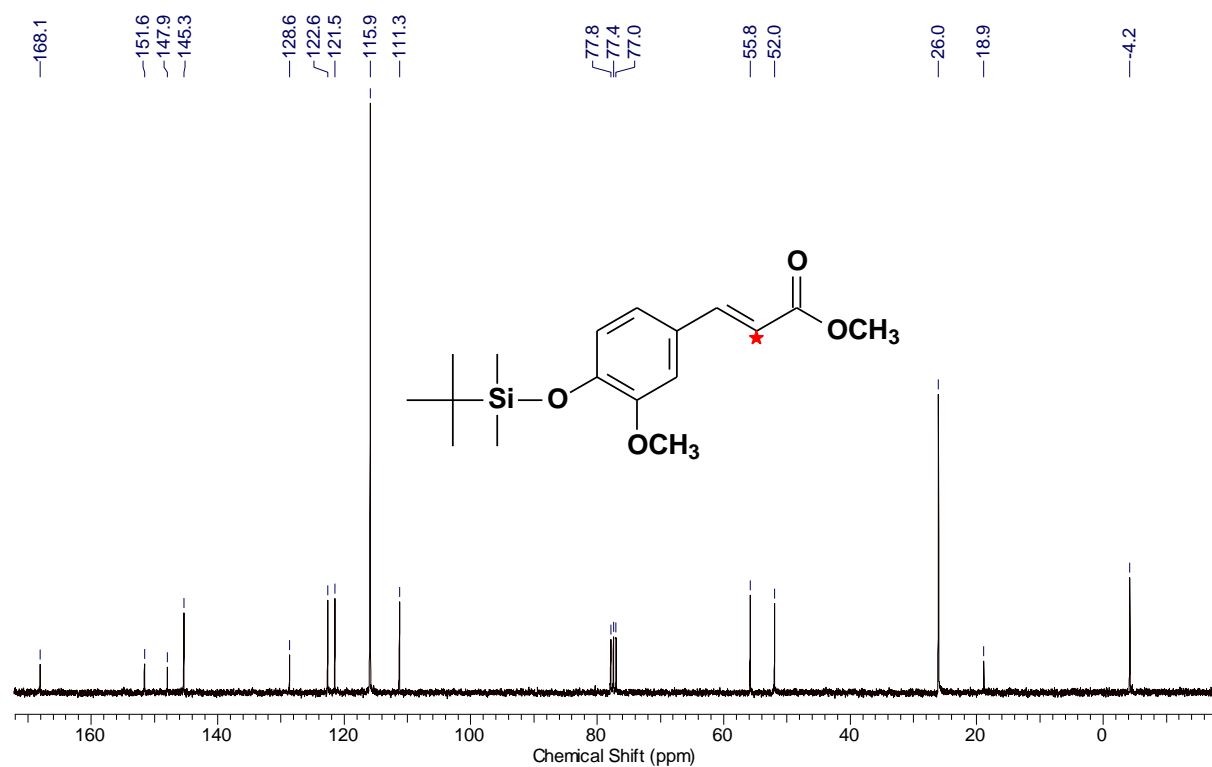


Figure S8. ^{13}C NMR (CDCl_3 , 50 MHz) spectrum of methyl $[8\text{-}^{13}\text{C}]$ -ferulate protected with TBS.

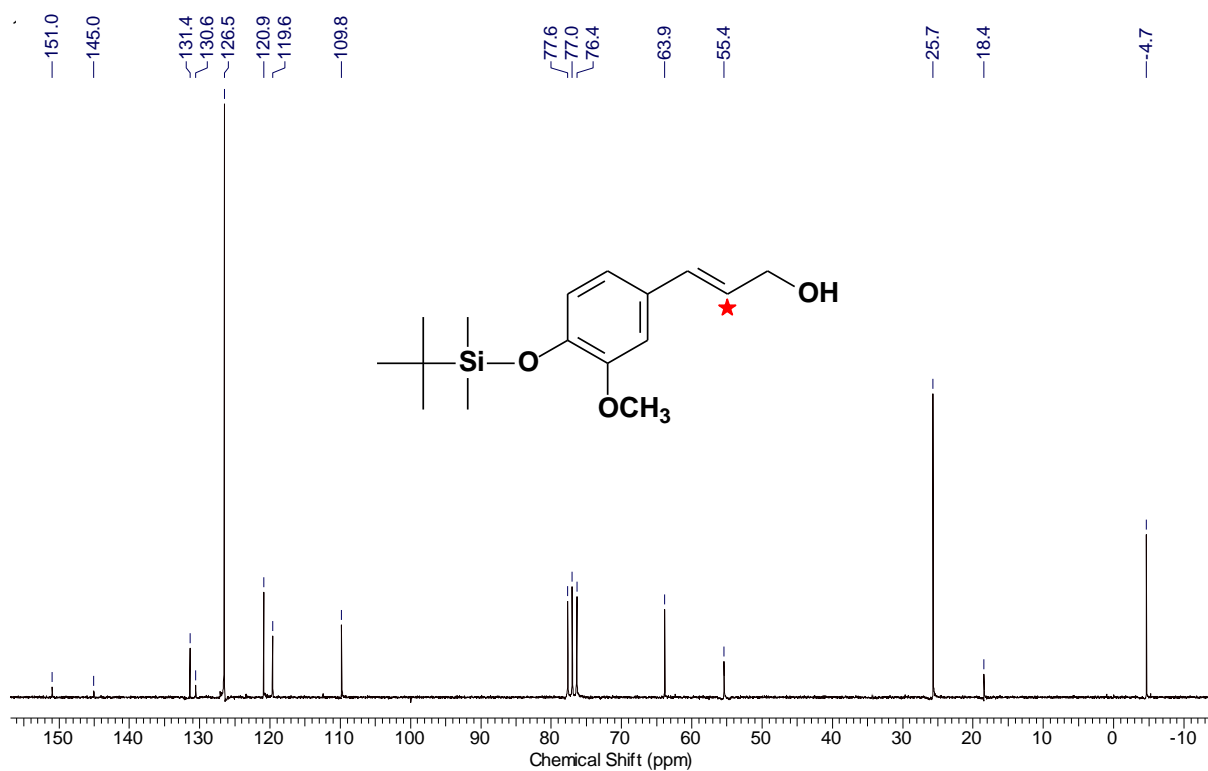


Figure S9. ¹³C NMR (CDCl₃, 50 MHz) spectrum of [8-¹³C]-coniferyl alcohol protected with TBS.

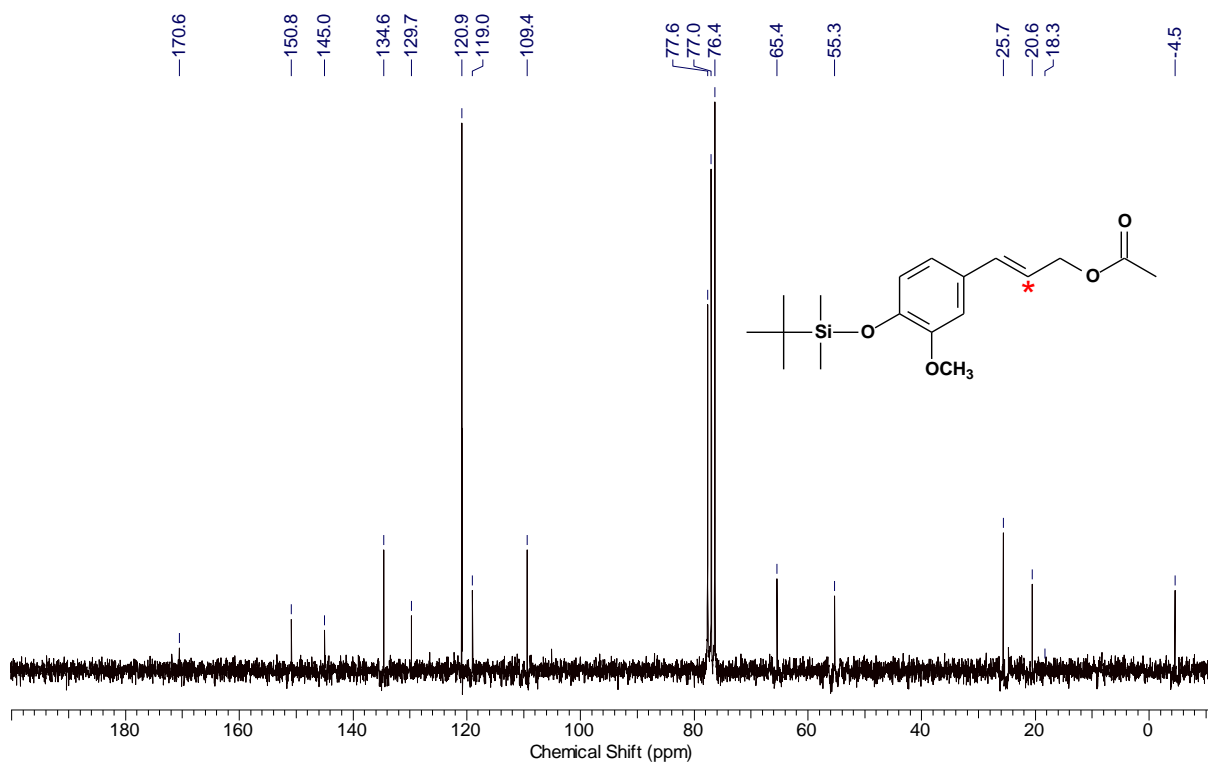


Figure S10. ¹³C NMR (CDCl₃, 50 MHz) spectrum of [8-¹³C]-coniferyl acetate protected with TBS.

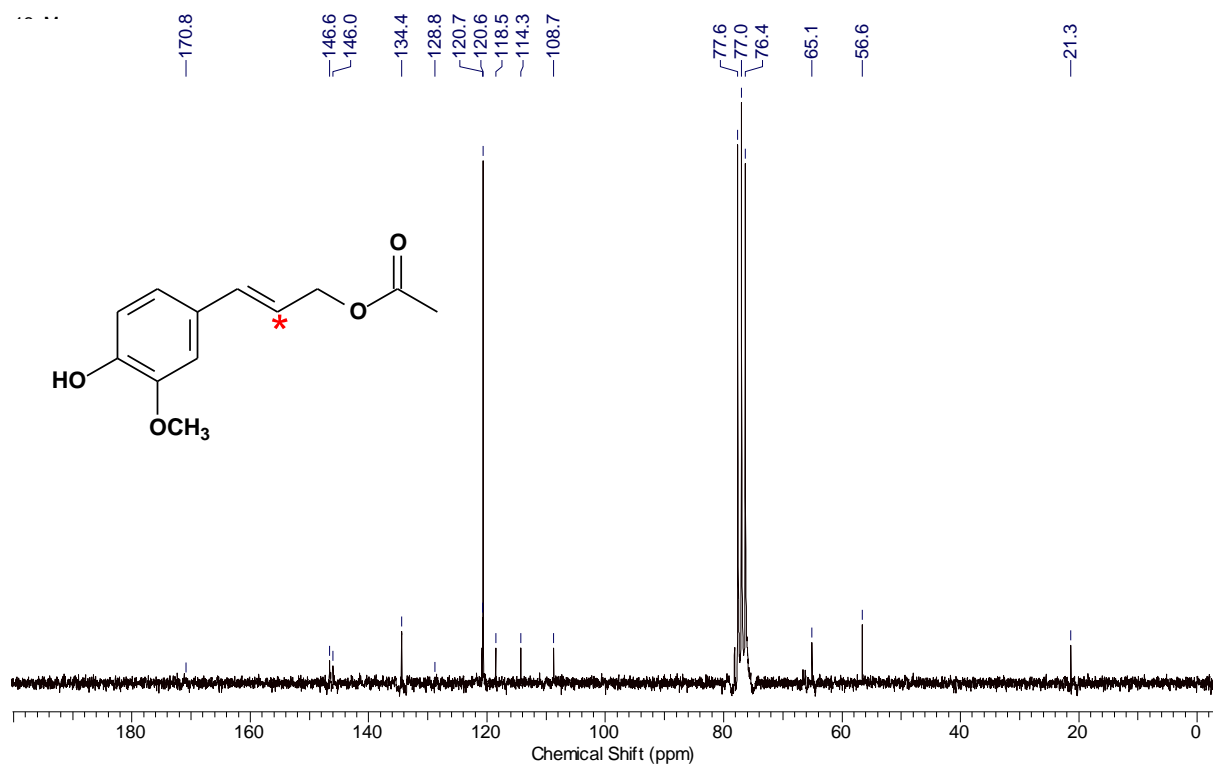
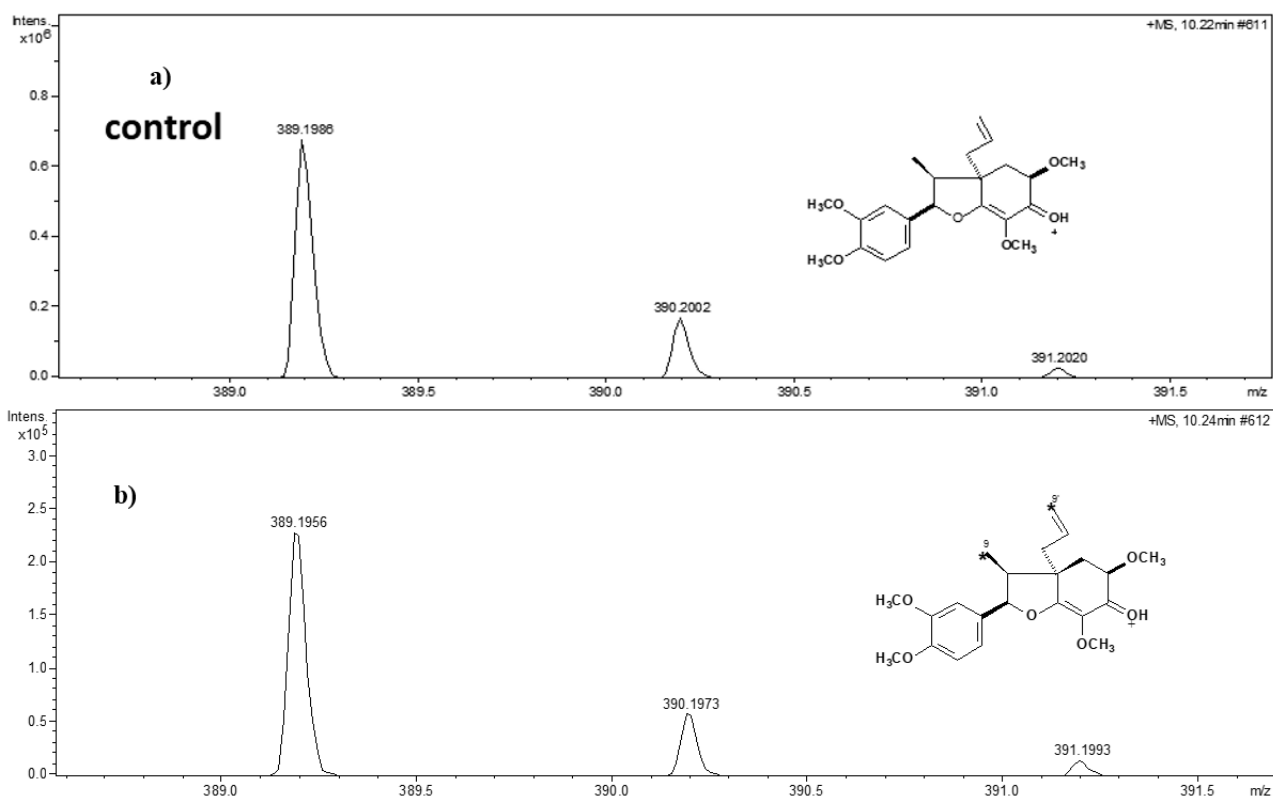


Figure S11. ^{13}C NMR spectrum (CDCl_3 , 50 MHz) of $[8-^{13}\text{C}]$ -coniferyl acetate.



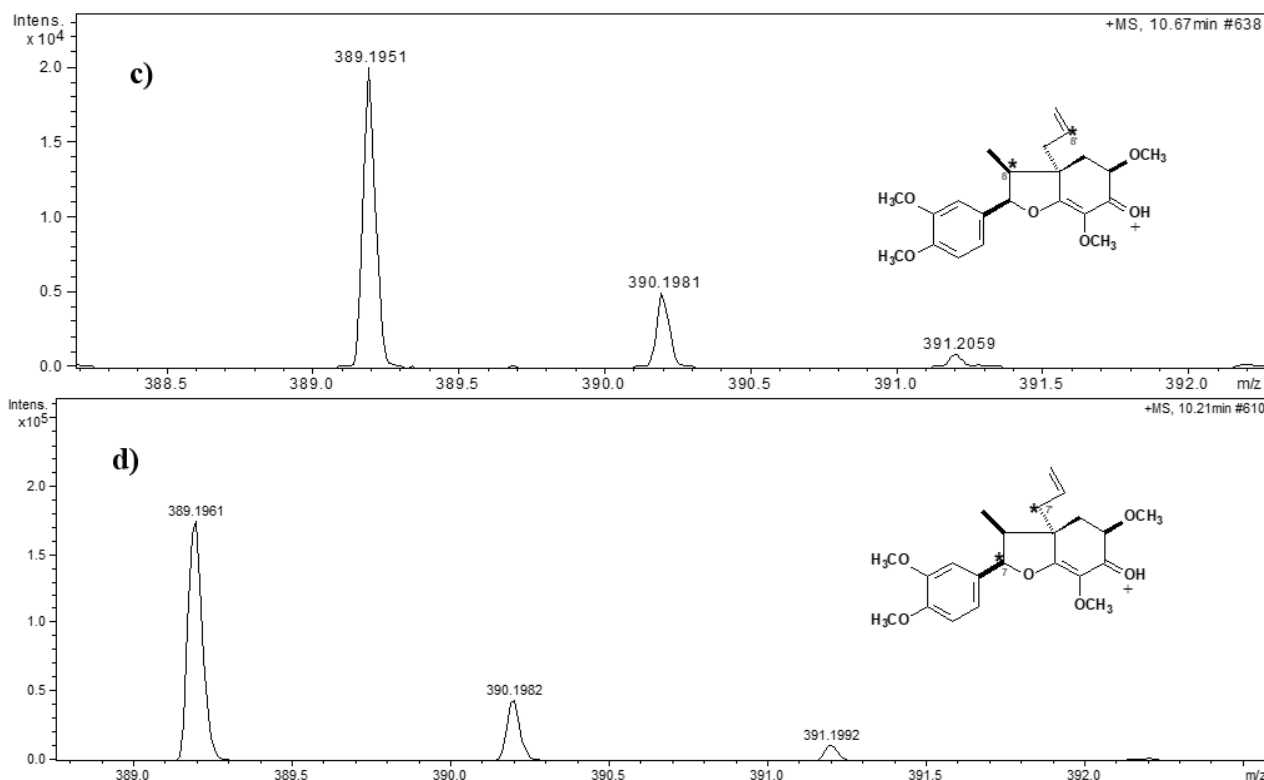
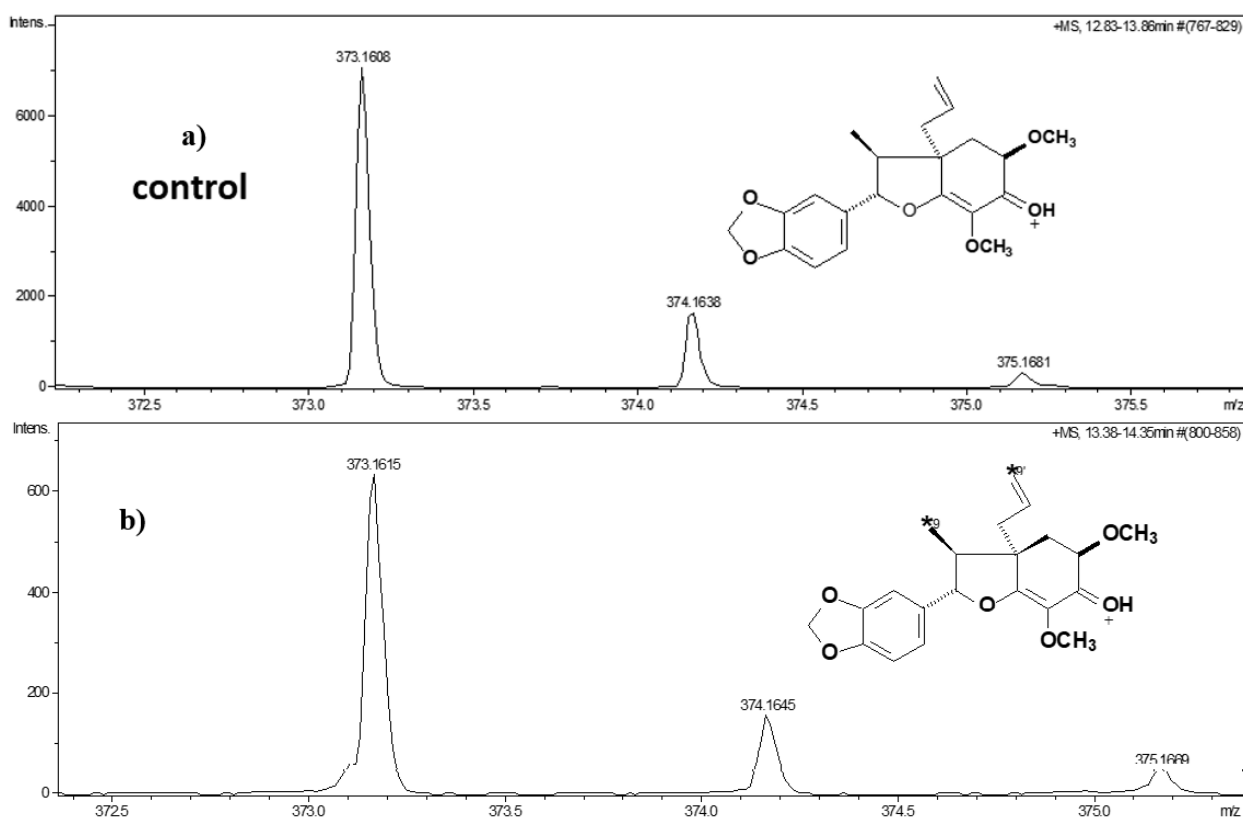


Figure S12. Mass spectra (ESI) of ^{13}C incorporation in 5'-methoxy porosin. **(a)** Control; **(b)–(d)** 5'-methoxy-porosin incorporated with *L*-[1- ^{13}C], *L*-[2- ^{13}C] and *L*-[3- ^{13}C]-phenylalanine, respectively.



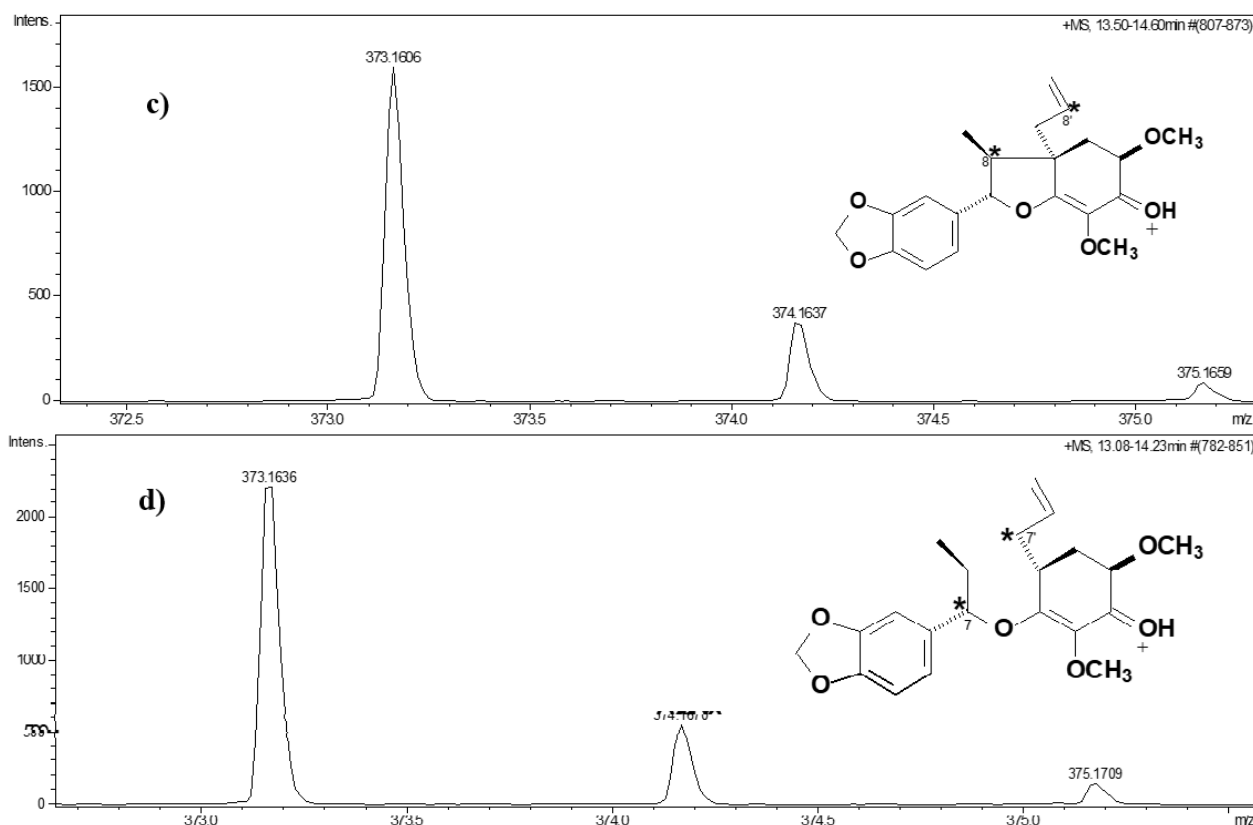


Figure S13. Mass spectra (ESI) of ^{13}C incorporation in armenin B. (a) Control; (b)–(d) armenin B incorporated with L -[1- ^{13}C], L -[2- ^{13}C] and L -[3- ^{13}C]-phenylalanine, respectively. *Positions enriched with ^{13}C .

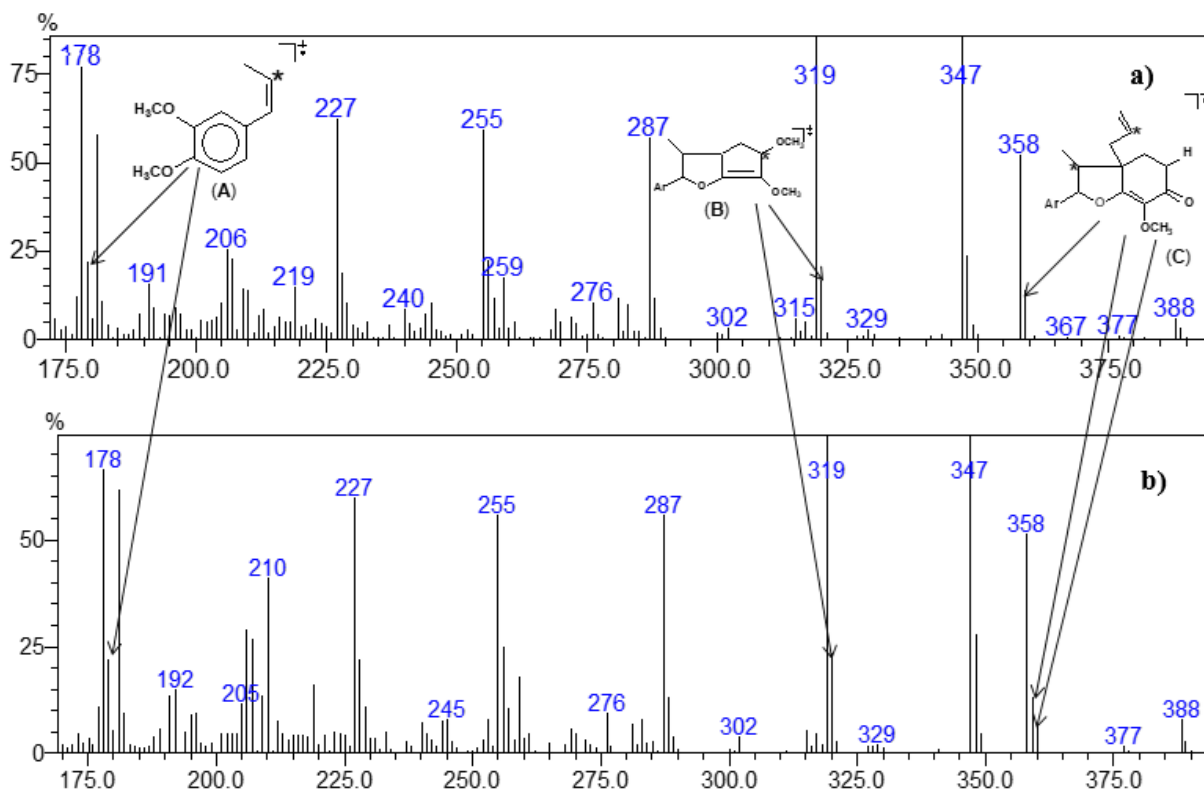


Figure S14. Mass spectra (EI) of 5'-methoxy-porosin with natural abundance (A); (B) Incorporation of [8- ^{13}C]-coniferyl acetate; (a) Expansion of (A); (b) Expansion of (B).

References

Bastos, E. L.; Ciscato, L. F. M. L.; Baader, W. J., Microwave-assisted protection of phenols as tert-butyldimethylsilyl (TBDMS) ethers under solvent-free conditions. *Synth. Commun.* **2005**, *35* (11), 1501–1509. <https://doi.org/10.1081/SCC-200057992>

Boschi, D.; Tron, G. C.; Lazzarato, L.; Chegaev, K.; Cena, C.; Di Stilo, A.; Giorgis, M.; Bertinaria, M.; Fruttero, R.; Gasco, A. NO-donor phenols: a new class of products endowed with antioxidant and vasodilator properties. *J. Med. Chem.* **2006**, *49* (10), 2886–2897. <https://doi.org/10.1021/jm0510530>

Katayama, T.; Davin, L. B.; Lewis, N. G. An extraordinary accumulation of (–)-pinoresinol in cell-free extracts of *Forsythia intermedia*: evidence for enantiospecific reduction of (+)-pinoresinol. *Phytochemistry*. **1992**, *31* (11), 3875–3881. [https://doi.org/10.1016/S0031-9422\(00\)97545-9](https://doi.org/10.1016/S0031-9422(00)97545-9)

Koeduka, T.; Fridman, E.; Gang, D. R.; Vassao, D. G.; Jackson, B. L.; Kish, C. M.; Orlova, I.; Spassova, S. M.; Lewis, N. G.; Noel, J. P.; Baiga, T. J.; Dudareva, N.; Pichersky, E. Eugenol and isoeugenol, characteristic aromatic constituents of spices, are biosynthesized via reduction of a coniferyl alcohol ester. *Proc. Natl. Acad. Sci.* **2006**, *103* (26), 10128–10133. <https://doi.org/10.1073/pnas.0603732103>

Mohri, K.; Watanabe, Y.; Yoshida, Y.; Satoh, M.; Isobe, K.; Sugimoto, N.; Tsuda, Y., Synthesis of glycosylcurcuminoids. *Chem. Pharm. Bull.* **2003**, *51* (11), 1268–1272. <https://doi.org/10.1248/cpb.51.1268>

Schiaffo, C. E.; Dussault, P. H. Ozonolysis in Solvent/Water Mixtures: Direct Conversion of Alkenes to Aldehydes and Ketones. *J. Organic Chemistry* **2008**, *73* (12), 4688–4690. <https://doi.org/10.1021/jo800323x>

Stöckigt, J.; Klischies, M. Biosynthesis of lignans: Part I. Biosynthesis of arctiin (3) and phillyrin (5). *Holzforschung* **1977**, *31* (2), 41–44. <https://doi.org/10.1515/hfsg.1977.31.2.41>

Phenylalanine ammonia lyase: new insights from Piperaceae species

Andreia de Araújo Morandim-Giannetti¹, Lidiane Gaspareto Felipe², Vânia Aparecida de Freitas Formenton Macedo dos Santos², Massuo Jorge Kato³, Maysa Furlan²⁺

1. FEI University Center, Department of Chemical Engineering, São Bernardo do Campo, Brazil.
2. Paulista State University, Institute of Chemistry, Araraquara, Brazil.
3. University of São Paulo, Institute of Chemistry, São Paulo, Brazil.

+Corresponding author: Maysa Furlan, Phone: +551633019500, Email address: maysa.furlan@unesp.br

ARTICLE INFO

Article history:

Received: October 19, 2021

Accepted: February 22, 2022

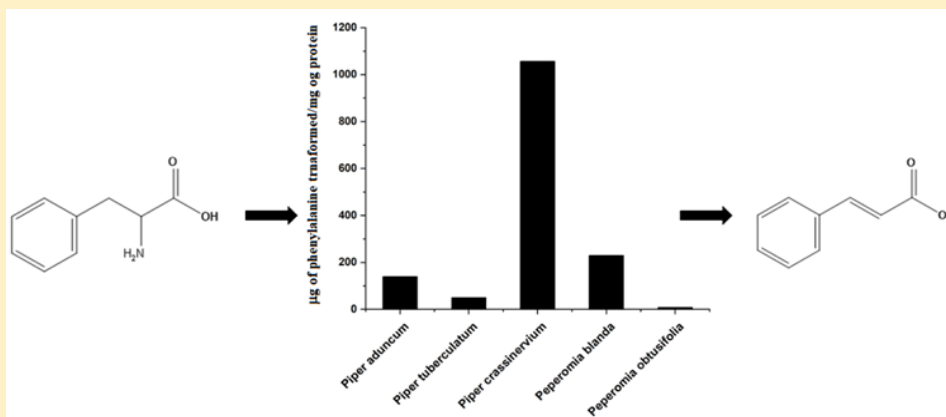
Published: August 17, 2022

Section Editor: Assis Vicente Benedetti

Keywords

1. *Peperomia*
2. *Piper*
3. phenylalanine ammonia lyase
4. phenylpropanoid derivatives
5. Thermal stability

ABSTRACT: The enzyme PAL (phenylalanine ammonia lyase) mediates the key entry point to the general phenylpropanoid pathway, which is involved in the lignification process and in the formation of a myriad of secondary compounds in plants that show a variety of biological activities. Soluble fractions containing PAL extracted from *Piper* and *Peperomia* species had the optimal catalytic activity analyzed by statistical design model. This analysis revealed that the best conversion of *L*-phenylalanine to *trans*-cinnamic acid was pH 9.3 and 58 °C after 25 h, corroborating interesting thermal stability. Additionally, the pre-purification of PAL using ammonium sulfate precipitation (25-55%) increased its specific activity, approximately 133% in *P. aduncum* and more than 900% in *P. crassinervium*. The content of lignin was higher for *P. tuberculatum* (25.71%), while only a small amount of lignin was observed in *Peperomia blanda* (11.95%). It is interesting to note that *Peperomia* plants are succulent and without significant amounts of lignin. However, the phenylpropanoid biosynthetic pathway is apparently addressed to produce predominantly tetrahydrofuran lignans with biological interest.



1. Introduction

Phenylalanine ammonia lyase (PAL, EC 4.3.1.24) (Toscano *et al.*, 2018) plays a crucial role at the interface between primary and secondary metabolism in plants - it catalyzes the *trans*-deamination of *L*-phenylalanine to *trans*-cinnamic acid, which is the first step in the general phenylpropanoid pathway (Huang *et al.*, 2020; Levy *et al.*, 2018; Machado *et al.*, 2013). This enzyme has an important role in plant growth since it is required to produce the macromolecule lignin in plants, which has a primary structural function and acts as physical and chemical barriers against pathogens (Gutiérrez-Quequezana *et al.*, 2020; Vanholme *et al.*, 2019; You *et al.*, 2020).

The phenylpropanoid pathway, one of the most important secondary metabolism pathways, leads to the biosynthesis of a wide range of secondary metabolites, such as flavonoids, isoflavonoids, anthocyanins (Dong *et al.*, 2016; Mota *et al.*, 2011; Prabpreet *et al.*, 2018), phenylalanine derivatives (Batista Junior *et al.*, 2009; 2010; Batista *et al.*, 2012; Felipe *et al.*, 2012; Moraes and Kato, 2021; Ramos *et al.*, 2013; Yoshida *et al.*, 2018; You *et al.*, 2020), phytoalexins (Dong *et al.*, 2016), chromenes (Batista *et al.*, 2017; Kitamura *et al.*, 2006; Lago *et al.*, 2004; Morandim *et al.*, 2005; Salazar *et al.*, 2005; Souza *et al.*, 2019), chromanes (Batista Junior *et al.*, 2012; El Babili *et al.*, 2021), amides (García-Huertas *et al.*, 2018; Lopes *et al.*, 2007; López *et al.*, 2010; Mota *et al.*, 2009), monolignols (Macêdo *et al.*, 2020), coumarins (Banu *et al.*, 2019), and lignans (Dong *et al.*, 2016) (Fig. 1).

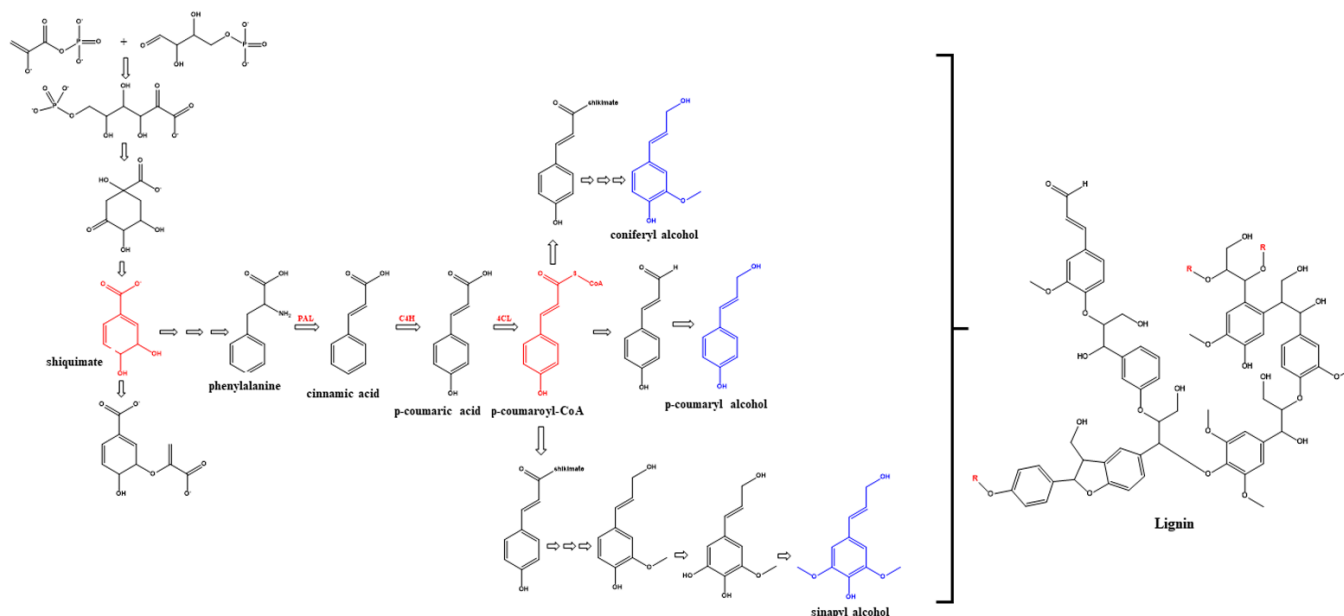


Figure 1. Phenylpropanoid pathways involved in the formation of lignin.

Source: Adapted from Vanholme *et al.* (2019).

In the lignin pathway, three principal enzymes are involved: phenylalanine ammonia lyase (PAL), cinnamate 4-hydroxylase, and 4-coumarate: CoA ligase (Banu *et al.*, 2019; Vanholme *et al.*, 2019). In the lignin biosynthesis in plants, PAL is the primer enzyme that mediates the formation of the cinnamic acid, which is the first product in the general phenylpropanoid pathway (Dong *et al.*, 2016; Felipe *et al.*, 2012; Klejdus *et al.*, 2013; Machado *et al.*, 2013). A series of enzymes are required to produce the cinnamyl alcohols required for the radical reaction: hydroxycinnamoyl CoA:shikimate hydroxycinnamoyl transferase, hydroxycinnamoyl

CoA:quinate hydroxycinnamoyl transferase, *p*-coumaroyl shikimate 3'-hydroxylase, and ferulate (coniferaldehyde) 5-hydroxylase (Kamdee *et al.*, 2014). These units are mainly oxidized by the action of peroxidases and laccases. Subsequently, the lignin phenoxyl radicals react to form lignin (A. Silva *et al.*, 2019a; Veronico *et al.*, 2018; Weiss *et al.*, 2020).

In this context, in the plant biomass, lignin (whose content depends on plant species and tissues) is associated with cellulose and hemicellulose and prevents biological degradation of these materials, as well as providing mechanical support for plant tissues.

Therefore, lignin confers strength and rigidity to the cellulose fiber's assembly (Gao *et al.*, 2019). After cellulose, lignin is the second most abundant organic compound in plants, representing approximately 30% of the organic carbon in the biosphere (Kamdee *et al.*, 2014). From a functional point of view, lignin imparts strength to cell walls, facilitates water transport, and prevents degradation of wall polysaccharides, thereby acting as a major defense line against pathogens, insects, and other herbivores (Tronchet *et al.*, 2010).

However, the genetic manipulation of the enzymatic routes, e.g., the PAL enzyme production, may favor the optimization of the separation of lignin from the cellulose pulp. This causes a reduction in the cost and pollution during the lignocellulosic processes, once the lignification is controlled by many enzymes including PAL (Hamedan *et al.*, 2019; Liu *et al.*, 2019; Toscano *et al.*, 2018). Therefore, by reducing the PAL activity, it is possible to minimize the lignin content resulting in weak stem physical strength (Hussain *et al.*, 2019).

This enzyme is mainly responsible for the biosynthesis of many activity compounds. Previous studies showed that these classes of secondary metabolites are among the most potent biologically active compounds found in *Piper* and *Peperomia* species, mainly species of the Piperaceae (Alves *et al.*, 2019; Kato and Furlan, 2007). Species of this family present the following activities: antioxidant (Regasini *et al.*, 2008; J. Silva *et al.*, 2011; N. Silva *et al.*, 2019b; Yamaguchi *et al.*, 2006), anxiolytic, antiplatelet (Sant'Ana *et al.*, 2020), antitumoral (Cortez *et al.*, 2017; H. Silva *et al.*, 2018), cytotoxic (Ferreira *et al.*, 2014; Freitas *et al.*, 2014; Maleck *et al.*, 2014), trypanocidal (Batista Junior *et al.*, 2008; Felipe *et al.*, 2008; García-Huertas *et al.*, 2018; Martins *et al.*, 2003; Mota *et al.*, 2009; Regasini *et al.*, 2009), hypertension (Durant-Archibold *et al.*, 2018), leishmanicidal (Araújo-Vilges *et al.*, 2017; Macêdo *et al.*, 2020; Neves *et al.*, 2019; Oliveira *et al.*, 2012; M. Silva *et al.*, 2021), insecticidal, antifungal, bactericidal, acaricidal, molluscicidal (Corral *et al.*, 2018; Danelutte *et al.*, 2003; Ferreira *et al.*, 2014; Lago *et al.*, 2004; 2007; Marques *et al.*, 2010; Miranda *et al.*, 2003; Navickiene *et al.*, 2000; 2003; Ramos *et al.*, 2020; Reigada *et al.*, 2007; Santos *et al.*, 2013; R. Silva *et al.*, 2002), anti-inflammatory (Arunachalam *et al.*, 2020), larvicidal (Mgbeahuruike *et al.*, 2017; Pereira Filho *et al.*, 2021; Pinheiro *et al.*, 2011; N. Silva *et al.*,

2019b), antiherbivore (Jeffrey *et al.*, 2014), and antimalarial (Campelo *et al.*, 2018; Moraes *et al.*, 2013; H. Silva *et al.*, 2018). Additionally, studies on the applications of the PAL enzyme have reported its use to treat diseases, such as phenylketonuria (Burton *et al.*, 2020; Hartnett *et al.*, 2013; Levy *et al.*, 2018). This disease is a genetic mutation that inactivates the phenylalanine-4-hydroxylase (Burton *et al.*, 2020; Levy *et al.*, 2018; Sarkissian *et al.*, 2011; Vogel *et al.*, 2013), resulting in augmented levels of *L*-phenylalanine in the bloodstream by the inability to metabolize *L*-phenylalanine. In excess, phenylalanine itself shows a neurotoxic effect. The lack of treatment at birth leads to severe and irreversible mental retardation (Donlon *et al.*, 2004). Therefore, PAL has gained considerable significance in several clinical and industrial applications in the past three decades. In the clinical field, physicians have used PAL to determine the serum level of *L*-phenylalanine, monitoring patients with phenylketonuria (Burton *et al.*, 2020; Watanabe *et al.*, 1992) and then to prepare low phenylalanine diets. Enzyme substitution therapy with a recombinant form of PAL successfully converts the excess *L*-phenylalanine into harmless metabolites, *trans*-cinnamic acid, and ammonia, which can be excreted in the urine (Rocha *et al.*, 2021).

A major industrial application of PAL concerns the production of *L*-phenylalanine from *trans*-cinnamic acid by reversing the physiological reaction (Burton *et al.*, 2020; Hamilton *et al.*, 1985). The increasing demand for *L*-phenylalanine as a precursor of aspartame, a non-calorific sweetener (*L*-phenylalanyl-*L*-aspartyl methyl ester), has resulted in an industrial enzymatic process based on *Rhodotorula* cells immobilized in vermiculite, developed by Genex Corporation in the UK (Choudhary and Lee, 2018; Finkelman and Yang, 1985).

Herein, the results of the expression of PAL in leaves of five Piperaceae species are reported. The results provide insights into the PAL catalytic activities in these species, which are rich sources of the bioactive phenylpropanoid derivatives and open new opportunities to enhance the production of such class of metabolites. Furthermore, this study also provides relevant results about the activity effect on its concentration, which represents new opportunities for the industrial and agricultural applications, especially favored by its thermal stability.

2. Experimental

2.1 Plant material

Leaves of *Piper aduncum* L. and *Peperomia obtusifolia* (L.) A. Dietr. were collected at the Institute of Chemistry – UNESP, Araraquara–SP, Brazil (-21.806602382914665, -48.19284372352492). These specimens were identified by Dr. I. Cordeiro (Institute of Botany, SP). The voucher specimens (Cordeiro-PA0 and Kato-070) were deposited in the Herbarium at the Institute of Biosciences – USP, São Paulo–SP, Brazil.

Leaves of *Piper tuberculatum* Jacq. and *Piper crassinervium* Kunth were collected at the Institute of Chemistry - UNESP, Araraquara–SP, Brazil (-21.806602382914665, -48.19284372352492), and identified by Dr. G. E. D. Paredes (Universidad Nacional Pedro Ruiz Gallo, Peru). The voucher specimens (Kato-163 and Kato-0084) were deposited in the Herbarium at the Institute of Botany, São Paulo–SP, Brazil. Leaves of *Peperomia blanda* (Jacq.) were collected at Reserva da Ripasa, Ibaté–SP, Brazil (-22.237934727962543, -47.81789620915089) and identified by Dr. Elsie Franklin Guimarães (JBRJ). The voucher specimen (Kato-547) was deposited in the Herbarium at the Institute of Biosciences, USP, São Paulo–SP, Brazil.

2.2 Reagents and standards

Methanol (HPLC-grade) was purchased from Mallinckrodt (Baker, Xalostoc, Mexico); ascorbic acid, ethylenediamine tetraacetic acid (EDTA), sucrose, polyvinylpyrrolidone (PVPP), dithiothreitol (DTT), *L*-phenylalanine, cinnamic acid, boric acid, sodium borate, hydrochloric acid (HCl), and ammonium sulfate were acquired from Sigma-Aldrich (St. Louis, MO, USA). Nanopure water (> 18 MΩ cm) was produced using a Millipore (Bedford, MA, USA) purifier.

2.3 Enzyme Extraction

Fresh leaves of *Piper aduncum*, *P. tuberculatum*, *P. crassinervium*, as well *Peperomia blanda* and *P. obtusifolia* (25 g) were ground separately using liquid nitrogen. Then, 100 mL of borate buffer 0.1 M (pH 8.8) containing PVPP (10% w/w), sucrose (0.25 M), ascorbic acid (40 mM), EDTA (1 mM), and DTT (5 mM) were added. The suspensions were stirred for 15 min at 0 °C, filtered through cheesecloth, and centrifuged for 20 min at 4 °C and 11,950 g.

2.4 Enzymatic assay

The enzymatic assays were carried out by adding 250 μL of borate buffer 0.1 M, 125 μL of enzyme solution (0.2 mg/mL), and 150 μL of *L*-phenylalanine (10 mM) to Eppendorf tubes. The times (1, 6, 13, 20, and 25 h), temperatures (28, 35, 45, 55, and 62 °C) and pH values (7.8, 8.2, 8.8, 9.4, and 9.8) were modified as suggested by the statistical design to optimize the process (Tab. 1). All the reactions were performed under agitation and terminated by adding 25 μL of HCl (6 M), in duplicate assays (Toscano *et al.*, 2018). The solutions were stirred, neutralized, and then centrifugated at 7,000 g for 1 min, and the supernatants were analyzed by HPLC.

Table 1. Experimental conditions used to optimize the activity of the PAL (coded and non-coded variables).

Coded variables			Non-coded variables		
Time (min)	pH	T (°C)	Time (min)	pH	T (°C)
+1	-1	+1	20	8.20	55
+1	+1	+1	20	9.40	55
0	0	0	13	8.80	45
0	+√3	0	13	9.80	45
0	0	+√3	13	8.80	62
-√3	0	0	1	8.80	45
0	-√3	0	13	7.80	45
+1	-1	-1	20	8.20	35
-1	+1	-1	6	9.40	35
0	0	-√3	13	8.80	28
-1	-1	-1	6	8.20	35
-1	-1	+1	6	8.20	55
+1	+1	-1	20	9.40	35
-1	+1	+1	6	9.40	55
+√3	0	0	25	8.80	45
0	0	0	13	8.80	45

HPLC analyses were conducted on a Shimadzu pump model LC-6AD, with an SPD-M20A diode array ultraviolet detector (HPLC-DAD), SIL-10AF automatic injector, and CBM-20A controller. Separation was achieved on a Phenomenex C₁₈ reverse-phase column (25 cm × 4.6 mm, 5 μm) in the isocratic mode, using MeOH/H₂O (1:1, with 0.1% HOAc) at a flow of 1.0 mL min⁻¹ as the mobile phase. The formation of *trans*-cinnamic acid was monitored at a wavelength of 275 nm.

A standard RSM (Response Surface Methodology) design, known as CCRD (Central Composite Rotational Design), was used to model and analyze the data. The Analysis of Variance (ANOVA) using the Statistic Program 12.0 (StatSoft Inc., 2014, Oklahoma, USA) was

used to process the results. The significance of the main factors and their interactions were assessed by the F-test method with a confidence level of 95%. The response surface methodology and a mathematical–statistical tool were employed to model the *L*-phenylalanine conversion to *trans*-cinnamic acid using the temperature, pH, and reaction time as variables. The Response desirability profiling option, which is given by the geometric mean of all individual desirability (Eq. 1), was applied to determine the optimum reaction condition for the PAL enzyme.

$$D = \sqrt[m]{d_1 d_2 \dots d_m} \quad (1)$$

where, d describes the individual desirability and m the number of parameters analyzed.

The results of each CCRD were analyzed with the aid of the Statistic Program Software. The data was fitted to a second-order polynomial equation (Eq. 2).

$$Y = \beta_0 + \sum \beta_j X_j + \sum \beta_{ij} X_j^2 + \sum \beta_{jk} X_j X_k \quad (2)$$

2.5 Enzyme pre-purification

After determining the optimal reaction condition, new enzymatic extracts were obtained from the same plant species using the experimental procedures described above. In this case, 100 g of plant material and 400 mL of buffer were used. The protein extracts containing PAL were fractionated by ammonium sulfate saturation at 0–25, 25–55, and 55–80%. Each addition of ammonium sulfate was followed by agitation for 30 min at 4 °C and then centrifugated at 16,300 g for 30 min. The pellets were stored at -80 °C until use. The pellets were re-suspended in 3 mL of 0.1 mol L⁻¹ borate buffer and submitted to enzymatic assays. The amount of added ammonium sulfate to achieve the desired saturation was determined as described (Englard and Seifter, 1990). Protein was determined by the modified Bradford method, using bovine serum albumin (BSA) as standard.

2.6 Determination of lignin content

Leaves of the target plant species were dried at (70 ± 3) °C for 72 h, knife-ground in order to pass through a 1-mm sieve and be analyzed. The lignin

contents were determined using the TAPPI test method (Begović *et al.*, 2018; TAPPI, 1979).

3. Results and Discussions

The enzyme phenylalanine ammonia lyase (PAL) is the initial enzyme involved in the *trans*-deamination of *L*-phenylalanine leading to the formation of *trans*-cinnamic acid. PAL is a regulatory enzyme involved in the phenylpropanoid pathway of several plants and provides insights to control the production of these secondary metabolites (Akbarian *et al.*, 2021; Kawatra *et al.*, 2020).

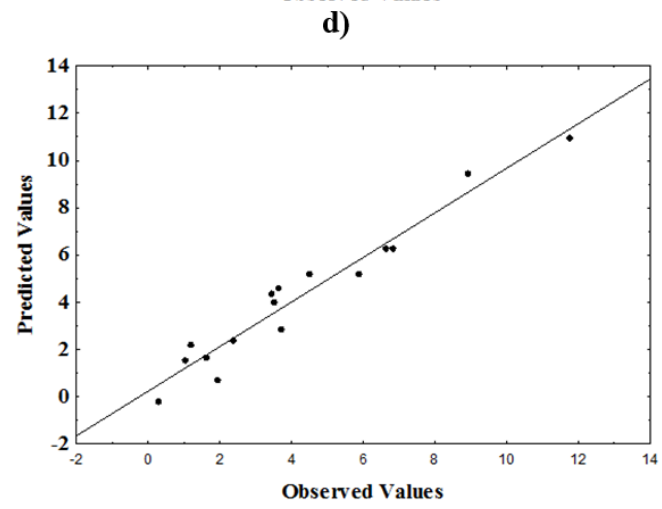
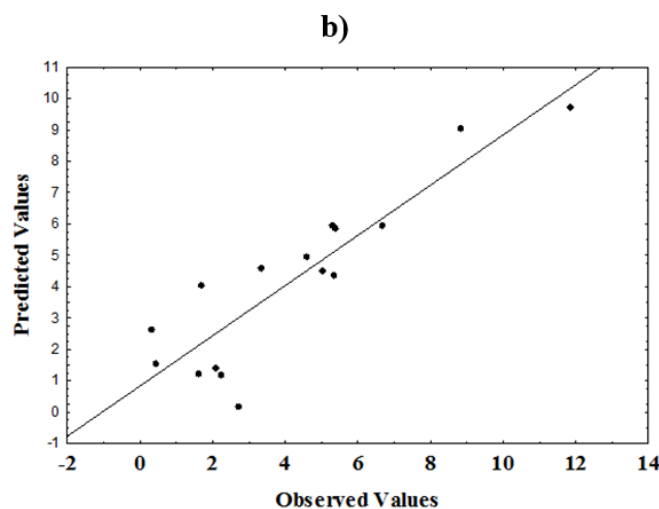
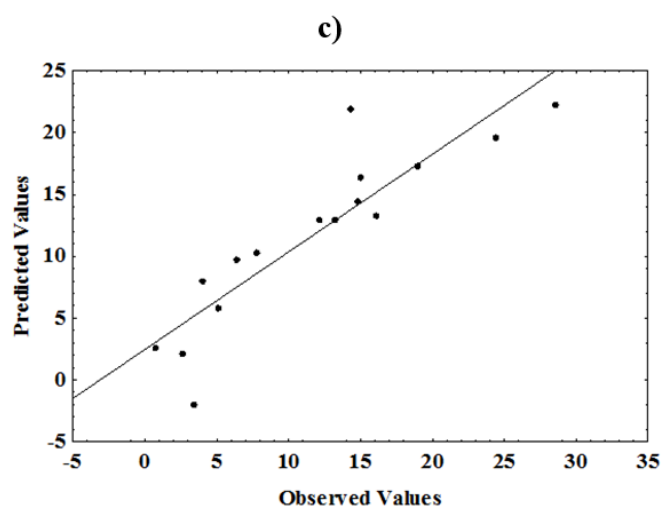
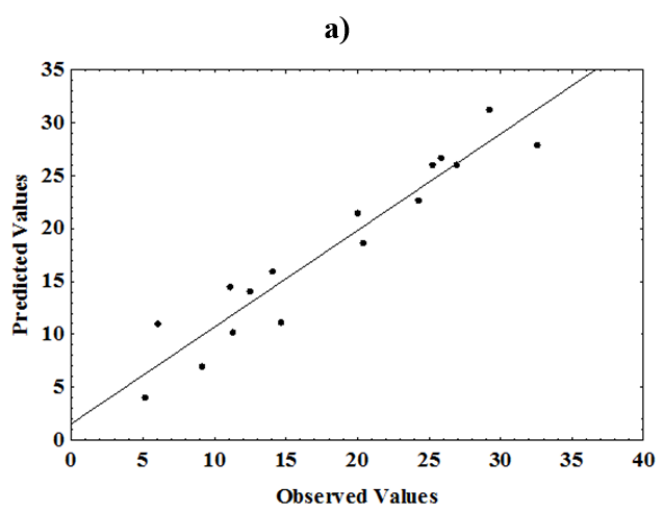
The first step of this work consisted in optimizing the reaction conditions for the measurement of the PAL activity. Since several Piperaceae species belonging to *Piper* (*P. aduncum*, *P. tuberculatum*, *P. crassinervium*) and *Peperomia* (*P. blanda* and *P. obtusifolia*) species have been characterized to produce cinnamic acid derivatives, they were considered as potential sources of the PAL enzyme. *Peperomia obtusifolia*, which shows chromanes as the major metabolites, was selected as no model plant for PAL.

Another important physiological aspect of these plant species is their relatively easy propagation and fast growth. Therefore, crude enzymatic extracts from the five Piperaceae species were obtained, and the relative activities of PAL determined, monitoring the conversion of phenylalanine into cinnamic acid by HPLC. Then, the reaction conditions were optimized regarding temperature, pH, and reaction time for each *Piper* and *Peperomia* species (Tab. 1 and 2). The results showed that the increase in reaction time also increases the *trans*-cinnamic acid conversion. The same occurred regarding pH and temperature, with a great reaction observed at around 50 °C and pH 8.8. Therefore, in order to investigate the influence of all process variables and determine the optimal PAL activity, a statistical study was performed.

The Statistic 12.0 Program helped to analyze the data and to optimize the operation conditions for the PAL enzyme. The data were evaluated using the linear and quadratic terms model. The relationship between the proposed model and the theoretical data was outlined and the results are shown in Fig. 2. The results evidenced the normality of the residues, since all the points were close to the expected values.

Table 2. Reaction conditions for PAL and conversion % of *L*-phenylalanine into cinnamic acid for each Piperaceae species.

Time (min)	pH	T (°C)	<i>P. aduncum</i>	<i>P. tuberculatum</i>	<i>P. crassinervium</i>	<i>P. blanda</i>	<i>P. obtusifolia</i>
			(a)	(b)	(c)	(d)	(e)
13	8.80	28	14.06	2.23	6.38	1.19	0.77
6	8.20	35	9.14	1.62	3.46	1.05	0.53
20	8.20	35	12.46	4.57	7.74	3.70	3.49
6	9.40	35	14.65	2.06	5.07	1.96	0.41
20	9.40	35	25.81	1.68	18.96	6.64	3.88
13	7.80	45	5.18	0.42	2.58	0.28	0.47
1	8.80	45	6.08	0.32	0.79	2.39	0.01
13	8.80	45	26.93	6.66	13.20	5.90	4.36
13	8.80	45	25.25	5.28	12.16	4.51	3.48
25	8.80	45	32.58	11.85	24.43	8.93	5.72
13	9.80	45	20.02	5.32	16.08	3.62	3.34
6	8.20	55	11.25	2.71	4.04	1.64	1.20
20	8.20	55	11.11	5.36	14.96	3.43	3.71
20	9.40	55	29.17	8.81	14.27	11.74	6.07
6	9.40	55	20.39	5.01	14.80	3.50	1.83
13	8.80	62	24.29	3.35	28.59	6.82	4.69



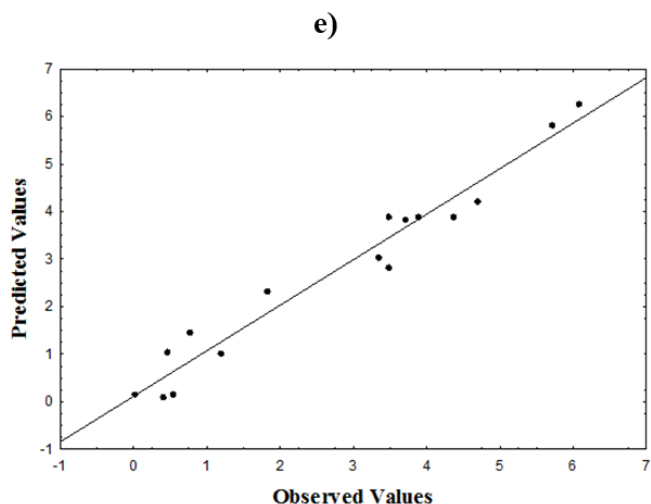


Figure 2. A comparative plot between the experimental and the predicted yield as a function of time (h), temperature (°C), and pH for the enzymatic extracts from (a) *P. aduncum*, (b) *P. tuberculatum*, (c) *P. crassinervium*, (d) *Peperomia blanda*, and (e) *P. obtusifolia*.

After adjusting the model, the data were analyzed using the desirability function. After 20 h of reaction, the conversion of *L*-phenylalanine into *trans*-cinnamic acid did not increase significantly, and it proved to be the best reaction time. The analysis of its thermal resistance showed a maximum performance after 40 °C, with an even larger increase above 49 °C. The optimal pH for the reaction was 9.4 (Fig. 3).

The plot contour surface obtained for the enzymatic extracts illustrates the results (Fig. 4). Basic pH values (9.0 to 9.8) afforded the best results of *L*-phenylalanine conversion into *trans*-cinnamic acid. The thermostability of the enzyme was also evident: optimal reaction occurred at temperatures above 40 °C. The conversion persisted even after 20 h despite the low rate. The previously described statistical procedure provided the Equations, which showed the r^2 value at a level of confidence of 95% for *P. aduncum* (A), *P. tuberculatum* (B), *P. crassinervium* (C), *P. blanda* (D), and *P. obtusifolia* (E) (Tab. 3).

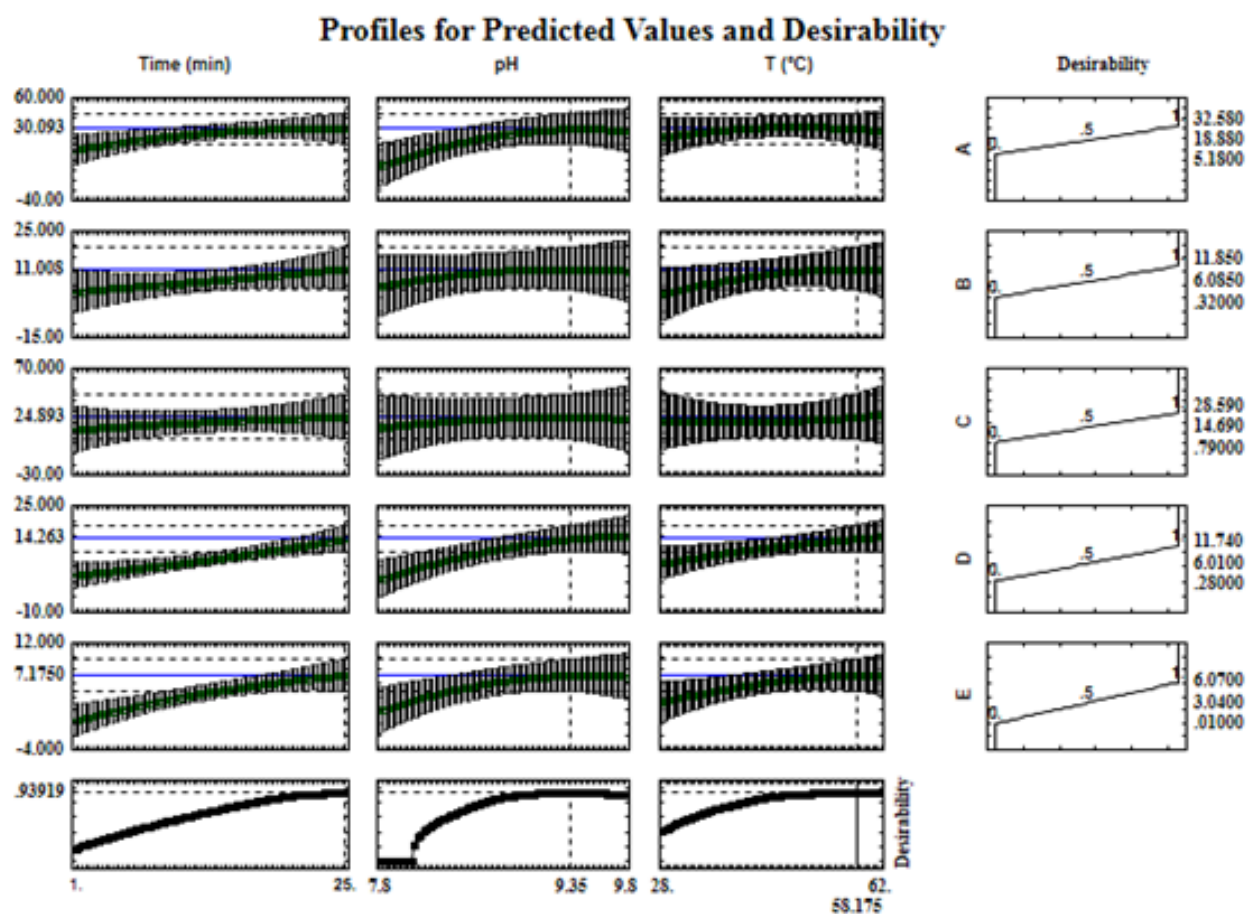


Figure 3. PAL activity from Piperaceae species taking independent and dependent variables into account: (A) *P. aduncum*, (B) *P. tuberculatum*, (C) *P. crassinervium*, (D) *Peperomia blanda*, and (E) *P. obtusifolia*.

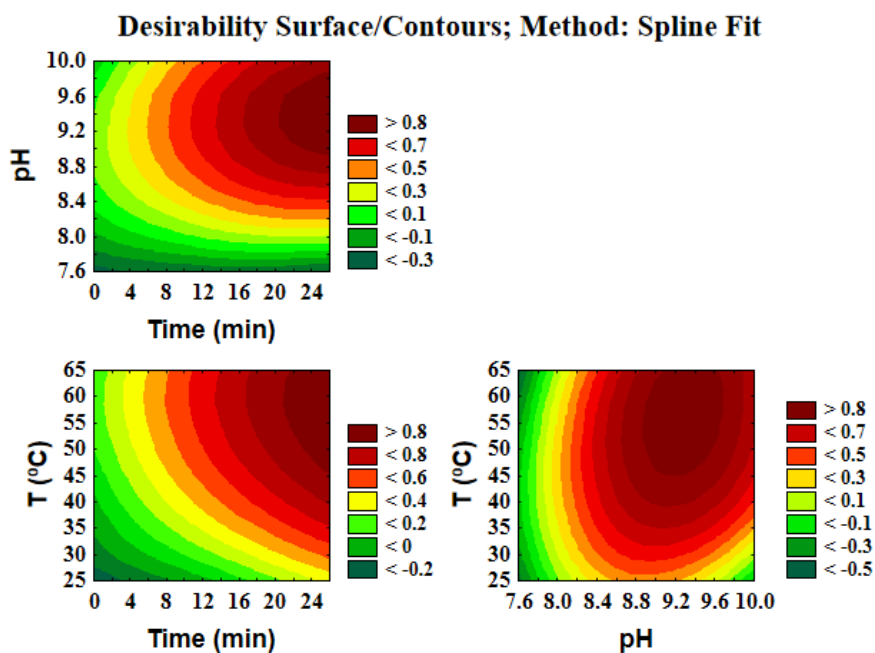
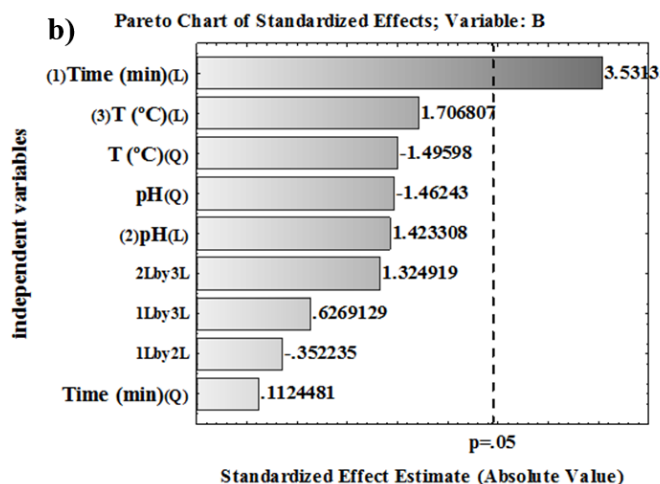
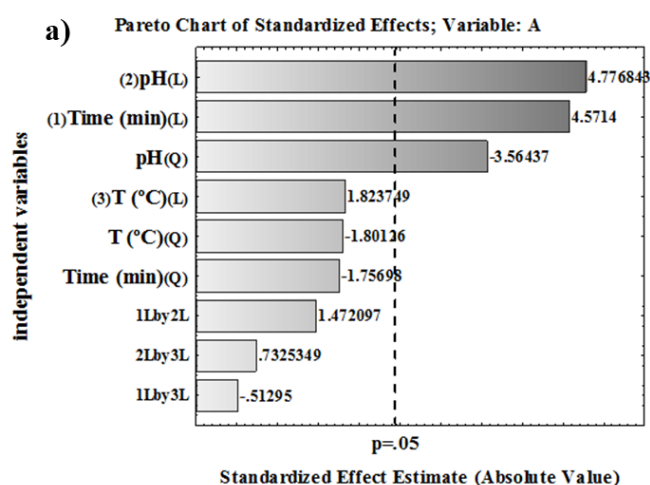


Figure 4. Contour surface graphs for the activity of the PAL enzyme using Response desirability surface/Contours.

Table 3. Coefficients of the Fitted Equations for the Construction of the Surface Response Plots.

Polynomial equation: $a_0 + a_1X_1 + a_2X_2 + a_3X_3 + a_4X_1X_2 + a_5X_1X_3 + a_6X_2X_3 + a_7X_1^2 + a_8X_2^2 + a_9X_3^2$											
		Linear parameters						Quadratic Parameters			
	R ²	a ₀	a ₁	a ₂	a ₃	a ₄	a ₅	a ₆	a ₇	a ₈	a ₉
a	0.91284	-1038.26	-2.02	229.43	0.92	0.50	-0.01	0.17	-0.05	-13.35	-0.02
b	0.80069	-202.386	0.514	46.986	-0.539	-0.065*t	0.007	0.171	0.002	-2.978	-0.011
c	0.78952	-476.660	2.136	99.124	0.092	-0.055	-0.014	-0.058	-0.012	-5.127	0.011
d	0.94398	-176.934	-2.275	45.454	-0.814	0.252	0.05	0.132	0.005	-2.969	-0.003
e	0.95724	-134.596	-0.210	30.532	-0.097	0.067	0.001	0.057	-0.006	-1.873	-0.004

Besides checking the fit of the model and optimizing the operation conditions, the variables that most influenced the PAL activity of the different plant extracts were investigated (Fig. 5).



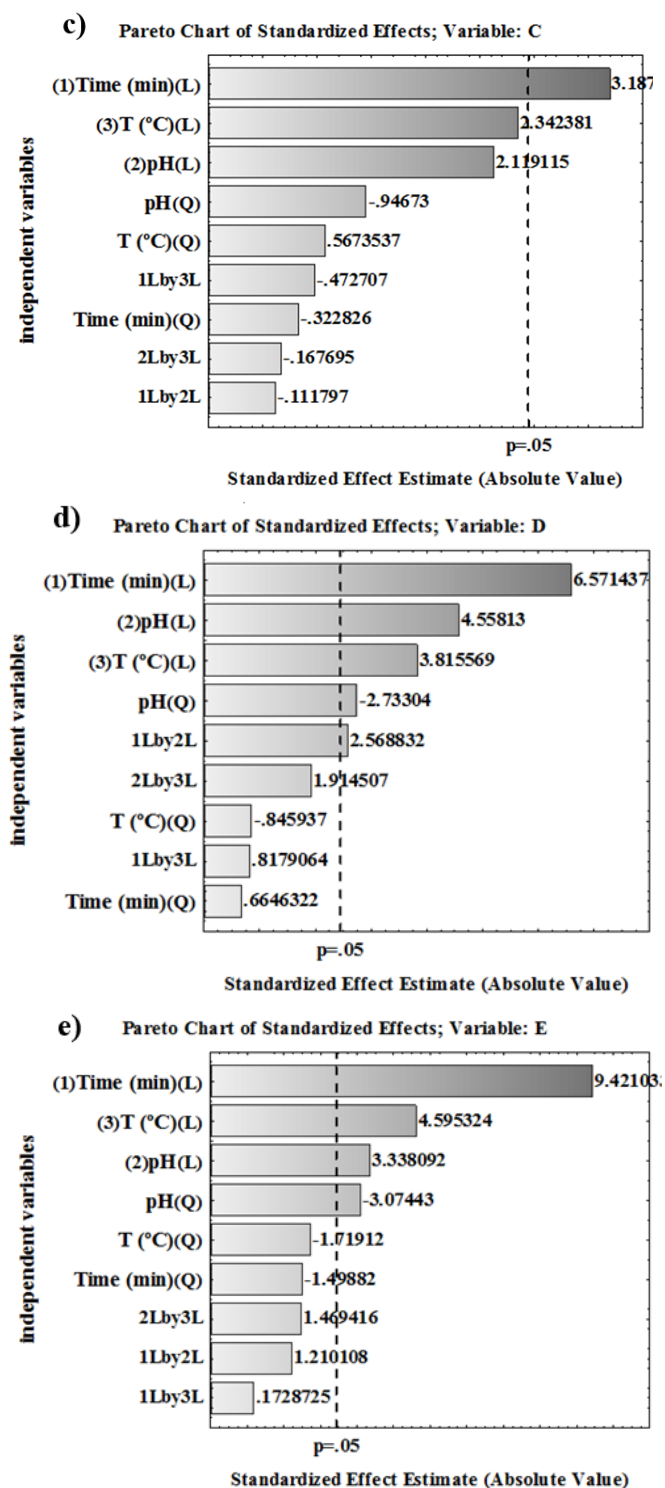


Figure 5. Analysis of the variables that most affect the activity of the PAL enzyme.

The variables that most influenced the process were pH and time. Regarding temperature, PAL showed the optimum activity at 58 °C in all plant species, showing thermal stability. These results corroborate their possible application in biotechnological processes.

Therefore, after determining the PAL optimum conditions, an ammonium sulfate precipitation was performed, and fractions of 0-25%, 25-55%, and 55-80 were obtained. The protein content of the enzymatic extracts obtained from leaves was determined and revealed that higher protein concentrations with 25-55% saturation were found in *P. aduncum*, *P. tuberculatum*, and *P. blanda*. However, *P. crassinervium* and *P. obtusifolia* displayed a higher protein content in the fraction with 55-80% saturation (Fig. 6a).

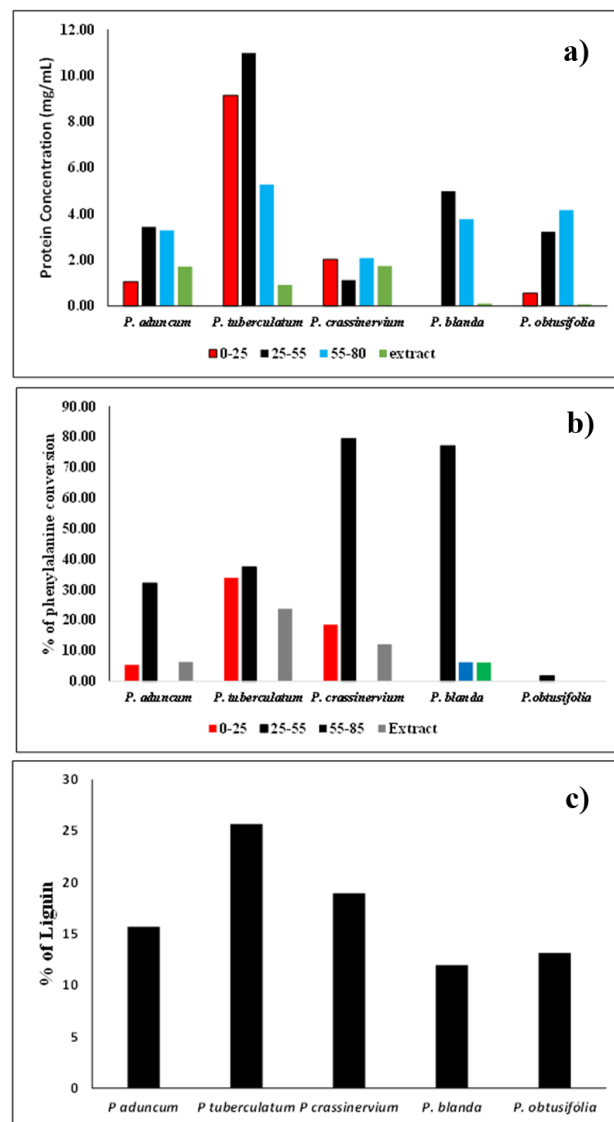


Figure 6. (a) Protein content in each of the fractions obtained after saline precipitation, (b) comparison of the degree of phenylalanine conversion to cinnamic acid, and (c) percentage of lignin.

By analyzing the obtained fraction with 25-55% of saturation with ammonium sulfate, it was verified that the specific activity in the *P. aduncum* species increased

by approximately 133% (Tab. 4, Fig. 6b). Regarding *P. tuberculatum*, the specific activity decreased by 87.5% after the saline precipitation step. In *Peperomia blanda*, it was possible to verify a reduction in specific

activity of 72.6%, also observed in *P. tuberculatum*. However, in *P. crassinervium*, the specific activity increased by more than 900% (Tab. 4), demonstrating to be an excellent source of PAL.

Table 4. Specific activity of PAL observed in the extracts and fractions after precipitation.

	<i>P. aduncum</i>	<i>P. tuberculatum</i>	<i>P. crassinervium</i>	<i>P. blanda</i>	<i>P. obtusifolia</i>
	(a)	(b)	(c)	(d)	(e)
Extract	60	400	100	840	0
0-25%	80	60	130	0	0
25-55%	140	50	1057	230	9
55-85%	0	0	0	20	0

Considering the last species studied, *P. obtusifolia*, it was possible to observe a significant increase in the specific activity of the PAL enzyme. However, as the protein concentration was too low (Fig. 6b), the use of the species during the attainment of the PAL enzyme in a large scale was not feasible (Tab. 4).

These fractions served as the source of the PAL enzyme in further experimental reactions. HPLC analyses evidenced that most of the desired enzyme, PAL, was concentrated in the fraction with 25-55% saturation, attested to the efficiency of the PAL concentration process. The degree of *L*-phenylalanine conversion to *trans*-cinnamic acid increased considerably in all cases, which facilitated the subsequent purification process (Fig. 6b).

Starting from the same mass of fresh leaves, the enzymatic extracts from *P. crassinervium*, *P. tuberculatum*, and *P. blanda* precipitated with 25-55% saturation of ammonium sulfate afforded the highest specific activities of PAL. However, the major secondary metabolites found in *P. obtusifolia* are chromanes. They differ from chromenes of *P. aduncum*, originated from the shikimate pathway and which require the *p*-hydroxybenzoic acid as a precursor. The chromanes are structurally related to the orsellinic acid, which is produced by the polyketide pathway. Therefore, these two distinct biosynthetic routes match with the lower PAL activity for *P. obtusifolia*.

In order to better characterize the Piperaceae species with a low level of phenylpropanoids pathway, experiments were conducted to examine the original lignin content in each species using the TAPPI test method (Fig. 6c). Data analyses of lignin contents demonstrated that the more rigid the leaves, the higher the lignin content (see data for *P. aduncum*, *P. tuberculatum*, and *P. crassinervium*). A small amount of lignin accumulated in the *P. blanda* species suggested that the biosynthetic pathway operated to produce secondary metabolites such as lignoids.

4. Conclusions

This work enabled the optimization of the reaction conditions to convert *L*-phenylalanine to *trans*-cinnamic acid catalyzed by the PAL enzyme extracted from five Piperaceae species (*Piper aduncum*, *P. tuberculatum*, *P. crassinervium*, *Peperomia blanda* and *P. obtusifolia*). The 76nzyme exhibited thermostability, and the best reaction condition was pH 9.3 at a temperature of 58 °C for 25 h. It is important to mention that reaction times longer than 20 h do not give rise to significant improvement in the conversion, which did not justify longer reaction times. Pre-purification of the enzyme by ammonium sulfate precipitation showed that the ideal saturation was 25-55% — it increased the enzyme's concentration and effectively improved phenylalanine's conversion to cinnamic acid. Additionally, the thermal stability of the PAL may enable the use of the five studied Piperaceae species in specific green industrial processes.

Authors' contribution

Conceptualization: Morandim-Giannetti, A. A.; Felipe, L. G.; Santos, V. A. F. F. M.; Kato, M. J.; Furlan, M.

Data curation: Morandim-Giannetti, A. A.; Felipe, L. G.; Santos, V. A. F. F. M.

Formal Analysis: Morandim-Giannetti, A. A.; Felipe, L. G.; Santos, V. A. F. F. M.; Kato, M. J.; Furlan, M.

Funding acquisition: Kato, M. J.; Furlan, M.

Investigation: Morandim-Giannetti, A. A.; Felipe, L. G.; Santos, V. A. F. F. M.; Kato, M. J.; Furlan, M.

Methodology: Morandim-Giannetti, A. A.; Felipe, L. G.; Santos, V. A. F. F. M.

Project administration: Morandim-Giannetti, A. A.; Felipe, L. G.; Furlan, M.

Resources: Morandim-Giannetti, A. A.; Felipe, L. G.; Santos, V. A. F. F. M.; Kato, M. J.; Furlan, M.

Software: Not applicable.

Supervision: Morandim-Giannetti, A. A.; Kato, M. J.; Furlan, M.

Validation: Morandim-Giannetti, A. A.

Visualization: Morandim-Giannetti, A. A.; Felipe, L. G.; Santos, V. A. F. F. M.; Kato, M. J.; Furlan, M.

Writing – original draft: Morandim-Giannetti, A. A.; Felipe, L. G.; Santos, V. A. F. F. M.; Kato, M. J.; Furlan, M.

Writing – review & editing: Morandim-Giannetti, A. A.; Furlan, M.

Data availability statement

All data generated or analyzed during this study are included in this published article.

Funding

São Paulo Research Foundation (FAPESP). Grant No: 2013/07600-3; 2014/50926-0.

Conselho Nacional de Desenvolvimento Científico e Tecnológico (CNPq). Grant. No: 2014/465637-0.

Acknowledgments

MF and MJK are grateful to the National Council for Scientific and Technological Development (CNPq) for their research fellowships.

References

Alves, N. S. F.; Setzer, W. N.; Silva, J. K. R. The chemistry and biological activities of *Peperomia pellucida* (Piperaceae): A critical review. *J. Ethnopharmacol.* **2019**, *232*, 90–102. <https://doi.org/10.1016/j.jep.2018.12.021>

Akbarian, A.; Rahimmalek, M.; Sabzalian, M. R.; Hodaie, M. Sequencing and phylogenetic analysis of phenylalanine ammonia lyase (*pal*) and chalcone synthase (*chs*) genes in some Iranian endemic species of Apiaceae. *Gene Rep.* **2021**, *23*, 101147. <https://doi.org/10.1016/j.genrep.2021.101147>

Arunachalam, K.; Damazo, A. S.; Macho, A.; Lima, J. C. S.; Pavan, E.; Figueiredo, F. F.; Oliveira, D. M.; Cechinel-Filho, V.; Wagner, T. M.; Tabajara, D.; Martins, D. T. O. *Piper umbellatum* L. (Piperaceae): Phytochemical profiles of the hydroethanolic leaf extract and intestinal anti-inflammatory mechanisms on 2, 4, 6 trinitrobenzene sulfonic acid induced ulcerative colitis in rats. *J. Ethnopharmacol.* **2020**, *254*, 112707. <https://doi.org/10.1016/j.jep.2020.112707>

Araújo-Vilges, K. M.; Oliveira, S. V.; Couto, S. C. P.; Fokoue, H. H.; Romero, G. A. S.; Kato, M. J.; Romeiro, L. A. S.; Leite, J. R. S. A.; Kuckelhaus, S. A. S. Effect of piplartine

and cinnamides on *Leishmania amazonensis*, *Plasmodium falciparum* and on peritoneal cells of Swiss mice. *Pharm. Biol.* **2017**, *55* (1), 1601–1607. <https://doi.org/10.1080/13880209.2017.1313870>

Banu, J. R.; Kavitha, S.; Kannah, R. Y.; Devi, T. P.; Gunasekaran, M.; Kim, S.-H.; Kumar, G. A review on biopolymer production via lignin valorization. *Bioresour. Technol.* **2019**, *290*, 121790. <https://doi.org/10.1016/j.biortech.2019.121790>

Batista, A. N. L.; Batista Junior, J. M.; Zocolo, G. J.; Zanoni, M. V. B.; Kato, M. J.; López, S. N.; Furlan, M. Protein and metabolic profiles of *Peperomia obtusifolia* (Piperaceae). *Planta Med.* **2012**, *78* (11), PB3. <https://doi.org/10.1055/s-0032-1320332>

Batista, A. N. L.; Santos-Pinto, J. R. A. D.; Batista Junior, J. M.; Souza-Moreira, T. M.; Santoni, M. M.; Zanelli, C. F.; Kato, M. J.; López, S. N.; Furlan, M. The Combined Use of Proteomics and Transcriptomics Reveals a Complex Secondary Metabolite Network in *Peperomia obtusifolia*. *J. Nat. Prod.* **2017**, *80* (5), 1275–1286. <https://doi.org/10.1021/acs.jnatprod.6b00827>

Batista Junior, J. M.; Lopes, A. A.; Ambrosio, D. L.; Regasini, L. O.; Kato, M. J.; Bolzani, V. S.; Cicarelli, R. M. B.; Furlan, M. Natural chromenes and chromene derivatives as potential anti-trypanosomal agents. *Biol. Pharm. Bull.* **2008**, *31* (3), 538–540. <https://doi.org/10.1248/bpb.31.538>

Batista Junior, J. M.; López, S. N.; Mota, J. S.; Vanzolini, K. L.; Cass, Q. B.; Rinaldo, D.; Vilegas, W.; Bolzani, V. S.; Kato, M. J.; Furlan, M. Resolution and absolute configuration assignment of a natural racemic chromane from *Peperomia obtusifolia* (Piperaceae). *Chirality* **2009**, *21* (9), 799–801. <https://doi.org/10.1002/chir.20676>

Batista Junior, J. M.; Batista, A. N. L.; Rinaldo, D.; Vilegas, W.; Cass, Q. B.; Bolzani, V. S.; Kato, M. J.; López, S. N.; Furlan, M.; Nafie, L. A. Absolute configuration reassignment of two chromanes from *Peperomia obtusifolia* (Piperaceae) using VCD and DFT calculations. *Tetrahedron Asymmetry* **2010**, *21* (19), 2402–2407. <https://doi.org/10.1016/j.tetasy.2010.09.004>

Batista Junior, J. M.; Batista, A. N. L.; Kato, M. J.; Bolzani, V. S.; López, S. N.; Nafie, L. A.; Furlan, M. Further monoterpene chromane esters from *Peperomia obtusifolia*: VCD determination of the absolute configuration of a new diastereomeric mixture. *Tetrahedron Lett.* **2012**, *53* (45), 6051–6054. <https://doi.org/10.1016/j.tetlet.2012.08.113>

Begović, L.; Abičić, I.; Lalić, A.; Lepeduš, H.; Cesar, V.; Leļjak-Levanić, D. Lignin synthesis and accumulation in barley cultivars differing in their resistance to lodging. *Plant Physiol. Biochem.* **2018**, *133*, 142–148. <https://doi.org/10.1016/j.plaphy.2018.10.036>

- Burton, B. K.; Longo, N.; Vockley, J.; Grange, D. K.; Harding, C. O.; Decker, C.; Li, M.; Lau, K.; Rosen, O.; Larimore, K.; Thomas, J. Pegvaliase for the treatment of phenylketonuria: Results of the phase 2 dose-finding studies with long-term follow-up. *Mol. Genet. Metab.* **2020**, *130* (4), 239–246. <https://doi.org/10.1016/j.ymgme.2020.06.006>
- Campelo, Y.; Ombredane, A.; Vasconcelos, A. G.; Albuquerque, L.; Moreira, D. C.; Plácido, A.; Rocha, J.; Fokoue, H. H.; Yamaguchi, L.; Mafud, A.; Mascarenhas, Y. P.; Delerue-Matos, C.; Borges, T.; Joanitti, G. A.; Arcanjo, D. D. R.; Kato, M. J.; Kuckelhaus, S. A. S.; Silva, M. P. N.; Moraes, J.; Leite, J. R. S. Structure–Activity relationship of piplartine and synthetic analogues against *Schistosoma mansoni* and cytotoxicity to mammalian cells. *Int. J. Mol. Sci.* **2018**, *19* (6), 1802. <https://doi.org/10.3390/ijms19061802>
- Choudhary, A. K.; Lee, Y. Y. The debate over neurotransmitter interaction in aspartame usage. *J. Clin. Neurosci.* **2018**, *56*, 7–15. <https://doi.org/10.1016/j.jocn.2018.06.043>
- Corral, A. C. T.; Queiroz, M. N.; Andrade-Porto, S. M.; Morey, G. A. M.; Chaves, F. C. M.; Fernandes, V. L. A.; Ono, E. A.; Affonso, E. G. Control of *Hysterothylacium* sp. (Nematoda: Anisakidae) in juvenile pirarucu (*Arapaima gigas*) by the oral application of essential oil of *Piper aduncum*. *Aquaculture.* **2018**, *494*, 37–44. <https://doi.org/10.1016/j.aquaculture.2018.04.062>
- Cortez, A. P.; Menezes, E. G. P.; Benfica, P. L.; Santos, A. P.; Cleres, L. M.; Ribeiro, H. O.; Lima, E. M.; Kato, M. J.; Valadares, M. C. Grandisin induces apoptosis in leukemic K562 cells. *Braz. J. Pharm. Sci.* **2017**, *53* (1), e15210. <https://doi.org/10.1590/s2175-97902017000115210>
- Danelutte, A. P.; Lago, J. H. G.; Young, M. C. M.; Kato, M. J. Antifungal flavanones and prenylated hydroquinones from *Piper crassinervium* Kunth. *Phytochemistry.* **2003**, *64* (2), 555–559. [https://doi.org/10.1016/S0031-9422\(03\)00299-1](https://doi.org/10.1016/S0031-9422(03)00299-1)
- Dong, C.-J.; Cao, N.; Zhang, Z.-g.; Shang, Q.-m. Phenylalanine ammonia-lyase gene families in cucurbit species: Structure, evolution, and expression. *J. Integr. Agric.* **2016**, *15* (6), 1239–1255. [https://doi.org/10.1016/S2095-3119\(16\)61329-1](https://doi.org/10.1016/S2095-3119(16)61329-1)
- Donlon, J.; Levy, H.; Scriver, C. R. Hyperphenylalaninemia: phenylalanine hydroxylase deficiency. In *The metabolic and molecular bases of inherited disease*. Scriver, C. R.; Beaudet, A. R.; Sly, W.; Valle, D. (Eds.). McGraw Hill, 2004; 1821–1838.
- Durant-Archibold, A. A.; Santana, A. I.; Gupta, M. P. Ethnomedical uses and pharmacological activities of most prevalent species of genus *Piper* in Panama: A review. *J. Ethnopharmacol.* **2018**, *217*, 63–82. <https://doi.org/10.1016/j.jep.2018.02.008>
- Englard, S.; Seiffter, S. In *Methods in Enzymology*. Guide to Protein Purification. Academic Press, 1990; 285–300. [https://doi.org/10.1016/0076-6879\(90\)82024-V](https://doi.org/10.1016/0076-6879(90)82024-V)
- El Babili, F.; Rey-Rigaud, G.; Rozon, H.; Halova-Lajoie, B. State of knowledge: Histolocalisation in phytochemical study of medicinal plants. *Fitoterapia.* **2021**, *150*, 104862. <https://doi.org/10.1016/j.fitote.2021.104862>
- Felippe, L. G.; Baldoqui, D. C.; Kato, M. J.; Bolzani, V. S.; Guimarães, E. F.; Cicarelli, R. M. B.; Furlan, M. Trypanocidal tetrahydrofuran lignans from *Peperomia blanda*. *Phytochemistry.* **2008**, *69* (2), 445–450. <https://doi.org/10.1016/j.phytochem.2007.08.012>
- Felippe, L. G.; Batista Junior, J. M.; Baldoqui, D. C.; Nascimento, I. R.; Kato, M. J.; He, Y.; Nafie, L. A.; Furlan, M. (2012). VCD to determine absolute configuration of natural product molecules: secolignans from *Peperomia blanda*. *Org. Biomol. Chem.* **2012** *10* (21), 4208–4214. <https://doi.org/10.1039/c2ob25109d>
- Ferreira, E. A.; Reigada, J. B.; Correia, M. V.; Young, M. C. M.; Guimarães, E. F.; Franchi Junior, G. C.; Nowill, A. E.; Lago, J. H. G.; Yamaguchi, L. F.; Kato, M. J. Antifungal and cytotoxic 2-acylcyclohexane-1, 3-diones from *Peperomia alata* and *P. trineura*. *J. Nat. Prod.* **2014**, *77* (6), 1377–1382. <https://doi.org/10.1021/np500130x>
- Finkelman M. A. J.; Yang, H. H. Production of phenylalanine ammonia lyase by fermentation. *Genex Corporation, European Pat.* **1985**, *140*, 714.
- Freitas, G. C.; Batista Junior, J. M.; Franchi Junior, G. C.; Nowill, A. E.; Yamaguchi, L. F.; Vilcachagua, J. D.; Favaro, D. C.; Furlan, M.; Guimarães, E. F.; Jeffrey, C. S.; Kato, M. J. Cytotoxic non-aromatic B-ring flavanones from *Piper carniconnectivum* C. DC. *Phytochemistry.* **2014**, *97*, 81–87. <https://doi.org/10.1016/j.phytochem.2013.10.012>
- Gao, Z.; Sun, W.; Wang, J.; Zhao, C.; Zuo, K. GhbHLH18 negatively regulates fiber strength and length by enhancing lignin biosynthesis in cotton fibers. *Plant Sci.* **2019**, *286*, 7–16. <https://doi.org/10.1016/j.plantsci.2019.05.020>
- García-Huertas, P.; Olmo, F.; Sánchez-Moreno, M.; Dominguez, J.; Chahboun, R.; Triana-Chávez, O. Activity in vitro and in vivo against *Trypanosoma cruzi* of a furofuran lignan isolated from *Piper jericense*. *Exp. Parasitol.* **2018**, *189*, 34–42. <https://doi.org/10.1016/j.exppara.2018.04.009>
- Gutiérrez-Quequezana, L.; Vuorinen, A. L.; Kallio, H.; Yang, B. Impact of cultivar, growth temperature and developmental stage on phenolic compounds and ascorbic acid in purple and yellow potato tubers. *Food Chem.* **2020**, *326*, 126966. <https://doi.org/10.1016/j.foodchem.2020.126966>
- Hamedan, H. J.; Sohani, M. M.; Aalami, A.; Nazarideljou, M. J. Genetic engineering of lignin biosynthesis pathway

- improved stem bending disorder in cut gerbera (*Gerbera jamesonii*) flowers. *Sci. Hortic.* **2019**, *245*, 274–279. <https://doi.org/10.1016/j.scienta.2018.10.013>
- Hamilton, B. K.; Hsiao, H.-Y.; Swann, W.; Anderson, D. M.; Delente, J. J. Manufacture of L-amino acids with bioreactors. *Trends Biotechnol.* **1985**, *3* (3), 64–68. [https://doi.org/10.1016/0167-7799\(85\)90079-4](https://doi.org/10.1016/0167-7799(85)90079-4)
- Hartnett, C.; Salvarinova-Zivkovic, R.; Yap-Todos, E.; Cheng, B.; Giezen, A.; Horvath, G.; Lillquist, Y.; Vallance, H.; Stockler-Ipsiroglu, S. Long-term outcomes of blood phenylalanine concentrations in children with classical phenylketonuria. *Mol. Gen. Metab.* **2013**, *108* (4), 255–258. <https://doi.org/10.1016/j.ymgme.2013.01.007>
- Huang, S.-J.; Lin, S.-Y.; Wang, T.-T.; Hsu, F.-C. Combining acetic acid and ethanol as an anti-browning treatment for lettuce butt discoloration through repression of the activity and expression of phenylalanine ammonia lyase. *Postharvest Biol. Technol.* **2020**, *164*, 111151. <https://doi.org/10.1016/j.postharvbio.2020.111151>
- Hussain, S.; Iqbal, N.; Pang, T.; Khan, M. N.; Liu, W.-g.; Yang, W.-y. Weak stem under shade reveals the lignin reduction behavior. *J. Integr. Agric.* **2019**, *18* (3), 496–505. [https://doi.org/10.1016/S2095-3119\(18\)62111-2](https://doi.org/10.1016/S2095-3119(18)62111-2)
- Jeffrey, C. S.; Leonard, M. D.; Glassmire, A. E.; Dodson, C. D.; Richards, L. A.; Kato, M. J.; Dyer, L. A. Antiherbivore Prenylated Benzoic Acid Derivatives from *Piper kelleyi*. *J. Nat. Prod.* **2014**, *77* (1), 148–153. <https://doi.org/10.1021/np400886s>
- Kamdee, C.; Imsabai, W.; Kirk, R.; Allan, A. C.; Ferguson, I. B.; Ketsa, S. Regulation of lignin biosynthesis in fruit pericarp hardening of mangosteen (*Garcinia mangostana* L.) after impact. *Postharvest Biol. Technol.* **2014**, *97*, 68–76. <https://doi.org/10.1016/j.postharvbio.2014.06.004>
- Kato, M. J.; Furlan, M. Chemistry and evolution of the Piperaceae. *Pure Appl. Chem.* **2007**, *79* (4), 529–538. <https://doi.org/10.1351/pac200779040529>
- Kawatra, A.; Dhankhar, R.; Mohanty, A.; Gulati, P. Biomedical applications of microbial phenylalanine ammonia lyase: current status and future prospects. *Biochimie.* **2020**, *177*, 142–152. <https://doi.org/10.1016/j.biochi.2020.08.009>
- Kitamura, R. O. S.; Romoff, P.; Young, M. C. M.; Kato, M. J.; Lago, J. H. G. Chromenes from *Peperomia serpens* (Sw.) Loudon (Piperaceae). *Phytochemistry.* **2006**, *67* (21), 2398–2402. <https://doi.org/10.1016/j.phytochem.2006.08.007>
- Klejduš, B.; Kováčik, J.; Babula, P. PAL inhibitor evokes different responses in two *Hypericum* species. *Plant Physiol. Biochem.* **2013**, *63*, 82–88. <https://doi.org/10.1016/j.plaphy.2012.11.019>
- Lago, J. H. G.; Ramos, C. S.; Casanova, D. C. C.; Morandim, A. A.; Bergamo, D. C. B.; Cavalheiro, A. J.; Bolzani, V. S.; Furlan, M.; Guimarães, E. F.; Young, M. C. M.; Kato, M. J. Benzoic acid derivatives from *Piper* species and their fungitoxic activity against *Cladosporium cladosporioides* and *C. sphaerospermum*. *J. Nat. Prod.* **2004**, *67* (11), 1783–1788. <https://doi.org/10.1021/np030530j>
- Lago, J. H. G.; Young, M. C. M.; Reigada, J. B.; Soares, M. G.; Roesler, B. P.; Kato, M. J. Antifungal derivatives from *Piper mollicomum* and *P. lhotzkyanum* (Piperaceae). *Quim. Nova* **2007**, *30* (5), 1222–1224. <https://doi.org/10.1590/S0100-40422007000500032>
- Levy, H. L.; Sarkissian, C. N.; Scriver, C. R. Phenylalanine ammonia lyase (PAL): From discovery to enzyme substitution therapy for phenylketonuria. *Mol. Genet. Metab.* **2018**, *124* (4), 223–229. <https://doi.org/10.1016/j.ymgme.2018.06.002>
- Liu, W.-g.; Hussain, S.; Liu, T.; Zou, J.-l.; Ren, M.-l.; Zhou, T.; Liu, J.; Yang, F.; Yang, W.-y. Shade stress decreases stem strength of soybean through restraining lignin biosynthesis. *J. Integr. Agric.* **2019**, *18* (1), 43–53. [https://doi.org/10.1016/S2095-3119\(18\)61905-7](https://doi.org/10.1016/S2095-3119(18)61905-7)
- Lopes, A. A.; Baldoqui, D. C.; López, S. N.; Kato, M. J.; Bolzani, V. S.; Furlan, M. Biosynthetic origins of the isoprene units of gaudichaudianic acid in *Piper gaudichaudianum* (Piperaceae). *Phytochemistry.* **2007**, *68* (15), 2053–2058. <https://doi.org/10.1016/j.phytochem.2007.04.025>
- López, S. N.; Lopes, A. A.; Batista Junior, J. M.; Flausino Junior, O.; Bolzani, V. S.; Kato, M. J.; Furlan, M. Geranylation of benzoic acid derivatives by enzymatic extracts from *Piper crassinervium* (Piperaceae). *Bioresour. Technol.* **2010**, *101* (12), 4251–4260. <https://doi.org/10.1016/j.biortech.2010.01.041>
- Macêdo, C. G.; Fonseca, M. Y. N.; Caldeira, A. D.; Castro, S. P.; Pacienza-Lima, W.; Borsodi, M. P. G.; Sartoratto, A.; Silva, M. N.; Salgado, C. G.; Rossi-Bergmann, B.; Castro, K. C. F. Leishmanicidal activity of *Piper marginatum* Jacq. from Santarém-PA against *Leishmania amazonensis*. *Exp. Parasitol.* **2020**, *210*, 107847. <https://doi.org/10.1016/j.exppara.2020.107847>
- Machado, M.; Felizardo, C.; Fernandes-Silva, A.; Nunes, F. M.; Barros, A. Polyphenolic compounds, antioxidant activity and L-phenylalanine ammonia-lyase activity during ripening of olive cv. “Cobrançosa” under different irrigation regimes. *Food Res. Int.* **2013**, *51* (1), 412–421. <https://doi.org/10.1016/j.foodres.2012.12.056>
- Maleck, M.; Ferreira, B.; Mallet, J.; Guimarães, A.; Kato, M. J. Cytotoxicity of Piperamides Towards *Aedes aegypti* (Diptera: Culicidae). *J. Med. Entomol.* **2014**, *51* (2), 458–463. <https://doi.org/10.1603/ME13069>

- Marques, J. V.; Oliveira, A. D.; Raggi, L.; Young, M. C. M.; Kato, M. J. Antifungal activity of natural and synthetic amides from *Piper* species. *J. Braz. Chem. Soc.* **2010**, *21* (10), 1807–1813. <https://doi.org/10.1590/S0103-50532010001000003>
- Martins, R. C. C.; Lago, J. H. G.; Albuquerque, S.; Kato, M. J. Trypanocidal tetrahydrofuran lignans from *Piper solmsianum*. *Phytochemistry*. **2003**, *64* (2), 667–670. [https://doi.org/10.1016/S0031-9422\(03\)00356-X](https://doi.org/10.1016/S0031-9422(03)00356-X)
- Mgbeahuruike, E. E.; Yrjönen, T.; Vuorela, H.; Holm, Y. Bioactive compounds from medicinal plants: Focus on *Piper* species. *S. Afr. J. Bot.* **2017**, *112*, 54–69. <https://doi.org/10.1016/j.sajb.2017.05.007>
- Miranda, J. E.; Navickiene, H. M. D.; Nogueira-Couto, R. H.; Bortoli, S. A.; Kato, M. J.; Bolzani, V. S.; Furlan, M. Susceptibility of *Apis mellifera* (Hymenoptera: Apidae) to pellitorine, an amide isolated from *Piper tuberculatum* (Piperaceae). *Apidologie*. **2003**, *34* (4), 409–415. <https://doi.org/10.1051/apido:2003036>
- Moraes, J.; Keiser, J.; Ingram, K.; Nascimento, C.; Yamaguchi, L. F.; Bittencourt, C. R.; Bemquerer, M. P.; Leite, J. R.; Kato, M. J.; Nakano, E. In vitro synergistic interaction between amide pipartine and antimicrobial peptide dermaseptin against *Schistosoma mansoni* schistosomula and adult worms. *Curr. Med. Chem.* **2013**, *20* (2), 301–309. <https://doi.org/10.2174/092986713804806694>
- Moraes, M. M.; Kato, M. J. Biosynthesis of Pellucidin A in *Peperomia pellucida* (L.) HBK. *Front. Plant Sci.* **2021**, *12*, 641717. <https://doi.org/10.3389/fpls.2021.641717>
- Morandim, A. A.; Bergamo, D. C. B.; Kato, M. J.; Cavalheiro, A. J.; Bolzani, V. S.; Furlan, M. Circadian rhythm of anti-fungal prenylated chromene in leaves of *Piper aduncum*. *Phytochemical Anal.* **2005**, *16* (4), 282–286. <https://doi.org/10.1002/pca.843>
- Mota, J. S.; Leite, A. C.; Batista Junior, J. M.; López, S. N.; Ambrósio, D. L.; Passerini, G. D.; Kato, M. J.; Bolzani, V. S.; Cicarelli, R. M. B.; Furlan, M. In vitro Trypanocidal Activity of Phenolic Derivatives from *Peperomia obtusifolia*. *Planta Med.* **2009**, *75* (6), 620–623. <https://doi.org/10.1055/s-0029-1185364>
- Mota, J. S.; Leite, A. C.; Kato, M. J.; Young, M. C. M.; Bolzani, V. D. S.; Furlan, M. Isoswertisin flavones and other constituents from *Peperomia obtusifolia*. *Nat. Prod. Res.* **2011**, *25* (1), 1–7. <https://doi.org/10.1080/14786410903244954>
- Navickiene, H. M. D.; Alécio, A. C.; Kato, M. J.; Bolzani, V. D. S.; Young, M. C. M.; Cavalheiro, A. J.; Furlan, M. Antifungal amides from *Piper hispidum* and *Piper tuberculatum*. *Phytochemistry*. **2000**, *55* (6), 621–626. [https://doi.org/10.1016/S0031-9422\(00\)00226-0](https://doi.org/10.1016/S0031-9422(00)00226-0)
- Navickiene, H. M. D.; Bolzani, V. S.; Kato, M. J.; Pereira, A. M. S.; Bertoni, B. W.; Furlan, M. Quantitative determination of anti-fungal and insecticide amides in adult plants, plantlets and callus from *Piper tuberculatum* by reverse-phase high-performance liquid chromatography. *Phytochem. Anal.* **2003**, *14* (5), 281–284. <https://doi.org/10.1002/pca.716>
- Neves, A. R.; Trefzger, O. S.; Barbosa, N. V.; Honorato, A. M.; Carvalho, D. B.; Moslaves, I. S.; Kadri, M. C. T.; Yoshida, N. C.; Kato, M. J.; Arruda, C. C. P.; Baroni, A. C. Effect of isoxazole derivatives of tetrahydrofuran neolignans on intracellular amastigotes of *Leishmania (Leishmania) amazonensis*: A structure–activity relationship comparative study with triazole-neolignan-based compounds. *Chem. Biol. Drug Des.* **2019**, *94* (6), 2004–2012. <https://doi.org/10.1111/cbdd.13609>
- Oliveira, A.; Mesquita, J. T.; Tempone, A. G.; Lago, J. H. G.; Guimarães, E. F.; Kato, M. J. Leishmanicidal activity of an alkenylphenol from *Piper malacophyllum* is related to plasma membrane disruption. *Exp. Parasitol.* **2012**, *132* (3), 383–387. <https://doi.org/10.1016/j.exppara.2012.08.019>
- Pereira Filho, A. A.; Pessoa, G. C. D.; Yamaguchi, L. F.; Stanton, M. A.; Serravite, A. M.; Pereira, R. H. M.; Neves, W. S.; Kato, M. J. Larvicidal activity of essential oils from *Piper* species against strains of *Aedes aegypti* (Diptera: Culicidae) resistant to pyrethroids. *Front. Plant Sci.* **2021**, *12*. <https://doi.org/10.3389/fpls.2021.685864>
- Pinheiro, B. G.; Silva, A. S. B.; Souza, G. E. P.; Figueiredo, J. G.; Cunha, F. Q.; Lahlou, S.; Silva, J. K. R.; Maia, J. G. S.; Sousa, P. J. C. Chemical composition, antinociceptive and anti-inflammatory effects in rodents of the essential oil of *Peperomia serpens* (Sw.) Loud. *J. Ethnopharmacol.* **2011**, *138* (2), 479–486. <https://doi.org/10.1016/j.jep.2011.09.037>
- Prabpree, A.; Sangsil, P.; Nualsri, C.; Nakkanong, K. Expression profile of *phenylalanine ammonia-lyase (PAL)* and phenolic content during early stages of graft development in bud grafted *Hevea brasiliensis*. *Biocatal. Agric. Biotechnol.* **2018**, *14*, 88–95. <https://doi.org/10.1016/j.bcab.2018.02.010>
- Ramos, C. S.; Kato, M. J. Metabolism of neolignans from *P. regnellii* (Piperaceae) in the beetle *Naupactus bipes* (Coleoptera: Curculionidae). *Chemoecology*. **2013**, *23* (3), 143–148. <https://doi.org/10.1007/s00049-013-0129-y>
- Ramos, C. S.; Silva, M. W.; Moraes, M. M.; Almeida, A. V.; Vanin, S. A.; Kato, M. J. Metabolization of Insecticidal Amides from Leaves of *Piper tuberculatum* by *Heraclides hectorides* and *Naupactus bipes*. *J. Braz. Chem. Soc.* **2020**, *31* (4), 724–730. <https://doi.org/10.21577/0103-5053.20190236>
- Regasini, L. O.; Cotinguiba, F.; Siqueira, J. R.; Bolzani, V. S.; Silva, D. H.; Furlan, M.; Kato, M. J. Radical scavenging capacity of *Piper arboreum* and *Piper tuberculatum* (Piperaceae). *Lat. Am. J. Pharm.* **2008**, *27* (6), 900–903.

- Regasini, L. O.; Cotinguiba, F.; Passerini, G. D.; Bolzani, V. D. S.; Cicarelli, R. M. B.; Kato, M. J.; Furlan, M. Trypanocidal activity of *Piper arboreum* and *Piper tuberculatum* (Piperaceae). *Rev. Bras. Farmacogn.* **2009**, *19* (1b), 199–203. <https://doi.org/10.1590/S0102-695X2009000200003>
- Reigada, J. B.; Tcacenco, C. M.; Andrade, L. H.; Kato, M. J.; Porto, A. L.; Lago, J. H. G. Chemical constituents from *Piper marginatum* Jacq. (Piperaceae)—antifungal activities and kinetic resolution of (RS)-marginatumol by *Candida antarctica* lipase (Novozym 435). *Tetrahedron Asymmetry* **2007**, *18* (9), 1054–1058. <https://doi.org/10.1016/j.tetasy.2007.05.006>
- Rocha, J. C.; Bausell, H.; Bélanger-Quintana, A.; Bernstein, L.; Gökmen-Özel, H.; Jung, A.; MacDonald, A.; Rohr, F.; van Dam, E.; Heddrich-Ellerbrok, M. Development of a practical dietitian road map for the nutritional management of phenylketonuria (PKU) patients on pegvaliase. *Mol. Genet. Metab.* **2021**, *28*, 100771. <https://doi.org/10.1016/j.ymgmr.2021.100771>
- Salazar, K. J. M.; Paredes, G. E. D.; Lluncor, L. R.; Young, M. C. M.; Kato, M. J. Chromenes of polyketide origin from *Peperomia villipetiola*. *Phytochemistry*. **2005**, *66* (5), 573–579. <https://doi.org/10.1016/j.phytochem.2005.01.003>
- Sant’Ana, M.; Souza, H. R.; Possebon, L.; Cornélio, M. L.; Riffo-Vasquez, Y.; Girol, A. P.; Oliani, S. M. Effect of piperlongumine during exposure to cigarette smoke reduces inflammation and lung injury. *Pulm. Pharmacol. Ther.* **2020**, *61*, 101896. <https://doi.org/10.1016/j.pupt.2020.101896>
- Santos, R. A.; Ramos, C. S.; Young, M. C. M.; Pinheiro, T. G.; Amorim, A. M.; Kato, M. J.; Batista, R. Antifungal constituents from the roots of *Piper dilatatum* Rich. *J. Chem.* **2013**, *2013*, 160165. <https://doi.org/10.1155/2013/160165>
- Sarkissian, C. N.; Kang, T. S.; Gámez, A.; Sriver, C. R.; Stevens, R. C. Evaluation of orally administered PEGylated phenylalanine ammonia lyase in mice for the treatment of Phenylketonuria. *Mol. Gen. Metab.* **2011**, *104* (3), 249–254. <https://doi.org/10.1016/j.ymgme.2011.06.016>
- Silva, R. V.; Navickiene, H. M. D.; Kato, M. J.; Bolzani, V. D. S.; Méda, C. I.; Young, M. C. M.; Furlan, M. Antifungal amides from *Piper arboreum* and *Piper tuberculatum*. *Phytochemistry*. **2002**, *59* (5), 521–527. [https://doi.org/10.1016/S0031-9422\(01\)00431-9](https://doi.org/10.1016/S0031-9422(01)00431-9)
- Silva, J. K. R.; Andrade, E. H. A.; Kato, M. J.; Carreira, L. M. M.; Guimaraes, E. F.; Maia, J. G. S. Antioxidant capacity and larvicidal and antifungal activities of essential oils and extracts from *Piper krukoffii*. *Nat. Prod. Comm.* **2011**, *6* (9), 1361–1366. <https://doi.org/10.1177/1934578X1100600936>
- Silva, H. A.; Yamaguchi, L. F.; Young, M. C. M.; Ramos, C. S.; Amorim, A. M. A.; Kato, M. J.; Batista, R. Antifungal piperamides from *Piper mollicomum* Kunth (Piperaceae). *Eclét. Quím. J.* **2018**, *43* (1), 33–38. <https://doi.org/10.26850/1678-4618eqj.v43.1.2018.p33-38>
- Silva, N. V.; Mazzafera, P.; Cesarino, I. Should I stay or should I go: are chlorogenic acids mobilized towards lignin biosynthesis? *Phytochemistry*. **2019a**, *166*, 112063. <https://doi.org/10.1016/j.phytochem.2019.112063>
- Silva, A. C. A.; Diodato, J. S.; Castro, J. W.; Matias, E. F. F.; Silva, L. E.; Amaral, W.; Maia, B. H. L. N. S.; Ferriani, A. P.; Souza, A. K.; Quintans-Júnior, L. J.; Coutinho, H. D. M. Effect of the essential oils from *Piper* sp. and blue led lights in the enhancement of the antibiotic activity of drugs against mdr bacterial strains. *J. Photochem. Photobiol. B.* **2019b**, *199*, 111604. <https://doi.org/10.1016/j.jphotobiol.2019.111604>
- Silva, M. A.; Fokoue, H. H.; Fialho, S. N.; Santos, A. P. A.; Rossi, N. R. D. L. P.; Gouveia, A. J.; Ferreira, A. S.; Passarini, G. M.; Garay, A. F. G.; Alfonso, J. J.; Soares, A. M.; Zanchi, F. B.; Kato, M. J.; Teles, C. B. G.; Kuehn, C. C. Antileishmanial activity evaluation of a natural amide and its synthetic analogs against *Leishmania* (V.) *braziliensis*: an integrated approach in vitro and in silico. *Parasitol. Res.* **2021**, *120* (4), 2199–2218. <https://doi.org/10.1007/s00436-021-07169-w>
- Souza, A. A.; Vessecchi, R.; Castro-Gamboa, I.; Furlan, M. Combined use of tandem mass spectrometry and computational chemistry to study 2H-chromenes from *Piper aduncum*. *J. Mass Spectrom.* **2019**, *54* (7), 634–642. <https://doi.org/10.1002/jms.4378>
- TAPPI - Technical Association of the Pulp and Paper Industry. *Official Test Methods, Provisional Test Methods, and Useful Test Methods* - Fibrous Materials and Pulp. Testing. Atlanta, 1979.
- Toscano, S.; Ferrante, A.; Leonardi, C.; Romano, D. PAL activities in asparagus spears during storage after ammonium sulfate treatments. *Postharvest Biol. Technol.* **2018**, *140*, 34–41. <https://doi.org/10.1016/j.postharvbio.2018.02.010>
- Tronchet, M.; Balagué, C.; Kroj, T.; Jouanin, L.; Roby, D. Cinnamyl alcohol dehydrogenases C and D, key enzymes in lignin biosynthesis, play an essential role in disease resistance in *Arabidopsis*. *Mol. Plant Pathol.* **2010**, *11* (1), 83–92. <https://doi.org/10.1111/j.1364-3703.2009.00578.x>
- Vanholme, R.; Meester, B.; Ralph, J.; Boerjan, W. Lignin biosynthesis and its integration into metabolism. *Curr. Opin. Biotechnol.* **2019**, *56*, 230–239. <https://doi.org/10.1016/j.copbio.2019.02.018>
- Veronico, P.; Paciolla, C.; Pomar, F.; De Leonardis, S.; García-Ulloa, A.; Melillo, M. T. Changes in lignin biosynthesis and monomer composition in response to benzothiadiazole and root-knot nematode *Meloidogyne*

incognita infection in tomato. *J. Plant Physiol.* **2018**, *230*, 40–50. <https://doi.org/10.1016/j.jplph.2018.07.013>

Vogel, K. R.; Arning, E.; Wasek, B. L.; Bottiglieri, T.; Gibson, K. M. Characterization of 2-(methylamino) alcanoic acid capacity to restrict blood-brain phenylalanine transport in *Pahe^{mut}* mice: Preliminary findings. *Mol. Gen. Metab.* **2013**, *110* (Suppl), S71–S78. <https://doi.org/10.1016/j.ymgme.2013.08.004>

Watanabe, S. K.; Hernandez-Velazco, G.; Iturbe-Chiñas, F.; Lopez-Mungia, A. Phenylalanine ammonia lyase from *Sporidiobolus pararoseus* and *Rhodospiridium toruloides*: application for phenylalanine and tyrosine deamination. *World J. Microbiol. Biotechnol.* **1992**, *8* (4), 406–410. <https://doi.org/10.1007/BF01198755>

Weiss, R.; Guebitz, G. M.; Pellis, A.; Nyanhongo, G. S. Harnessing the Power of Enzymes for Tailoring and Valorizing Lignin. *Trends Biotechnol.* **2020**, *38* (11), 1215–1231. <https://doi.org/10.1016/j.tibtech.2020.03.010>

Yamaguchi, L. F.; Lago, J. H. G.; Tanizaki, T. M.; Di Mascio, P.; Kato, M. J. Antioxidant activity of prenylated hydroquinone and benzoic acid derivatives from *Piper crassinervium* Kunth. *Phytochemistry.* **2006**, *67* (16), 1838–1843. <https://doi.org/10.1016/j.phytochem.2006.03.001>

Yoshida, N. C.; Benedetti, A. M.; Santos, R. A.; Ramos, C. S.; Batista, R.; Yamaguchi, L. F.; Kato, M. J. Alkenylphenols from *Piper dilatatum* and *P. diospyrifolium*. *Phytochemistry Lett.* **2018**, *25*, 136–140. <https://doi.org/10.1016/j.phytol.2018.04.006>

You, X.; Fang, H.; Wang, R.; Wang, G.-L.; Ning, Y. Phenylalanine ammonia lyases mediate broad-spectrum resistance to pathogens and insect pests in plants. *Sci. Bull.* **2020**, *65* (17), 1425–1427. <https://doi.org/10.1016/j.scib.2020.05.014>

Studies of curing cycle of carbon fiber/epoxy resins (8552® and M21®) preregs based on thermal and rheological analyses

Sheila Marques Silva¹, Carolina Paiva Nascimento Silva^{2,3}, Thiago de Carvalho Silva^{2,4}, Mirabel Cerqueira Rezende², Edson Cocchieri Botelho¹, Michelle Leali Costa^{1,3+}

1. São Paulo State University, Department of Materials and Technology, Guaratinguetá, Brazil.
2. Federal University of São Paulo, Institute of Science and Technology, São José dos Campos, Brazil.
3. Lightweight Structures Laboratory, LEL/IPT, São José dos Campos, Brazil.
4. Federal Center for Technological Education Celso Suckow da Fonseca, Angra dos Reis, Brazil.

+Corresponding author: Michelle Leali Costa, **Phone:** +5511983266474, **Email address:** michelle.leali@unesp.br

ARTICLE INFO

Article history:

Received: August 23, 2021

Accepted: March 10, 2022

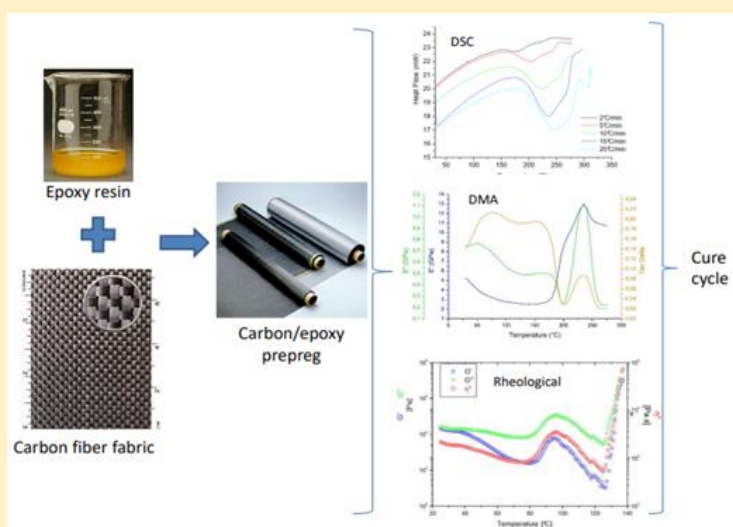
Published: August 17, 2022

Section Editor: Assis Vicente Benedetti

Keywords

1. cure kinetic
2. DSC
3. DMA
4. rheology
5. FTIR

ABSTRACT: Thermal and rheological characterizations were performed on prepreg produced with two different commercial epoxy resins - M21® and 8552® – aiming to study and optimize the curing cycle of structural components used in aerospace industry. Characterizations were performed by differential scanning calorimetry (DSC), rheology and dynamic mechanical analysis techniques were assessed and the results were correlated and supported by Fourier Transform Infrared spectroscopy. Additionally, to heating rates suggested by the material supplier, DSC analysis allowed to evaluate further heating rates: 2, 5, 10, 15 and 20 °C/min. Materials presented the n fractional order kinetic of cure and have in its formulation the presence of thermoplastics, in addition to epoxy and amine. Results confirmed that the best heating rates for processing both materials are the lower ones, as they result in a better control of the reactions between chemical compounds involved and the physical changes that are part of curing process stages. Results have analytically confirmed the suggested proposal for curing cycle from supplier is the best choice for materials involved.



1. Introduction

Polymeric composites have been widely used to produce lighter structures that have high specific strength, stiffness and good fatigue resistance (Mphahlele *et al.*, 2019). This class of materials has been used in an over an extensive range of applications such as aerospace, military, automotive, sporting and construction industries (Liu *et al.*, 2018). Polymeric composites manufacture can be processed by using thermoset resins, as epoxy, pre-impregnated in carbon fiber reinforcement. This pre-impregnated material, named also as prepreg, to be composed of a reinforcing fiber (carbon, glass, aramid, and others) that has been impregnated with a thermoset resin (epoxy, phenolic, for example) prior to the molding process. This way, parts and pieces can be produced into the desired shape and then be cured by the application of heat with the use of the prepreg. Thermoset polymers, such as epoxy resins, are the most commonly used in composites for aerospace, adhesives, hardware components, coatings and due to their good adhesion properties and thermal stability coupled with sufficient chemical resistance. However, the performance in each application is dependent on the cure process, i.e., the transformation of the resin into insoluble and infusible three-dimensional structures, by means of crosslinking reactions with curing agents and/or catalyst (Hatter *et al.*, 2020).

The polymeric matrix is an important component in a composite structure, which protects fibers or fillers against abrasion and harsh environmental conditions, and also transfer stress from the matrix to the reinforcement. In this way, the final performance of polymeric composite is strongly influenced by the interface between the matrix and the reinforcement (González-Benito, 2003; Hatter *et al.*, 2020; Liu *et al.*, 2018; Mphahlele *et al.*, 2019). Polymeric composites with similar chemical compositions may exhibit different properties, like transparency, elasticity, toughness and permeability depend on important factors such as physical dimensions and the curing cycles used (González-Benito, 2003; Hexcel Corporation, 2021a; b; Hubert *et al.*, 2019; Mesogitis *et al.*, 2019; Newcomb, 2019; Nixon-Pearson *et al.*, 2017; Ribeiro *et al.*, 2013; Wang *et al.*, 2020).

In actual use, many thermosets are cured using complex cure cycles to optimize the tradeoff between the processing time and final product's properties. This way, the low-molecular weight viscoelastic constituents of the thermoset must undergo a transformation to an amorphous high-molecular weight solid, through chemical reactions of the thermoset system, typically driven by temperature. Thus, knowing and

understanding the viscoelastic properties of the thermoset resin is essential for establishing an adequate curing cycle. Among these properties that must be monitored are minimum viscosity temperature; gel temperature; onset and peak curing temperature; minimum viscosity time; vitrification, degree of cure and glass transition temperature (Newcomb, 2019). Cure cycles used in the aircraft industry generally consist of alternating stages of heating ramps at slow rates followed by isotherms and pressure to ensure the slow, controlled, and complete cure of the thermoset resin systems used in prepregs. Heating rates must be slow to ensure that parts cured within autoclaves (which are not conventional ovens but complex pressure and temperature vessel systems) do not undergo exotherm (uncontrolled release of heat caused by the exothermic reaction of the epoxy resin cure) which could cause accidents inside the autoclaves (explosion) and generate parts with defects such as air bubbles caused by the uncontrolled release of volatiles (Agius *et al.*, 2013; Botelho *et al.*, 2001; Costa *et al.*, 2005; Hexcel Corporation, 2021a; b; Mphahlele *et al.*, 2019; Oishi *et al.*, 2013).

The quality of composites is controlled to a great extent by the cure cycle parameters such as time, temperature, pressure and their sequence of combination. Traditionally a composite manufacturer just follows the cure schedule suggested by the supplier. This cycle is usually determined in an ideal situation where the resin is still "fresh" and may not be representative to the actual curing state of the resin in a composite manufacturing facility (Liu *et al.*, 2018). The purpose of this study is to characterize thermally and rheologically the carbon fiber prepreg with commercial epoxy resins, known in the aerospace industry as M21[®] and 8552[®] systems, both produced by the Hexcel Composite, aiming to optimize de curing cycle of prepregs used in aerospace area. For this, analysis was made using differential scanning calorimetry (DSC), rheology characterization, dynamic mechanical analysis (DMA) and Fourier Transform Infrared (FTIR) spectroscopy techniques.

2. Experimental

2.1 Materials

In the present study, two different prepregs were analyzed: the first with epoxy resin type 8552[®] and the second with type M21[®], both reinforced with carbon fiber and supplied to EMBRAER by Hexcel Composites. These two systems are interesting because they are examples of two different toughening strategies. Resin 8552[®] is toughened through the introduction of a

submicron phase of a thermoplastic material that is dissolved in the uncured thermosetting epoxy resin. While the resin M21[®] is characteristic of the interlayer class of toughened thermosetting epoxy system that presents thermoplastic particles in the order of tens of microns, which are responsible for the creation of a resin-rich region between the layers (Wang *et al.*, 2020). The thermoplastic phase is introduced to address the common problem of composite brittleness as it enhances the fracture toughness and impacts laminate performance. At the same time thermoplastics affect prepreg processing characteristics. The toughening elevates the prepreg viscosity, changes inter-ply friction and morphology (Nixon-Pearson *et al.*, 2017).

2.2 Samples prepreps

The prepreps were previously conditioned in sealed plastic films, they were removed from the freezer to a controlled environment and left at room temperature for approximately 1 h. This duration time was experimentally identified for this specific sample size. After this period, the prepreps were removed from the plastic bags and cut with scissors to the appropriate sizes to be used in this study.

2.3 Differential scanning calorimetry (DSC)

The DSC is a thermal analysis technique that measures the difference in energy provided to a sample and a reference material in function of a controlled temperature programming. The DSC technique monitors the endothermic, exothermic and specific heat variations experienced by a sample (Braga *et al.*, 2011). In this study, the DSC technique was used to determine the temperature and cure enthalpy of the prepreps and the results obtained were used to determine the curing kinetics.

The equipment used in this study is a PerkinElmer model Pyris 1 linked to a cooling system model Intracooler 2P. This arrangement is a DSC power compensated coupled with a low mass furnace (~1 g) that minimize the effect of thermal gradient. First of all, calibration was performed using indium standard as per equipment supplier instructions, ASTM E967-18 (2018) and ASTM E968-02 (2014b), which suggest calibrating temperature and enthalpy using metallic standard. The DSC equipment was calibrated for each heating rate studied in the present work (Vyazovkin *et al.*, 2011). Samples (~5 mg) were placed into hermetic aluminum pans and heated from room temperature (22 °C) to 300 °C, using different heating rates (2, 5, 10, 15, and

20 °C min⁻¹) under a constant flow of N₂ at a rate of 20 mL min⁻¹. After curing, the same sample was subjected to further heating from room temperature to 250 °C, at a heating rate of 20 °C min⁻¹ to determine the glass transition temperature (T_g) (ASTM E1356-08, 2014a; Vyazovkin *et al.*, 2011).

2.4 Rheological characterization

Classically, a thermoset resin undergoes two main phase transitions during cure, gelation and vitrification. Rheological tests were assessed aiming to determine resin changes during the cure cycle (temperature conditions only) recommended by Hexcel Composites Co. (for autoclave processing of laminates <15 mm) (Hexcel Corporation, 2021a; b). The correlation between viscosity and temperature or viscosity and time of the thermoset resin cure or the prepreg systems is very useful information for composite processing. The viscosity control during the autoclave processing allows the optimization of the resin infiltration inside the reinforcement, and, consequently, a larger densification of the composite materials in a shorter time (ASTM D4473-08, 2021; Costa *et al.*, 2006; Das and Chaudhary, 2019; Paiva *et al.*, 2006). Rheological analyses were performed on the equipment Rheometric Scientific, model SR-5 with parallel plates, a constant frequency of 0.16 Hz ($\omega = 1 \text{ rad s}^{-1}$), 500 Pa of stress, H (gap) of 0.3 mm for M21 and 0.4 mm for the sample 8552, using different heating rates (2.5; 5.0, and 10 °C min⁻¹), heating from room temperature (22 °C) to gel temperature. The method was based on the ASTM D4473-08 (2021) - Standard Test Method for Plastics: Dynamic Mechanical Properties: Cure Behavior. This way, during the cure, viscoelastic properties of the sample can be measured such as shear storage modulus (G'), shear loss modulus (G''), loss tangent or loss factor, $\tan \delta = G''/G'$ and the complex dynamic viscosity (η^*).

2.5 Dynamic Mechanical Analysis (DMA)

DMA is currently used to study viscoelastic behavior of polymer composites and its basic principle are the same of the rheology (Das and Chaudhary, 2019; Ştefanov *et al.*, 2020). In this way, depending on the testing mode, three quantities are usually monitored, i.e., the storage modulus, E' , which is a measure of the stored energy (the elastic part), the loss modulus, E'' , which is a measure of the energy lost as heat (the viscous part), and the loss tangent or loss factor, $\tan \delta = E''/E'$, which indicates how efficiently the material loses energy due to internal friction and molecular rearrangement. One of the

most important transitions in polymers is the T_g . This is the temperature region where the material changes from a glassy to a rubbery state. While materials can be used above, below, and within this region, thermosets tend to be used below T_g , because approaching T_g , stiffness decreases significantly resulting in a corresponding decrease in strength (Stefanov *et al.*, 2020).

The DMA characterization of the studied epoxy systems was assessed using the equipment TA2980 supplied by TA Instruments, with single cantilever, frequency of 1 Hz, 10 μm of amplitude, heating rates (2, 5, 10, 15, and 20 $^\circ\text{C min}^{-1}$), heating from 30-300 $^\circ\text{C}$. After curing, the same prepreg sample inside the equipment was again subjected to DMA analysis, at a heating rate of 2.0 $^\circ\text{C min}^{-1}$, frequency of 1 Hz, heating from 30-300 $^\circ\text{C}$ for the determination of T_g .

2.6 Fourier transform infrared spectroscopy (FTIR)

The FTIR is a technique that allows following the curing reactions, studying and quantifying the conversion of different representative functional groups (Sánchez-Soto *et al.*, 2007). In this study, the equipment used was a Spectrum One supplied by PerkinElmer with the Universal Attenuated Total Reflectance (UATR) accessory. This equipment works in the regions from 4000 to 400 cm^{-1} , resolution of 0.5 cm^{-1} and 20 scan were performed. The analyses of the two prepreg samples used the samples as received and also after a carefully preparation, to emphasize the main bands of the modifiers present in the epoxy resin samples. In order to separate the polymeric matrix from the fibers, a treatment with cold acetone was carried out. During the treatment with cold acetone, the sample showed a cloudy color coming from a fine light gray solid and the sample was centrifuged, treated with acetone and again centrifuged for a better elimination of interferers. Afterwards, a fraction of the sample was treated with pyridine and the soluble part evaporated. This procedure resulted in a film that was analyzed. Pyridine was used because it is a good solvent for polyethersulfones (PES), according to the literature (Silverstein *et al.*, 2000). A fraction of the sample was also pretreated with formic acid and the soluble part evaporated, as this acid is a good diluent for polyamides in general.

3. Results and discussions

3.1 DSC

The first step to calculate exothermic heat flow on DSC measurements is to determinate the appropriate heat flow 'baseline' for the instrument. Heat flow at any time can then be calculated from the difference between the established baseline and the actual measured heat flow. For dynamic scans, the baseline is calculated by measuring the heat flow at reaction start and at its completion, assuming a linear variation between the extremes. For an isothermal experiment, this baseline is constant and it can be determined from the measured flow at the completion of the reaction (Hubert *et al.*, 2019).

3.1.1 Prepreg 8552

Figure 1 shows DSC and conversion degree curves for the 8552-epoxy system. A typical dynamic DSC curve can be seen in Fig. 1a and shows the results obtained for the 8552-epoxy system in different heating rates. By assuming that the heat evolved during cure is directly related to the disappearance of the epoxy groups during the reaction, the area above the peak at the exothermic region was used to determine the epoxy resin fractional conversion.

The kinetic parameters in this work were obtained by dynamic DSC scans using the mathematical model described by Eq. 1 (Agius *et al.*, 2013; Costa *et al.*, 2005; Friedman, 1964; Paiva *et al.*, 2006; Paris *et al.*, 2010; Vyazovkin *et al.*, 2014):

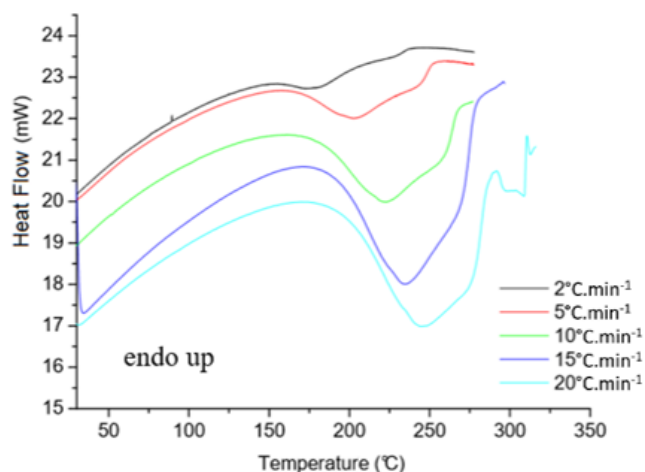
$$\frac{d\alpha}{dt} = k(1 - \alpha)^n \quad (1)$$

where α is the degree of chemical conversion, n is the order of the reaction, k is the reaction rate constant and da/dt is the derivative α with respect to time or temperature or reaction rate (Costa *et al.*, 2005; Friedman, 1964).

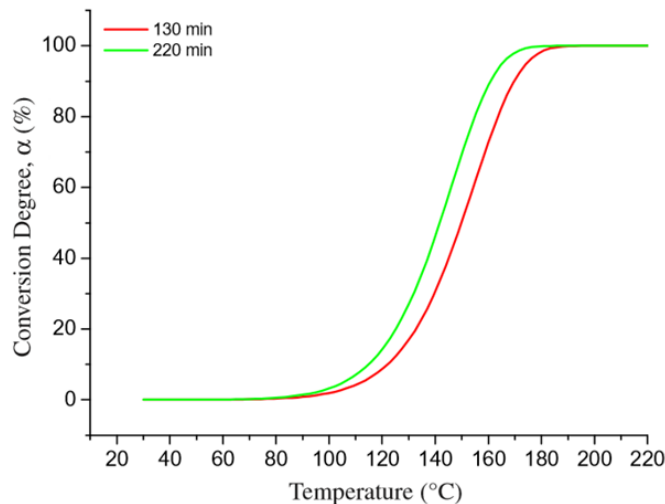
The reaction rate is generally assumed to have a temperature dependence characterized by the Arrhenius relationship (Eq. 2):

$$k = Ae^{\frac{-E_a}{RT}} \quad (2)$$

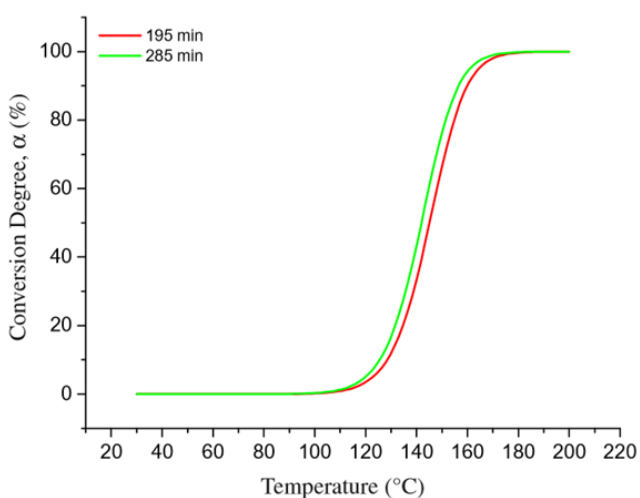
where A is the pre-exponential constant, E_a is the activation energy for the reaction, R is the universal gas constant, and T is the absolute temperature in degrees Kelvin.



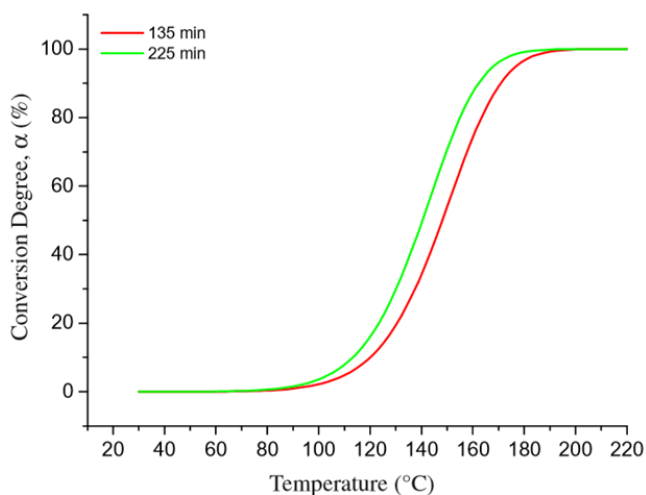
(a)



(d)



(b)



(c)

Figure 1. DSC and conversion degree curves for the Carbon/8552 epoxy prepreg. (a) Dynamic DSC curve. (b) Degree of conversion, α , at 2 °C min⁻¹, (c) 10 °C min⁻¹, and (d) 15 °C min⁻¹ considering isotherms of 120 and 210 min (b).

When Eqs. 1 and 2 are combined, they produce Eq. 3:

$$\frac{d\alpha}{dt} = A \exp\left(\frac{-E_a}{RT}\right) (1 - \alpha)^n \quad (3)$$

which yields one independent variable (t), two dependent variables (α and T), three unknown constants (A , E_a , and n), and the universal gas constant (R). Equation 4 has three degrees of freedom, or three variables. In order to have a definite solution, one variable may either be held as a constant during the reaction process or it may be related to another variable; therefore, the reaction process can be defined.

In the DSC, the temperature varies linearly with the time, following the relation (Eq. 4):

$$T - T(0) = \beta t \quad (4)$$

and

$$\beta = \frac{dT}{dt} \quad (5)$$

where T is the current temperature, $T(0)$ is the initial temperature, t is the time, and β is the heating rate.

Furthermore, the $\frac{d\alpha}{dt}$ can be described by the following equation:

$$\frac{d\alpha}{dt} = \frac{dT}{dt} \frac{d\alpha}{dT} = A \exp\left(\frac{-E_a}{RT}\right) (1 - \alpha)^n \quad (6)$$

Combining Eqs. 5 and 6 with Eq. 3, which will give:

$$\beta \frac{d\alpha}{dT} = A \exp\left(\frac{-E_a}{RT}\right) (1 - \alpha)^n \quad (7)$$

The Eq. 7 represents the theoretical shape of DSC curve that is determined in this work. The value of degree of chemical conversion, α , is obtained by dividing the $\Delta H_{\text{partial}}$ by total the heat ΔH generated during the whole reaction, as shown in Eq. 8.

$$\alpha = \frac{\Delta H_{\text{partial}}}{\Delta H} \quad (8)$$

In the present work, the values for $\Delta H_{\text{partial}}$ and ΔH are evaluated from the area above the DSC curve. Equation 9 can be obtained to a linear form by taking the natural logarithm of both sides of Eq. 7 and can be solved by a multilinear regression $\ln\left(\beta \frac{d\alpha}{dT}\right)$ with $-\frac{1}{RT}$ and $\ln(1 - \alpha)$ as variables, which have been evaluated from DSC data and solving for A , E_a and n .

$$\ln\left(\beta \frac{d\alpha}{dT}\right) = \ln A - \frac{E_a}{RT} + n \ln(1 - \alpha) \quad (9)$$

So, it was possible to determine the kinetic parameters of both systems and compare the results using the equations described above and with the results of the dynamic scanning of the M21 and 8552 epoxy prepreg systems at different heating rates.

Table 1 shows all kinetic parameters obtained by dynamic method for the five heating rates: 2, 5, 10, 15, and 20 °C min⁻¹ for carbon/8552 epoxy resin prepreg. T_{initial} and T_{final} describe the temperature rate in that the prepreg cure kinetic was studied. The T_{peak} and T_{final} of the cure shows an increase with the increment of the heating rate used, showing a displacement of the beginning and final of the cure. This fact shows that despite the reduction in the curing time of the material, it does not represent an advantage for the selection of curing cycle. Higher temperature in the autoclave would be required to reduce the curing cycle leading to a much higher cost of the process than curing at lower rates. The T_g values reduce with increasing heating rate, due to the decrease in the formation of cross-links. It is known that greater density of crosslinks system contributes to increase the T_g (Agius *et al.*, 2013; Costa *et al.*, 2005; Paris *et al.*, 2010).

Table 1. DSC results and kinetic parameters obtained for the 8552 prepreg at different heating rates.

Heating Rate (°C min ⁻¹)	T _{initial} (°C)	T _{onset} (°C)	T _{peak} (°C)	T _{final} (°C)	-ΔH (J g ⁻¹)	n	lnA (s ⁻¹)	E _a (kJ mol ⁻¹)	T _g (°C)
2	145	171	181	220	106	1.5±0.1	39.4	170 ± 4	215
5	158	176	204	256	142	1.4±0.1	18.9	98 ± 9	211
10	161	185	224	273	171	1.2±0.1	18.0	96 ± 7	210
15	172	190	236	281	201	1.1±0.1	17.5	94 ± 6	205
20	172	197	248	291	203	1.0±0.1	16.6	91 ± 5	197

As the DSC equipment was calibrated for each heating rate studied, it can be stated that T_{onset} , T_{peak} , T_{final} and the enthalpy value increase with increasing the heating rate. This indicates that slower heating rates, such as 2 °C min⁻¹, favor higher collision between the molecules, allowing a greater interaction between the components (epoxy and curing agent) even promoting a more controlled curing of the material with less exotherm (high energy release during the cure) and at lower temperatures. Therefore, a recommended heating rate to be used for curing this prepreg in an autoclave is 2 °C min⁻¹.

The heats of reaction, ΔH , are over the range 106-203 J g⁻¹ and the order of reaction found is between 1.5 and 1.0. This evidence demonstrates that there is a consistent dependence among the kinetic parameters and the heating rate using in the curing process.

The fractional cure reaction order ($n \sim 1.5$ to 1.0) found implies in complex reaction mechanisms. The

appearance of the fractional reaction order suggests the existence of a reaction mechanism via formation of free radicals. The beginning of the curing reaction of the epoxy resin requires the opening of the epoxy groups through the amine catalyzed by the temperature. The curing reaction of epoxy resin with amine hardeners leads to formation of two main reactions: secondary amine and tertiary amine formation. The groups hydroxyls generated during the reaction or from the addition of solvents or others catalysts, or by the presence of impurities and even moisture, accelerate significantly the reaction between the glycidyl ether and the amine. However, in all cases, the hydroxyl groups behave only as reaction catalysts and not as consumers of epoxy groups in competition with the amine group (Agius *et al.*, 2013; Costa *et al.*, 2005; 2006; Paiva *et al.*, 2006; Paris *et al.*, 2010; Sánchez-Soto *et al.*, 2007). Thus, complex reaction mechanisms characterize the cure of epoxy resin with amine hardeners.

The activation energy, E_a , was determined using the variation of the maximum temperature of the exothermic peak with the heating rate based on the Ozawa and Arrhenius method (Costa *et al.*, 2006; Paiva *et al.*, 2006). The E_a and reaction order (n) decrease with increasing heating rate, showing that the higher the temperature, lower the dependence on reaction with the formation of products and less is the amount of energy needed to overcome the activation barrier. Increased heating rate increase the speed of transfer of thermal energy, which consequently decrease the curing reaction time. On the other hand, enthalpy increases with the increment in the heating rate, suggesting that higher heating rates favor the release of energy by the system. This fact must be studied carefully, if high heating rates used in the autoclave to cure large parts, there is a risk of high energy release (phenomenon called exotherm), which may compromise the quality of the part or even damage the autoclave.

The use of two-stage cure cycles is known to develop stronger laminates in the aerospace industry and the cycle suggest by the 8552 prepreg supplier is: heating from 30 to 180 °C at 0.6-2.8 °C min⁻¹ and holding at 180 °C for 120 to 210 min. Based on this information, mathematical simulations of the degree of conversion of 8552 epoxy resin was carried out. Figure 1b presents the simulation of the prepreg system conversion degree as function of temperature for 195 and 285 min. This is the time necessary to elevate the temperature from 30 to 180 °C, using the heating rates of 2 °C min⁻¹ and holding at 180 °C by 120 min (total cycle of 195 min) and 210 min (total cycle of 285 min). This curve was obtained based on Eq. 10 (Costa *et al.*, 2006), using a predetermined time and temperature range.

$$\alpha = 1 - [1 - (1 - n) \cdot A \cdot t \cdot \exp\left(-\frac{E_a}{RT}\right)]^{\frac{1}{1-n}} \quad (10)$$

For the heating rate of 2 °C min⁻¹ in Fig. 1b, the conversion degree of a temperature below 120 °C is less than 5% and that after 120 °C the cure actually begins. When the temperature of 180 °C is reached, practically 100% of the conversion has been completed, for both the 120- and 210-min isotherms. However, the degree of conversion at the other heating rates (Fig. 1c and d) is observed that at a temperature of 120 °C the degree of conversion is high (> 5%), showing that the rise in temperature stimulates the start of curing in a disordered way. But the temperature of 180 °C is not sufficient to ensure a complete cure of the prepreps at these higher rates (considering the isotherm of 120 min).

3.1.2 Prepreg M21

Figure 2 shows DSC and conversion degree curves for the Carbon/M21 epoxy. Figure 2a shows the dynamic DSC curve with the presence of an endothermic peak in the region of 190-200 °C more accentuated at the rates of 2 and 5 °C min⁻¹. This behavior can be directly related to the formulation of prepreg M21, because, according to the literature, it has polyamide and poly(ether sulfone) thermoplastics in its composition (Mesogitis *et al.*, 2018; Paris *et al.*, 2012).

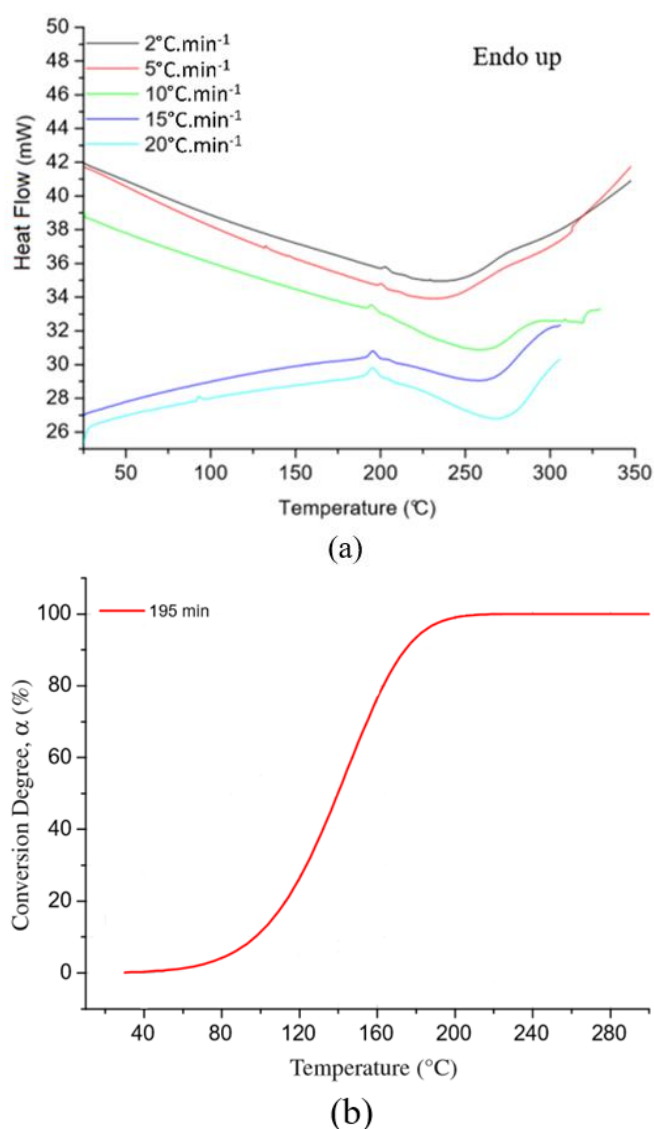


Figure 2. DSC and conversion degree curves for the Carbon/M21 epoxy prepreg. (a) Dynamic DSC curve at different heating rates. (b) Degree of conversion, α , at 2 °C min⁻¹, considering an isotherm of 120 min.

According to Paris *et al.* (2012), prepreg M21 is a thermoset resin loaded with thermoplastic particles, which limit the propagation of cracks. Thermoplastics, which represent around 30% by weight of the resin, consist of polyamide 6; polyamide 6/12 copolymers introduced as nodules after mixture of the reagent system and the melted poly(ether sulfone) (PES). Although the composition of the epoxy/amine system is a classic composition, the presence of polyamides suggests that after the melting of the particles (the melting of the polyamide occurs at temperatures greater than 190 °C-PA 6/12), they can react with the epoxy resin, modifying the curing kinetics of the conventional epoxy/amine system. This reaction can either improve the functional characteristics of the system, but it can also cause a rupture in the property of resistance to crack propagation.

Due to the possible complex chemical formulation of M21 (Paris *et al.*, 2010; 2012), it can be understood that the physical-chemical study itself is not trivial, both for the characterization of its chemical components and for the kinetic study, since, as previously noted, kinetics involves so much the available reagents as to the stoichiometric proportion present in the resin.

Thus, identifying trends in Tab. 2 becomes a difficult task. The initial temperature of cure was identified as occurring immediately after the endothermic peak. It can

be observed that the cure of M21 in the DSC starts at practically all heating rates studied around 202 °C and finished around 303 °C.

According to Tab. 2, the reaction order (n), the activation energy (E_a) and the pre-exponential factor ($\ln A$) increase with the reduction of the heating rate. The order of reaction and the enthalpy are related to the area of the curve obtained in the DSC graph, which is straightly involved with the disappearance of epoxy groups during curing. As also found for prepreg 8552, the cure reaction order is fractional ($n \sim 1.8$ to 0.6), implying complex reaction mechanisms.

The enthalpy value decreases with increasing heating rate. It was expected that the greater the enthalpy, the greater the formation of cross-links, that is, the greater the crosslinking and, consequently, the greater the value of the T_g found. However, the highest T_g value found was for the heating rate of 5 °C min⁻¹, suggesting that for this system the enthalpy value, that is, the heat of reaction generated during curing should not be considered as an indication of the T_g reached. For all these reasons, it is observed that an interpretation of the data in Tab. 2 is very difficult, a fact that can be attributed to the formulation of M21, as shown in the literature (Costa *et al.*, 2005; Paris *et al.*, 2010; 2012).

Table 2. DSC results and kinetic parameters obtained for the M21 prepreg at different heating rates.

Heating Flow (°C/min)	T _{initial} (°C)	T _{onset} (°C)	T _{peak} (°C)	T _{final} (°C)	-ΔH (J g ⁻¹)	n	lnA (s ⁻¹)	E _a (kJ mol ⁻¹)	T _g (°C)
2	206	213	242	310	194	1.8 ± 0.1	20.3	112 ± 9	178
5	200	206	239	303	158	1.2 ± 0.1	18.3	101 ± 3	183
10	201	207	258	304	153	0.8 ± 0.1	11.9	75 ± 2	176
15	204	206	268	304	125	0.7 ± 0.1	10.1	67 ± 1	168
20	203	207	270	306	137	0.7 ± 0.1	11.3	71.6 ± 0.4	170

An important factor to remember is that the cure cycle suggested by the manufacturer (Hexcel Corporation, 2021a), shows that M21 must be cured at a maximum temperature of 180 °C. This may be an indication of confirmation of the presence of polyamide 6/12 in the formulation, as this curing temperature prevents the polyamide from melting (melting of polyamide 6/12 occurs at 190 °C (Paris *et al.*, 2010; 2012) and begins to react with the epoxy resin during its cure with the amine (Paris *et al.*, 2012). Ersoy and Tugutlu (2010) state that there are thermal events occurring in the M21 formulation below 150 °C, however, such events are of low intensity and therefore are not registered by the DSC equipment. This explains why although the DSC does not record cure before 200 °C, it is occurring at 180 °C,

as suggested by the prepreg supplier's cure cycle (Hexcel Corporation, 2021b). To try to confirm this information, rheological studies were carried out in order to find the system's gelling temperature, thus indicating the actual beginning of M21 cure. This subject is covered in the topic Rheological Characterization.

The cure cycle suggested by the prepreg supplier is constituted by two steps: heating from 30 °C to 180 °C at 2.0 °C min⁻¹ and holding at 180 °C for 120 min. Thus, Fig. 2b represents the mathematical simulations of the degree of conversion of the M21-epoxy resin obtained from the time and temperature values suggested by the cure cycle provided by the supplier.

In Fig. 2b, it is possible to identify an important data for the heating rate of 2 °C min⁻¹ (heating rate suggested

by the prepreg supplier), with the gradual increase in temperature at this rate, a degree of conversion close to 10% of the total cure at 100 °C. Another important point is that when the temperature of 180 °C is reached, the degree of conversion is already greater than 90% for this heating rate.

3.2 DMA

3.2.1 Prepreg 8552

Pre-impregnated epoxy resin 8552 was cured at the different heating rates studied (2, 5, 10, 15, and 20 °C min⁻¹) inside the DMA equipment. Then, after dynamic curing of the material, the same sample was heated again at a rate of 2 °C min⁻¹, according to the [ASTM D7028-07 \(2015\)](#) standard, to obtain the T_g . This study was carried out with the objective of evaluating the influence of the heating rate used on the curing of the material and on the T_g .

Figure 3 shows the DMA, storage modulus (E'), loss modulus (E'') and tan delta curves as a function of the temperature of the 8552-epoxy resin prepreg samples cured at 2 °C min⁻¹ and **Tab. 3** summarizes the values found for T_g . At the start of heating at 2 °C min⁻¹ the storage modulus (E') is 5.1 GPa, after the temperature of 160 °C the (E') begins to increase again until reaching its maximum value of 12.9 GPa at around 240 °C. This probably occurs due to the reduction of the viscosity of the resin with the increase of the temperature, consequently reducing the rigidity of the material (E') and, after reaching the gelation point, the curing process of the prepreg begins, until its consolidation, where the (E') presents its maximum value.

The same behavior is observed for all heating rates studied (although the E' values are lower) with the exception of the rate of 20 °C min⁻¹, which does not appear to allow an adequate cure of the prepreg. The heat transfer carried out inside the DMA furnace occurs through radiation and convection, therefore, heat transfer processes are not as efficient as in a DSC, where the heat transfer occurs by conduction (thermal contact). Therefore, high heating rates in DMA are not widely used due to the inefficiency in controlling the sample temperature, which is much higher than that used in a DSC. Thus, these factors can damage the cure of the prepreg inside the DMA.

Another interesting fact observed in **Fig. 3a** is that the tan delta presents several peaks during the heating of the material, suggesting that different thermal events are happening during/final cure. This event illustrates that the formulation of epoxy resin 8552 does not consist only

of epoxy resin and amine, but of other components such as thermoplastics. This fact is investigated with FTIR technique.

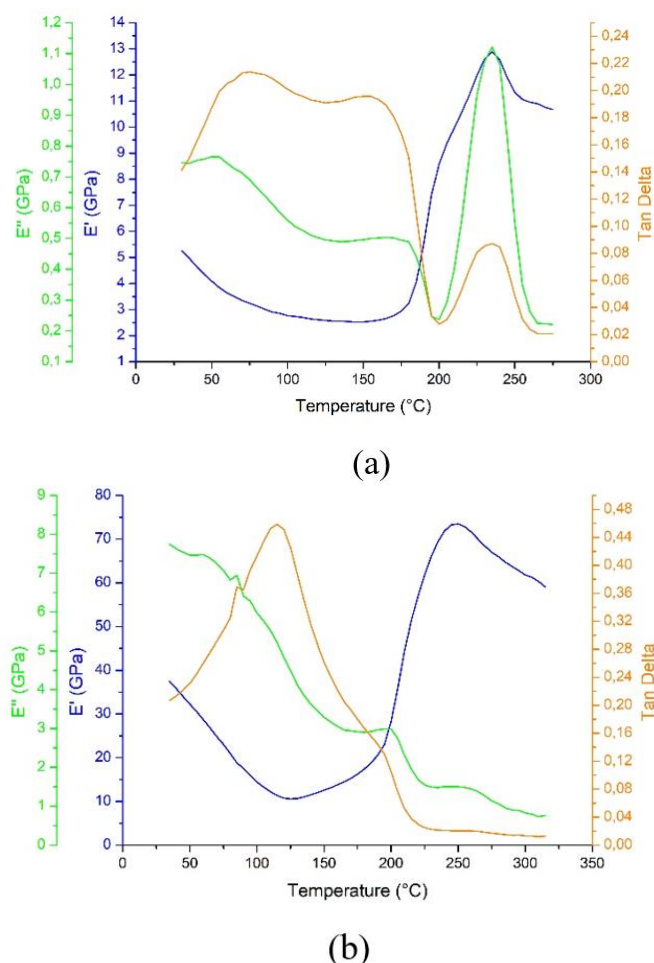


Figure 3. DMA curve of curing of prepreg systems at a heating rate of 2 °C min⁻¹. (a) Carbon/8552 prepreg and (b) Carbon/M21 prepreg.

For amorphous polymers, as in the case of epoxy resin prepreps, the dynamic-mechanical behavior in the glass transition region can change from a typical behavior of rigid materials to that of an elastomeric material and its modulus, on average, from 10³ to 10⁴ Pa. Therefore, it is possible to observe in this region a reduction in the storage module (E') and increments in both the loss module (E'') and the mechanical damping or internal friction in a viscoelastic system tan delta ([Wetton et al., 1991](#)).

The value obtained from T_g by E' onset (215 °C) for the prepreg cured at 2 °C min⁻¹ is greater than the value reported by the prepreg supplier (195 °C) ([Hexcel Corporation, 2021a](#)). Although the T_g measurement technique is the same in both cases (E' onset), the curing cycle, the size of the specimen and the apparatus used in

the prepreg processing were different. In the case of the prepreg supplier, it was used an autoclave to cure a laminate with defined thickness and with a curing cycle with dynamic temperature variations and isotherms. In the present study, only a dynamic cure of one pre-impregnated ply at a constant heating rate. Thus, different types of processing generate materials with different thermal and mechanical properties.

Table 3. Glass transition temperature obtained DMA by different methods: Onset E'; Peak E'', and tan delta for the 8552-prepreg cured at different heating rates.

Heating Rate (°C min ⁻¹)	T _g (onset of E')	T _g (peak of E'')	T _g (peak tan delta)
2	215	232	236
5	211	229	231
10	210	227	230
15	205	224	227
20	197	223	230

3.2.2 Prepreg M21

M21 prepreg was also cured at the different heating rates studied (2, 5, 10, 15, and 20 °C min⁻¹) inside DMA equipment. Then, after dynamic curing of the material, the same sample was also heated again at a rate of 2 °C min⁻¹, according to the [ASTM D7028-07 \(2015\)](#) standard, to obtain the glass transition temperature.

Figure 4 shows the DMA for M21 prepreg samples cured at 2 °C min⁻¹. It is observed that E' starts on heating with a value of approximately 40 GPa at 30 °C (2 °C min⁻¹) and decreases with the temperature increasing. From the heating temperature of 120 °C, the E' starts to rise again until it reaches its maximum value of 73 GPa around 250 °C. This probably occurs due to the reduction of the resin viscosity with increasing temperature, consequently reducing E' and, after reaching the gelation point, the prepreg curing process begins, until its solidification, where E' presents its maximum. The same behavior is observed for all rates studied (not showed in the presented work) with the exception of the rate 20 °C min⁻¹, similar to the process in prepreg 8552.

The existence of more than one thermal event is also confirmed by the loss modulus and tan delta curves in the M21 prepreg sample, with increasing temperature, since more than two peaks are generated in (E'') and tan delta.

These events, as shown by DSC, must be related to the complex cure of M21, associated with its formulation, which has other constituents besides epoxy resin and amine.

Figure 4 and **Tab. 4** shows that the M21 glass transition temperature measured by E' onset was between 168 to 184 °C. It is not possible to establish a relationship between the heating rate used in curing the material and the T_g obtained. The E'' and tan delta curves (**Fig. 4**) show graphs with more than one peak, suggesting that the material may not have homogeneously cured. For this reason, different types of cures obtain different values of T_g, a fact that suggests a material consisting of several components or some other thermal event, such as melting.

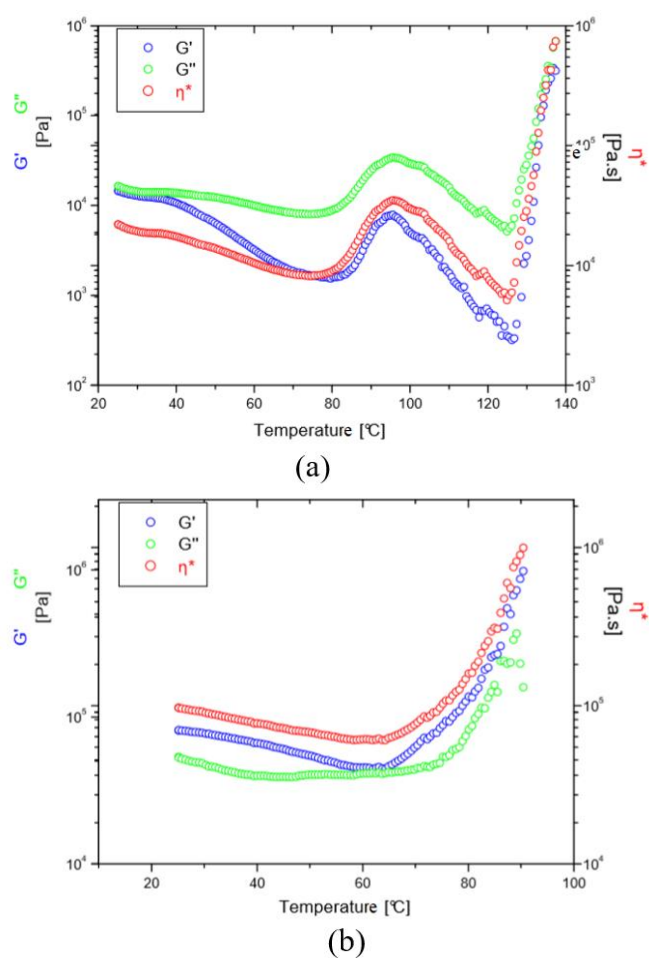


Figure 4. Rheological curves obtained for prepreg systems at 2.5 °C min⁻¹. (a) 8552 and (b) M21.

Table 4. Glass transition temperature obtained by DMA by different methods: Onset E'; Peak E'' and tan delta for prepregs M21 cured at different heating rates.

Heating Rate (°C min ⁻¹)	T _g onset of E' (°C)	T _g peak ₁ of E'' (°C)	T _g peak ₂ of E'' (°C)	T _g peak ₁ tan delta (°C)	T _g peak ₂ tan delta (°C)
2	178	207	248	205	253
5	184	-	214	-	257
10	177	-	218	-	222
15	168	-	221	-	223
20	170	-	221	-	223

The variation of T_g that occurs in the material can be studied through the tan delta (relation between the values of elasticity moduli (E''/E')) that has influence of the internal and/or external characteristics of the phase. The presence of a more rigid phase in the material can move the T_g to higher values. This increase can be caused by the polymeric chain (inclusion of rigid groups, bulky side groups, low symmetry of the molecule, increased molar mass or through secondary forces). On the other hand, the plasticization of a phase by external agents or low molar mass fractions increases the mobility of polymer chains within this phase, reducing the T_g measured by tan delta (Menard, 1999; Urban *et al.*, 2007).

The M21 epoxy resin system showed an endothermic event in the DSC experiments, recognized by Paris *et al.* (2010; 2012) as the melting of polyamide 6/12, and it is important to note that the T_g of the material is very close to the temperature of melting, which can cause interference when assessing M21 by DMA and DSC techniques.

For more detailed studies of the factors, which can influence the curing kinetics and the T_g of the material, it is important to use techniques that can identify and also quantify the components present in the M21 resin system.

3.3 Rheological characterization

As previously described, a parallel plate rheometer was used to measure the gelation temperature of the prepreg studied. The gel temperature (T_g) of a thermoset system is specific to each system, depending on the purity, shelf life, chemical nature, and degree of cure of resin. In T_g , there is an infinite three-dimensional network coexisting with countless free chains. When the system reaches the gel time, the polymer network becomes denser, with the consequent branching and increase of the molecular chains and, due to this behavior, the flexibility and mobility of the material decreases (Costa *et al.*, 2006).

3.3.1 Prepreg 8552

Figure 4a and Tab. 5 show the rheological parameters for epoxy resin type 8552 analyzed at various heating rates. It was found that the region of minimum viscosity occurred at higher temperatures with the increase in the heating rate, probably due to slower curing kinetics, caused by the faster heating of the analyzed sample. However, the minimum viscosity value decreased significantly with the increase in the heating rate, due to the higher temperatures favoring the breaking of secondary bonds existing in the polymer matrix structure and also the increase in free volume (Menard, 1999).

During the rheological analysis, a significant evolution of the complex viscosity was verified after passing through the region of minimum viscosity, characterizing a continuous increase of the elastic component, due to a network formed by particles or aggregates interconnected by elastic interactions, characterizing the phase from a Newtonian system to a viscoelastic system. During polymerization, as the reaction occurs, the polymer chains grow, and then branch and, depending on the density of cross-links, their flexibility and mobility decrease (Menard, 1999).

The gradual increase in viscosity after the minimum point is due to a slow restructuring of the system. Thus, simply by observing the evolution of the complex viscosity allowed determining the gel time or temperature. The gel temperature increased with increasing heating rate ranging between 130 and 177 °C.

Rheological curves obtained in this work (not showed in this article) showed initially $G'' > G'$ (i.e., viscous behavior dominates elastic behavior: liquid behavior). This behavior was followed by the gel state with $G' > G''$ (gel or solid-like behavior). When the curves of G' and G'' intersect ($G' = G''$ or $\tan \delta = G''/G' = 1$) the sol-gel transition point or the gelation point was achieved. At this point the epoxy resin is in the liquid state and the curves of G' , G'' , and η^* show minimum values. This decrease in the η^* value is attributed to the gradual destruction of existing interaction forces, i.e., gradual destruction of van der Waals forces. The observed viscosity behavior shows that the heating rate increasing

shifts the minimum viscosity temperature to higher value (T_{η} minimum) (Tab. 5). Subsequently, over time, the curves of G' , G'' , and η^* increase due to the curing reaction and the formation of a three-dimensional network of crosslinked molecules. After the gel time, the

network of polymeric chains densifies and the molecular chains growth, with a decrease in the flexibility and mobility of the polymer (Costa *et al.*, 2006; Mphahlele *et al.*, 2019).

Table 5. Prepreg rheological parameters for M21 and 8552 epoxy systems at different heating rates.

	Heating Rate (°C min ⁻¹)	η^*_{minimum} (Pa.s)	$T_{\eta^*_{\text{minimum}}}$ (°C)	T_{gel} (°C)	T_{gel} (°C) $G'=G''$
Prepreg M21	2.5	60406	64	67	-
	5.0	419	64	96	106
	10.0	2014	75	96	108
Prepreg 8552	2.5	5133	125	130	137
	5.0	340	156	163	169
	10.0	6.77	158	177	189

Table 5 shows for prepreg 8552 that the increase of the heating rate reflected in the reduction complex viscosity (η^*) associate with the increase of the temperature of minimum viscosity. This decrease in viscosity occurs due to the increase in free volume and the gradual destruction of interaction forces (van der Waals interactions). After this point the curing process of the prepreg begins, with the formation of a three-dimensional network.

3.3.2 Prepreg M21

Figure 4b and Tab. 5 present the rheological parameters determined for the resin M21 analyzed at different heating rates. It was found, again, that the region of minimum viscosity occurred at higher temperatures, with the increase in the heating rate. However, the value of the minimum viscosity decreased significantly with the heating rate increase, mainly for the rate of 5 °C min⁻¹, not showing a linear behavior when compared to the heating rate of 10 °C min⁻¹, also observed by Paris *et al.* (2010; 2012). They have used on their research with M21 resin, six heating rates (1, 3, 5, 10, 20, and 50 °C min⁻¹) and observed that the complex viscosity decreases with the increase of heating rate, however when comparing the heating rate of 5 °C min⁻¹ and 10 °C min⁻¹, the rate of 5 °C min⁻¹ has a lower viscosity than 10 °C min⁻¹.

In viscoelastic monitoring, the gel time/temperature can still be obtained by two other methods: by crossing

G' (storage module) with G'' (loss module) or by varying the $\tan \delta$ (damping), in which the curing temperature starts to occur for values of $\tan \delta$ equal to 1 ($\tan \delta = G''/G'$).

The gel temperature (T_{gel}) observed from η^* curves vary between 67 and 96 °C, depending on the heating rate used. The gel point obtained from the crossing of G' with G'' is not observed for 2.5 °C min⁻¹, but it is verified in the other heating rates studied, and varied between 106 and 108 °C. The difference between the T_{gel} values obtained by method of in η^* analysis and by the crossing of G' with G'' was 10% on average.

3.4 FTIR

3.4.1 Prepreg 8552

The UATR accessory was used to evaluate the studied samples. Figure 5 line A (spectrum A) shows the spectrum obtained for the prepreg 8552 without any treatment and shows the presence of epoxy resin, and some absorption of an amino component, probably due to the curing agent. The presence of absorption in the carbonyl region was observed and it can come from a modified epoxy resin or reaction product with the curing agent used. Table 6 presents the main bands of the components that are probably part of the composition of the 8552 and M21 epoxy resin systems studied.

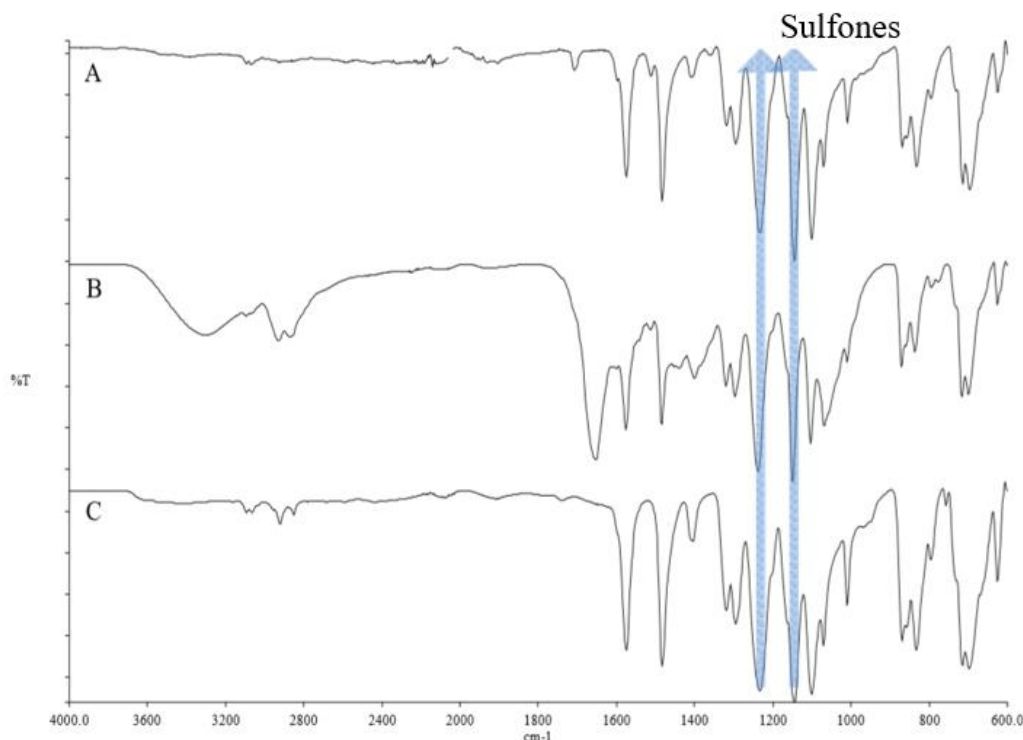


Figure 5. Infrared spectra obtained for the Carbon/8552 prepreg system. Spectrum (A) Surface of the prepreg sample 8552 using the UATR technique, (B) Part soluble in hot pyridine, (C) pure PES obtained using the UATR technique.

Table 6. Main FTIR bands of prepreg 8552 and M21 (Silverstein, *et al.*, 2006).

Component	Technical features	
	8552	M21
Amines	Average ~3400	Average ~3400
	Strong ~1510	Strong ~1510
Epoxy	Average ~2990 – 3050	Average ~2990 – 3050
	Average ~815 – 950	Average ~815 – 950
Sulfones	Strong ~1290 – 1340	Strong ~1290 – 1340
	Strong ~1120 – 1165	Strong ~1120 – 1165
Amides	-	Strong ~3300
	-	Strong ~1550

Figure 5 shows the spectrum of 8552 sample using the UATR (A), and also from the film obtained after treatment with acetone and dilution with pyridine (B), and the spectrum of pure PES (C). The similarity between the spectra showed that the PES polymer is part of the composition of this epoxy resin system.

Although the infrared spectroscopy technique is not a separation technique, the treatments with solvents allowed identify, even at low levels, the presence of thermoplastics. So, based on the analysis performed by infrared spectroscopy of the prepreg sample 8552, it is possible to observe the presence of epoxy resin, probably bisphenol-A diglycidyl ether (DGEBA), amine curing agent and PES.

3.4.2 Prepreg M21

The UATR was also used to evaluate the prepreg M21. Figure 6a shows the spectrum obtained from the surface of M21 prepreg (A) and the spectrum of pure PES (B). The spectrum A shows the presence of typical contributions of epoxy resin, and some absorptions of amine component. It is also observed the presence of absorption in the carbonyl region and its presence may come from a modified epoxy resin or reaction product. This spectrum when analyzed by means of polymer libraries for commercial use (HR Hummel Polymer and Additives) brought a good correlation to the product called poly(1,4-phenyleneethersulfone), commercially known as PES. Table 6 presents the main contributions present in the M21 epoxy system. The similarity between

the spectra A and B in Fig. 6a and the correlation provided by the commercial polymer library shows that the PES polymer is part of the composition of the M21 epoxy resin system.

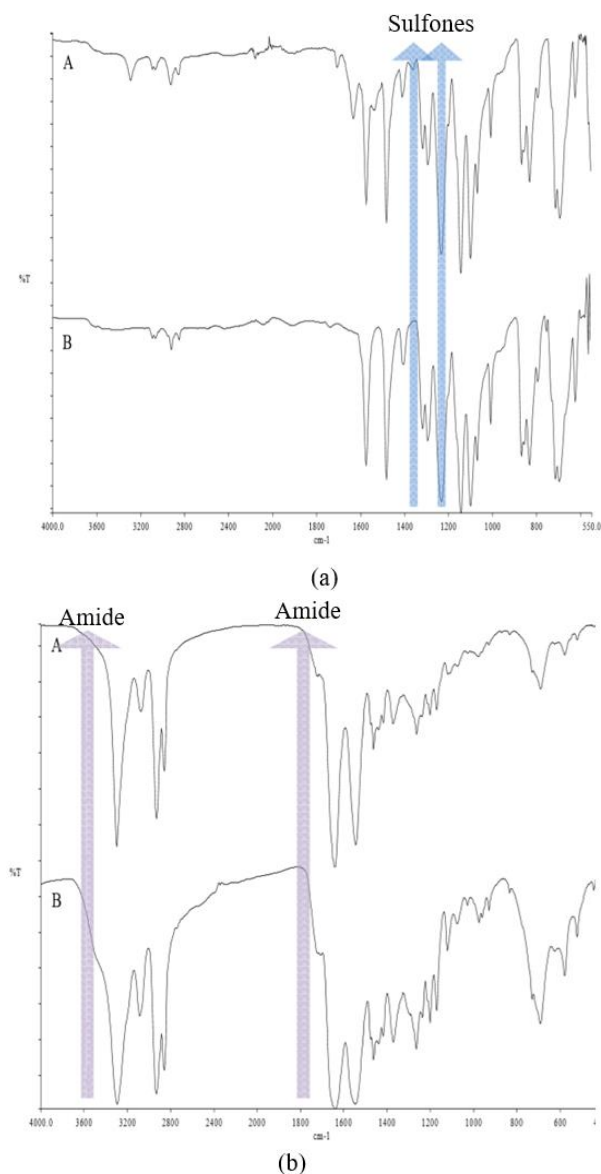


Figure 6. Infrared spectra obtained for the Carbon/M21 prepreg system. (a) Spectrum (A) surface of the prepreg sample M21 and (B) pure PES, both obtained using the UATR technique. (b) Spectrum (A) part soluble in hot formic acid of the M21 sample using the cast film technique and (B) pure polyamide.

In addition, there is a small band in the region of 3295 cm⁻¹, region of the NH groups and also in the regions of 1634 and 1543 cm⁻¹ (Fig. 6b) which, as described by Silverstein *et al.* (2000), are regions of the polyamides. This sample was treated with hot formic acid in order to dissolve the PES and/or the separation of

a possible polyamide present in M21 prepreg. Figure 6b shows the spectrum generated in line A and also the spectrum of a pure polyamide Line B. In the spectrum obtained, it is not possible to classify polyamide 6, 6/6 or even 6/12, it is possible to conclude only the presence of polyamide in the composition of prepreg M21. This result was also found by Paris *et al.* (2010; 2012) and Ueda *et al.* (1994), which suggest a peak melting of the polyamide during curing of the material in the DSC.

Based on the analysis carried out by infrared spectroscopy of the prepreg sample M21, it is possible to observe the presence of epoxy resin, probably DGEBA, based on bisphenol A, amine curing agent of the type diaminodimethylsulfone (DDS), polyethersulfone (PES), and polyamide, probably 6/12.

4. Conclusions

In the present study, the cure kinetics for M21 and 8552 prepreps, used in the aeronautical industry, was evaluated by DSC, DMA, rheometry, and FTIR spectroscopy. DSC results demonstrated that the heating rate of 2.0 °C min⁻¹ prepreps is more adequate to manufacture the polymeric composite and that the kinetic of cure occurs according to order n. M21 prepreg showed that thermoplastic components are present in its formulation due to an endothermic peak. DMA analysis confirmed that the more adequate heating rate is 2.0 °C min⁻¹ for both prepreps. The 8552 and M21 resins prepreps showed in their DMA curves, other thermal transitions, which show other components in their formulations, not only epoxy resin and amine. The glass transition temperature obtained for the 8552-resin cured at a dynamic rate of 2 °C min⁻¹ is 215 °C and for the M21 is 178 °C. The rheological results are consistent with DMA and with the results predicted in the literature for epoxy resins toughened with unknown agents, having contributed to confirm the presence of thermoplastic in the formulation of the studied resins. In addition, the rheological analysis confirms the use of rates lower than 2 °C min⁻¹ for curing these materials, as well as the need for curing ramps. The results obtained by FTIR show that in prepreg 8552 the resin contains epoxy, probably DGEBA based on bisphenol A, amine curing agent and polyethersulfone (PES). For M21 resin, it includes epoxy resin type DGEBA, curing agent type DDS, polyamide and PES. DSC, DMA and rheological analyses have proven to be adequate techniques to establish proper curing cycles for M21 and 8552. This study contributes to the processing of structural composite materials for aerospace use, supporting to establish adequate curing cycles that prevent material losses.

Authors' contribution

Conceptualization: Rezende, M. C.; Botelho, E. C.; Costa, M. L.

Data curation: Silva, S. M.; Silva, C. P. N.; Silva, T. C.

Formal Analysis: Rezende, M. C.; Botelho, E. C.; Costa, M. L.

Funding acquisition: Not applicable.

Investigation: Silva, S. M.

Methodology: Silva, S. M.; Rezende, M. C.; Costa, M. L.

Project administration: Not applicable

Resources: Not applicable.

Software: Not applicable.

Supervision: Rezende, M. C.; Costa, M. L.

Validation: Rezende, M. C.; Botelho, E. C.; Costa, M. L.

Visualization: Silva, C. P. N.; Silva, T. C.

Writing – original draft: Silva, S. M.; Silva, C. P. N.; Silva, T. C.

Writing – review & editing: Rezende, M. C.; Botelho, E. C.; Costa, M. L.

Data availability statement

All dataset were generated or analyzed in the current study.

Funding

Fundação de Amparo à Pesquisa do Estado de São Paulo (FAPESP). Grant No: 2017/16970-0.

Conselho Nacional de Desenvolvimento Científico e Tecnológico (CNPq). Grant No: 306576/2020-1; 304876/2020-8.

Coordenação de Aperfeiçoamento de Pessoal de Nível Superior (CAPES). Finance Code 001.

Acknowledgments

The authors would like to thank Milton Faria Diniz from the Chemistry Division/IAE/DCTA for his assistance in the FTIR analysis.

References

Agius, S. L.; Magniez, K. J. C.; Fox, B. L. Cure behaviour and void development within rapidly cured out-of-autoclave composites. *Compos. B. Eng.* **2013**, *47*, 230–237. <https://doi.org/10.1016/j.compositesb.2012.11.020>

ASTM E1356-08. Standard Test Method for Assignment of the Glass Transition Temperatures by Differential Scanning Calorimetry. ASTM International, 2014a. <https://doi.org/10.1520/E1356-08R14>

ASTM E968-02. Standard Practice for Heat Flow Calibration of Differential Scanning Calorimeters. ASTM International, 2014b. <https://doi.org/10.1520/E0968-02R14>

ASTM D7028-07e1. Standard Test Method for Glass Transition Temperature (DMA T_g) of Polymer Matrix Composites by Dynamic Mechanical Analysis (DMA). ASTM International, 2015. <https://doi.org/10.1520/D7028-07E01>

ASTM E967-18. Standard Test Method for Temperature Calibration of Differential Scanning Calorimeters and Differential Thermal Analyzers. ASTM International, 2018. <https://doi.org/10.1520/E0967-18>

ASTM D4473-08. Standard Test Method for Plastics: Dynamic Mechanical Properties: Cure Behavior. ASTM International, 2021. <https://doi.org/10.1520/D4473-08R21>

Botelho, E. C.; Scherbakoff, N.; Rezende, M. C. Porosity control in glassy carbon by rheological study of the furfuryl resin. *Carbon*. **2001**, *39* (1), 45–52. [https://doi.org/10.1016/S0008-6223\(00\)00080-4](https://doi.org/10.1016/S0008-6223(00)00080-4)

Braga, C. I.; Rezende, M. C.; Costa, M. L. Methodology for DSC calibration in high heating rates. *J. Aerosp. Technol. Manag.* **2011**, *3* (2), 179–192. <https://doi.org/10.5028/jatm.2011.03021911>

Costa, M. L.; Botelho, E. C.; Paiva, J. M. F. D.; Rezende, M. C. Characterization of cure of carbon/epoxy prepreg used in aerospace field. *Mater. Res.* **2005**, *8* (3), 317–322. <https://doi.org/10.1590/S1516-14392005000300016>

Costa, M. L.; Rezende, M. C.; Paiva, J. M. F.; Botelho, E. C. Structural carbon/epoxy prepregs properties comparison by thermal and rheological analyses. *Polym. Plast. Technol. Eng.* **2006**, *45* (10), 1143–1153. <https://doi.org/10.1080/03602550600887251>

Das, P. P.; Chaudhary, V. Tribological and dynamic mechanical analysis of bio-composites: A review. *Mater. Today: Proc.* **2019**, *25* (4), 729–734. <https://doi.org/10.1016/j.matpr.2019.08.233>

Ersoy, N.; Tugutlu, M. Cure kinetics modeling and cure shrinkage behavior of a thermosetting composite. Istanbul: Bogazici University. *Polym. Eng. Sci.* **2010**, *50* (2), 84–92. <https://doi.org/10.1002/pen.21514>

Friedman, H. L. Kinetics of thermal degradation of char-forming plastics from thermogravimetry. Application to a phenolic plastic. *J. Polym. Sci., polym. Symp.* **1964**, *6* (1), 183–195. <https://doi.org/10.1002/polc.5070060121>

- González-Benito, J. The nature of the structural gradient in epoxy curing at a glass fiber/epoxy matrix interface using FTIR imaging. *J. Colloid Interface Sci.* **2003**, *267* (2), 326–332. [https://doi.org/10.1016/S0021-9797\(03\)00550-2](https://doi.org/10.1016/S0021-9797(03)00550-2)
- Hatter, C. B.; Shah, J.; Anasori, B.; Gogotsi, Y. Micromechanical response of two-dimensional transition metal carbonitride (MXene) reinforced epoxy composites. *Compos. B. Eng.* **2020**, *182*, 107603. <https://doi.org/10.1016/j.compositesb.2019.107603>
- Hexcel Corporation. *HexPly® 8552 Epoxy matrix (180°C/356°F curing matrix)*. 2021a. https://www.hexcel.com/user_area/content_media/raw/HexPly_8552_us_DataSheet.pdf (accessed 2021-08-11).
- Hexcel Corporation. *HexPly® M21 Epoxy matrix (180°C/350°F curing matrix)*. 2021b. https://www.hexcel.com/user_area/content_media/raw/HexPly_M21_global_DataSheet.pdf (accessed 2021-08-11).
- Hubert, P.; Johnston, A.; Poursartip, A.; Nelson, K. Cure kinetics and viscosity models for Hexcel 8552 epoxy resin. In *International SAMPE symposium and exhibition*. SAMPE. 2019.
- Liu, H.; Falzon, B. G.; Tan, W. Experimental and numerical studies on the impact response of damage-tolerant hybrid unidirectional/woven carbon-fibre reinforced composite laminates. *Compos. B. Eng.* **2018**, *136*, 101–118. <https://doi.org/10.1016/j.compositesb.2017.10.016>
- Menard, K. P. *Dynamic mechanical analysis: A practical introduction*. CRC Press. 1999. <https://doi.org/10.1201/9781420049183>
- Mesogitis, T.; Kratz, J.; Skordos, A. A. Heat transfer simulation of the cure of thermoplastic particle interleaf carbon fibre epoxy prepregs. *J. Compos. Mater.* **2018** *53* (15), 2053–2064. <https://doi.org/10.1177/0021998318818245>
- Mphahlele, K.; Ray, S. S.; Kolesnikov, A. Cure kinetics, morphology development, and rheology of a high-performance carbon-fiber-reinforced epoxy composite. *Compos. B. Eng.* **2019**, *176*, 107300. <https://doi.org/10.1016/j.compositesb.2019.107300>
- Newcomb, B. A. Time-Temperature-Transformation (TTT) diagram of a carbon fiber epoxy prepreg. *Polym. Test.* **2019**, *77*, 105859. <https://doi.org/10.1016/j.polymertesting.2019.04.006>
- Nixon-Pearson, O. J.; Belnoue, J. H.; Ivanov, D. S.; Potter, K. D.; Hallett, S. R. An experimental investigation of the consolidation behaviour of uncured prepregs under processing conditions. *J. Compos. Mater.* **2017**, *51* (13), 1911–1924. <https://doi.org/10.1177/0021998316665681>
- Oishi, S. S.; Rezende, M. C.; Origo, F. D.; Damião, A. J.; Botelho, E. C. Viscosity, pH, and moisture effect in the porosity of poly(furfuryl alcohol). *J. Appl. Polym. Sci.* **2013**, *128* (3), 1680–1686. <https://doi.org/10.1002/app.38332>
- Paiva, J. M.; Costa, M. L.; Rezende, M. C. Evaluation of thermal stability and glass transition temperature of different aeronautical polymeric composites. *Polym. Plast. Technol. Eng.* **2006**, *45* (2), 157–164. <https://doi.org/10.1080/03602550500373915>
- Paris, C.; Olivier, P. A.; Bernhart, G. Modelling of the thermokinetic behaviour and the phases transitions of a carbon/polymeric composite submitted to high heating rate ramps. *Int. J. Mater. Form.* **2010**, *3* (1), 639–642. <https://doi.org/10.1007/s12289-010-0851-8>
- Paris, C.; Bernhart, G.; Olivier, P. A.; Almeida, O. Influence of fast curing cycles on aeronautical prepreg M21/T700: polymerization control and mechanical properties. *Mater. Tech.* **2012**, *100* (6–7), 611–622. <https://doi.org/10.1051/mattech/2012010>
- Ribeiro, B.; Nohara, L. B.; Oishi, S. S.; Costa, M. L.; Botelho, E. C. Carbon nanotubes/polyamide 6.6 nanostructured composites crystallization kinetic study. *J. Thermoplast. Compos. Mater.* **2013**, *26* (7), 893–911. <https://doi.org/10.1177/0892705711430532>
- Sánchez-Soto, M.; Pagés, P.; Lacorte, T.; Briceño, K.; Carrasco, F. Curing FTIR study and mechanical characterization of glass bead filled trifunctional epoxy composites. *Compos. Sci. Technol.* **2007**, *67* (9), 1974–1985. <https://doi.org/10.1016/j.compscitech.2006.10.006>
- Silverstein, M.; Webster, F. X.; Kiemle, D. J. *Spectrometric identification of organic compounds*. John Wiley & sons. 2000.
- Ștefanov, T.; Ryan, B.; Ivanković, A.; Murphy, N. Dynamic mechanical analysis of carbon black filled, elastomer-toughened ethyl cyanoacrylate adhesive bulk films. *Int. J. Adhes. Adhes.* **2020**, *101*, 102630. <https://doi.org/10.1016/j.ijadhadh.2020.102630>
- Ueda, M.; Yokoo, T.; Nakamura, T. Synthesis of poly (ether-sulfone-amide)s by palladium-catalyzed polycondensation of aromatic dibromides containing ether sulfone structure, aromatic diamines, and carbon monoxide. *J. Polym. Sci., Part A: Polym. Chem.* **1994**, *32* (15), 2989–2995. <https://doi.org/10.1002/pat.4328>
- Urban, V. M.; Machado, A. L.; Vergani, C. E.; Jorge, E. G.; Santos, L. P.; Leite, E. R.; Canevarolo, S. V. Degree of conversion and molecular weight of one denture base and three relines submitted to post-polymerization treatments. *Mat. Res.* **2007**, *10* (2), 191–197. <https://doi.org/10.1590/S1516-14392007000200016>

Vyazovkin, S.; Burnham, A. K.; Criado, J. M.; Pérez-Maqueda, L. A.; Popescu, C.; Sbirrazzuoli, N. ICTAC Kinetics Committee recommendations for performing kinetic computations on thermal analysis data. *Thermochim. Acta.* **2011**, *520* (1–2), 1–19. <https://doi.org/10.1016/j.tca.2011.03.034>

Vyazovkin, S.; Chrissafis, K.; Di Lorenzo, M. L.; Koga, N.; Pijolat, M.; Roduitf, B.; Sbirrazzuoli, N.; Suñol, J. J. ICTAC Kinetics Committee recommendations for collecting experimental thermal analysis data for kinetic computations. *Thermochim. Acta.* **2014**, *590*, 1–23. <https://doi.org/10.1016/j.tca.2014.05.036>

Wang, Y.; Chea, M. K.; Belnoue, J. P.-H.; Kratz, J.; Ivanov, D. S.; Hallett, S. R. Experimental characterisation of the in-plane shear behaviour of UD thermoset prepregs under processing conditions. *Compos. - A: Appl. Sci. Manuf.* **2020**, *133*, 105865. <https://doi.org/10.1016/j.compositesa.2020.105865>

Wetton, R. E.; Marsh, R. D. L.; Van-de-Velde, J. G. Theory and application of dynamic mechanical thermal analysis. *Thermochim. Acta.* **1991**, *175* (1), 1–11. [https://doi.org/10.1016/0040-6031\(91\)80240-J](https://doi.org/10.1016/0040-6031(91)80240-J)

Analysis of the $\text{Pb}_{0.30}\text{Ca}_x\text{Sr}_y\text{TiO}_3$ ternary system: The effect of Ca^{2+} and Sr^{2+} cations on the electrical properties of PbTiO_3

Amanda Fernandes Gouveia^{1†}, Lara Kelly Ribeiro^{2†}, Marcelo Assis^{2†}, Elson Longo^{2†}, Juan Andrés^{1†}, Fenelon Martinho Lima Pontes^{3†}

1. University Jaume I, Department of Physical and Analytical Chemistry, Castelló, Spain.
2. Federal University of São Carlos, CDMF, São Carlos, Brazil.
3. São Paulo State University, Department of Chemistry, Bauru, Brazil.

+Corresponding author: Amanda Fernandes Gouveia, **Phone:** +5534964728071, **Email address:** gouveiad@uji.es

ARTICLE INFO

Article history:

Received: September 22, 2021

Accepted: May 19, 2022

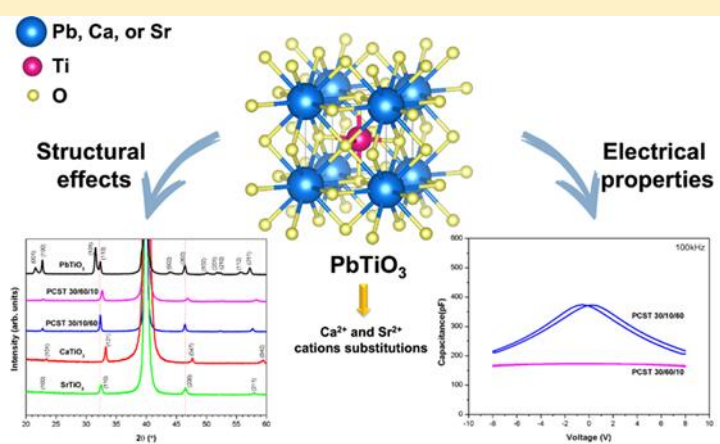
Published: August 17, 2022

Keywords

1. PCST ternary system
2. thin films
3. electrical properties
4. phase transition

Section Editor: Assis Vicente Benedetti

ABSTRACT: Powder and thin films of the $\text{Pb}_{0.30}\text{Ca}_{0.10}\text{Sr}_{0.60}\text{TiO}_3$ (PCST 30/10/60) and $\text{Pb}_{0.30}\text{Ca}_{0.60}\text{Sr}_{0.10}\text{TiO}_3$ (PCST 30/60/10) ternary system were synthesized by the polymeric precursor method and the thin films deposited on the Si/SiO₂/Ti/Pt substrate. The effects of the Sr^{2+} and Ca^{2+} cations substitutions on the electrical and structural properties of the PbTiO_3 were characterized by X-ray diffraction, Infrared, and Raman spectroscopy. Theoretical calculations were performed using the CRYSTAL06 program associated with the density functional theory and the B3LYP functional hybrid. Structural and electronic properties of the system were analyzed. The band gap values calculated for the PCST 30/10/60 and PCST 30/60/10 models were 3.35 and 3.41 eV, respectively. The results showed an evolution to a greater symmetry in the direction to the cubic SrTiO_3 structure and the phase transition was characterized by the Curie temperature dependence. The broad bands above FE-PE phase transition temperature suggest a phase transition diffuse type. It is explained by a local symmetry disorder due to a higher Sr^{2+} and Ca^{2+} cations concentration in the PbTiO_3 host lattice.



1. Introduction

Ferroelectric ceramics are among the several nanostructured materials (Yuan *et al.*, 2021; Zhang *et al.*, 2022). The idea that electronic information can be stored in the electrical polarization states of a ferroelectric material is known for a long time. Therefore the need for new information technologies, heavy incentive has been given to the development of materials and methods related to ferroelectric semiconductor memory devices by many countries and high-tech companies (e.g. Seiko Epson Corporation, Symetrix Corporation, IBM, Matsushita Electric, Sharp, Fujitsu, Ramtron International Corporation and many others) focused on the search for new materials that enable the evolution of current ones, or preferably, the creation of new technologies (Daglish and Kemmitt, 2000; Muller *et al.*, 2003).

Nanostructured ferroelectric memory systems are strong candidates for this mission due to the combination of several and interesting features in a single material (Y. Yang *et al.*, 2020). In recent years, these systems have been used in the form of nanostructured thin films. In particular, the dynamic random-access memory (DRAM) (Ling *et al.*, 2006), where the material is above the ferroelectric transition temperature or the ferroelectric random-access memory (FeRAM) (Crawford, 1971; Eshita *et al.*, 2014; 2018; Mao *et al.*, 2013), where in the ferroelectric state, below the ferroelectric transition temperature, the ability to reorient the polarization spontaneously has aroused its use as a nonvolatile memory element (Han *et al.*, 2013; Vopson and Tan, 2016). Consequently, these memories have expanded, being used in cell phones, digital cameras, electric vehicles, computers (notebooks or PCs), smart cards, etc. (Kim and Lee, 2006; Mao *et al.*, 2013). In this strategic market, there is also the possibility of using products such as identification data (ID) tag cards, where large information technology (IT) and telecommunications companies are involved. Among them, the Japanese company Matsushita Electric (best known for its Panasonic household product brand), Toshiba, IBM and others in the field stand out. These companies invest millions of dollars a year in the development and improvement of DRAM and FeRAM memories.

Surprisingly, the area of ferroelectric memories is relatively unexplored. However, this is a field of particular importance for developing knowledge and technologies related to the properties, and applications

on a nanometric scale of ferroelectric memories. Among these materials, the one with a perovskite-type structure (ABO_3 composition) stands out with its high interaction with various metals substrates, insulators, and semiconductor industry (Kour and Pradhan, 2021; J. Lee, 1999).

The phenomenon of ferroelectricity in complex oxides of the ABO_3 perovskite-type can be controlled if the characteristic size of the crystal can also be controlled (at a certain critical size (J. Lee, 1999), ferroelectricity can even be suppressed) (Ahmadi and Araghi, 2021). Understanding the properties of ABO_3 films and their interrelationship at the nanoscale may be the basis for developing a new generation of devices that will allow for the long-awaited transition from microelectronics to nanoelectronics. The perovskite with the ABO_3 structure is composed by $[AO_{12}]$ and $[BO_6]$ clusters and, according to the material, can crystallize, for example, in a cubic, tetragonal and/or orthorhombic structure (Souza, 2021).

The interest in ferroelectric thin films, especially thin films based on lead (Pb), such as $PbTiO_3$ (PT) is motivated by its potential applications as nonvolatile ferroelectric memory devices, an application based on the long retention period of the polarization and low polarization fatigue (Lázaro *et al.*, 2005; C. Yang *et al.*, 2021). Both parameters are related to the degradation phenomenon strongly dependent on the preparation process (Zhao *et al.*, 2019).

Aiming at controlling the ferroelectric properties, the coupling between the properties of the PT, $CaTiO_3$ (CT) and $SrTiO_3$ (ST) perovskites opens new possibilities for data storage in DRAM's or FeRAM's elements, which can be prepared to maximize the memory capacity in a small volume. There are several publications that bring different combinations of PT, CT and ST perovskites, resulting systems as: $Pb_{0.90}Ca_{0.10}TiO_3$ (F. Pontes *et al.*, 2008), $Pb_{0.60}Ca_{0.20}Sr_{0.20}TiO_3$, $Pb_{0.50}Ca_{0.25}Sr_{0.25}TiO_3$ and $Pb_{0.40}Ca_{0.30}Sr_{0.30}TiO_3$ (D. Pontes *et al.*, 2014), $Pb_{0.60}Sr_{0.40}TiO_3$ (Leal *et al.*, 2004), $Pb_{0.74}Ca_{0.26}TiO_3$ (Capeli *et al.*, 2017), $Pb_{0.76}Ca_{0.24}TiO_3$ (D. Pontes *et al.*, 2001a; b), and $Pb_{0.50}Sr_{0.50}TiO_3$ (F. Pontes *et al.*, 2005).

To achieve the great potential of $Pb_{0.30}Ca_xSr_yTiO_3$ (PCST) thin films (formed from the combination of PT, CT and ST perovskites) for applications in DRAM or FeRAM semiconductors, one should know how to synthesize these materials and control the stability of the perovskite phase during its processing. In this paper, it was proposed to fix the Pb^{2+} cations concentration in 0.30 and use different concentration of Ca^{2+} and Sr^{2+} cations to obtain distinct PCST ternary systems from that found in the literature.

2. Methods

2.1 Experimental procedure

The procedure for synthesizing powder and thin films of $\text{Pb}_{0.30}\text{Ca}_{0.10}\text{Sr}_{0.60}\text{TiO}_3$ and $\text{Pb}_{0.30}\text{Ca}_{0.60}\text{Sr}_{0.10}\text{TiO}_3$ (abbreviated as PCST 30/10/60 and PCST 30/60/10, respectively) consisted of producing a polymeric resin using the soft chemistry method known as polymeric precursor route. Details of the preparation method can be found in literature (Longo *et al.*, 2004; D. Pontes *et al.*, 2001a; F. Pontes *et al.*, 2003; 2004). The resin was burned at 400 °C for 4 h at a heating rate of 5 °C min⁻¹ to form a powder. The powder was characterized by X-ray diffraction (XRD) and by Raman-spectroscopy to verify the incorporation of the Ca²⁺ and Sr²⁺ cations in the PT host matrix. The ferroelectric thin films were deposited on Si/SiO₂/Ti/Pt, using spin-coating process at 6500 rpm for 30 s, and crystallized in conventional oven in a two-stage heat treatment carried out as follow: initial heating rate of 5 °C min⁻¹ until reach 400 °C and maintained for 4 h in an oxygen atmosphere to pyrolyze the organic material, followed by heating at 700 °C for 2 h at a heating rate of 5 °C min⁻¹ in the same atmosphere for crystallization. Measurements of dielectric and ferroelectric properties were taken in the Au/thin films/Pt/Ti/SiO₂/Si multilayer structure configuration. Regarding the measurement of electrical properties, circular top Au electrodes were prepared by evaporation through a shadow mask with a 4.9×10^{-2} mm² dot area to obtain an array of capacitors. The deposition was conducted under vacuum down to 10⁻⁶ torr. The frequency dependence of the capacitance was measured by an Agilent 4294A Precision Impedance Analyzer in the frequency ranging from 100 Hz to 10 MHz. The capacitance–voltage (C–V) curves were obtained using an Agilent 4294A Precision Impedance Analyzer with an AC signal of 50 mV_{rms} at 100 kHz; all measurements were taken at 25 °C.

Temperature-dependent capacitance measurements of thin films were taken from 10 to 300 K using a closed-cycle helium cryostat and a G^w Instek LCR 819 meter for capacitance measurements; all measurements were performed at 100 kHz. For these measurements, circular Au electrodes with an area of approximately 4.9×10^{-2} mm² were deposited (using a shadow mask) by evaporation on the heat-treated film surfaces which served as top electrodes in an Au/thin films/Pt/Ti/SiO₂/Si configuration.

2.2 Theoretical procedures

Theoretical calculations of electronic structure ab-initio level for the studied PCST ternary systems were performed using the CRYSTAL06 program (Dovesi *et al.*, 2005), associated with density functional theory (DFT) and the B3LYP functional hybrid (Becke, 1993; C. Lee *et al.*, 1988). The XCrySDen (2019) program was used to draw the density of states of each atom models.

The experimental results shown that the PCST ternary systems present a local organization toward to the cubic ST structure. Therefore, from the unit cell of cubic ST optimized structure, expansions in the z-axis were made to simulate a supercell, where the percentages of cations could be simulated accurately. The structural and electronic properties of these materials were analyzed to corroborate the experimental results.

3. Results and discussion

To verify the formation of the PCST ternary systems the XRD analysis was performed for the powder, as illustrated in Fig. 1. From the results, it is possible to affirm that the incorporation of Sr²⁺ and Ca²⁺ cations in the PCST ternary system was effective, obtaining a pure phase without the presence of one or more intermediate stages or even other phases, like PT, CT, ST, $\text{Pb}_x\text{Ca}_y\text{TiO}_3$, or $\text{Pb}_x\text{Sr}_z\text{TiO}_3$.

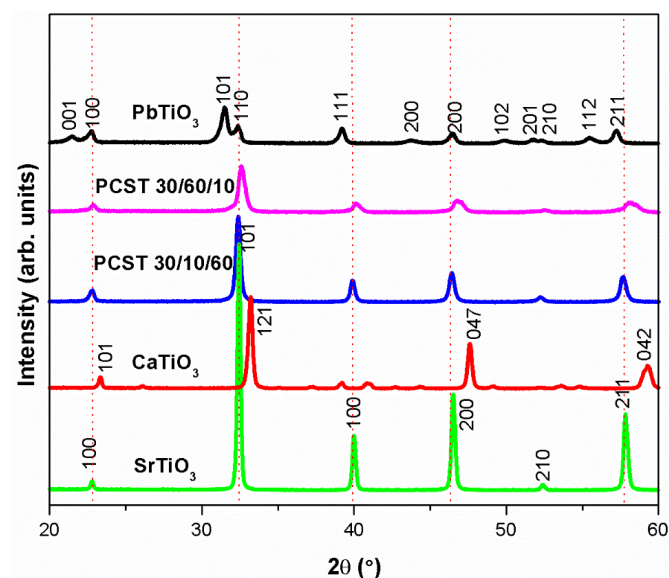


Figure 1. XRD pattern of the powder of PCST30/10/60, PCST30/60/10, PT, CT, and ST heat treated at 700 °C.

It is observed that the PCST ternary systems have evolved to a higher symmetry, in this case, toward a cubic ST structure. However, there are still weak diffraction peaks observed in the system PCST 30/60/10, which correspond to the diffraction planes of PbTiO_3 .

From the PIKFIT program, the lattice parameters were calculated for each system based on the tetragonal structure (Tab. 1). Table 1 also shows the parameters obtained from the DFT calculations. The data show that

there is a distortion in the structure, changing from tetragonal to cubic, by increasing the Sr^{2+} cations concentration in the system, as there is a decrease in the parameter c , which indicates the tetragonality factor, while the parameter a remains practically unchanged. The same result was theoretically obtained using the CRYSTAL06 program, confirming the data obtained experimentally.

Table 1. Lattice parameters (\AA) for ternary systems.

Sample	Experimental			Theoretical		
	a	c	c/a	a	c	c/a
PCST 30/10/60	3.9117	3.9122	1.000	3.8938	3.8918	0.999
PCST 30/60/10	3.8756	3.8880	1.003	3.8789	3.8771	0.999

To corroborate data of XRD analysis, the micro-Raman spectroscopy was performed. Figure 2 illustrates the micro-Raman spectra for the PCST ternary systems and for the PT standard system as reference. It is possible to observe a decrease in the tetragonality by the overlap of the micro-Raman modes $E(1\text{LO})/A1(1\text{TO})$ and $B1+E/A1(2\text{TO})$ with the incorporation of the Sr^{2+} and Ca^{2+} cations into the PT system. The $E(1\text{TO})$ soft mode decreases to lower wavelength and tends to complete disappearing, indicating a change of symmetry of a tetragonal to cubic system.

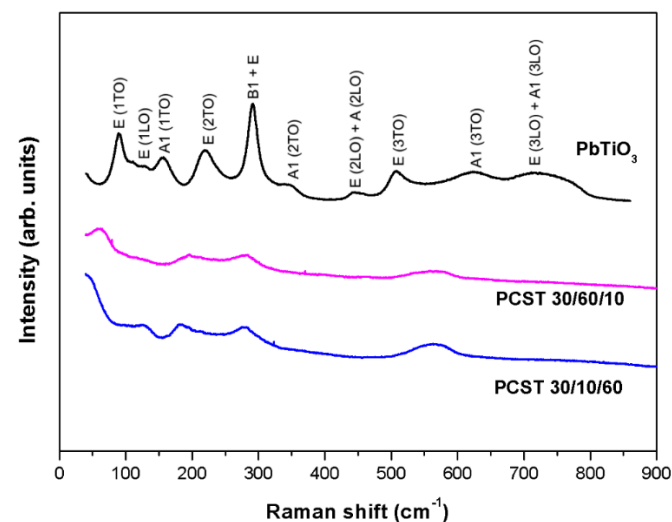


Figure 2. Micro-Raman spectra for PbTiO_3 , PCST30/10/60, and PCST30/60/10 systems.

The micro-Raman spectrum for PCST 30/60/10 system was also analyzed for different temperatures between 20 and 500 °C (Fig. 3). This study aimed at investigating the behavior of micro-Raman bands as the temperature increases, as well as to search for signs of structural changes.

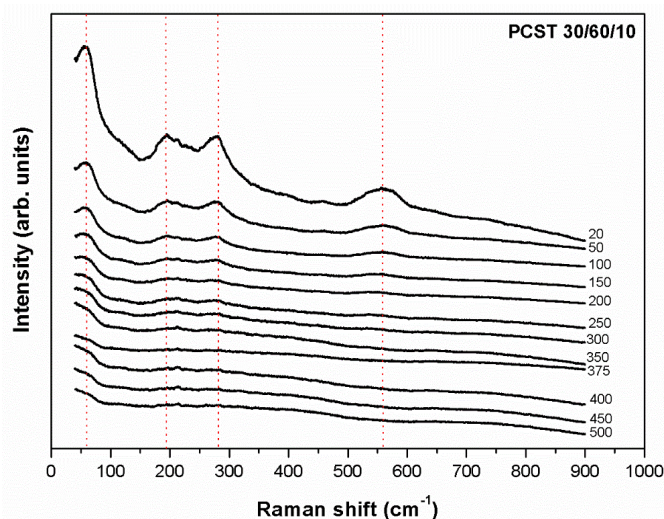


Figure 3. Micro-Raman spectrum for powder of PCST30/60/10 ternary system as function of the temperature.

It is well-known that the active micro-Raman modes $E(1\text{TO})$ and $A1(1\text{TO})$ for pure PT, and in particular the $E(1\text{TO})$ mode are soft modes, which are directly related to the transition from tetragonal to cubic type.

The phase transition temperature can be determined by micro-Raman spectroscopy by observing the temperature in which the soft mode disappears. Thus, Fig. 4 reveals that there was no phase transition from tetragonal to cubic, as the soft mode did not disappear with the increase of temperature, there is only an enlargement of the $E(1\text{TO})$ mode. An alternative for this case is an analysis as a function of pressure, i.e., to study the phase transition by applying hydrostatic pressure to the sample inside a diamond cell. Another solution is to prepare thin films of this composition and investigate its electrical properties at low temperature, for example,

from 10 to 300 K to check if a certain phase transition temperature exists.

For the analysis of the PCST ternary systems in powder form and after confirming the Ca^{2+} and Sr^{2+} cations incorporation in the system without the formation of second phase, the thin films were then prepared and characterized.

Figure 4 illustrates the XRD pattern for the thin films of the PCST ternary systems, as well as the PT, CT and ST structures.

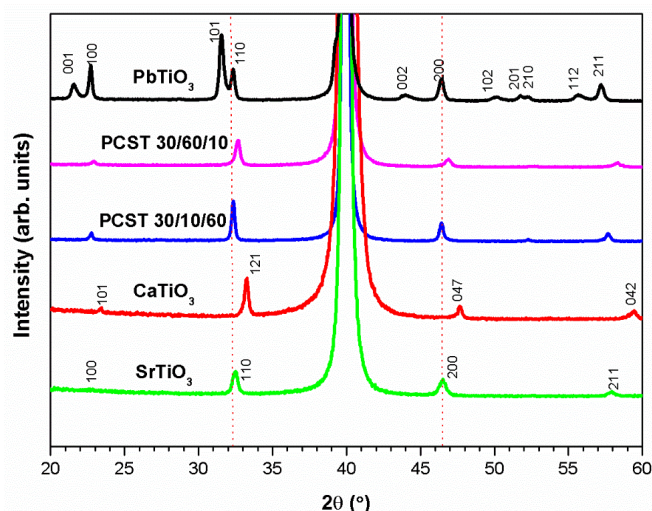


Figure 4. XRD pattern of the thin films of PCST 30/10/60, PCST 30/60/10, PT, CT, and ST on $\text{Si}/\text{SiO}_2/\text{Ti}/\text{Pt}$ substrate heat treated at 700 °C.

Table 2. Lattice parameters for the PCST ternary systems thin films. The cubic system was considered for all PCST thin films.

Sample	Structure	Parameters	Special group
* PbTiO_3	Tetragonal	$a = b = 3.899(0)$ $c = 4.153(0)$	$P4mm$
* CaTiO_3	Orthorhombic	$a = 5.3796(1)$ $b = 5.4423(3)$ $c = 7.6401(5)$	$Pbnm$
* SrTiO_3	Cubic	$a = b = c = 3.905$	$Pm3m$
PCST 30/60/10	Cubic	$a = b = c = 3.877$	$Pm3m$
PCST 30/10/60	Cubic	$a = b = c = 3.910$	$Pm3m$

Note. The unit of the parameters (a; b; c) are in Å; *data extracted from JCPDS forms.

To corroborate the XRD data the infrared spectroscopic response was analyzed with reflectance accessory. Figure 5 shows the reflectance spectra for thin films, as well as standards for SrTiO_3 and CaTiO_3 systems. These standards are important to clearly confirm the evolution to a structure with very similar characteristics of SrTiO_3 .

As can be seen in Fig. 5, there is a similarity between the spectra of thin films and ST, assuming three infrared active modes for the cubic structure, much more than that

Figure 4 allows to affirm that the replacement of the Pb^{2+} cations by Ca^{2+} and Sr^{2+} cations at the A site ($[\text{AO}_{12}]$ clusters) caused a drastic change in the XRD patterns of the PT structure. All thin films have a polycrystalline nature. Therefore, the striking tetragonal characteristic of the PCST ternary system thin film disappeared due to the substitution in the $[\text{AO}_{12}]$ cluster, as can be seen by comparing it with the PT standard.

The lattice parameters were also calculated (Tab. 2). The XRD pattern of the samples are very similar to the pure ST system, proving the complete replacement of Ca^{2+} and Sr^{2+} cations in the Pb site, mainly for the Sr^{2+} cations, as also observed in the PCST powder. Therefore, it is deduced that the Sr^{2+} cations are responsible for the transition from a tetragonal to a cubic phase; otherwise, an orthorhombic phase or even a mixture of phases would be observed. So, it can be assumed that the effect of substitution of Pb by Ca^{2+} cations is less pronounced than the effect of its substitution by Sr^{2+} cations at the $[\text{AO}_{12}]$ clusters since it presents a very similar XRD pattern to ST structure. This effect can be caused by the change in the type of bond involved, now between Sr^{2+} and Ca^{2+} cations, where Sr^{2+} cations will form a bond with a much higher ionic character (with radial characteristic) than Ca^{2+} cations. This difference in bond type is a determining factor for these structural changes. Moreover, it may have a system tending to stabilize a more symmetrical structure.

for the system CT, in which the mode identified by c is not present in any sample of PCST thin films (Tab. 3).

The spectra showed well-defined bands and characteristics of a crystalline material. The bands in the region between 400–1000 cm^{-1} are due to the longitudinal (LO) and transverse (TO) optical modes, which are associated with the crystallinity of the material (Liu *et al.*, 2010; F. Pontes *et al.*, 2002; 2003). These absorption bands obtained by the reflectance technique in the infrared spectrum are caused by the excitation of

optically active vibrations. The main band observed for the different compositions of PCST thin films located in the 600–800 cm^{-1} region is characterized by the stretch vibration of the Ti–O bond (metal-oxygen in the $[\text{TiO}_6]$ clusters). The bands in the shorter wavelength region can be attributed to Pb–O, Ca–O or Sr–O stretch vibrations.

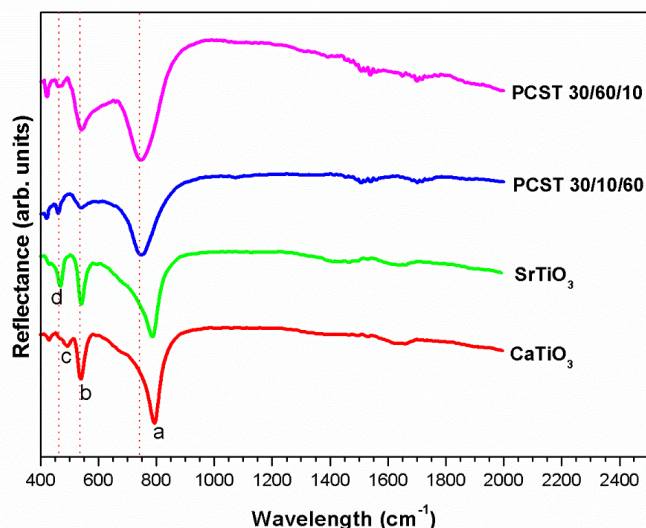


Figure 5. FT-IR reflectivity spectra for CaTiO_3 , SrTiO_3 , PCST30/10/60, and PCST30/60/10.

In the FT-IR spectrum obtained by reflectance, changes in vibrational modes and their displacements are indications of structural evolution, i.e., change from a tetragonal phase to a pseudo cubic, cubic, or orthorhombic phases. Therefore, the vibrational analysis of these materials revealed some changes in vibrational modes. These changes occurred both in displacement level and in the band width of vibrational modes. Thus, the substitution at A-site in the PT structure corresponds to a change in the distances of the A–O and/or Ti–O bonds, and this substitution is responsible for the large coupling effect in the higher energy bands.

The difference between the ST and CT spectra for the PCST systems and their similarity to ST suggest that the $[\text{TiO}_6]$ clusters present greater symmetry for the PCST system in both compositions. The simplicity of this qualitative analysis suggests that the octahedral environment at site Ti is symmetrical, not reflecting large distortions to the tetragonal or orthorhombic structure, which could be responsible for the polarization, that is caused by the presence of permanent dipoles within the material.

After confirming the effective incorporation of Ca^{2+} and Sr^{2+} cations at A-site into the PT structure, forming PCST ternary system, the nanostructured thin films were characterized for their dielectric and ferroelectric properties.

Table 3. FT-IR frequencies modes for the ST, CT, and PCST thin films.

System	a	b	c	d
SrTiO_3	786.84	541.92	-	468.63
CaTiO_3	794.56	539.99	493.70	430.06
PCST30/60/10	747.31	541.92	460.92	422.35
PCST30/10/60	746.34	541.92	461.88	420.42

Figure 6 illustrates the dielectric capacitance results in function of the frequency for the PCST 30/60/10 and PCST 30/10/60 ternary systems.

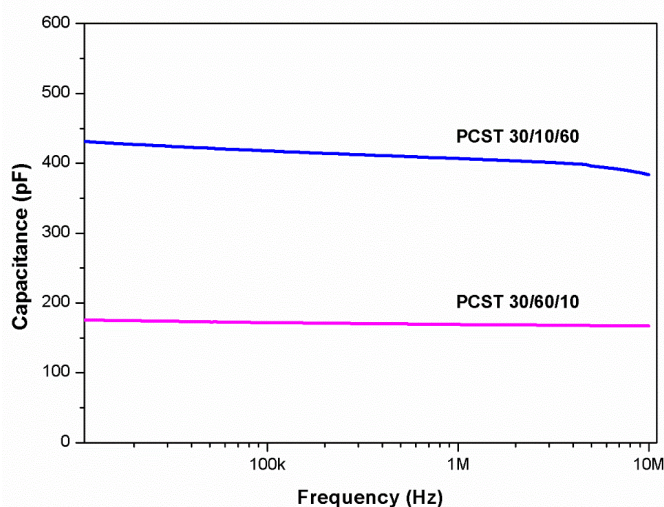


Figure 6. Dielectric capacitance of the PCST thin films prepared in O_2 atmosphere.

The results shown that the PCST30/10/60 thin film presents good values of dielectric capacitance, while the thin film with higher Ca^{2+} cations concentrations, the PCST 30/60/10, shows a lower value of dielectric capacitance, which causes an influence in the material's ferroelectric properties.

The curves of capacity vs. voltage (C–V curves) for the nanostructured PCST thin films are shown in Fig. 7. This graphic represents two measurements: one sweep from a negative to a positive electric field (*sweep up*), and another from the positive to negative field (*sweep down*).

For the ternary PCST30/10/60 system, the sweep up and sweep down measurement curves are symmetrical and not overlapped due to the ferroelectric nature of the thin film; however, this behavior is less pronounced than in the pure PT system. With the increase of the Ca^{2+} cations and the decreases of Sr^{2+} cations incorporation (PCST30/60/10 system), there is an overlapping of the sweep up and sweep down curves, which is a characteristic due to the non-ferroelectric nature of the material, i.e., a tendency towards a paraelectric phase properties.

manifested by the lack of effective local and long-range polarization.

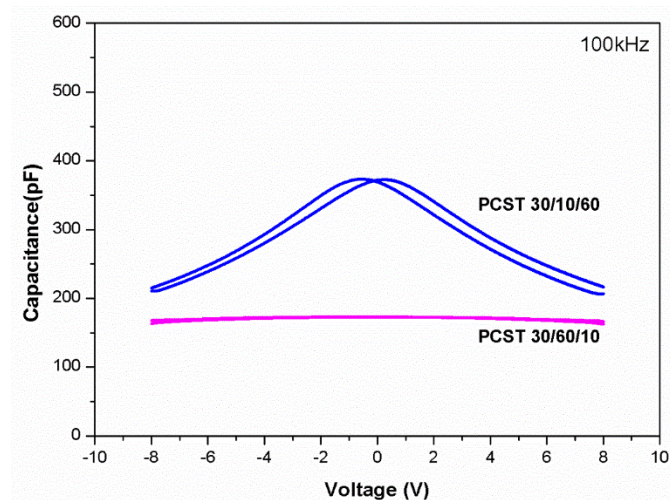


Figure 7. C–V curves for the PCST thin films prepared in O₂ atmosphere.

The phase transition of the PCST thin films was also studied by electrical characterization. Structural phase transitions are changes in crystal structure caused by changes in an order parameter, which is defined as any physical quantity describing the phase transition. In ferroelectric materials there is a temperature, called Curie temperature (T_C), in which a structural transition between the paraelectric and ferroelectric phases is observed, that is associated with a change in the material's crystalline structure to a new symmetry. An important feature of the ferroelectric phase transition is that the dielectric permittivity increases considerably at the transition temperature. Figures 8 and 9 illustrate the phase transition temperature for thin films PCST30/10/60 and PCT 30/60/10, respectively.

Figures 8 and 9 show the T_C changes as a function of the Ca²⁺ e Sr²⁺ cations concentration. The decrease of the T_C is expected since the matrix of the PCST system, PT, has a T_C ~763 K, while ST has a T_C ~105 K for a ferroelectric to paraelectric transition accompanied by a change from tetragonal to cubic structure, respectively. On the other hand, the CT presents an orthorhombic structure at room temperature and tetragonal structure at 1500 K and finally cubic structure at T_C ~1580 K. Therefore, the results confirm, once again, the strong influence of Sr²⁺ on Ca²⁺ cations and its competition within the crystal lattice of ternary PCST structure.

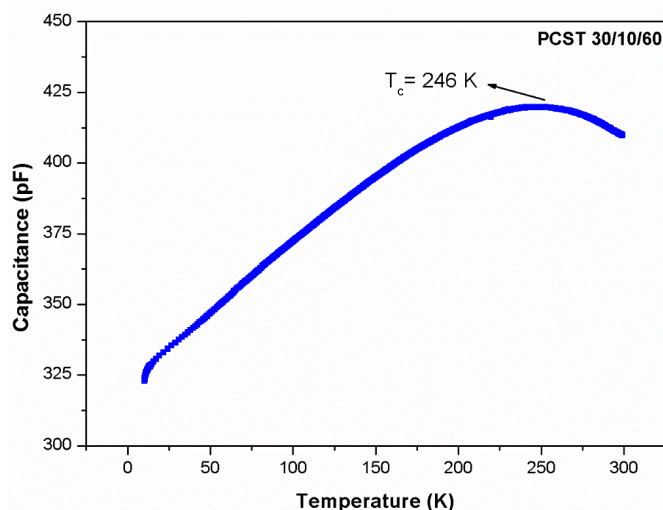


Figure 8. Dependence of capacitance as a function of temperature for PCST 30/10/60 thin film.

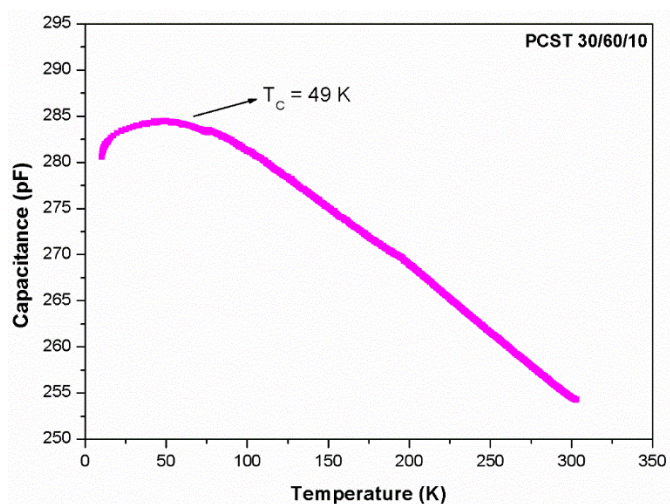


Figure 9. Dependence of capacitance as a function of temperature for PCST 30/60/10 thin film.

To check the influence of Sr²⁺ on Ca²⁺ cations in the crystal lattice of PT structure, a theoretical study of the electronic properties of the materials was performed with the analysis of the band gap value and the density of states (DOS). Figure 10 shows the DOS for the ternary PCST systems. For both systems, the contribution of Pb, Ca, and Sr to conduction band is small compared to the contribution of Ti atoms. To the valence band there is a prevailing contribution of atomic orbitals from the O atoms.

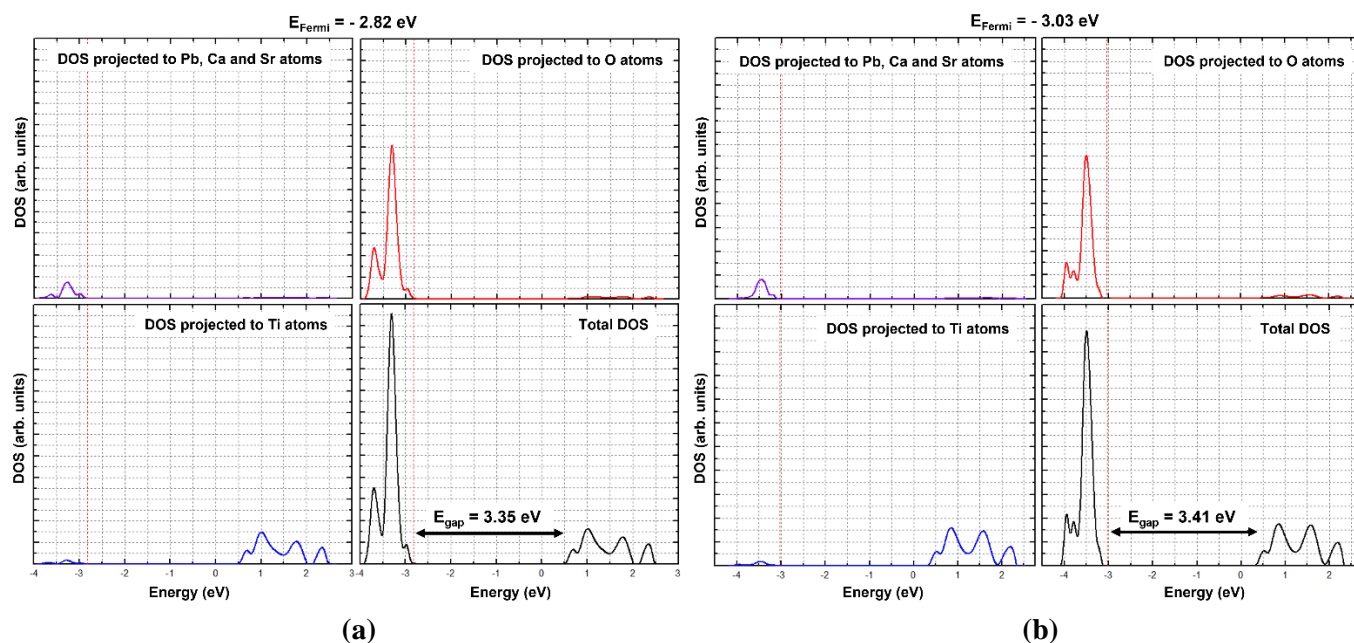


Figure 10. Total DOS: (a) PCST 30/10/60 and (b) PCST 30/60/10.

5. Conclusions

In this study, a very efficient and inexpensive chemical method to produce a good quality of ternary PCST powder and thin films were presented. In the PCST 30/10/60 and PCST 30/60/10 samples was possible to incorporate simultaneously Ca^{2+} and Sr^{2+} cations in the site AO_{12} in place of Pb^{2+} cations without phase separation, such as PbTiO_3 , CaTiO_3 , SrTiO_3 , or even as complex phase $(\text{Pb,Sr})\text{TiO}_3$ or $(\text{Pb,Ca})\text{TiO}_3$.

The studied systems, PCST 30/60/10 and PCST 30/10/60, presented a tetragonal to cubic phase transition due to the simultaneous incorporation of Ca^{2+} and Sr^{2+} cations at low temperature, thus causing the absence of the ferroelectric nature present in PT at room temperature. The results show that this fact it was more evident in PCST 30/10/60 system, where the concentration of Sr^{2+} cations in the system is greater. These incorporations decreased the tetragonality and significantly reduced the octahedron distortion, promoting the elimination of ferroelectric character at room temperature. This elimination was confirmed in the analysis of DOS projected onto the atomic orbitals of Pb, then, Pb stopped contributing to the conduction band with $6p_z$ atomic orbitals, which is responsible by ferroelectricity.

Authors' contribution

Conceptualization: Gouveia, A. F.; Pontes, F. M. L.

Data curation: Gouveia, A. F.; Ribeiro, L. K.; Assis, M.; Pontes, F. M. L.

Formal Analysis: Gouveia, A. F.; Ribeiro, L. K.; Assis, M.; Pontes, F. M. L.

Funding acquisition: Gouveia, A. F.; Longo, E.; Pontes, F. M. L.

Investigation: Gouveia, A. F.; Pontes, F. M. L.

Methodology: Gouveia, A. F.; Ribeiro, L. K.; Assis, M.; Pontes, F. M. L.

Project administration: Gouveia, A. F.; Longo, E.; Andrés, J.; Pontes, F. M. L.

Resources: Gouveia, A. F.; Longo, E.; Andrés, J.;

Software: Gouveia, A. F.; Pontes, F. M. L.

Supervision: Longo, E.; Andrés, J.;

Validation: Gouveia, A. F.; Pontes, F. M. L.

Visualization: Gouveia, A. F.; Pontes, F. M. L.

Writing – original draft: Gouveia, A. F.; Ribeiro, L. K.; Assis, M.; Pontes, F. M. L.

Writing – review & editing: Gouveia, A. F.; Ribeiro, L. K.; Longo, E.; Andrés, J.; Pontes, F. M. L.

Data availability statement

All data sets were generated or analyzed in the current study.

Funding

Fundação de Amparo à Pesquisa do Estado de São Paulo (FAPESP). Grant No: 2009/53433-6; 2013/07296-2; 2019/01732-1.

Universitat Jaume I (UJI). Grant No: POSDOC/2019/30; UJI-B2019-30.

Ministerio de Ciencia, Innovación y Universidades (Spain). Grant No: PGC2018094417-B-I00.

Acknowledgments

This work used experimental resources from Centro de Desenvolvimento de Materiais Funcionais (CDMF). A. F. G acknowledges the Universitat Jaume I for the postdoctoral contract and FAPESP for the postdoctoral fellowship. J. A. acknowledges Universitat Jaume I and the Ministerio de Ciencia, Innovación y Universidades (Spain) for financially supporting this research.

References

- Ahmadi, F.; Araghi, H. Electro-optical and phonon properties of $\text{PbTiO}_3/\text{CaTiO}_3/\text{SrTiO}_3$ ferroelectric superlattices: a first-principles calculation. *J. Nanophotonics* **2021**, *15* (2), 026003. <https://doi.org/10.1117/1.Jnp.15.026003>
- Becke, A. D. Density-Functional Thermochemistry. The Role of Exact Exchange. *J. Chem. Phys.* **1993**, *98* (7), 5648–5652. <https://doi.org/10.1063/1.464913>
- Capeli, R. A.; Pontes, F. M. L.; Chiquito, A. J.; Bastos, W. B.; Pereira-da-Silva, M. A.; Longo, E. Annealing temperature dependence of local piezoelectric response of $(\text{Pb,Ca})\text{TiO}_3$ ferroelectric thin films. *Ceram. Int.* **2017**, *43* (6), 5047–5052. <https://doi.org/10.1016/j.ceramint.2017.01.015>
- Crawford, J. C. Ferroelectric-Piezoelectric Random Access Memory. *IEEE Tran. Electron Devices.* **1971**, *18* (10), 951–958. <https://doi.org/10.1109/T-ED.1971.17309>
- Daglish, M.; Kemmitt, T. Ferroelectric thin films – research, development and commercialization. *IPENZ Transactions.* **2000**, *27* (1), 21–24. <https://search.informit.org/doi/abs/10.3316/INFORMIT.185207029730394> (accessed 2022-05-18).
- Dovesi, R.; Orlando, R.; Civalleri, B.; Roetti, C.; Saunders, V. R.; Zicovich-Wilson, C. M. CRYSTAL: a computational tool for the *ab initio* study of the electronic properties of crystals. *Z. Kristallogr.* **2005**, *220* (5–6), 571–573. <https://doi.org/10.1524/zkri.220.5.571.65065>
- Eshita, T.; Tamura, T.; Arimoto Y. Ferroelectric random access memory (FRAM) devices. *Advances in Non-Volatile Memory and Storage Technology.* **2014**, 434–454. <https://doi.org/10.1533/9780857098092.3.434>
- Eshita, T.; Wang, W. S.; Nomura, K.; Nakamura, K.; Saito, H.; Yamaguchi, H.; Mihara, S.; Hikosaka, Y.; Kataoka, Y.; Kojima, M. Development of highly reliable ferroelectric random access memory and its Internet of Things applications. *Jpn. J. Appl. Phys.* **2018**, *57*, 11UA01. <https://doi.org/10.7567/JJAP.57.11UA01>
- Han, S. T.; Zhou, Y.; Roy, V. A. L. Towards the Development of Flexible Non-Volatile Memories. *Adv. Mater.* **2013**, *25* (38), 5425–5449. <https://doi.org/10.1002/adma.201301361>
- Kim, K.; Lee, S. Integration of lead zirconium titanate thin films for high density ferroelectric random access memory. *J. Appl. Phys.* **2006**, *100* (5), 051604. <https://doi.org/10.1063/1.2337361>
- Kour, P.; Pradhan, S. K. Perovskite Ferroelectric. *IntechOpen.* **2021**. <https://doi.org/10.5772/intechopen.98382>
- Lázaro, S. R. D.; Longo, E.; Beltran, A.; Sambrano, J. R. Propriedades eletrônicas e estruturais do PbTiO_3 : teoria do funcional de densidade aplicada a modelos periódicos theory applied to periodic models. *Quim. Nova.* **2005**, *28* (1), 10–18. <https://doi.org/10.1590/S0100-40422005000100003>
- Leal, S. H.; Pontes, F. M. L.; Leite, E. R.; Longo, E.; Pizani, P. S.; Chiquito, A. J.; Machado, M. A. C.; Varela, J. A. Ferroelectric phase transition in $\text{Pb}_{0.60}\text{Sr}_{0.40}\text{TiO}_3$ thin films. *Mater. Chem. Phys.* **2004**, *87* (2–3), 353–356. <https://doi.org/10.1016/j.matchemphys.2004.05.032>
- Lee, C. T.; Yang, W. T.; Parr, R. G. Development of the Colle-Salvetti Correlation-Energy Formula into a Functional of the Electron-Density. *Phys. Rev. B.* **1988**, *37*, 785–789. <https://doi.org/10.1103/PhysRevB.37.785>
- Lee, J. D. *Química Inorgânica não tão concisa*. Blucher-São Paulo, 1999.
- Ling, Q.-D.; Chang, F.-C.; Song, Y.; Zhu, C.-X.; Liaw, D.-J.; Chan, D. S.-H.; Kang, E.-T.; Neoh, K.-G. Synthesis and dynamic random access memory behavior of a functional polyimide. *J. Amer. Chem. Soc.* **2006**, *128* (27), 8732–8733. <https://doi.org/10.1021/ja062489n>
- Liu, X. D.; Zhang, D. C.; Zhang, Y.; Dai, X. T. Preparation and characterization of p-type semiconducting tin oxide thin film gas sensors. *J. Appl. Phys.* **2010**, *107* (6), 064309. <https://doi.org/10.1063/1.3354092>
- Longo, E.; Orhan, E.; Pontes, F. M. L.; Pinheiro, C. D.; Leite, E. R.; Varela, J. A.; Pizani, P. S.; Boschi, T. M.; Lanciotti, F.; Beltrán, A.; Andrés, J. Density functional theory calculation

- of the electronic structure of $\text{Ba}_{0.5}\text{Sr}_{0.5}\text{TiO}_3$: Photoluminescent properties and structural disorder. *Phys. Rev. B*. **2004**, *69*, 125115. <https://doi.org/10.1103/PhysRevB.69.125115>
- Mao, D.; Mejia, I.; Salas-Villasenor, A. L.; Singh, M.; Stiegler, H.; Gnade, B. E.; Quevedo-Lopez, M. A. Ferroelectric random access memory based on one-transistor-one-capacitor structure for flexible electronics. *Org. Electron.* **2013**, *14* (2), 505–510. <https://doi.org/10.1016/j.orgel.2012.10.035>
- Muller, G.; Nagel, N.; Pinnowa, C. U.; Rohr, T. *Emerging non-volatile memory technologies*. 29th European Solid-State Circuits Conference. Estoril, Portugal, 2003.
- Pontes, D. S. L.; Leite, E. R.; Pontes, F. M. L.; Longo, E.; Varela, J. A. Microstructural, dielectric and ferroelectric properties of calcium-modified lead titanate thin films derived by chemical processes. *J. Eur. Ceram. Soc.* **2001a**, *21* (8), 1107–1114. [https://doi.org/10.1016/S0955-2219\(00\)00307-1](https://doi.org/10.1016/S0955-2219(00)00307-1)
- Pontes, D. S. L.; Leite, E. R.; Pontes, F. M. L.; Longo, E.; Varela, J. A. Preparation and properties of ferroelectric $\text{Pb}_{1-x}\text{Ca}_x\text{TiO}_3$ thin films produced by the polymeric precursor method. *Journal of Materials Science*. **2001b**, *36* (14), 3461–3466. <https://doi.org/10.1023/A:1017916213489>
- Pontes, F. M. L.; Leite, E. R.; Pontes, D. S. L.; Longo, E.; Santos, E. M. S.; Mergulhao, S.; Pizani, P. S.; Lanciotti, F.; Boschi, T. M.; Varela, J. A. Ferroelectric and optical properties of $\text{Ba}_{0.8}\text{Sr}_{0.2}\text{TiO}_3$ thin film. *J. Appl. Phys.* **2002**, *91* (9), 5972–5978. <https://doi.org/10.1063/1.1466526>
- Pontes, F. M. L.; Pontes, D. S. L.; Leite, E. R.; Longo, E.; Santos, E. M. S.; Mergulhao, S.; Varela, J. A. Synthesis, ferroelectric and optical properties of $(\text{Pb,Ca})\text{TiO}_3$ thin films by soft solution processing. *J. Sol-Gel Sci. Technol.* **2003**, *27* (2), 137–147. <https://doi.org/10.1023/A:1023742315962>
- Pontes, F. M. L.; Pontes, D. S. L.; Leite, E. R.; Longo, E.; Chiquito, A. J.; Machado, M. A. C.; Pizani, P. S.; Varela, J. A. A Raman and dielectric study of a diffuse phase transition in $(\text{Pb}_{1-x}\text{Ca}_x)\text{TiO}_3$ thin films. *Appl. Phys. A*. **2004**, *78* (3), 349–354. <https://doi.org/10.1007/s00339-003-2287-1>
- Pontes, F. M. L.; Leal, S. H.; Leite, E. R.; Longo, E.; Pizani, P. S.; Chiquito, A. J.; Machado, M. A. C.; Varela, J. A. Absence of relaxor-like ferroelectric phase transition in $(\text{Pb,Sr})\text{TiO}_3$ thin films. *Appl. Phys. A*. **2005**, *80* (4), 813–817. <https://doi.org/10.1007/s00339-003-2490-0>
- Pontes, F. M. L.; Galhiane, M. S.; Santos, L. S.; Rissato, S. R.; Pontes, D. S. L.; Longo, E.; Leite, E. R.; Chiquito, A. J.; Pizani, P. S.; Jardim, R. F.; Escote, M. T. Pressure-induced electrical and structural anomalies in $\text{Pb}_{1-x}\text{Ca}_x\text{TiO}_3$ thin films grown at various oxygen pressures by chemical solution route. *J. Phys. D: Appl. Phys.* **2008**, *41* (11), 115402. <https://doi.org/10.1088/0022-3727/41/11/115402>
- Pontes, D. S. L.; Pontes, F. M. L.; Capeli, R. A.; Garzim, M. L.; Chiquito, A. J.; Longo, E. Structural, ferroelectric, and optical properties of $\text{Pb}_{0.60}\text{Ca}_{0.20}\text{Sr}_{0.20}\text{TiO}_3$, $\text{Pb}_{0.50}\text{Ca}_{0.25}\text{Sr}_{0.25}\text{TiO}_3$ and $\text{Pb}_{0.40}\text{Ca}_{0.30}\text{Sr}_{0.30}\text{TiO}_3$ thin films prepared by the chemical solution deposition technique. *Ceram. Int.* **2014**, *40* (8 Part B), 13363–13370. <https://doi.org/10.1016/j.ceramint.2014.05.052>
- Souza, R. A. Transport properties of dislocations in SrTiO_3 and other perovskites. *Curr. Opin. Solid State Mater. Sci.* **2021**, *25* (4), 100923. <https://doi.org/10.1016/j.cossms.2021.100923>
- Vopson, M. M.; Tan, X. Four-State Anti-Ferroelectric Random Access Memory. *IEEE Electron Device Lett.* **2016**, *37* (12), 1551–1554. <https://doi.org/10.1109/LED.2016.2614841>
- XCrySDen. *X-window CRYstalline Structures and DENsities*. 2019. <http://www.xcrysden.org/> (accessed 2022-05-18).
- Yang, C.; Xu, X. J.; Ali, W.; Wang, Y. J.; Wang, Y. P.; Yang, Y.; Chen, L.; Yuan, G. L. Piezoelectricity in Excess of 800 pC/N over 400 °C in BiScO_3 - PbTiO_3 - CaTiO_3 Ceramics. *ACS Appl. Mater. Interfaces*. **2021**, *13* (28), 33253–33261. <https://doi.org/10.1021/acsmi.1c07492>
- Yang, Y. H.; Wu, M.; Li, X. F.; Hu, H. H.; Jiang, Z. Z.; Li, Z.; Hao, X. T.; Zheng, C. Y.; Lou, X. J.; Pennycook, S. J.; Wen, Z. The Role of Ferroelectric Polarization in Resistive Memory Properties of Metal/Insulator/Semiconductor Tunnel Junctions: A Comparative Study. *ACS Appl. Mater. Interfaces*. **2020**, *12* (29), 32935–32942. <https://doi.org/10.1021/acsmi.0c08708>
- Yuan, H.; Li, L.; Hong, H.; Ying, Z.; Zheng, X.; Zhang, L.; Wen, F.; Xu, Z.; Wu, W.; Wang, G. Low sintering temperature, large strain and reduced strain hysteresis of BiFeO_3 - BaTiO_3 ceramics for piezoelectric multilayer actuator applications. *Ceram. Int.* **2021**, *47* (22), 31349–31356. <https://doi.org/10.1016/j.ceramint.2021.08.008>
- Zhang, S.; Li, Z.; Zhang, M.; Zhang, D.; Yan, Y. Enhanced piezoelectric properties of PYN-PHT ceramics by LiF addition in low temperature sintering. *J. Alloys Compd.* **2022**, *889*, 161649. <https://doi.org/10.1016/j.jallcom.2021.161649>
- Zhao, T.-L.; Bokov, A. A.; Wu, J. G.; Wang, H. L.; Wang, C.-M.; Yu, Y.; Wang, C.-L.; Zeng, K. Y.; Ye, Z.-G.; Dong, S. X. Giant Piezoelectricity of Ternary Perovskite Ceramics at High Temperatures. *Adv. Funct. Mater.* **2019**, *29* (12), 1807920. <https://doi.org/10.1002/adfm.201807920>